Forschungsbericht 2026-17

In-situ Automated Fiber Placement Manufacturing for Complex Geometries

Lukas Raps

Deutsches Zentrum für Luft- und Raumfahrt
Institut für Bauweisen und Strukturtechnologie
Stuttgart

DLR Deutsches Zentrum
für Luft- und Raumfahrt

Forschungsbericht 2026-17

In-situ Automated Fiber Placement Manufacturing for Complex Geometries

Lukas Raps

Deutsches Zentrum für Luft- und Raumfahrt
Institut für Bauweisen und
Strukturtechnologie
Stuttgart

218 Seiten
102 Bilder
24 Tabellen
313 Literaturstellen

DLR Deutsches Zentrum
für Luft- und Raumfahrt

Herausgeber:

Deutsches Zentrum
für Luft- und Raumfahrt e. V.
Wissenschaftliche Information
Linder Höhe
D-51147 Köln

ISSN 1434-8454
ISRN DLR-FB-2026-17
Erscheinungsjahr 2026
DOI: 10.57676/se3f-pv94

in-situ Tapelegen, thermoplastische Faserverbundwerkstoffe, Steering, Gap und Overlap Defekte, komplexe Geometrien, Pfadplanung, Mechanische Prüfung

Lukas RAPS
DLR, Institut für Bauweisen und Strukturtechnologie, Stuttgart

Automatisiertes Tapelegen mit in-situ Konsolidierung für komplexe Geometrien
Universität Stuttgart

Thermoplastisches Automated Fiber Placement (AFP) hat großes Potenzial für die zeit- und kosteneffiziente Herstellung von großen Strukturbauteilen für die Luft- und Raumfahrt, indem mittels in-situ-Konsolidierung auf die anschließende zeit- und kostenaufwändige Autoklav-Konsolidierung verzichtet werden kann. Während ebene Laminate bereits mit dem in-situ AFP-Verfahren hergestellt wurden und dabei ähnliche Eigenschaften wie autoklav- oder presskonsolidierte Referenzbauteile erreicht wurden, stellen komplexe doppelt gekrümmte Geometrien eine zusätzliche Herausforderung für den ohnehin schon anspruchsvollen Prozess dar. Mit dem Einsatz von in-situ AFP werden Defekte, die beim Aufbringen von zweidimensionalen Tapes auf dreidimensionale (doppelt gekrümmte) Geometrien unweigerlich entstehen, nicht in einem nachfolgenden Nachkonsolidierungsprozess abgemildert. Inwieweit diese Defekte im Laminat toleriert werden können und welchen Einfluss sie auf die mechanischen Eigenschaften haben, ist das Thema dieser Dissertation.

Diese Arbeit betrachtet daher die Interaktion von Effekten, die sich aus dem Prozess und der komplexen Geometrie ergeben. Drei komplexe Referenzgeometrien wurden hierzu als relevante Anwendungen des in-situ AFP Prozesses betrachtet: Ein Variable Stiffness Panel mit konstanter Bahnkrümmung, welches eine zweidimensionale akademische Repräsentation einer steifigkeitsoptimierten Struktur darstellt; eine rotationssymmetrische Wasserstofftankgeometrie; und ein komplexer Rumpfabschnitt, welcher Freiformgeometrien repräsentiert. Mithilfe von Pfadplanungssimulation und speziell entwickelter Python-Skripte wurden Ablegestrategien entwickelt und die resultierenden Steering-Defekte, Winkelabweichungen und Gap- oder Overlap-defekte quantifiziert, um eine Korrelation mit den Parametern der Ablegestrategie zu bestimmen.

Die ermittelten Krümmungsradien wurden als Ausgangswerte für eine umfassende experimentelle Studie zu Steering-Defekten verwendet. Aus den Versuchsergebnissen ergaben sich Erkenntnisse zu den Mechanismen und der Initiierung verschiedener Defekttypen infolge der Bahnkrümmung. Ein neuartiges Konzept der kritischen Bogenlänge wurde entwickelt und validiert, das den Lösungsraum der nutzbaren Krümmungsradien durch die Implementierung radiusabhängiger Bogenlängengrenzen erweitert. Mittels hochauflösender optischer 3D-Vermessungen wurde ein empirisches Modell zur Vorhersage der bahnkrümmungsinduzierten Geometrieänderungen des konsolidierten Tapes erstellt. Anhand des Modells wurden optimierte Ablegepfade entwickelt, um Gap-Defekte zwischen schmäler werdenden gekrümmten Tapes zu vermeiden. Die Methodik wurde in beispielhaften Fertigungsexperimenten erfolgreich validiert. Zur Validierung der Konsolidierungsqualität wurden Laminate mit unterkritischen Krümmungsradien hergestellt und mit mechanischen Vier- und Fünf-Punkt-Biegeversuchen getestet. Dabei wurden ähnliche Ergebnisse für die interlaminare Scherfestigkeit und die Biegefestigkeit erreicht wie bei den Referenzproben mit geraden Ablegebahnen. Somit wurde ein neuartiges erweitertes Kriterium für Steering erfolgreich eingeführt und validiert.

Die zweite wichtige Defektart, Gaps und Overlaps, wurde in einer weiteren Versuchsreihe untersucht. Realistische dreieckige, versetzt angeordnete Gap- und Overlap-Defekte, wie aus den Simulationsergebnissen abgeleitet, wurden in die Testlaminate eingebracht. Die Mikrostruktur der Laminate mit Defekten wurde mittels zerstörungsfreier Prüfung und mikroskopischer Bildgebungsverfahren detailliert analysiert und es wurden Poren in den Defektbereichen in Abhängigkeit vom Defekttyp und der Lagenorientierung über den Defekten identifiziert. Zug- und Druckversuche mit Defektproben wurden durchgeführt und mittels digitaler Bildkorrelation im Hinblick auf Festigkeit, Steifigkeit und Versagensmodi analysiert. Insgesamt führten die realistischen, versetzt angeordneten Defekte jedoch zu einer unterkritischen Veränderung der Laminatkomposition und die daraus resultierenden mechanischen Eigenschaften auf Coupon-Ebene zeigten nur einen geringen statistisch signifikanten Einfluss der Defekte. Ein größerer Einfluss wurde für das in-situ AFP-Prozessfenster in Bezug auf die

Werkzeugtemperatur und die Einhaltung der optimalen Prozessparameter festgestellt.

Diese Arbeit stellt eine umfassende Analyse der Korrelationen und Mechanismen zwischen komplexen Geometrien, Ablegestrategien und resultierenden Defekten für den in-situ AFP-Prozess dar. Sie liefert einen ersten Beweis dafür, dass komplexe in-situ AFP-Strukturen von hoher Qualität erreicht werden können.

in-situ Automated Fiber Placement, thermoplastic composites, steering, gap and overlap defects, complex geometries, path planning, mechanical testing

(Published in English)

Lukas RAPS
German Aerospace Center (DLR), Institute of Structures and Design, Stuttgart

In-situ Automated Fiber Placement Manufacturing for Complex Geometries

University of Stuttgart

Thermoplastic Automated Fiber Placement (AFP) has great potential for the time- and cost-efficient manufacturing of large-scale aerospace components by means of in-situ consolidation, omitting subsequent time-consuming and costly autoclave consolidation. While flat laminates have been manufactured using the in-situ AFP process, achieving properties similar to autoclave- or press-consolidated references, complex double-curved geometries present an additional challenge to the already ambitious process. Defects, which inevitably arise when applying two-dimensional tape material to three-dimensional (double-curved) geometries, are not mitigated by subsequent bulk consolidation when opting for in-situ manufacturing. The extent to which these defects can be tolerated in the laminate and what influence they have on the mechanical properties is the subject of this dissertation.

The work presented here addresses the combination of complications arising from the process and from the part geometry. To this end three, complex reference geometries were employed as relevant applications of the in-situ AFP process: A constant curvature Variable Stiffness Panel, which is a two-dimensional academic representation of a stiffness-optimized structure; a rotationally symmetrical hydrogen tank geometry; and a complex fuselage section, representing free-form geometries. Using tape placement simulation and specially developed Python scripts, layup strategies were developed and resulting steering defects, angle deviation and gap or overlap defects were quantified to determine a correlation with parameters of the layup strategy.

The derived steering radii were used as starting values for a comprehensive experimental study on steering defects. The experimental results provided insight into the mechanisms and onset of different defect types following in-plane path curvature. A novel concept of critical arc length was developed and validated expanding the design space of usable steering radii by introducing radius-dependent arc length limits. High-resolution optical 3D scans were used to develop an empirical model to predict the steering-induced geometry changes of the consolidated tape. From the model, coverage-optimized layup paths were developed to avoid gap defects between narrowing steered tapes. The methodology was successfully validated in example manufacturing experiments. Laminates with subcritical steered plies were manufactured and the consolidation quality was validated using mechanical four and five-point bending tests. Similar interlaminar shear strength and bending strength results were found as vin straight-path reference samples. A novel boundary condition allowing for steering was thus successfully established.

The second major defect type, gaps and overlaps, was investigated in another comprehensive test campaign. Realistic triangular staggered gap and overlap defect patterns as derived from the simulation results were introduced into test laminates. The microstructure of the defect laminates was analyzed in detail using advanced non-destructive testing and micro imaging methods and pores were identified as a function of the coverage ratio and ply orientation following the defects. Tensile and compressive coupon tests were carried out and analyzed using Digital Image Correlation with regard to strength, stiffness and failure modes. Overall the realistically staggered defects resulted in a subcritical disruption of the laminate composition and the resulting coupon-level mechanical properties showed little if any statistically significant impact of defects. A greater influence was found for the in-situ AFP process window with regard to tool temperature and close adherence to the optimal process parameters.

This work presents a comprehensive analysis of correlations between complex geometries, layup strategies and resulting defects for the in-situ AFP process. It provides initial proof that high quality complex in-situ AFP structures can be achieved.

In-situ Automated Fiber Placement Manufacturing for Complex Geometries

A thesis approved by the Faculty of Aerospace Engineering and Geodesy of the University of Stuttgart for the degree of Doctor of Engineering Sciences (Dr.-Ing.)

submitted by
Lukas Raps
born in
Baden-Baden

Principal Advisor:	Prof. Dr.-Ing. Heinz Voggenreiter
Co-Advisor:	Farjad Shadmehri, Ph.D., P.Eng., Associate Professor
Date of Defense:	31.03.2026

Institute of Aircraft Design
University of Stuttgart
2026

Contents

Contents **i**

Abstract **v**

Kurzfassung **vii**

Acknowledgements **ix**

List of Nomenclature **x**

List of Figures **xiii**

List of Tables **xviii**

1 Introduction **1**

1.1 Motivation 1

1.2 Thermoplastic Composites 1

1.3 Research Outline 2

2 State of the Art **3**

2.1 In-situ consolidation Automated Fiber Placement 3

2.1.1 In-situ consolidation: Process level impacting factors and mechanisms . . 10

2.1.2 Laminate level effects 18

2.1.3 Mechanical performance of flat laminates 19

2.2 Geometry-induced defects 21

2.2.1 Layup strategies 23

2.2.2 Steering 27

2.2.3 Gap and Overlap defects 31

2.3 Complex geometry applications 39

2.3.1 Variable Stiffness Panels 39

2.3.2 In-situ AFP technology demonstrators 41

2.4 Summary of the State of the Art 42

3 Research Aim and Outline **45**

3.1 Research Gap 45
3.2 Research Aim and Objectives 45
3.3 Outline of the thesis 46

4 Methodology 47
4.1 Material 47
4.2 Thermoplastic Automated Fiber Placement 47
4.3 Hot pressing 49
4.4 Process Parameter Analysis 50
4.5 Ultrasonic Testing 51
4.6 Optical 3D Scanning 52
4.7 Computed Tomography 52
4.8 Microscopy 52
4.9 Mechanical Testing 52
4.10 Digital Image Correlation 55
4.11 Statistical Methods 56

5 Geometry and Analysis of Layup paths 57
5.1 Variable Stiffness Panels 57
  5.1.1 Analytic algorithm for Variable Stiffness Panel analysis 58
  5.1.2 Results of Variable Stiffness Panel analysis 60
  5.1.3 Summary of Variable Stiffness Panel analysis 66
5.2 Hydrogen tank structure 66
  5.2.1 Tape placement simulation for hydrogen tank geometry analysis 68
  5.2.2 Results of hydrogen tank geometry analysis 70
  5.2.3 Summary of hydrogen tank geometry analysis 75
5.3 Complex fuselage section 75
  5.3.1 Tape placement simulation for complex fuselage geometry analysis 75
  5.3.2 Results of complex fuselage geometry analysis 76
  5.3.3 Summary of complex fuselage geometry analysis 78
5.4 Experimental validation of layup path analysis 78
  5.4.1 Manufacture of validation laminate 78
  5.4.2 Results of validation laminate analysis 79
  5.4.3 Summary of validation laminate analysis 80
5.5 Conclusion 81

6 In-plane path curvature 83
6.1 Analytical considerations for geodesic curvature and in-situ AFP 84

6.2 Experimental Analysis of in-plane curvature 87
6.2.1 Methodology 87
6.2.2 Results and discussion 87
6.3 Impact of sub-critical steering radii on in-situ consolidation laminate properties 91
6.3.1 Methodology 91
6.3.2 Results and Discussion 93
6.4 Development of an optimized steering layup strategy 97
6.4.1 Methodology 97
6.4.2 Results and discussion 99
6.5 Conclusion 107

7 Structural Impact of Gap and Overlap Defects 109
7.1 Experimental design 109
7.2 Results and discussion 114
7.2.1 Process Temperature 114
7.2.2 Positioning Accuracy 116
7.2.3 Ultrasonic Testing 118
7.2.4 Microsectioning 120
7.2.5 Computed Tomography 122
7.2.6 Tensile Testing 124
7.2.7 Compression Testing 132
7.3 Conclusion 142

8 Conclusion and Implications 145
8.1 Summary of Results 145
8.2 Discussion 146
8.3 Limitations and outlook 147
8.4 Conclusion 148

Appendix 149
A1 Literature 149
A2 Constant curvature Variable Stiffness Panel Algorithm 156
A3 Results of complex fuselage geometry analysis 162
A4 Bivariate spline coefficients 166

Bibliography 167

Abstract

Thermoplastic Automated Fiber Placement (AFP) has great potential for the time- and cost-efficient manufacturing of large-scale aerospace components by means of in-situ consolidation, omitting subsequent time-consuming and costly autoclave consolidation. While flat laminates have been manufactured using the in-situ AFP process, achieving properties similar to autoclave- or press-consolidated references for optimum manufacturing conditions, complex double-curved geometries present an additional challenge to the already ambitious process. Defects, which inevitably arise when applying two-dimensional tape material to three-dimensional (double-curved) geometries, are not mitigated by subsequent bulk consolidation when opting for in-situ manufacturing. The extent to which these defects can be tolerated in the laminate and what influence they have on the mechanical properties is the subject of this dissertation.

The work presented here addresses the combination of complications arising from the process and from the part geometry. To this end three, complex reference geometries were employed as relevant applications of the in-situ AFP process: A constant curvature Variable Stiffness Panel, which is a two-dimensional academic representation of a stiffness-optimized structure; a rotationally symmetrical hydrogen tank geometry; and a complex fuselage section, representing free-form geometries. Using tape placement simulation and specially developed Python scripts, layup strategies were developed and resulting steering defects, angle deviation and gap or overlap defects were quantified to determine a correlation with parameters of the layup strategy.

The derived steering radii were used as starting values for a comprehensive experimental study on steering defects. The experimental results provided insight into the mechanisms and onset of different defect types following in-plane path curvature. A novel concept of critical arc length was developed and validated expanding the design space of usable steering radii by introducing radius-dependent arc length limits. High-resolution optical 3D scans were used to develop an empirical model to predict the steering-induced geometry changes of the consolidated tape. From the model, coverage-optimized layup paths were developed to avoid gap defects between narrowing steered tapes. The methodology was successfully validated in example manufacturing experiments. Laminates with subcritical steered plies were manufactured and the consolidation quality was validated using mechanical four and five-point

bending tests. Similar interlaminar shear strength and bending strength results were found as in straight-path reference samples. A novel boundary condition allowing for steering was thus successfully established.

The second major defect type, gaps and overlaps, was investigated in another comprehensive test campaign. Realistic triangular staggered gap and overlap defect patterns as derived from the simulation results were introduced into test laminates. The microstructure of the defect laminates was analyzed in detail using advanced non-destructive testing and micro imaging methods and pores were identified as a function of the coverage ratio and ply orientation following the defects. Tensile and compressive coupon tests were carried out and analyzed using Digital Image Correlation with regard to strength, stiffness and failure modes. Overall the realistically staggered defects resulted in a subcritical disruption of the laminate composition and the resulting coupon-level mechanical properties showed little if any statistically significant impact of defects. A greater influence was found for the in-situ AFP process window with regard to tool temperature and close adherence to the optimal process parameters.

This work presents a comprehensive analysis of correlations between complex geometries, layup strategies and resulting defects for the in-situ AFP process. It provides initial proof that high quality complex in-situ AFP structures can be achieved.

Kurzfassung

Thermoplastisches Automated Fiber Placement (AFP) hat großes Potenzial für die zeit- und kosteneffiziente Herstellung von großen Strukturbauteilen für die Luft- und Raumfahrt, indem mittels in-situ-Konsolidierung auf die anschließende zeit- und kostenaufwändige Autoklav-Konsolidierung verzichtet werden kann. Während ebene Laminate bereits mit dem in-situ AFP-Verfahren hergestellt wurden und dabei, unter optimalen Prozessbedingungen, ähnliche Eigenschaften wie autoklav- oder presskonsolidierte Referenzbauteile erreicht wurden, stellen komplexe doppelt gekrümmte Geometrien eine zusätzliche Herausforderung für den ohnehin schon anspruchsvollen Prozess dar. Mit dem Einsatz von in-situ AFP werden Defekte, die beim Aufbringen von zweidimensionalen Tapes auf dreidimensionale (doppelt gekrümmte) Geometrien unweigerlich entstehen, nicht in einem nachfolgenden Nachkonsolidierungsprozess abgemildert. Inwieweit diese Defekte im Laminat toleriert werden können und welchen Einfluss sie auf die mechanischen Eigenschaften haben, ist das Thema dieser Dissertation.

Diese Arbeit betrachtet daher die Interaktion von Effekten, die sich aus dem Prozess und der komplexen Geometrie ergeben. Drei komplexe Referenzgeometrien wurden hierzu als relevante Anwendungen des in-situ AFP Prozesses betrachtet: Ein Variable Stiffness Panel mit konstanter Bahnkrümmung, welches eine zweidimensionale akademische Repräsentation einer steifigkeitsoptimierten Struktur darstellt; eine rotationssymmetrische Wasserstofftankgeometrie; und ein komplexer Rumpfabschnitt, welcher Freiformgeometrien repräsentiert. Mithilfe von Pfadplanungssimulation und speziell entwickelter Python-Skripte wurden Ablegestrategien entwickelt und die resultierenden Steering-Defekte, Winkelabweichungen und Gap- oder Overlap-defekte quantifiziert, um eine Korrelation mit den Parametern der Ablegestrategie zu bestimmen.

Die ermittelten Krümmungsradien wurden als Ausgangswerte für eine umfassende experimentelle Studie zu Steering-Defekten verwendet. Aus den Versuchsergebnissen ergaben sich Erkenntnisse zu den Mechanismen und der Initiierung verschiedener Defekttypen infolge der Bahnkrümmung. Ein neuartiges Konzept der kritischen Bogenlänge wurde entwickelt und validiert, das den Lösungsraum der nutzbaren Krümmungsradien durch die Implementierung radiusabhängiger Bogenlängengrenzen erweitert. Mittels hochauflösender optischer 3D-Vermessungen wurde ein empirisches Modell zur Vorhersage der bahnkrümmungsinduzierten Geometrieänderungen des konsolidierten Tapes erstellt. Anhand des Modells wurden optimierte Ablegepfade entwickelt, um Gap-Defekte zwischen schmäler werdenden gekrümmten Tapes zu vermeiden. Die Methodik wurde in beispielhaften Fertigungsexperimenten erfolgreich validiert. Zur Validierung der Konsolidierungsqualität wurden Laminate mit unterkritischen Krümmungsradien hergestellt und mit mechanischen Vier- und Fünf-Punkt-Biegeversuchen getestet. Dabei wurden ähnliche Ergebnisse für die interlaminare Scherfestigkeit und die Biegefestigkeit erreicht wie bei den Referenzproben mit geraden Ablegebahnen. Somit wurde ein neuartiges erweitertes Kriterium für Steering erfolgreich eingeführt und validiert.

Die zweite wichtige Defektart, Gaps und Overlaps, wurde in einer weiteren Versuchsreihe untersucht. Realistische dreieckige, versetzt angeordnete Gap- und Overlap-Defekte, wie aus den Simulationsergebnissen abgeleitet, wurden in die Testlaminate eingebracht. Die Mikrostruktur der Laminate mit Defekten wurde mittels zerstörungsfreier Prüfung und mikroskopischer Bildgebungsverfahren detailliert analysiert und es wurden Poren in den Defektbereichen in Abhängigkeit vom Defekttyp und der Lagenorientierung über den Defekten identifiziert. Zug- und Druckversuche mit Defektproben wurden durchgeführt und mittels digitaler Bildkorrelation im Hinblick auf Festigkeit, Steifigkeit und Versagensmodi analysiert. Insgesamt führten die realistischen, versetzt angeordneten Defekte jedoch zu einer unterkritischen Veränderung der Laminatkomposition und die daraus resultierenden mechanischen Eigenschaften auf Coupon-Ebene zeigten nur einen geringen statistisch signifikanten Einfluss der Defekte. Ein größerer Einfluss wurde für das in-situ AFP-Prozessfenster in Bezug auf die Werkzeugtemperatur und die Einhaltung der optimalen Prozessparameter festgestellt.

Diese Arbeit stellt eine umfassende Analyse der Korrelationen und Mechanismen zwischen komplexen Geometrien, Ablegestrategien und resultierenden Defekten für den in-situ AFP-Prozess dar. Sie liefert einen ersten Beweis dafür, dass komplexe in-situ AFP-Strukturen von hoher Qualität erreicht werden können.

Acknowledgements

First and foremost, I would like to thank my technical supervisor Ashley, who introduced me to the world of science and the mysteries of thermoplastic Automated Fiber Placement. His early promotion of the doctoral project, support in finding a research topic, years of professional supervision, close friendly cooperation and, last but not least, editing of the manuscript were invaluable for this work. My doctoral supervisor Heinz, who, despite his extensive commitments, always had an open ear and encouraged me in my research project in inspiring conversations. As the department head, Sebastian supported the doctoral project as a mentor from the very beginning and on the project side, I found extensive support from Georg, who helped me integrate the work into projects and finance the research.

On the experimental side, Samuel, as the operator of the AFP facility, was of central importance to the work. His tireless commitment to improving the thermoplastic AFP process and his willingness to implement my special requests for the manufacturing trials was essential for the success of the experiments. I would also like to thank the other members of the AFP team, Ines and Daniel, for integrating my experiments within the tight schedule of the AFP facility and for their support in analyzing the results. I hired Yannick as a bachelor thesis student and later an assistant scientist, and he proved so helpful to the AFP team that we ended up hiring him for a follow-up PhD project. I also want to thank Andreas for the pleasant cooperation in the technical center and his patient understanding of my special requests. Mathieu and Tobias were a great support for all questions about mechanical tests and I have made use of their helpfulness far too often.

And finally, there was the Pavoni Round Table with alternating members, in which, in addition to the fine art of espresso extraction, the challenges of the doctoral students involved were discussed and sometimes even solutions found.

To all the students and DLR colleagues involved in the department and beyond, I want to express my deepest gratitude.

List of Nomenclature

A_{defect}	Cumulated gap or overlap defect area [mm^2]
A_{dome}	Area of spherical dome [mm^2]
B_0	Variable stiffness panel inflection point x-coordinate [mm]
$B(i)$	Variable stiffness panel inflection point x-coordinate of individual tows [mm]
D	Shifting distance [mm]
D_0	Variable stiffness panel shifting distance (Overlaps) [mm]
$D_{0,gaps}$	Variable stiffness panel shifting distance (Gaps) [mm]
D_h	Degree of Healing [-]
D_{ic}	Degree of Intimate Contact [-]
E	Fundamental coefficient of Surface S [-]
E_b	Flexural modulus [MPa]
E_c	Compressive modulus [MPa]
E_t	Tensile modulus [MPa]
F	Fundamental coefficient of Surface S [-]
F_{con}	Consolidation force [N]
F_t	Tape force [N]
G	Fundamental coefficient of Surface S [-]
K	Curvature [1/mm]
K_g	Geodesic curvature [1/mm]
K_n	Normal curvature [1/mm]
L	Support span [mm]
P	Load [N]
P_{Laser}	Laser power [W]
P_u	Ultimate load [N]
PBS	Percent bending strain [%]
R	Radius [mm]
S	Staggering factor [-]
$S(u,v)$	Parametric surface [-]
T_0	Angle between y-axis and reference curve at origin of VSP [°]

T_1	Reference curve angle at the lateral boundaries of VSP [°]
T_g	Glass transition temperature [°C]
T_m	Melting temperature [°C]
T_{np}	Nip point temperature [°C]
T_{ply}	Ply temperature [°C]
T_{set}	Set point temperature [°C]
T_{tape}	Tape temperature [°C]
T_{tool}	Tool temperature [°C]
l_{crit}	Critical arc length [mm]
n	Number of parallel tows in a track (course) [-]
p_{app}	Applied pressure [N/m^2]
r	Radius of the polar opening of a tank geometry [mm]
s_0	Shift distance [mm]
t	Time [s]
t_c	Contact time [s]
t_f	Final bonding time [s]
t_n	Specimen thickness [mm]
t_w	Welding time [s]
t_t	Tape thickness [mm]
u	Surface parameter [-]
v	Surface parameter [-]
v_{layup}	Layup speed [mm/s]
w	Specimen width [mm]
w_c	Course width [mm]
w_t	Tape width [mm]
$w_{t,c}$	Consolidated tape width [mm]

Greek Symbols

α	Gradient of a loxodrome on a sphere [-]
α_{arc}	Central angle of circular steering path [rad]
α_{defect}	Area related fraction of gap or overlap defects [-]
γ	Shear strain [-]
γ_{defect}	Opening angle of gap or overlap defects [°]
Γ_{ij}^k	Christoffel symbol for the surface S [-]
δ	Mid-span deflection [mm]

$\Delta\sigma$	Stress difference [Mpa]
$\Delta\epsilon$	Strain difference [-]
ε	Tensile strain [-]
ε_b	Bending strain [-]
ε_c	Compressive strain [-]
ε_e	Thermal emissivity [-]
θ	Polar angle (colatitude angle) in spherical coordinates [rad]
θ_{dev}	Fiber angle deviation [°]
θ_f	Fiber angle [°]
ρ	Steering radius in VSP design [mm]
ρ_w	Width Parameter in in-plane path curvature strain analysis [mm]
σ_0	Tape tension [MPa]
σ_b	Bending stress [MPa]
σ_{cu}	Ultimate compressive strength [MPa]
σ_{tu}	Ultimate tensile strength [MPa]
τ	Interlaminar shear stress [MPa]
ϕ	Angle between loxodrome curve and meridians on a sphere [rad]
φ	Azimuthal angle in spherical coordinates [rad]

Acronyms

$4PB$	Four point bending
$5PB$	Five point bending
AFP	Automated Fiber Placement
$ANOVA$	Analysis of Variance
ATL	Automated Tape Laying
CAD	Computer aided design
CAI	Compression after impact
CF	Carbon fiber
CNC	Computerized Numerical Control
CT	Computed tomography
DCB	Double cantilever beam
DIC	Digital image correlation
FE	Finite Element
FVF	Fiber volume fraction
$HCCF$	Hydraulic Compression Test Kit for Composites

HP	Hot pressed
HT	Heated tooling
ILSS	Interlaminar shear strength
IPSS	In-plane shear strength
LM-PAEK	Low-melt polyaryletherketone
MTLH	Multi tape laying head
Nd : YAG	Neodymium-doped yttrium aluminum garnet
NIR	Near infrared
n.s.	Not (statistically) significant
OoA	Out of Autoclave
*PA*6	Polyamide 6
PEEK	Polyether ether ketone
PEKK	Polyether ketone ketone
PPS	Polyphenylene sulfide
Prepreg	Preimpregnated composite semi-finished product
QI	Quasi-isotropic
RMSE	Root mean square error
RT	Room temperature
SLS	Single lap shear
TCP	Tool center point
UD	Unidirectional
VCSEL	Vertical-cavity surface-emmitting laser
VSP	Variable stiffness panel
VSS	Variable spot size

List of Figures

2.1 (a) Automated Fiber Placement end-effector and multiple tape layup, (b) Drawing of Hercules FPM1 4

2.2 Sikorsky ACAP tail cone 4

2.3 NASA FPX Fiber Placement System (a) Drawing of 7-axis machine design, (b) Advanced steering capabilities 5

2.4 In-situ AFP process principle diagram 6
2.5 Nitrogen hot gas torch AFP systems: (left) Automated Dynamics end-effector, (right) Accudyne Systems end-effector 7
2.6 Diode laser intensity distribution with rectangular wave guide 8
2.7 Diode laser heating systems: (left) AFP end-effector at DLR Stuttgart with laser optics and animated laser beam, (right) Electroimpact end-effector with variable spot size laser system 9
2.8 In-situ AFP process mechanisms and variables 10
2.9 Temperature and consolidation pressure profile during in-situ AFP 11
2.10 Toray TC1225 CF/LM-PAEK 12.7 mm prepreg tape profilometry surface scan . 13
2.11 Quasi-isotropic laminate microsection with gap defect between adjacent tapes . . 19
2.12 Layup strategies and resulting gap defects, steering radii and angle deviation of a spherical reference surface geometry 22
2.13 Fixed angle reference curve definition via projection of a major axis onto the surface 23
2.14 Linear angle variation reference curve 25
2.15 Path propagation strategies 26
2.16 Thermoset AFP steering defects 28
2.17 Thermoplastic AFP steering-induced out-of-plane wrinkle defect 30
2.18 Coverage ratio and resulting gaps and overlaps 32
2.19 Single sided cuts and Zipper cut strategy 32
2.20 Scanning Electron Microscopy cross-section images of cross-ply laminates with 3.175 mm rectangular gap and overlap defects, cured with and without caul plate 33
2.21 Microsection of defects 34
2.22 Computed tomography scan of triangular gap defects 37
2.23 Variable Stiffness Panels: (a) Thermoset AFP laminate with central cut-out, (b) Dry fiber placement laminate 40
2.24 Thermoplastic wing box segment 41
2.25 Clean Sky 2 in-situ AFP demonstrator components 42

4.1 Thermoplastic tape placement facility at DLR Stuttgart 48
4.2 Hot press facilities at DLR Stuttgart 50
4.3 AFP end effector thermal camera temperature measurement principle 51
4.4 Four point bending DIC deflection analysis 54
4.5 Mechanical test setups with DIC 55

5.1 Constant curvature Variable Stiffness Panel design with 0 % coverage ratio . . . 58
5.2 Constant curvature Variable Stiffness Panel design with 100 % coverage ratio . . 59
5.3 Variable Stiffness Panel Python algorithm - Input parameters and analysis results 60

5.4 Variable Stiffness Panel angle deviation analysis 61
5.5 Maximum and average angle deviation for Variable Stiffness Panels with varying number of parallel tows and tape width 61
5.6 Steering visualization of Variable Stiffness Panels with tow cuts on the inside radius 62
5.7 Variable Stiffness Panel analysis of minimum and maximum steering radii of individual tows for varying number of parallel tows and tape width 63
5.8 Overlap defect visualization of Variable Stiffness Panels with tow cuts on the inside radius 63
5.9 Variable Stiffness Panel defect analysis for varying number of parallel tows and tape width 64
5.10 Staggered plies and resulting overlap defect pattern of a Variable Stiffness Panel 65
5.11 Filament wound composite pressure vessels: (left) Example tank structure with geodesic winding pattern, (right) Dome thickness profiles for filament wound composite pressure vessels 66
5.12 NASA and Boeing thermoset AFP composite tank 67
5.13 Spherical coordinate system of tank geometry and loxodrome reference curve definition 68
5.14 VCP gap defect misscalculation 69
5.15 VCP tank layup simulation and analysis 70
5.16 Angle deviation analysis for fixed angle layup on spherical domes with varying number of parallel tows and tape width 71
5.17 Geodesic curvature of loxodrome curves on spherical tank domes 72
5.18 Hydrogen tank geometry gap defect analysis for 1000 mm diameter, varying ply angles, number of parallel tows and tape width 73
5.19 1000 mm diameter spherical dome section gap defect staggering analysis 74
5.20 Complex fuselage geometry with boundary curve and central cutout 75
5.21 Complex fuselage geometry layup analysis result 77
5.22 Tank section laminate 78
5.23 Comparison of VCP defect simulation and experimental result 80

6.1 Analytical derivation of stress distribution of constant curvature steered path with straight lead-in 85
6.2 Steering stress-induced tape deformation modes 86
6.3 Steering experiment example image with steering radius 800 mm 88
6.4 Preliminary steering critical arc length and tape width measurement results . . . 89
6.5 Heatmap and average track temperature curves of steering and straight reference experiments 90

6.6 Steering laminate design with example layup paths and specimen positions . . . 92
6.7 Steering laminate ultrasonic C-Scan backwall results 94
6.8 Steering laminate microsections 95
6.9 Five point bending test results 95
6.10 Four point bending strength and modulus results 97
6.11 Optical 3D scan analysis of steering experiments 99
6.12 Critical arc length and arc angle analysis for onset of out-of-plane defects with hot-pressed substrate 100
6.13 Resulting steering panel and analysis of straight half-inch reference tracks 101
6.14 Optical 3D scan analysis results for superimposed 1500 mm, 1250 mm and 1000 mm steering radii with half-inch tape 101
6.15 Optical 3D scan analysis results for superimposed 1500 mm, 1250 mm and 1000 mm steering radii with quarter-inch tape 102
6.16 Bivariate spline fits for average track edges of 1500 mm, 1250 mm and 1000 mm steering radii with half-inch tape 103
6.17 Steering radius match and evaluation of curve fits 105
6.18 Optimized example steering plies and manufactured validation plies 106
6.19 Optical 3D scans of steering plies 107

7.1 Derivation and design of defect laminates and resulting tensile and compressive specimens 111
7.2 Measurement of triangular defect positions 112
7.3 Defect specimen manufacturing process steps 113
7.4 Overlap and quarter-inch gap defect laminate design 113
7.5 Heatmap and average track temperature curves of gap ply 115
7.6 Measured corner points of half-inch triangular defects compared to the reference geometry 117
7.7 Ultrasonic C-Scan backwall and internal echo test results of in-situ consolidated defect laminates 118
7.8 Ultrasonic C-Scan backwall test result of hot pressed laminates 119
7.9 Half-inch gap and overlap defect microsection results 121
7.10 Quarter-inch gap defect microsection results 122
7.11 Computed Tomography RT half-inch gap defect images 123
7.12 Compiled computed tomography results of tensile specimens before testing . . . 124
7.13 Reference specimen tensile test results 126
7.14 Room temperature gap specimen tensile test results 127
7.15 Heated tooling gap and overlap specimen tensile test results 128

7.16 Hot pressed gap specimen tensile test results 129
7.17 Tensile strength and modulus results of reference, gap and overlap defect specimens 130
7.18 Reference half-inch specimen compressive test results 133
7.19 Reference quarter-inch specimen compressive test results 135
7.20 Room temperature gap specimen compressive test results 136
7.21 Heated tooling gap and overlap specimen compressive test results 137
7.22 Hot pressed gap and overlap specimen compressive test results 139
7.23 Compressive strength and modulus results of reference, gap and overlap defect specimens 140

8.1 Constant curvature Variable Stiffness Panel design with one-sided tow cuts: (a) definition of intersection points, (b) 100 % coverage ratio tow cuts, (c) 0 % coverage ratio tow cuts 159
8.2 Constant curvature Variable Stiffness Panel design with tow cuts at the inner radius: (a) definition of intersection points, (b) 100 % coverage ratio tow cuts, (c) 0 % coverage ratio tow cuts 159
8.3 Mirrored constant curvature Variable Stiffness plies: (a) Mirrored reference curves, (b) One-sided tow cuts and 100 % coverage ratio, (c) tow cuts at the inner radius and 100 % coverage ratio tow cuts 160
8.4 Variable Stiffness defect analysis: (a) Steering arc length analysis, (b) Defect area analysis, (c) Angle deviation analysis 161
8.5 Complex fuselage geometry layup analysis results of 1st 45 ° ply 163
8.6 Complex fuselage geometry layup analysis results of 1st 0 ° ply 164
8.7 Complex fuselage geometry layup analysis results of 1st 90 ° ply 165

List of Tables

2.1 Diode laser in-situ AFP, 200 °C heated tooling and hot-press re-consolidated reference results . . . 21
2.2 Thermoset AFP critical steering radii . . . 28
2.3 Thermoplastic AFP steering experiments . . . 31
2.4 Literature overview of achieved relative mechanical results of autoclave-consolidated thermoset samples with rectangular defects compared to defect-free reference . . . 36

4.1 Thermoplastic prepreg materials . . . 47
4.2 Laser optics used for varying track width configurations . . . 48
4.3 AFP manufacturing parameters . . . 49
4.4 Consolidated tape widths . . . 49
4.5 Hot press consolidation process parameters . . . 50

5.1 Composite tank geometries . . . 68

6.1 Experimental design of steering laminates . . . 93
6.2 Median and standard deviation of nip point temperatures over all plies in areas of mechanical test specimen positions . . . 93
6.3 Iterations of steering radii and respective tape width . . . 98
6.4 Bivariate spline fitting parameters and residuals . . . 104

7.1 Factorial design of gap and overlap defect laminates . . . 110
7.2 Overview of the influence of defects on mechanical properties: statistically significant changes in the median values compared to the reference median of the respective sample configuration rounded to integer percentages . . . 142

8.1 Literature overview of achieved relative Short Beam Strength of in-situ AFP compared to press- and autoclave-consolidated reference samples . . . 150
8.2 Literature overview of achieved laminate porosity of in-situ AFP samples . . . 151
8.3 Literature overview of achieved relative tensile results of autoclave-consolidated thermoset samples with rectangular defects compared to defect-free reference . . . 152

8.4 Literature overview of achieved relative tensile results of autoclave-consolidated thermoset samples with rectangular defects compared to defect-free reference . . 153
8.5 Literature overview of achieved relative compressive results of autoclave-consolidated thermoset samples with rectangular defects compared to defect-free reference 154
8.6 Literature overview of achieved relative compressive results of autoclave-consolidated thermoset samples with rectangular defects compared to defect-free reference 155
8.7 Complex fuselage section layup strategy: start point coordinates for fixed angle reference curves, maximum and minimum number of parallel tows 162
8.8 Angle deviation and steering results of complex fuselage geometry 166

Chapter 1

Introduction

1.1 Motivation

Carbon-fiber-reinforced composites are the state of the art material system for airframe manufacture of large commercial aircraft. The latest generation of commercial aircraft is made of 50 % composite material. (Boeing 787: 50 % [1] and Airbus A350: 54 % [2]). Composite materials have superior specific strength- and stiffness properties, which make them excellent lightweight engineering materials. Furthermore, very good fatigue properties allow high utilization of the machanical properties and extended service intervals. This results in low operating cost of the aircraft over its lifespan. The manufacture of these large-scale primary composite aircraft structures using the state of the art technology is however time-, energy- and cost-intensive. In order to adopt large scale primary composite structures for the next generation of short- to medium range aircraft such as the Airbus A320- and Boeing 737-series successor aircraft, higher manufacturing rates and lower production cost have to be achieved. While as of 2023, 6 and 4 units per month are manufactured of composite aircraft A350 and 787, respectively, 60 units per month are manufactured of both A320- and 737-series aircraft, respectively and increasing demand in the sector requires even higher rates of 80 to 100 units per month in the future [3, 4].

To this end, large American- and European research projects are currently investigating the challenge of high rate manufacturing of large composite aircraft structures: The American HiCAM project led by NASA and the European Clean Sky 2 program with the Large Passenger Aircraft (LPA) Demonstrator project and the follow-up Clean Aviation program [5–7].

1.2 Thermoplastic Composites

One promising approach to achieving high-rate capability, which is being considered in the aforementioned research projects, is the use of thermoplastic composites. Out-of-Autoclave (OoA) manufacturing technologies such as thermoplastic Automated Fiber Placement (AFP) and Thermoforming in combination with advanced joining processes by thermoplastic welding theoretically represent a significant speed advantage over conventional thermoset autoclave design and rivet joints [8, 9]. Furthermore, structural mass decrease could be achieved by advancing from state of the technology thermoset composite airframes to thermoplastic composite materials. Dispensing with riveted joints can save the structural mass of the rivets themselves as well as potentially decrease required laminate thickness, which the rivet joint is often the dimensioning factor for. AFP is the most suitable process for the production of large-area structural parts such as fuselage skins or wing shells and its thermoset variant represents the state of the art manufacturing technology for these structural components. In its ultimate form, thermoplastic AFP enables so-called in-situ consolidation, i.e. its use as a purely additive manufacturing process without post-consolidation in an autoclave or pressing process. As it dispenses with post-consolidation process steps, in-situ AFP offers particularly great potential for high rate manufacturing [7]. At the same time, it poses a particularly great challenge, as process- or material-related defects remain in the manufactured part. Recent developments in automated manufacturing technology, process control, data analysis and newly developed thermoplastic composite materials have led to renewed interest in applying the process to aerospace structures.

1.3 Research Outline

This work examines the application of the in-situ AFP process for complex (double-curved) structural parts and analyzes the resulting key mechanisms whereby the analysis is based on relevant application-related component geometries. Solution spaces and limits of the process and possible part curvatures are outlined and the expected mechanical properties of complex laminates are quantified. The result thus makes a relevant contribution to evaluating the applicability of the process for double-curved structures, presents advanced manufacturing strategies optimized for in-situ AFP and provides the basis for subsequent investigations of complex test specimens and detailed mechanical simulations.

Chapter 2

State of the Art

The following section presents a review of the literature on in-situ consolidation Automated Fiber Placement (in-situ AFP) and its application for complex geometries. Key milestones in the development of the AFP technology are briefly summarized. The process principle of in-situ AFP, relevant process-specific parameters and mechanisms are illustrated. The currently achievable laminate quality of in-situ AFP manufactured structures is eventually presented as a baseline for the subsequent investigation of the application of the process for complex geometry structures. The second part of the literature review focuses on complex geometries and concomitant effects on the AFP process. Since many effects and concepts apply to all AFP technologies, thermoset and dry fiber AFP for complex geometries must be included in addition to the focal thermoplastic approach. Layup strategies and their influence on resulting geometry-related defects are presented. These defects can be categorized into two main areas, steering effects and gaps/overlap defects, both of which are presented in the context of the existing literature. Finally, complex parts already shown in the literature that were manufactured using in-situ AFP are presented.

2.1 In-situ consolidation Automated Fiber Placement

The following is an overview of the in-situ AFP process and the achievable laminate quality, which is the reference against which complex laminates are later compared. Detailed literature reviews can be found in [10–14]

Automated Fiber Placement (AFP) is an additive manufacturing technology that originated as an evolution of Automated Tape Laying (ATL) and was first mentioned in a patent in 1974 (Figure 2.1(a)) [15]. While in ATL one single wide prepreg tape is deposited, the AFP process uses multiple parallel narrow tapes, also referred to as tows, simultaneously. This enables the manufacture of more complex geometries compared to ATL, with the reduced tape width of deposited tows able to adapt more easily to surface contours and curvatures [16].

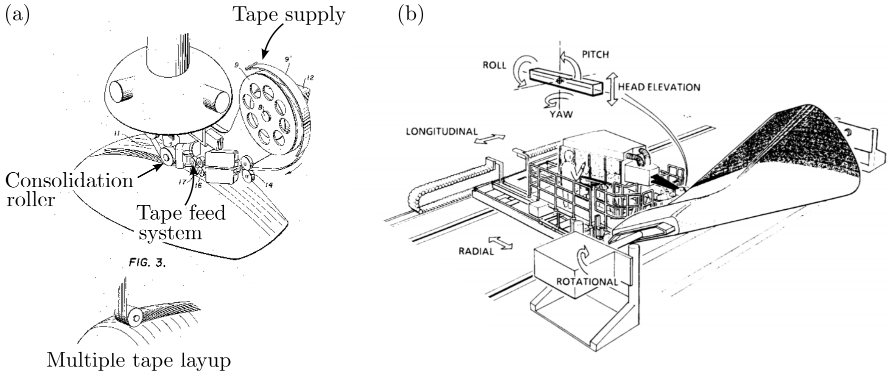

Figure 2.1: (a) Automated Fiber Placement end-effector and multiple tape layup [15], (b) Drawing of Hercules FPM1 [17]

Hercules Aerospace started developing the first AFP machine in 1980, with the first functional machine presented in 1983 (Figure 2.1(b)) [17]. Relatively cheap dry fiber filament was impregnated using hot melt resin in the delivery system of the machine. At the same time it was able to lay down tape at orientations from 0 ° to 90 ° and cut and restart individual tows. The process thus combined the complex geometry capabilities of filament winding with the ability of ATL to produce large non-rotationally symmetrical components.

Within the Advanced Composite Airframe Program (ACAP), Sikorsky successfully manufactured a helicopter tail cone using this technology (Figure 2.2). In the same year the first pre-impregnated tow (prepreg) material was developed for AFP to increase resin content control [18–20].

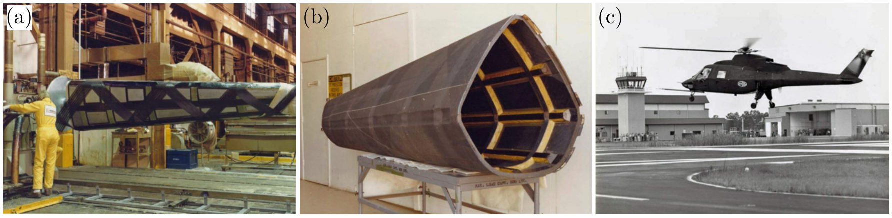

Figure 2.2: Sikorsky ACAP tail cone: (a) Tail cone manufacture using a combination of Filament Winding and Fiber Placement [19, 20], (b) Finished integral tail cone structure [19], (c) Sikorsky S-75 ACAP prototype first flight 1984 [18, 19]

The principle of AFP was first presented to the public at SAMPE conference in 1989 [21] [22]. At NASA Marshall Space Center, Vickers et al. developed a functional AFP machine (Fiber Placement System, FPX) for layup in complex-shaped geometries, capable of depositing up to 24 3.175 mm wide tows. The system was based on a CNC machine and allowed for individual tow cuts and restarts. Even advanced steering capabilites were already presented (Figure 2.3) [23].

At the same time as thermoset AFP facilities were being developed and tested in the late 1980s, thermoplastic tape consolidation was also under investigation in the context of filament winding [24]. Thermoplastic tape consolidation was implemented into an AFP machine for the first time in 1992 [25]. In contrast to thermoset tape placement, which relies on tackiness of the uncured thermoset prepreg for the deposited tape to remain in position, thermoplastic tape consolidation requires a more powerful heating source to heat the polymer matrix above or close to the melting temperature to create a temporary bond or ideally full consolidation. It should however be noted that the temperatures at which thermoset tack and thermoplastic consolidation occur are drastically different for aerospace-grade composite materials; 60 °C and >300 °C, respectively.

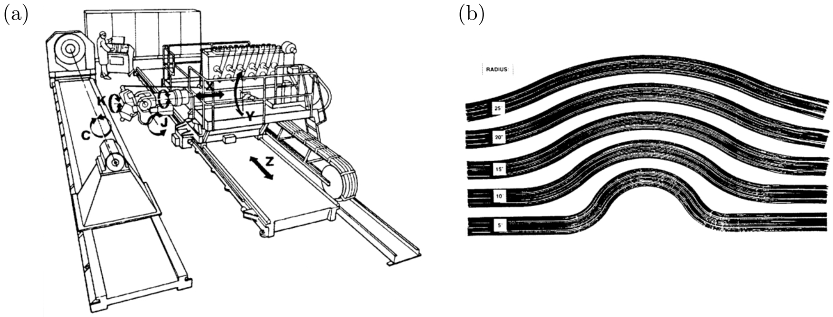

Figure 2.3: NASA FPX Fiber Placement System [23] (a) Drawing of 7-axis machine design, (b) Advanced steering capabilities

In-situ AFP process principle

The in-situ AFP process is a special form of thermoplastic AFP process that is characterized by the fact that it is a purely additive process without post-consolidation. The aim is to achieve full consolidation in the short time window of the additive tape placement process. A principle diagram of the process is shown in Figure 2.4.

Unidirectional (UD) prepreg tape is conveyed through a tape guiding system towards the consolidation roller. Both, the incoming tape and the already deposited prepreg material (substrate) are heated by a heat source, often a laser close to the melting temperature of the thermoplastic resin material (heating phase). The heated surfaces leave the laser spot shortly before the point of first contact between the tape and substrate due to a geometry-induced laser shadow and the cooling phase begins. The point of first contact is called nip point. The consolidation roller then presses the incoming tape onto the substrate.

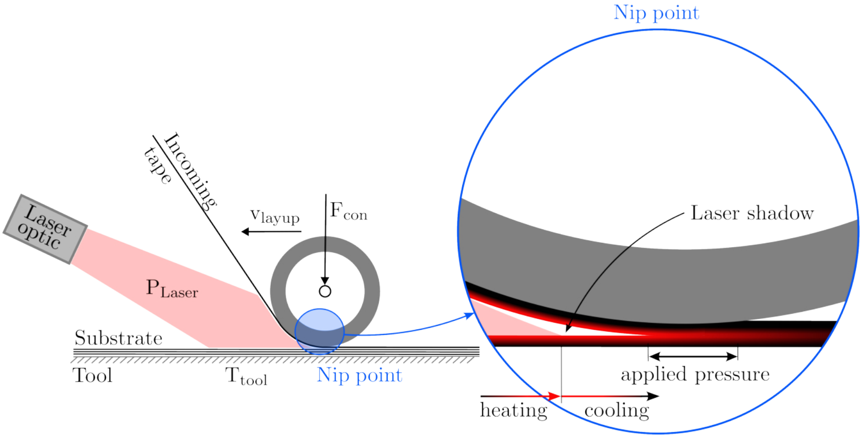

Figure 2.4: In-situ AFP process principle diagram

Depending on the consolidation roller geometry and material, particularly its degree of elastic deformation, a given compaction (consolidation) area with a specific pressure distribution is following the nip point. Rigid (steel) rollers result in smaller consolidation areas than conformable (silicone or polyurethane) rollers. During the time of applied pressure, the bond between incoming tape and substrate is formed and ideally, full consolidation is achieved. Typically multiple tapes (tows) are layed simultaneously and form a course (also referred to as a track).

In-situ AFP heat sources

Despite commencing development at the same time, convective heat sources in the form of hot gas torch and hot flame heating systems were primarily used for in-situ AFP prior to laser heating sources reaching technological maturity and becoming widely accepted. Hot gas torch and hot flame heating systems employ simple convective heating to achieve matrix melting at the prepreg surface. Mantell et al. were the first to implement thermoplastic tape consolidation in an AFP system using a nitrogen hot gas torch as a heat source and measured short beam shear strength of CF/PEEK at 45 % of a press-consolidated reference [25]. Commercially available systems were developed by Automated Dynamics (Niskayuna, NY, US, now part of Trelleborg Group, SWE) [26–29] and Accudyne Systems Inc. (Newark, DE, US) [30–35]. The Automated Dynamics system consisted of a hot gas torch and a consolidation roller (Fig. 2.5 left) whereas the Accudyne system used two or more nitrogen hot gas torches and two consolidation rollers (Fig. 2.5 right). In a recent (2009) iteration of the Accudyne system, the first compaction unit was heatable whereas the second compaction unit could be cooled for optimized heating and cooling rates [33]. Mechanical properties of 76 % (short beam shear strength) to 97 % (axial compression strength) of autoclave reference using standard APC-2 Prepreg tape were achieved with this technology [33–35]. The layup rate of 30.5 mm/s was however low compared to modern laser heating systems achieving more than three times higher layup rates [36]. In addition, the two-stage consolidation unit limits the potential for more complex geometry layup.

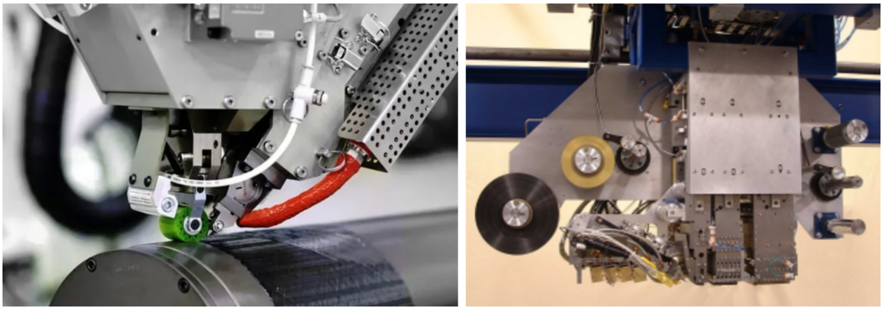

Figure 2.5: Nitrogen hot gas torch AFP systems: (left) Automated Dynamics end-effector [37] with permission from Trelleborg Sealing Solutions, Albany, (right) Accudyne Systems end-effector, reprinted from [33] with permission from SAMPE

Khan et al. investigated hydrogen/oxygen hot flame as a heat source, reaching hot gas temperatures of up to 1300 °C [38, 39]. In combintation with a 280 °C heated tooling, the high process temperature resulted in very high interlaminar shear strength results of 85.5 MPa (91 % of autoclave reference).

Compared to convective heat sources, laser heat sources are characterized by even higher energy density and good controllability. Laser heating systems using CO_2 lasers [24, 40–44], Nd:YAG lasers [45] and diode lasers [7, 36, 46–69] have been used for thermoplastic AFP. CO_2 lasers produce a wavelength of around 10.6 μm, which is absorbed by the resin of processed composite materials. This is most similar to the convective heating produced by a hot gas source and thus heats the very surface of the prepreg. However, this same mechanism also increases the probability of local overheating and burning of the resin material. Also due to the short wavelength, the use of optics to expand the laser beam into a rectangular focal spot is not feasible and so the temperature distribution across the width of the prepreg material is not uniform. Mirror scanning systems and lenses to convert the laser spot into line geometries were investigated but result in short dwell time in the heating zone. [11, 40, 70] Nd: YAG and diode lasers used for AFP produce near infrared (NIR) wavelengths of 1064 nm and 900 - 1080 nm, respectively [71]. The composite resin material is transparent to these wavelengths, which instead heat the fibers directly. Due to the high thermal conductivity of the carbon-fibers, local overheating is less likely as the thermal energy can travel along the continuous fiber in preference to the polymer matrix [11]. Diode lasers and Nd:YAG lasers can be fiber-coupled, allowing transmission via fiber-optic cables and compact optics generating optimized rectangular spots [71]. Homogenizing optics enable top-hat laser power intensity distributions over the rectangular laser spot (Figure 2.6) [72–75].

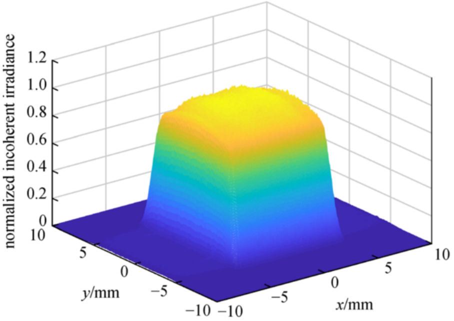

Figure 2.6: Diode laser intensity distribution with rectangular wave guide, reproduced from [75] with permission from Springer Nature

Together with the coupling into the carbon fibers, this leads to uniform heating of the material with minimal local overheating. The rectangular laser spots enable longer heating lengths and thus greater heat soak compared to line-type laser heating resulting in better consolidation [36]. Laser optics are interchangeable, allowing for the use of different spot geometries to adjust the rectangular spot for different tape widths and heating lengths.

Diode lasers outperform Nd: YAG lasers in terms of higher efficiency and their modular design. The laserpower of diode laser systems is easily scalable. Within the wavelength range, the wavelength can be adjusted according to the processed material properties. Diode lasers are also very responsive and thus controlleable. Kölzer used the short response time of the diode laser system and implemented a closed loop control system for controlling the laser power, as well as the laser angle, which determines the proportion of heating between tape and substrate. The control system was based on non-contact long wave infrared sensor array measurements of the observeable tape and substrate surface in front of the consolidation zone [76]. Today closed-loop-controlled diode laser heating systems represent the state of the art and are predominantly used for in-situ AFP (Fig. 2.7 left) [11–13]. The main disadvantage of laser systems is that a safety enclosure is required, wherein no personnel may work while the laser is in operation. Furthermore, the operating costs of lasers are higher than hot gas torch heating systems [13].

Further developments in diode laser technology are currently being considered in the literature. Variable Spot Size (VSS) laser systems combine multiple diode laser heat sources, to heat individual tows during the simultaneous layup of multiple tows, taking advantage of the modularity of diode laser systems. This enables tow drops or varying laser power for individual tows which is primarily of interest for industrialization and upscaling of the process to achieve higher production rates (Figure 2.7 right) [7, 77]. Motorized zoom homogenizing optics were also considered to adjust the size of the laser spot during the process [78]. The second direction of development is high-power vertical-cavity surface-emmitting laser (VCSEL) systems. VCSELs consist of up to several thousand small diode laser sources, each with its own micro lens. Instead of using light cables and homogenizing optics as in state of the art diode laser heating systems, VCSEL modules can be mounted directly onto the AFP end-effector and thus can offer space and cost-saving potential [67]. Weiler et al. and Brecher et al. found improved constant temperature for three-dimensional part geometries using VCSEL heating technology [79, 80]. Both systems offer interesting possibilities for adjusting the heating power over the width or length of the laser spot. This is particularly interesting for depositing multiple tapes simultaneously or for the layup of curved paths, which can lead to a different temperature at the inner and outer radius [81]. The ability of variably adjusting the heating length during the process could contribute to better consolidation at higher process speeds [78].

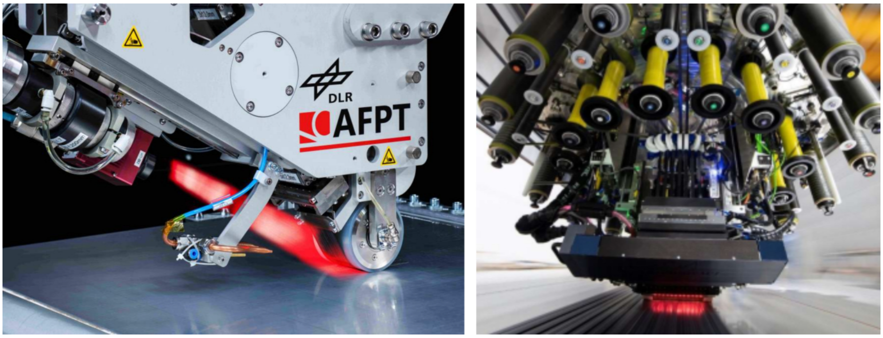

Figure 2.7: Diode laser heating systems: (left) AFP end-effector at DLR Stuttgart with laser optics and animated laser beam, (right) Electroimpact end-effector with variable spot size laser system, reprinted from [77] with permission from SAMPE

Stokes-Griffin [69] carried out a meta analysis of preceeding experimental work on in-situ AFP with different heat sources and found CO_2 lasers and hot gas torches to perform worse than hydrogen flame and NIR laser heat sources with respect to mechanical properties. This was explained by the process history. CO_2 laser line-type heating results in very short heating length and low overall heat soak compared to rectangular spots and longer heat length in NIR systems. Hydrogen flame likely achieved higher bond strength due to higher gas temperature (up to 1300 °C [38,39]) than nitrogen hot gas torch heating systems (900 °C to 975 °C [28,29,82]) and thus increased rate of convective heat transfer. Convective heat tranfer rate is proportional to the temperature difference between the heating gas and the surface of the heated tape and substrate. Over the course of the heating length, the temperature difference between heating gas and surface temperatures decreases, which also results in a decrease in heat transfer rate. For the laser heating, the heating rate is largely independent of the substrate temperature. Higher heating rates can be achieved, making laser heating advantageous, specifically for high layup rates. Furthermore, the response time for temperature control is significantly faster in laser heating systems compared to convective heat sources. [36, 69]

Other heat sources were also investigated, but play a subordinate role in the literature. The alternative heat sources include infrared heating [83, 84], hot air convective preheating combined with hot shoe heating [85] and xenon flashlamp heating [86]. One of the limiting factors reported in the literature was insufficient energy density for in-situ consolidation at adequate process rates [13].

2.1.1 In-situ consolidation: Process level impacting factors and mechanisms

This section presents process parameters, mechanisms and modelling approaches that were investigated in the literature and play an important role in the detailed understanding of the process and the subsequent considerations for the application to complex geometries.

The in-situ AFP process is determined by a variety of chemical, thermal and physical mechanisms. A process diagram of the relevant factors and mechanisms is presented in Figure 2.8.

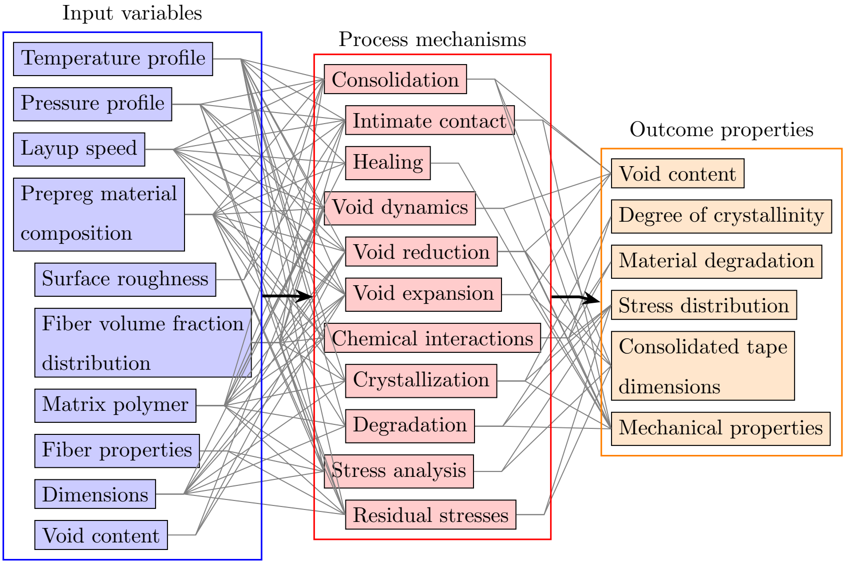

Figure 2.8: In-situ AFP process mechanisms and variables

The relevant input variables are first and foremost the temperature profile of the tape and substrate with respective heating and cooling rates, as well as through-tape-thickness temperature distribution. The temperature affects all four primary process mechanisms. It alters the resin viscosity which plays an important role in consolidation and void dynamics. Crystallinity, degradation and residual stresses also strongly depend on temperature and cooling rate during the process. While from a process perspective, the two-dimensional temperature profile remains stationary (three-dimensional when accounting for the width direction of the heating zone), from the laminate perspective, the transient, moving heat influx with high heating and cooling rates results in complex residual stresses [87–91].

Often, a heated tooling is used, which in interaction with the laser heat source and the layup speed results in the temperature profile of the final part. As it is the key factor in the process, extensive research has been focused on the experimental analysis and simulation of the temperature profile achieved in the process. Thermocouple measurements [51, 69, 92, 93] thermal cameras [47, 69, 92, 94–96] and Fiber Bragg Grating sensors [97, 98] were used in the literature to experimentally investigate the temperature profile. In numerous simulative studies numerical [47, 69, 76, 93, 94, 99] and analytical models [78, 100–103] were developed to determine the temperature profile in the in-situ AFP process. Numerical models achieved higher accuracy but required more computation time, compared to analytical models [78]. The pressure profile refers to the pressure distribution the tape is subjected to in the area of applied pressure. The consolidation pressure primarily impacts the consolidation and void dynamics mechanisms.

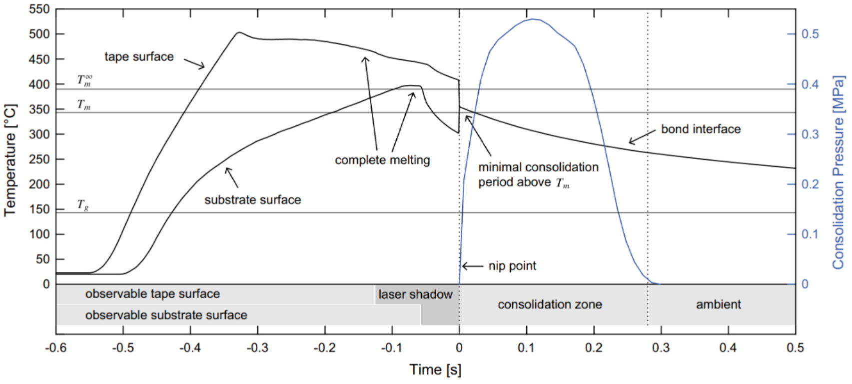

Figure 2.9: Temperature and consolidation pressure profile during in-situ AFP, reprinted from [104] with permission from Elsevier

Figure 2.9 shows a typical temperature and consolidation pressure profile for carbon-fiber PEEK prepreg tape and a layup speed of 100 mm/s, as determined by Stokes-Griffin and Compston [104]. Different heating curves can be observed for substrate and tape. The laser shadow in front of the consolidation roller results in a decrease in surface temperature just before reaching the nip point [95]. The tape surface reaches the laser shadow earlier than the substrate. However, depending on tool temperature, number of already deposited layers and thermal properties of the material, different heating rates and a higher cooling rate of the substrate after reaching the laser shadow result in a temperature difference between tape and substrate at the nip point. For an unheated tooling, a temperature drop of 130 °C and 60 °C was reported following the laser shadow for substrate and tape, respectively [95]. The heating curves can be adjusted using the tool temperature, laser power and the bias of the laser, which can be targeted more towards tape or substrate. Grouve et al. [47] found optimized consolidation results with the laser primarily focusing on the tape resulting in a 200 °C higher temperature of the tape compared to the substrate. The layup speed determines the time interval for the entire consolidation process to take place. Typical layup speeds for laser in-situ AFP are between 50 and 150 mm/s [65]. Assuming a length of applied pressure of 20 mm, this results in a time of 0.4 to 0.13 s for consolidation to take place. Finally, the input variable prepreg tape composition again impacts all process mechanisms, as it presents the initial state which is changed by the process mechanisms.

Contact and Bonding

The outcome properties of the laminate depend on many interdependent input variables and process mechanisms. However, the consolidation process mechanism plays a particularly important role. Intimate contact and healing first have to be established to create a bond between incoming tape and substrate [35]. Without a bond, none of the other properties such as, crystallinity or residual stresses are of relevance, as the deposited tapes do not represent a cohesive laminate, merely a series of partially connected prepreg strips. After establishing the bond, quality of bond and surrounding laminate composition can be analyzed. Bonding of thermoplastic composites can be determined using a combination of intimate contact and autohesion models. In order to create a bond between joining prepreg sides, physical contact must first be established. After establishing physical contact, the interfaces can be joined in the next step.

The surface roughness of realistic unidirectional prepreg tapes is more pronounced in the width direction than in the fiber direction. Additionally dry fibers are often observed at the tape surface. A representative surface scan of a standard prepreg tape is shown in Figure 2.10 [105, 106]. To determine the fraction of contact between joining prepregs, intimate contact models were developed. As the surface roughness is more pronounced in the width direction of the tape, two-dimensional models were mainly suggested. Prior to deformation, surface geometries of thermoplastic tapes determine the physical contact area. Added temperature and consolidation pressure result in a softening of the material and thus an increase in intimate contact.

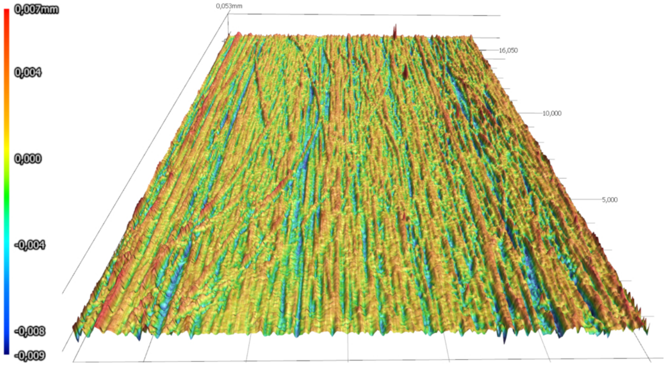

Figure 2.10: Toray TC1225 CF/LM-PAEK 12.7 mm prepreg tape profilometry surface scan [105]

Theoretical intimate contact models were develped based on simplified rectangular surface assumptions [107], Cantor set surface representation and squeeze flow models [108] and three-dimensional deformable cylinder surface models [109]. An experimental approach to intimate contact was introduced by Khodaei and Shadmehri [110] analyzing intimate contact comparing two-dimensional surface profile scans of tapes before and after processing using a bearing area ratio curve model.

Celik and Teuwen [111, 112] introduced the concept of effective intimate contact as the surface fraction that has made intimate contact and contains resin, not dry fibers, since only these areas of intimate contact can later enable healing. The authors developed an experimental methodology to determine the degree of intimate contact using two-dimensional surface micrographs and concluded that currently available intimate contact models could not predict effective intimate contact since they assume a homogeneous fiber-resin mixture at the tape surface which deforms following only squeeze flow mechanism. More complex intimate contact models need to be developed, to consider consolidation pressure-induced through-thickness and in-plane percolation of resin flow to impregnate dry fiber surface areas. To this end, realistic uneven tape surfaces with dry fiber regions should also be considered [111, 112].

Experimental investigation in accordance with intimate contact models showed increased consolidation with increasing consolidation pressure. Exaggerated pressure however led to waviness and matrix squeeze out [45, 54, 113]. The roller configuration determines the pressure distribution and area of applied pressure. Less waviness is induced with silicone rollers as opposed to rigid metal rollers [113]. For conformable rollers, both increases in consolidation pressure and roller diameter lead to increased consolidation length and thus slightly increased consolidation [54]. A heated tooling improved effective intimate contact via decreased heat loss and advantageous through thickness temperature distribution of the tape [110].

For the surface areas which have made (effective) intimate contact, healing can take place. The process of healing describes intermolecular diffusion across interfaces. Healing is strongly influenced by the temperature profile at the interface. Yang and Pitchumani successfully developed and validated a nonisothermal healing model [114] and combined contact and healing model [114, 115] for the in-situ AFP process.

The use of a conformable roller results in longer pressure application as compared to a rigid consolidation roller. There is also a significant decrease in bond interface temperature during the time of applied pressure. While simplifying assumptions for rigid rollers can be justified [82] [25], conformable rollers thus do not allow for simplifications. Stokes-Griffin and Compston found a time increment of 0.001 s to be sufficient for reliable bonding predictions [104]. The temperature present at the bonding interface is a key factor for the consolidation process. The temperature-dependent matrix-fiber viscosity decreases with increasing temperature, accelerating the healing- and thus bonding process. A heated tooling was shown to improve the degree of bonding achieving full bonding and high interlaminar shear strength [39]. While previous research assumed healing only to occur above the melting temperature T_m for semicrystalline polymers [25, 39, 82, 114], Stokes-Griffin and Compston [104] showed that this assumption results in significant underestimation of bonding strength, particularly for higher placement rates. Taking the glass transition temperature T_g to be the bonding threshold on the other hand leads to an overestimation of strength. The crystallization effects occurring between T_g and T_m result in decreasing polymer chain mobility, impeding healing the closer the temperature gets to the glass transition temperature. Temperature-dependent viscosity between T_g and T_m, considering crystallization effects have yet to be investigated to accurately model the sub-melt-temperature bonding of semicrystalline composites. Repeated heat influx due to the layup of subsequent layers or repasses scan lead to additional time for healing and improved bonding [33]. The impact on mechanical properties is however limited [62] as healing happens orders of magnitude faster then intimate contact [35].

Experimental investigations highlighted the significant impact of the composition of processed prepreg tape material on bonding performance in in-situ AFP [7, 29, 34, 35, 51, 57, 116]. High surface roughness and low amount of surface resin decreases effective intimate contact [35]. High surface roughness also leads to varying angle of incidence of the heat source and non-uniform temperature at the tape surface, resulting in local deconsolidation during the heating phase [117]. Smooth-surfaced AFP-grade tape achieved better intimate contact and higher degree of bonding [39], even outperforming autoclave reference specimens in some studies [34, 35].

Void compaction and expansion

Whereas contact and bonding models look at the interface between the layers and thus interlaminar porosity, void dynamics models deal with the intralaminar pores in the tape. These models are however closely interconnected and based on similar squeeze flow model approaches. Depending on the material quality, unprocessed prepreg tapes usually exhibit porosity values significantly larger than 1 % and in some cases even as high as 10 to 20 % [35]. Final consolidated laminate porosity is however required to be below 1 %. The voids thus need to be reduced during the in-situ consolidation AFP process. The consolidation pressure, applied during the AFP process compresses the voids and changes height and width of the tow. While Darcy's law has been used for thermoset AFP void dynamic simulation, thermoplastic AFP, due to the resin's inherently higher viscosity, requires different modelling approaches. Two-dimensional transversely isotropic fluid models with fibers aligned in one direction to predict void reduction and a non-isothermal compressible specific problem formulation yielded the highest applicability to thermoplastic AFP consolidation [118].

After leaving the consolidation zone, pressure is released from the tape and substrate. The internal pressure of the compressed voids in the incompressible fiber-matrix continuum creates an expansion pressure. The temperature state and thus viscosity of the material upon leaving the consolidation zone determines the magnitude of void expansion. Rapid cooling consequentially was shown to decrease void expansion [119]. This however presents a conflict of objectives, as other mechanisms such as crystallization and healing require slow cooling rates. Assuming an incompressible fiber-matrix continuum, the magnitude of void expansion can be approximated following the expansion of tape dimensions after leaving the zone of applied pressure. For rigid rollers, this was modelled and validated experimentally [119–122]. State of the art conformable consolidation rollers however achieve elongated consolidation zones, likely resulting in different void expansion characteristics [11]. Also the analysis of void geometries in thermoplastic prepreg material showed that the assumption of spherical voids is likely inadequate as the majority of voids is of rodlike shape, oriented primarily in the fiber direction [116, 123]. Tobin et al. [124] investigated tape deconsolidation following diode laser in-situ winding (hoop samples) and found decreased interlaminar shear strength due to void development within the tape as a results of deconsolidation. Saenz-Castillo et al. [53, 116] compared void content of vacuum-bag oven consolidation, hot-press and diode laser in-situ AFP and found higher void content for in-situ AFP laminates. The authors concluded that the increased void content was one of the main factors for lower mechanical performance compared to reference laminates.

Crystallization and degradation

Both polymer degradation and crystallization are temperature-dependent chemical processes. Polymer degradation is an irreversible process that results in a loss of the original properties [125]. High process temperatures are beneficial for intimate contact and healing due to decreased resin viscosity. However an excessive dwell time at high temperatures can lead to polymer degradation. The maximum exposure time to prevent polymer degradation decreases with increasing temperature. At 600 °C it is about 2 s for CF/PEEK [36,126]. The degradation temperature increases with increasing heating rate [127]. Fink et al. investigated the degradation effect on hot gas torch-manufactured CF/PEKK short beam strength specimens and concluded that there was a competing effect between bonding and degradation mechanisms [128]. The degradation thus depends on the layup speed and heating profile which determine the resulting temperature profile of prepreg tape and substrate. Zhao et al. [63] developed a kinetic model to predict degradation of CF/PPS for diode laser heating AFP and found no relevant thermal degradation for the investigated AFP parameters. Very high heating rates in the AFP process were given as the reason for the negligible degradation. Gaitanelis et al. [129] investigated laser heating of PEEK samples and found that short-duration heating resulted in an annealing effect and slight increases in crystallinity and hardness whereas longer than 4 ms heating time led to surface carbonisation and significant decreases in crystallinity and surface hardness. The carbonized surface however acts as a protective layer to prevent further thermal damage of the underlying material but at the same time impairs the bonding of subsequently placed tapes.

Crystallinity plays an important role in generating the advantageous properties of high-performance semi-crystalline thermoplastics such as thermal stability, chemical resistance and mechanical properties [130]. Upon cooling, lamellar crystals form around the fibers or spontaneously in the polymer volume, creating spherical crystalline structures called spherulites [12]. At low-enough cooling rates, spherulites can grow until they reach crystalline structures generated in the bulk of the matrix polymer. These crystalline layers, formed on the fiber surface are known as transcrystallinity and results in significantly improved longitudinal fatigue life [131, 132]. Final crystallinity depends on the cooling rate, and thus the time available for crystalline structures to form. At high cooling rates a lower degree of molecular perfection and lower mobility of polymer chains, which limits the chains movement toward the crystal front and thus crystal growth, leads to smaller crystals and less overall crystallinity. This also affects the fiber-matrix interface with slow cooling rates achieving higher interface shear strength but also more brittle matrix-dominant cohesive failure modes, whereas fast cooling rates result in more amorphous interfaces and ductile fiber-matrix interface debonding failure modes with higher degree of plastic deformation [133–135]. Crystallization models for thermoplastic AFP were developed by Tierney and Gillespie [136], as well as Guan and Pitchumani [137], and elaborated on by Gordnian [138] and showed good agreement with experimental results for CF/PEEK. Teltschik et al. extended the simulation for LM-PAEK composites [139]. Commercial software tools such as RAVEN by Convergent Manufacturing Technologies (Vancouver, CA) are available for the estimation of crystallinity, based on the processing parameters. A heated tooling was shown to increase overall crystallinity and created a more homogeneous morphology in the laminate [58, 59].

Stress Analysis

Residual stresses in in-situ AFP laminates arise from non-isotropic thermal expansion properties of the prepreg tape and volumetric changes during the cooling phase. In semi-crystalline composites such as PEEK or other polyaryletherketones, crystallization results in more-densely-packed crystalline regions as compared to the amorphous state prior to cooling, resulting in increased shrinkage [140]. These internal stresses can lead to a decrease in mechanical properties and defects such as microcracks [141]. In contrast to bulk consolidation processes (autoclave or oven consolidation), where the entire laminate undergoes controlled and uniform cooling, AFP processing results in very localized heat flux. Due to the high processing temperatures of high-performance thermoplastics, large temperature differences between the surrounding laminate and the local operating point in the additive manufacturing process produce a unique residual stress distribution. In addition, high cooling rates, as observed in thermoplastic AFP, lead to increased transverse residual stresses [142]. While these effects would produce symmetrical internal stresses in bulk-consolidated balanced and symmetric laminates, the time difference between the consolidation of the layers and tracks can result in asymmetric internal stress distributions and thus distortion and warpage for corresponding AFP laminates [89]. These deformations can be used to quantify the internal stresses and optimize the process accordingly [143]. A heated tooling was shown to decrease internal stresses and warpage in in-situ AFP manufactured laminates by means of lowering the cooling rate, decreasing the temperature difference between locally heated areas and the surrounding laminate and bulk cooling of the entire laminate after AFP layup with a controlled cooling rate [39, 91, 113]. Adusting the tape tension was also shown to decrease residual stresses [144]. Finally, using alternating layup sequences of individual tracks as compared to sequential layup of tracks was shown to decrease internal stresses and warpage by means of distributing the local heat influx [90].

2.1.2 Laminate level effects

This chapter looks at the in-situ AFP process in the context of the overall laminate. While the process-level optimization already presents a multifactorial challenge, additional complexity is added from the laminate structure. Most of the presented models and experimental investigations consider unidirectional layup with tape and substrate both oriented in the same direction. Realistic laminate layup however rarely consists of unidirectional layup but usually comprises 45 ° or 90 ° angular difference between tape and substrate. In unidirectional layup, the surface roughness orientation and direction of fibers of tape and substrate are aligned resulting in few crossing points of fibers and relatively easy intermeshing of the surfaces. For non-unidirectional layup, more crossing points of fibers and different roughness orientations of tape and substrate aggravate intimate contact [35]. This is more pronounced in non-AFP grade pregpreg tapes with low resin content at the tape surface and a high degree of surface roughness. Generally, higher porosity and lower degree of intimate contact are achieved for non-unidirectional layup [7].

A second challenge in the consideration of real laminates arises from the lateral boundaries of the consolidated tapes. The variation of consolidated tape dimensions and lateral movement of the tape with respect to the intended robot path can lead to lateral overlaps or gaps between adjacent tapes. In contrast to geometry-related gaps and overlaps, which are described in the second part of this chapter, these defects are caused by robot inaccuracy, lateral movement of the tape on the consolidation roller and in the tape guiding system of the AFP end-effector, varying tape compaction and dimensional variation in the as-delivered tape material [145]. An example of a gap defect between adjacent tapes is presented in Figure 2.11 in the fourth layer from the top [57]. For the in-situ AFP process, these inaccuracies result in increased porosity in the laminate. Furthermore, variations in ply thickness, as well as undulations in plies subsequently placed at the position of the defect can occur, which can be observed in Figure 2.11, as well. Wang and Gutowski [146] developed a transverse flow model to predict dimensional changes of the consolidated tape width to adjust the layup paths accordingly. In line process inspection is increasingly used to monitor theses defects. Real-time adaptations of the process parameters are investigated to minimize these effects [145, 147, 148]. Variations in ply thickness and undulations in subsequent plies can also be induced by the cross-section of consolidated tapes. The cross-section usually is not a perfect rectangle but flattened towards the edges and the tape boundaries usually exhibit a radius. The build up of these cross-sections leads to the characteristic surface waviness, which is part of the in-situ AFP manufacturing signature. Slight overlaps between adjacent tapes might be beneficial to mitigate this effect, though this approach can lead to another form of laminate waviness and, in turn, pores where prepreg material cannot achieve contact with the substrate.

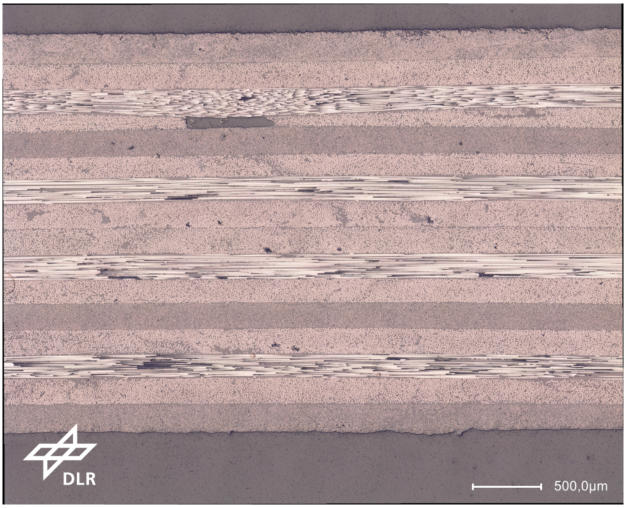

Figure 2.11: Quasi-isotropic laminate microsection with gap defect between adjacent tapes, reprinted from [57] with permission from SAMPE

As consolidation pressure is applied perpendicular to the tape surface, bonding between the tape and the substrate is primarily emphasized. The lateral contact between adjacent tapes within a ply however is made with less, if any consolidation pressure. The lateral bonding of tapes is thus a weak point. Khan et al. [39] found a heated tooling and the resulting higher lateral expansion of the tape in the consolidation process to be advantageous for transverse tensile strength of in-situ AFP-manufactured laminates. A well-established strategy to mitigate the above-mentioned defects on a laminate level is the staggering of plies of the same fiber-orientation throughout the laminate, to avoid superposition of defects and aggregation throughout the laminate. A staggering factor between plies of the same orientation, defining the lateral offset as a proportion of a consolidated tape width is typically used. Different staggering strategies were investigated and significant strength improvements were found for laminates that included a staggering strategy [149, 150].

2.1.3 Mechanical performance of flat laminates

Overall, the laminate level-induced effects presented in section 2.1.2 are hard to isolate and quantify. Combined with the effects presented in section 2.1.1, these effects can be defined as in-situ AFP manufacturing signature. Due to the complex superposition of these various effects, laminate machanical properties are often used as a general, if not somewhat crude, indicator of process performance. Laminate level mechanical test results are thus presented in this section as a baseline for subsequent complex laminate considerations. In terms of mechanical testing, in-situ AFP consolidation quality is assessed in the literature focusing primarily on the interlaminar laminate properties. Interlaminar toughness was tested using wedge peel [49, 51, 54, 151], mandrel peel [47, 94] and double cantilever beam (DCB) tests [29, 52, 60, 61, 149]. In-situ AFP samples achieved significantly higher mode I interlaminar toughness than respective autoclave references [47, 49, 51, 52].

Interlaminar shear strength was investigated in the literature using Single lap shear (SLS) [29, 55, 56, 152, 153] and three-point-bending tests [25, 29, 35, 36, 39–41, 44, 51, 70, 82, 84] [45, 59, 62, 65, 68, 116, 149, 150, 154–161]. The three-point-bending test following the test standards ASTM D2344 and EN 2563 was used most frequently due to its easy-to-prepare samples. Results by Stokes-Griffin et al. reported that similar short beam strength to autoclave reference can be achieved using in-situ AFP of unidirectional specimens [36]. Most other literature results however yielded significant knockdown factors for short beam strength results. Application related quasi-isotropic stacking sequences result in lower short beam strength than comparable unidirectional laminates. A 61 % and 48 % decrease in autoclave reference and in-situ consolidation strength was reported by Chanteli, respectively [62]. A comprehensive list of in-situ AFP three-point-bending test results can be found in Appendix A1 (Table 8.1). The three-point-bending test is also often referred to as interlaminar shear strength (ILSS) test. However according to the test standard only apparent interlaminar shear strength is actually measured, as a combination of interlaminar shear stress and bending stress is present in the specimens [162]. Especially in thermoplastic specimens, plastic deformation and non-standard failure modes are reported [29, 41, 160, 163]. According to the ASTM D2344 test standard, the strength results cannot be attributed to shear, if mid-plane interlaminar failure is not observed [162, 163]. To this end, a five-point-bending (double beam shear) test has also been investigated. This test following test standard ISO-19927 was shown to reproducibly achieve test results with pure interlaminar shear failure modes and very small standard deviation for in-situ AFP-manufactured samples [57, 106, 164, 165].

In-plane shear strength (IPSS) testing was also used to assess final laminate quality [53, 113, 116, 166]. Relative strength values between 75 % [166] and 123 % [113] were found for in-situ AFP specimens, however with significantly different reference values. Laminate level tensile strength tests showed similar results as autoclave reference [113]. Depending on the utilized prepreg material, manufacturing equipment and process parameters, laminate level compression strength test literature results showed a range of values from similar to the reference up to 26 % knockdown of in-situ AFP samples [33, 113, 156, 167].

In addition to the mechanical tests, other methods such as ultrasonic testing [53, 84, 108, 116, 168], computed tomography [51, 116, 169], microsectioning [28, 38, 51, 65, 161] as well as contact area [52, 110–112] and failure mode analysis [29, 36] were used in the literature to assess in-situ AFP consolidation quality. Porosity analysis by means of optical analysis of microsections, micro-computed tomography and acid digestion is most frequently used in the literature to assess overall laminate quality. A comprehensive list of in-situ AFP porosity test results can be found in Appendix A1 (Table 8.2). Using AFP-grade prepreg material and optimized process parameters, low porosity of 1 % or lower can be achieved, even for realistic laminates with quasi-isotropic stacking sequence and inter-tow gap or overlap defects (Figure 2.11) [57].

As was deduced in the last two chapters on the basis of the mechanisms, a heated tooling has a positive effect on in-situ consolidation. This is confirmed when analyzing the laminate-level mechanical properties [39, 113, 159]. While PEEK-based prepreg material was predominantly used for the bulk of the research in the literature, the newly developed LM-PAEK (Victrex plc, UK) has gained interest recently, due to its lower melt temperature and melt viscosity, promising improved AFP processability and similar mechanical properties as PEEK [55, 56]. Table 2.1 summarizes mechanical properties of in-situ AFP-manufactured specimens using CF/LM-PAEK AFP-grade prepreg tape, recently generated at DLR [57, 106, 160]. These results are used as a basis for comparison with further tests on complex laminates.

Table 2.1: Diode laser in-situ AFP, 200 °C heated tooling (AS7/LM-PAEK Suprem 55 % FVF) and hot-press re-consolidated (T700/LM-PAEK Toray 60 % FVF) reference results with quasi-isotropic stacking sequence $[0/45/90/\text{-}45]_{2S}$ [57, 106, 160]

Test standard	In-situ AFP	Hot-press
AITM 1-0007 Tensile strength [MPa]	855.3 ± 19.1	1040.2 ± 44.2
AITM 1-0008 Compressive strength [MPa]	430 ± 29.9	486 ± 31.8
ISO-19927 double-beam-bending strength [MPa]	64.2 ± 0.9	89.1 ± 2.0
Micro-computed tomography porosity [%]	0.92 ± 0.34	0 ± 0

2.2 Geometry-induced defects

Moving from realistic flat AFP laminates to double-curved geometries leads to additional complexity for all AFP manufacturing technologies. The layup of a two-dimensional tape on a three-dimensional double-curved surface results in defects of various kinds. The majority of research on complex AFP manufacture focuses on thermoset AFP. However, the geometric interactions are similar and the work is thus included in this review.

A distinction must be made between manufacturing (process-induced) defects and planned (geometry-induced) defects. Geometry-induced defects are unavoidable due to the effective two-dimensional nature of the AFP prepreg tows, which using current layup software are represented as discrete and constant-width paths along the tooling contour. These planned defects are strategically introduced into the laminate to allow for the layup on the complex surface as part of the layup strategy. Manufacturing defects occur in the real-world environment, typically as extensions of the geometry-induced defects. A comprehensive investigation of manufacturing defects defects is presented in [170, 171].

Planned (geometry-induced) defects can be categorized into gaps/overlaps, steering and angle deviation defects and are the subject of Section 2.2.2 and 2.2.3. Upon developing a layup strategy for a complex AFP laminate, the optimum compromise between the three interdependent defect types must be determined. For a given complex geometry, this is visualized in Figure 2.12.

(a) Parallel path propagation

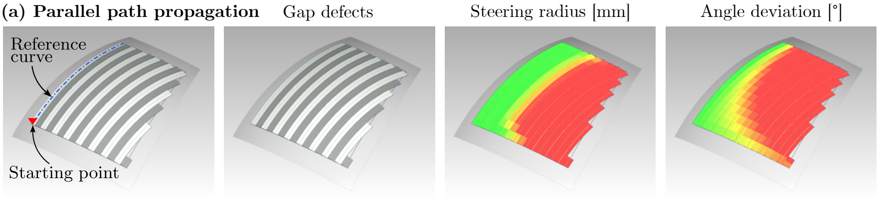

(b) Shifted path propagation

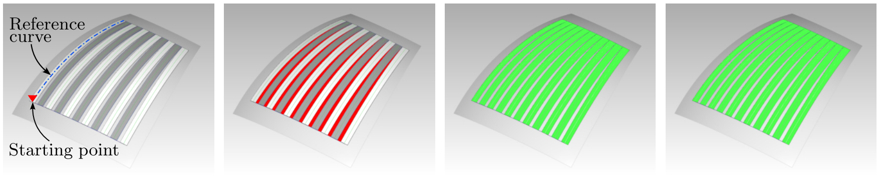

(c) Parallel and shifted path propagation

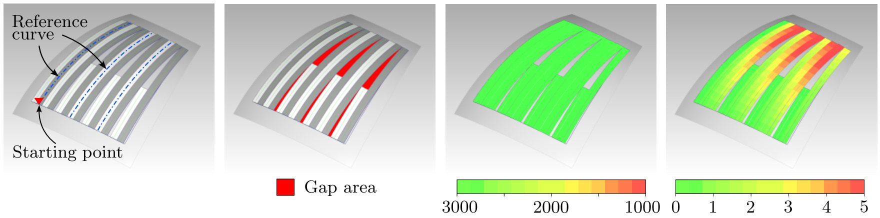

Figure 2.12: Layup strategies and resulting gap defects, steering radii and angle deviation of a spherical reference surface geometry

The laminate can be fully covered using a parallel layup strategy, avoiding gap or overlap defects but accepting steering and angle deviation, which increases with each subsequent tow placed further from the reference curve (Figure 2.12(a)). Alternatively, tows can be placed without angle deviation or steering using a shifted path propagation strategy, though this results in significant gap or overlap defects (Figure 2.12(b)). Typically, a combination of parallel and shifted path propagation is used (Figure 2.12(c)), whereby the reference curves and shifting parameters are determined as part of the layup strategy, which is discussed in the following section. It should be noted, that the severity of these three defect types is heavily dependent on the contour of the desired part and the planned (effective) width of prepreg tows.

2.2.1 Layup strategies

A layup strategy for a given complex surface is determined by an initial reference curve and a propagation method to find subsequent paths. Different approaches have been discussed in the literature and are presented below.

Reference curve

Starting points and reference curves are the foundation of any given layup strategy. The starting point defines the starting position of the reference curve which in turn defines the layup path of a given track on the part contour. Depending on the surface geometry, the position of the starting point can have a large impact on the resulting reference curve, layup outcome and position of planned defects. The position of the starting point is determined in an iterative trial and error process as there is no established prediction method available [172]. Depending on the layup strategy, either all paths can be related to the first reference curve or further reference curves can be created in the process. In a comprehensive review on path planning for AFP, Rousseau et al. [173] categorized reference curves into fixed angle, geodesic and variable angle reference curves.

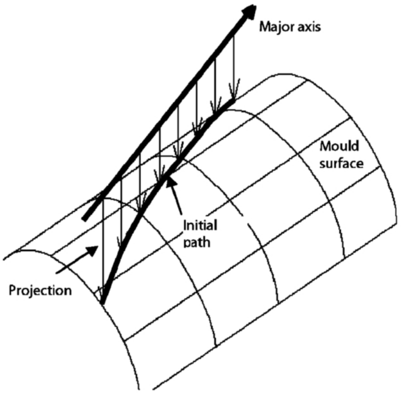

Figure 2.13: Fixed angle reference curve definition via projection of a major axis onto the surface, reprinted from [174] with permission from Elsevier

Fixed angle reference curves, also referred to as rosette rule, keep the local fiber angle at the nominal angle with regard to the part coordinate system. Consequently there is no fiber deviation, however, depending on the geometry severe steering can occur. A parametric approach is most commonly used in the literature for calculating a fixed angle reference curve [173]. The reference curve is defined as the intersection between a plane through a major axis and the starting point and geometric surface (Figure 2.13) [174–176]. For a parametric surface

$S(u,v) = [x(u,v), y(u,v), z(u,v)]$ and the projection $P(x,y,z)$ of the major axis $X(x,y,z)$, where

$$P(x,y,z) = ax + by + cz + d = 0 \tag{2.1}$$

the resulting intersection equation defines the reference curve $f(u,v)$ as

$$f(u,v) = ax(u,v) + by(u,v) + cz(u,v) + d = 0 \tag{2.2}$$

In the context of this work, the simplification is made that the natural path can be approximated by the geodesic path with sufficient accuracy. The natural path is defined for tapes of finite width as the path with minimal strain energy required to apply the tape onto a surface. The geodesic path is defined as the path without in-plane curvature [177]. For AFP, considering relatively narrow tape widths of up to 12.7 mm compared to much larger surface geometry curvatures, the internal shear deformation of the tape itself can be neglected. The natural path is approximated with sufficient accuracy by the geodesic path [178, 179]. The geodesic path can be calculated using a starting point and initial direction. For an arbitrary surface defined by a position vector $\vec{r}(u,v)$, the geodesic reference curve can be described by the following system of differential equations [173, 180]:

$$\begin{aligned}
\frac{du}{ds} &= u' \\
\frac{dv}{ds} &= v' \\
\frac{du'}{ds} &= -\Gamma_{11}^{1} U'^2 - 2\Gamma_{12}^{1} u'v' - \Gamma_{22}^{1} v'^2 \\
\frac{dv'}{ds} &= -\Gamma_{11}^{2} U'^2 - 2\Gamma_{12}^{2} u'v' - \Gamma_{22}^{2} v'^2
\end{aligned} \tag{2.3}$$

where s is the arc length and Γ_{ij}^{k} are Christoffel symbols for the surface S. The system of equations can be solved for the boundary conditions of a starting point u_0 and v_0 and starting direction u_0' and v_0' using numerical methods, such as the Runge-Kutta method [180].

Variable angle reference curves are primarily used to optimize stiffness properties of composite laminates by utilizing the steering capabilities of the AFP technology. Groundbreaking reseach by Gürdal et al. demonstrated significant improvements over standard laminates by using variable angle layup [181–185]. Blom et al. adapted the concept for cylindrical and conical geometries [186–190]. Different variable angle designs were investigated in the literature.

Constant curvature reference curves are paths that keep the same in-plane (geodesic) curvature. A parametric definition for a surface $S(u,v)$ and geodesic curvature K_g is presented in [173]:

$$\begin{aligned}
u'' + \Gamma_{11}^{1} u'^2 + 2\Gamma_{12}^{1} u'v' + \Gamma_{22}^{1} v'^2 &= \frac{k_g (Fu' + Gv')\sqrt{Eu'^2 + 2Fu'v' + Gv'^2}}{\sqrt{EG - F^2}} \\
v'' + \Gamma_{11}^{2} u'^2 + 2\Gamma_{12}^{2} u'v' + \Gamma_{22}^{2} v'^2 &= \frac{-k_g (Eu' + Fv')\sqrt{Eu'^2 + 2Fu'v' + Gv'^2}}{\sqrt{EG - F^2}}
\end{aligned} \tag{2.4}$$

where E, F and G are the fundamental coefficients of the surface $S(u,v)$, defined as

$$E(u,v) = \frac{\partial S}{\partial u} \cdot \frac{\partial S}{\partial u} \tag{2.5}$$
$$F(u,v) = \frac{\partial S}{\partial u} \cdot \frac{\partial S}{\partial v}$$
$$G(u,v) = \frac{\partial S}{\partial v} \cdot \frac{\partial S}{\partial v}$$

The differential equation system can be simplified for flat laminates:

$$x(t) = x_0 + \frac{1}{K}\cos(t) \tag{2.6}$$
$$y(t) = y_0 + \frac{1}{K}\sin(t)$$

where the curvature $K = K_g$ as the normal curvature of a flat surface is 0. Constant curvature variable stiffness reference curves were investigated for flat panels [183, 188, 191, 192], cylinders [186, 190] and cones [187].

Linear variation reference curves use linear angle variation along a straight path x'. The angle variation is described by a starting and end point and the respective angles T_0 and T_1, that are defined with respect to the straight path x'. The reference path x' can be rotated by the angle ϕ in relation to the global coordinate system [193]. For a flat laminate this is shown in Figure 2.14 [194]. The local fiber angle is defined as

$$\theta_f(x) = T_0 + (T_1 + T_0)\frac{|x|}{d} \tag{2.7}$$

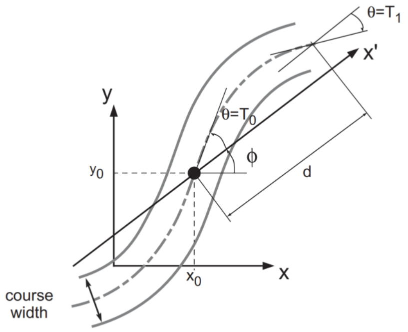

Figure 2.14: Linear angle variation reference curve, reprinted from [194] with permission from Elsevier

Blom et al investigated linear varying fiber angles for conical laminates [187]. Polynomial and free-form reference curves were also analyzed in the literature [173], but are not considered in this work.

The advantages and disadvantages of the reference curve types must be evaluated for a given component geometry. Fixed angle reference curves have the advantage that they do not involve any angle deviation. The part can be designed in relation to the global coordinate system. Depending on the geometry, however, strong steering can occur. In contrast, geodesic reference curves avoid steering, but can lead to angle deviation. Variable angle reference curves intentionally use in-plane path curvature (steering) and a varying angle in relation to the part coordinate system to increase stiffness properties of the part. The disadvantages of geometry-induced defects and the advantages of stiffness optimization must be weighed up.

Path propagation

The path propagation determines the layup paths of subsequent tapes after the first tape is placed on the reference curve. Either a new reference curve can be generated following the methods presented above, or the first reference curve can be propagated using one of two methods; parallel path or shifted [173].

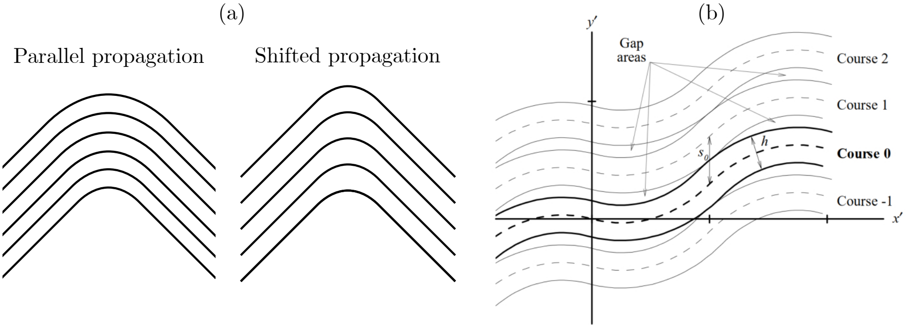

Figure 2.15: Path propagation strategies: (a) parallel and shifted paths, (b) shifted courses and resulting gap areas [183]

Parallel path propagation offsets the initial reference curve perpendicularly along the surface including adjusting the steering radius as shown in Figure 2.15(a). This results in a layup without gap or overlap defects [174]. For AFP multiple tow end-effectors, the tows of one course are placed in parallel. For complex geometries or curved reference paths on flat geometries, however, the parallel path propagation strategy can result in severe steering radii and fiber angle deviation. The shifted propagation translates the entire reference curve in one defined shifting direction without adjusting the steering radius, as shown in Figure 2.15 (a). While steering radii remain constant, for complex surfaces or curved reference paths this results in gap or overlap defects between the courses [195]. Figure 2.15(b) shows shifted courses by a shift distance s_0 in the direction of the y'-axis [183]. This results in gap areas between the courses. The individual courses can also be viewed as a finite number of tows layed up in parallel.

2.2.2 Steering

Steering is the forced in-plane curvature of the prepreg tape material resulting from the layup path which in turn is determined by the layup strategy. The local path curvature is determined by the surface curvature and the layup path C on the surface S. At any given point P, the curvature vector K of the path can be calculated as

$$K = \frac{dt}{ds} \tag{2.8}$$

where t is the tangent vector of the reference curve C in the point P [196]. The curvature vector can be decomposed into a geodesic and normal component, K_g and K_n, in the direction of the unit tangent vector u and the unit normal vector n, respectively.

$$K = K_g + K_n \tag{2.9}$$

The in-plane (geodesic) steering radius R is

$$R = \frac{1}{K_g} \tag{2.10}$$

Since the tape thickness is much smaller than the tape width, the normal curvature can be neglected. The geodesic curvature is the decisive factor for the occurrence of steering defects [196–198]. While there are numerous manifestations of steering defects (discussed presently), the underlying principle therof can be described as follows: The geodesic curvature induces different arc lengths at the inner and outer edge of the tape, resulting in tensile stress at the outer fibers and compressive stress at the inner fibers. As the tensile modulus of carbon fibers is approximately double that of the compressive modulus, tensile strain does not occur to any significant extend [199]. Instead, compressive stress at the inner tow edge results in compressive strain, buckling and undulations. The compressive strain ϵ_c can be calculated as [198, 200]

$$\epsilon_c = \frac{w_t}{R + w_t/2} = \frac{1}{\frac{1}{K_g w_t} + \frac{1}{2}} \tag{2.11}$$

where w_t is the tow width. Work by Belhaj and Hojjati [201] however suggests, that due to the high tensile modulus and buckling of carbon-fibers at the inner edge, a majority of the bending strain is compensated by compressive strain at the inner tape edge. This consequentially would results in higher compressive strain values at the inner tape edge than calculated in Equation 6.1. Observations of a shifted neutral fiber of the steered tape towards the outer edge of the tape support this theory [81, 201, 202].

For thermoset AFP, critical minimum steering radii were defined in the literature (Table 2.2). For steering radii above the critical value, layup without major defects is possible. These values can be regarded as reference values. The critical radii are highly dependent on the utilized material and process parameters such as tape tension and nip point temperature, as well as the manufacturing equipment [206].

Table 2.2: Thermoset AFP critical steering radii

Tape width [mm]	Critical steering radius R_{crit} [mm]	Reference
3.175	500-635	[186, 187, 191, 203–205]
6.35	1350-1778	[203, 205]
12.7	8890	[205]

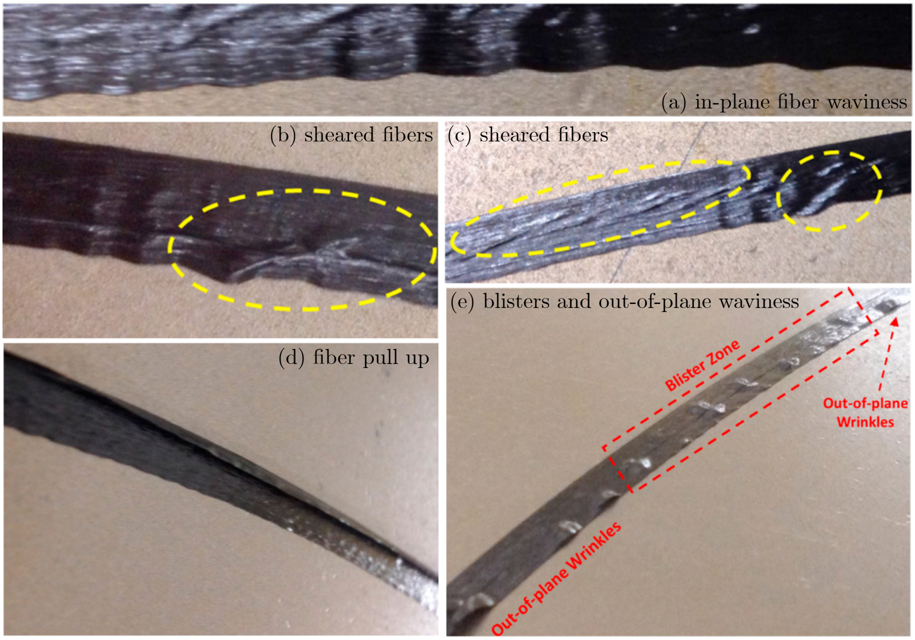

Figure 2.16: Thermoset AFP steering defects, reprinted from [207] with permission from Elsevier

Steering defects can be categorized into [207]:

- in-plane fiber waviness (Figure 2.16 (a))
- sheared fibers (Figure 2.16 (b) and (c))
- tow pull ups (Figure 2.16 (d))
- blisters (Figure 2.16 (e))
- out-of-plane wrinkles (Figure 2.16 (e))

Out-of-plane defects occur when the geodesic path curvature reaches a critical value. The compressive strain can no longer be absorbed only by in-plane waviness. In contrast to thermoplastic AFP, where largely complete consolidation is achieved, for thermoset AFP, tackiness of the uncured prepreg material is an important parameter, as it counteracts the out-of-plane buckling of the inner tow edge [207–209]. For thermoset AFP, a time-dependent increase in out-of-plane wrinkle amplitude was observed by Rajan et al. One hour after deposition, the amplitude almost doubled while the wrinkle pattern remained the same due to the viscoelastic effects in the prepreg tack [210].

Different experimental methodologies were developed to quantify primarily out-of-plane wrinkle defects. Qualitative analysis of occurring defects using visual inspection [203, 207, 211], wavelength measurement of wrinkles [209], digital image correlation analysis of wavelength and mean out-of-plane height of defects [210] and laser line scanning [212] are presented in the literature. Modeling approaches to predict out-of-plane wrinkle defects depending on geometry and prepreg material properties can also be found in the literature. Local modeling approaches consider sections of a steered tape as an orthotropic plate and investigated the buckling behavior of the unsupported inner tape edge [201, 202, 209, 213]. In contrast, global approaches take the entire length of the curved tape into account [207, 208, 214]. Wehbe et al. developed a wrinkling model assuming all differences in length between inner and outer edge of the tape is absorbed through out-of-plane wrinkle at inner tape edge [214].

After cutting a tow at the end of a track the shear stress in the steered tape results in a contrary motion upon leaving the tape guiding system of the AFP end-effector. Blom et al. [186] and Wu et al. [215] found fiber straightening after tow cuts at the outer radius of steered courses. It was recommended not to cut tows at the outside of a turn but preferably at the inner side of the steered courses.

Kim et al. [195, 216, 217] suggested a tow shearing technology of dry-fiber tape and semi-impregnation with resin film, which avoids steering-induced defects as well as gap or overlap defects. The end effector does not perform a rotational movement, but a translational movement in which the tapes are sheared. This technology achieves significant reduction of minimum steering radius. A steering radius as low as 30 mm was demonstrated. The total steering angle for this technology, however has to remain below 90 ° before an equivalent curved section in the opposite direction has to follow.

Thermoplastic steering

Steering of thermoplastic diode laser AFP was also investigated in the literature. Due to the relevance of the results for this work, these investigations are described in greater detail. Zenker and Schwab [81] investigated steering effects of carbon-fiber polyamide 6 (CF/PA6) 6.35 mm tape with the objective of manufacturing thermoplastic preforms. An infrared thermal camera and an optical fiber angle sensor were used to measure the process temperature and in-plane undulations of the steered tapes, respectively. Courses of 8 tows were placed on a $[0/90]_s$ substrate. The temperature of the tows on the inner side of the steered course was significantly higher than on the outer side. This was attributed to the larger effective steering radius and thus higher effective deposition rate at the outer radius while the laser power density remained constant over the course width. A temperature gradient was also detected for the individual tows with higher temperatures obtained at the inner edge. Steering-induced bending stress led to a loss of contact between the inner edge ot the tows and the roller, resulting in local thermal insulation from the roller, which acts as a heat sink. Local heat spots arose. The analysis of the in-plane fiber undulations showed a decrease in wavelength from the outer to the inner edge of the tape. Compressive stress at the inner edge resulted in low wavelengths of up to 3 mm. Straight fibers were observed at the outer edge and 1 mm towards the center of the tape, indicating a shift of the neutral fiber towards the outer edge of the tape and a very narrow region of tensile stress. In subsequent work, Zenker and Gnaedinger [218] investigated steering-induced in-plane undulations and resulting gap defects at the inner edge of 6.35 mm CF/PA6 tapes. An optical fiber angle sensor was used to generate gray-scale images and analyse the resulting gap fractions using image gray-scale analysis. Lower steering radii resulted in larger gap areas.

Clancy et al. [219] investigated steering effects of diode laser in-situ consolidation AFP for 6 mm and 6.35 mm CF/PEEK prepreg tape. Manufacturing experiments with different steering radii and layup speeds were carried out. For steered tapes, a decrease in consolidated tape width and increase in thickness was observed. Dimensional changes increased with decreasing steering radius. A Steering radius of 800 mm was achieved without visual defects. Minor wrinkling was observed for 600 mm steering radius and increased out-of-plane defects were observed for 400 mm and lower steering radii. Microsections showed a more visible bond line for lower steering radii compared to straight layup paths and larger steering radii. Microsections extracted at positions with wrinkles showed poor bond quality. A decrease in steering radii led to more severe and more frequent wrinkles (Figure 2.17).

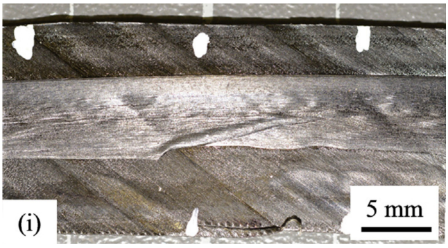

Figure 2.17: Thermoplastic AFP steering-induced out-of-plane wrinkle defect, reprinted from [219] with permission from Elsevier

An adapted wedge peel test was used to determine the impact on the consolidation quality. Resulting wedge peel strength decreased with both, increasing layup speed and decreasing steering radius. However, only 4 or less specimens were tested per parameter set. The authors concluded that equivalent or better steering results could be achieved with thermoplastic AFP as compared to thermoset or dry fiber placement.

Rajasekaran and Shadmehri [220] examined steering effects for 6.35 mm CF/PEEK prepreg tape nitrogen hot gas torch in-situ AFP. Steering without defects was achieved for radii up to 600 mm. For 400 mm steering radius tape buckling was observed. 200 mm steering radius resulted in severe buckling and folding defects. Similar to results by Clancy et al. [219], steering led to a reduction in consolidated tape width, and an increase in thickness. An adapted lap shear test with one steered tape layed on two separate $[0]_4$ laminates was used to determine the bond strength of steered tapes. Steering radii from 400 mm to 1000 mm resulted in similar lap shear strength as the straight tape reference. A decline was observed for the 200 mm steering radius, likely because of tape folding and poor consolidation at the outer edge of the tape. The baseline layup speed of 50.8 mm/s resulted in continuous defects for critical steering radii. Higher layup speed led to less frequent buckling defects but poor overall consolidation and lower lap shear strength. The substrate angle had similar effects for straight layup paths and steered tape. A slight linear decrease was observed with increasing substrate angle from 0 ° to 90 ° relative to the tape direction. Table 2.3 shows an overview of steering results in thermoplastic AFP literature.

Table 2.3: Thermoplastic AFP steering experiments

Ref	Material	AFP Process	Steering radii [mm]	Defect-free radius [mm]
[81]	CF/PA6 6.35	Diode laser	1200 - 200	-
[219]	CF/PEEK 6 - 6.35	Diode laser	2000 - 200	800
[220]	CF/PEEK 6.35	Nitrogen hot gas torch	1000 - 200	600

2.2.3 Gap and Overlap defects

Recent review papers present a detailed analysis of AFP gap and overlap defects [171, 221, 222]. In the literature, gap and overlap defects are primarily discussed in the context of tape width inaccuracies, intentionally distributed gaps to adhere to boundary curves, and missplaced tapes. These defects are thus rectangular gaps or overlaps between adjacent tapes or courses. For thermoplastic AFP, this is included in section 2.1.2 as part of the in-situ AFP manufacturing signature. Thermoset AFP manufacturing signature-induced gap and overlap defects are considered in this section, as there is a close connection to geometry-related gap and overlap defects in terms of methodology and results.

The second type of gap and overlap defects is caused by a combination of part geometry and layup strategy. Double-curved geometries in combined with non-parallel path propagation to avoid excessive steering and angle deviation result in characteristic triangular gap or overlap defects. The coverage ratio, as visualized in Figure 2.18, determines the ratio of gaps to overlaps for a given boundary curve [197, 223].

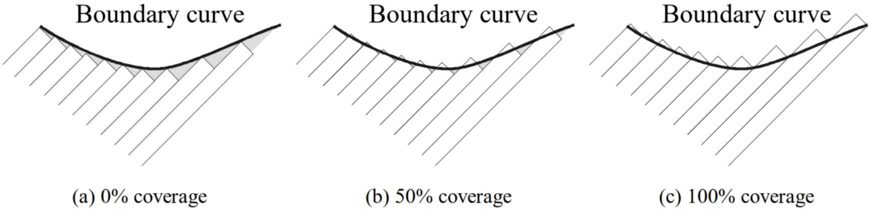

(a) 0% coverage (b) 50% coverage (c) 100% coverage

Figure 2.18: Coverage ratio and resulting gaps and overlaps [223]

The boundary curve can be interpreted either as a ply boundary or an adjacent tape, following converging layup curves. A coverage ratio of 0 % is synonymous with a pure gap design, whereas 100 % coverage ratio describes a complete overlap design. Any value in between 0 % and 100 % is a combination of gaps and overlaps [197, 223]. Single sided cuts are most commonly used in the literature. Mishra et al. introduced an alternative Zipper cut strategy, which used alternating cuts in adjacent courses (Figure 2.19). While less overall cuts are required in the single sided cut strategy, the Zipper cut strategy follows more closely the blue dotted line, which represents the intersection of converging courses [224].

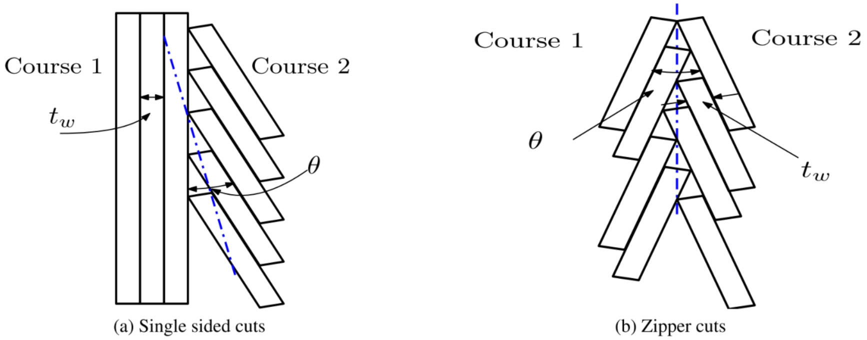

(a) Single sided cuts (b) Zipper cuts

Figure 2.19: Single sided cuts and Zipper cut strategy, reprinted from [224] with permission from Elsevier

Gap defects typically result in a local thickness reduction of the resulting laminate, whereas overlaps lead to a local thickness increase, where subsequently placed layers adapt to the local defect. Both defect types result in out-of-plane undulations in the laminate [225–230]. Due to applied pressure and heat in the autoclave process and resulting resin flow, gap width tends to decrease whereas overlap width increases [227, 231, 232].

Out-of-plane undulations angle of up to 15 ° were observed. The angle increases with increasing number of plies that contain defects and decreases with increasing defect width [233, 234]. The use of a caul plate during curing results in an even laminate surface with undulations moved to the center of the cross-section. Figure 2.20 shows cross-sections of specimens with rectangular gap and overlap defects, cured with and without a caul plate [235–237]. A microsection of the characteristic gap-induced triangular resin-rich region and fused layers in an overlap region is shown in Figure 2.21 [238].

(iii) AFP layup - Gap 3.175 mm - Without caul plate

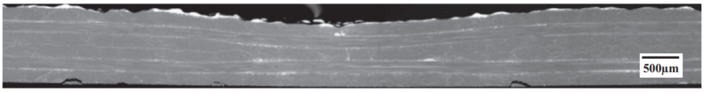

(iii) AFP layup - Gap 3.175 mm - With caul plate

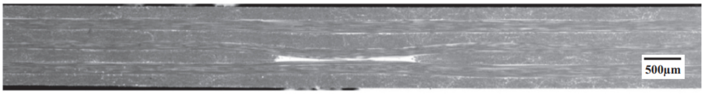

(iv) AFP layup - Overlap 3.175 mm - Without caul plate

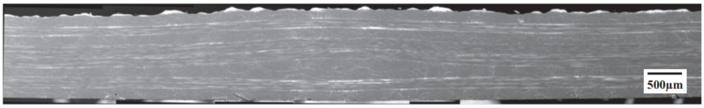

(iv) AFP layup - Overlap 3.175 mm - With caul plate

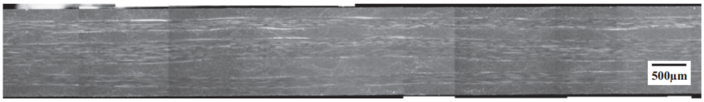

Figure 2.20: Scanning Electron Microscopy cross-section images of cross-ply laminates with 3.175 mm rectangular gap and overlap defects, cured with and without caul plate, reprinted from [236] with permission from Elsevier

Small triangular resin-rich areas are characteristically found at the edge of gap defects, as the fibers cannot fully adapt to the discrete ply drop due to their bending stiffness [188, 231, 239]. On the other hand, overlaps do not lead to resin-rich regions but to fiber-rich regions, i.e. local areas with a higher fiber volume content [229]. Staggering of defects across the thickness of the laminate can have an important effect on the resulting laminate geometry. While a superimposition of defects can lead to an aggravation of out-of-plane undulation and thickness variation, through-thickness staggering of defect positions can mitigate the effects [188, 233, 240–242].

The comprehensive experimental literature for thermoset AFP defects deals primarily with rectangular gap and overlap defects and their influence on mechanical properties of composite laminates. Tensile properties of laminates with rectangular gap and overlap defects were experimentally investigated in multiple studies [225, 227–230, 233, 235, 237, 243–248]. Depending on defect- and laminate configuration, gap defects yield between 0 % and up to 53 % tensile strength knockdown as well as up to 39 % tensile stiffness knockdown for 12.7 mm-wide

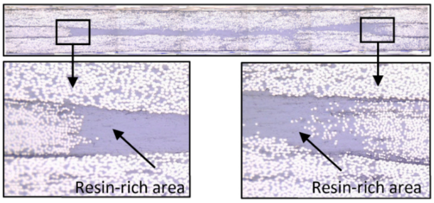

(a) Gap

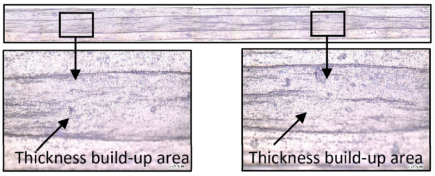

(b) Overlap

Figure 2.21: Microsection of defects: (a) gap defect, (b) overlap defect, reprinted from [238] with permission from Elsevier

aligned gap defects [230].

As pointed out by Yadav and Schledjewski [222], there are contradictory results regarding the influence of defect size on tensile properties. While Guin et al. [228] found 35 % tensile strength reduction for 1.27 mm gap defects in all plies of 16 ply quasi-isotropic laminates, Woigk et al. [244] achieved 1.3 % strength reduction for 2 mm gap defects in six plies of a 24 ply quasi-isotropic laminate. A direct comparison of the defect widths only appears permissible if all other parameters match. Nguyen et al. [230] found a correlation between gap defect size and tensile strength knockdown, with 12.7 mm gap defects resulting in the highest tensile strength knockdown, while Del Rossi et al. [227] found that increases in defect width did not necessarily increase strength knockdown. A 0 ° defect orientation is reported as the least critical, since the induced out-of-plane undulations in 45 ° and 90 ° plies is insignificant for tensile properties. Defects in 90 ° plies however induce out-of-plane undulations in 0 ° plies, which lead to decreased tensile strength and modulus [225]. The severity of out-of-plane undulations was shown to be a significant factor for tensile strength knockdown [247, 248].

Overlap defects tend to be less critical than gap defects in terms of tensile properties, and in some cases even lead to increased tensile properties [228–230, 233, 248]. Combinations of gaps and overlaps were shown to result in the more significant tensile strength knockdowns than only gap or overlap defects. This was explained by the larger degree of out-of-plane waviness, which is induced by this defect combination [244].

The use of a caul plate reduced thickness variation and tensile results even of severe superimposed gap defects in all plies were within 10 % of the reference strength. Without a caul plate, large thickness variations and resin-rich regions caused more significant tensile strength knockdown [227, 235]. Through-laminate thickness staggering of defects, as opposed to co-located defects was shown to significantly decrease strength knockdown in almost all cases [227, 229, 229, 244, 248]. Out-of-plane tensile strength was also shown to be affected by gap defects. Zhou et al. [246] found a correlation between gap size and quantity and the resulting out-of-plane tensile strength knockdown.

Numerous experimental studies also investigated the impact of rectangular gap and overlap defects on compressive properties [192, 225, 227–230, 233, 236, 237, 243–245, 247]. With the exception of Suemasu et al. [245], all studies comparing tensile and compressive properties of AFP laminates containing equal gap or overlap defect patterns found higher knockdown factors for compressive properties, than respective tensile properties [227, 228, 233, 237, 244, 247]. Out-of-plane undulations are more critical for compressive properties. Furthermore gap defects result in a through-thickness asymmetry and local shift of the mid-plane, which causes a bending moment in the compressive specimen and promotes local buckling [229, 230, 235, 249]. This effect can be mitigated by using a caul plate [235]. 90 ° rectangular gap and overlap defects result in the most significant knockdown of compressive strength results due to increased out-of-plane waviness in 0 ° plies [225, 243]. Overlap defects tend to be less critical than gap defects, and in some cases even lead to increased compressive strength [192, 229, 230, 245]. A combination of gap and overlap defects results in more severe out-of-plane undulations and higher strength knockdown than only gap or overlap defects [244]. Undulation angle [233, 234] and magnitude factor [247] were discussed to quantify out-of-plane undulation severity and positive correlations between these factors and compressive strength knockdown was demonstrated. Staggering again plays an important role in defect mitigation of compressive properties as well [227, 229, 230, 236]. For compression properties, just as for tensile properties, the defect size is not a sufficient criterion for assessing the influence on the mechanical properties, but must be considered in the context of staggering and the interaction of the individual defects [222]. Compression failure is introduced by an interaction of in-plane compression and interlaminar shear stresses in the 0 ° plies with out-of-plane undulations, resulting in kink-band type failure mode [243]. The introduction of severe defects can also result in buckling and premature failure [236].

An overview of the experimental literature on the impact of rectangular defects on tensile and compressive properties is presented in Table 2.4. A more comprehensive breakdown of literature defect types and sample setups can be found in Appendix A1, Tables 8.3-8.6.

Table 2.4: Literature overview of achieved relative mechanical results of autoclave-consolidated thermoset samples with rectangular defects compared to defect-free reference

Property	Defect Type	Reference	Proportional Results	
			Strength [%]	Modulus [%]
Tension	Gaps (aligned)	[225, 228, 230, 244, 248]	46.5 - 101.9	61.4 - 109.9
	Gaps (staggered)	[230, 244, 245]	78.1 - 99.8	81.2 - 104.4
	Overlaps (aligned)	[225, 230, 244, 248]	77.8 - 112.9	91.3 - 121.2
	Overlaps (staggered)	[230, 245]	81.7 - 123.6	95.1 - 122.2
	Combined Gap/Overlap	[225, 227, 233, 244]	78.8 - 102.6	103.6
Compression	Gaps (aligned)	[225, 228, 230, 244]	44.1 - 107.6	45.1 - 97.4
	Gaps (staggered)	[230, 244, 245]	62.1 - 101.3	76.0 - 100.0
	Overlaps (aligned)	[225, 230, 244, 248]	81.9 - 110.4	85.8 - 115.3
	Overlaps (staggered)	[230, 245]	91.3 - 104.2	87.5 - 113.9
	Combined Gap/Overlap	[225, 227, 233, 243, 244]	63.2 - 100.0	93.9

Bending strength and apparent interlaminar shear strength properties of laminates with gap and overlap defects were also investigated experimentally [234, 238, 248, 250–252]. Depending on the defect pattern some studies showed negligible influence of defects [252] whereas other investigations obtained significant strength decreases of up to 31 % [234, 250, 251]. Overlap defects were less critical for short beam bending strength and in some cases led to improved strength results, compared to laminates without defects [248]. While failure of defect-free three-point-bending specimens occured via matrix cracking and fiber fracture above the mid-plane in the vicinity of the central load application point, it shifted to shear failure of the resin pockets in the area of defect-induced out-of-plane wrinkles [234].

Simulation, once the model is validated, allows for larger variation of gap or overlap variations and staggering patterns as well as the analysis of larger structures. Progressive failure analysis based simulation models were proposed in several studies [192, 232, 237, 249, 253–255]. Marrouze et al. [253] found gap-induced waviness to be dependent on height of the gaps, which depends on the tape thickness, rather than the width of the gap defects. On coupon level, a critical defect width value can be determined, above which no further deterioration of the mechanical properties occurs. On panel level, less knockdown was observed than on coupon level due to load distribution. Li et al. [237] developed a meshing tool to generate gap and overlap models, successfully modeling out-of-plane undulations and thickness variation. Realistic gap and overlap representation compared with experimental specimen cross-sections was achieved. Different gap staggering strategies and defect geometries were analyzed, however the results were not validated experimentally. Ghayour et al. [255] introduced an Induced Defect Layer Method, which uses a geometrical parameter representing the local defect areas without the need for modeling the individual defects in the FE mesh. This allowed for efficient computation and and achieved good agreement with literature experimental values. Further coupon-level progressive failure analysis models were developed and validated for Open Hole Compression [232], Tension [249, 254] and compression properties [192]

Triangular gaps and overlap defects

Triangular gap defects with very small opening angle could be approximated by rectangular defects. Realistic triangular defects resulting from Variable Stiffness Panels or complex geometries are, however, often characterized by larger opening angles [240].

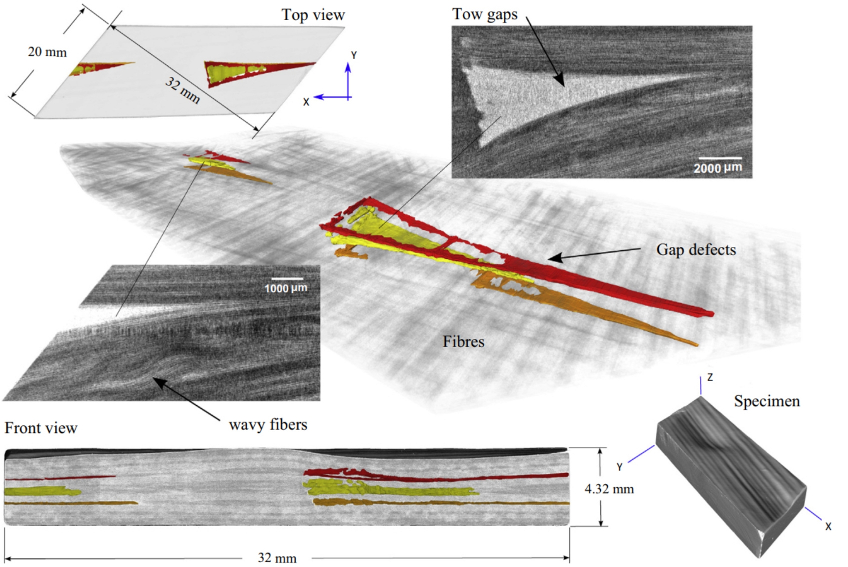

Figure 2.22: Computed tomography scan of triangular gap defects, reprinted from [239] with permission from Elsevier

To this end realistic triangular defects geometries were investigated in several studies. Falco et al. [226, 239–241, 256] investigated staggered and co-located realistic triangular gap and overlap defects of 12° opening angle and 6.35 mm width. The defects resulted from a (51 ° | 39 °) discontinuity in the ply that contained the defects, replacing a 45°-ply in an otherwise regular symmetric laminate. Distinctive triangular resin-rich areas were observed at the location of gap defects. Similar to rectangular defects, this resulted in out-of-plane waviness of subsequently-placed plies and total laminate thickness variation at the defect location (Figure 2.22) [239].

Coupon level tensile tests showed the most significant knockdown of 22 % for the co-located gap defects. Both co-located overlaps and staggered gaps led to less significant weakening of the laminate. Open hole tensile tests showed negligible impact of defects and strategically introduced defects could even be beneficial by extending the stress concentration region and thus lowering peak stress. Compression after impact (CAI) testing of staggered and co-located triangular gap defects showed little impact of gap defects at the tested impact energy levels [241]. Progressive Failure Analysis models of tensile and OHT coupon level simulation were successully validated for co-located triangular gap defects [239, 240].

Similar work by Nimbal et al. [257] investigated triangular gap defects in 90 ° plies of compressive test specimens and found increased out-of-plane waviness and significant decrease in compressive strength. Three-dimensional Finite Element models were created based on microsections of gap defects to represent defect-induced out-of-plane undulations and were successfully validated for compressive test results.

Zhang et al. [242] developed a layer-by-layer staggering strategy to avoid through-thickness overlap of triangular gap defects. Using ultrasonic scanning, microsections and FE models, the authors showed that this strategy reduced stress distribution and out-of plane waviness as compared to a standard staggering strategy, using the example of a C-shaped composite spar element. Similarly, Swingle et al. [258] investigated the scope of defect stacking of triangular geometry-induced gap and overlap defects and developed an optimization algorithm to minimize throught-thickness defect stack-up, using the example of a double-curved open surface with constant fiber angle layup.

Thermoplastic gap and overlap defects

So far, only a few publications on thermoplastic AFP and gap defects have been published. Zenker et al. [200, 259] investigated rectangular 7.35 mm and 2.5 mm gap and 7.35 mm and 1 mm overlap defects in 0 ° and 90 ° layers of CF/PPS QI laminates. Hot press and autoclave consolidation subsequent to AFP layup was used. 90 ° and 0 ° gap defects were found to significantly decrease both tensile and compressive strength results because of resulting out-of-plane undulations throughout the laminate and decreased fiber amount in primary load direction, respectively. Strain analysis showed strain concentration in the defect areas. Overlaps were generally found to be less severe then gap defects. The severity of out-of-plane undulation was found to affect strength knockdown, as similarly observed in thermoset defect investigations [225–230].

Rakhshbahar and Sinapius [260] introduced the approach of combining AFP and additive manufacturing to mitigate gap defects. Unidirectional test specimens were manufactured using hand-layup of thermoplastic prepreg and separately 3D-printed unidirectional carbon-fiber-reinforced gap inserts and subsequent hot pressing. Tensile testing, three- and four-point-bending tests showed strength and modulus results, close to the reference specimens without defects, mitigating the gap-induced strength knockdown factors.

Clancy et al. [261, 262] investigated in-situ spreading of thermoplastic prepreg tape in order to avoid gap or overlap defects for double-curved geometries. The principle was successfully demonstrated using a prototype device, reaching up to 62 % increase in tape width. While no influence on the properties could be determined, this approach is still in a very early concept stage and needs to be implemented in a functional end-effector.

Peeters et al. [263] investigated the composition of ply drops in laser in-situ AFP-manufactured laminates. The results can also be applied to gap defects, which can be viewed as local two-sided ply drops. The authors showed that triangular pores arise at ply drop locations as opposed to characteristic resin-rich areas in thermoset laminates. The pores can be avoided if the layup direction of the subsequent ply (belt ply) is oriented parallel to the ply drop edge. For belt plies perpendicular to the ply drop (90 ° ply) the layup direction was shown to play an important role. If the consolidation roller was ascending a larger triangular void was observed compared to descending layup direction, since in the latter case both the top and side of the dropped ply are heated, resulting in slightly stronger flattening of the edge of the dropped ply.

2.3 Complex geometry applications

This final section of the literature review on applications of complex components is divided into Variable Stiffness Panels and in-situ AFP technology demonstrators. Variable Stiffness Panels have not been investigated with regards to in-situ AFP in the literature yet. As this work, however, aims to adress this topic, the thermoset Variable Stiffness Panel literature is considered. In-situ AFP technology demonstrators were manufactured in a couple of research projects and are briefly introduced in this section.

2.3.1 Variable Stiffness Panels

As discussed in section 2.2.1, laminates with variable fiber orientation can result in improved stiffness and strength properties for the required load cases. Improvements of stress concentration around cut-outs, buckling performance and postbuckling stiffness were demonstrated in the literature [264]. Numerous publications deal with the theoretical design and optimization of such Variable Stiffness Laminates [181, 183, 184, 189, 193, 194, 206, 226, 265–269]. A detailed review can by found in [270].

The curved paths of Variable Stiffness Laminates result in the steering- and gap/overlap defects discussed in the previous chapter 2.2. Assuming thermoset AFP manufacturing signature, these effects were considered in further optimization approaches [183, 188, 191, 204, 226, 271–273]. The inclusion of a limit for the steering radius for example led to a reduction in buckling load improvement from 111 % to 57 % compared with a standard laminate design [192]. A defect layer method was introduced to precisely and efficiently model gap and overlap defects in the design [192, 224, 274]. The critical buckling load improvement over a standard design was shown to increase to 105 % with overlaps compared to 56 % without considering overlaps. A 0 % coverage ratio design (full gap design) on the other hand only allows for a 40 % buckling load improvement [192]. The use of wider prepreg tape results in larger triangular gap defects, resulting in lower strength performance [274].

Thermoset AFP variable stiffness laminates were also manufactured [182, 184, 223] and tested [275–279]. Marouene et al. [275, 276] manufactured and tested Variable Stiffness Panels with 0 % and 100 % coverage ratio and found 45 % and 22 % higher weight-normalized buckling loads for the overlap- and gap-panel, respectively, as compared to a quasi-isotropic reference laminate. Khani et al. [277] manufactured an optimized Variable Stiffness Panel with a central cut-out and performed component-level tensile tests (Figure 2.23(a)). The Variable Stiffness Panel achieved 85 % higher ultimate failure load than a quasi-isotropic reference laminate and 35 % higher ultimate failure load than a straight fiber stiffness optimized laminate. Zhu et al. [278] similarly found a 36 % relative improvement of an optimized Variable Stiffness Panel with central hole under tensile loading compared with a unidirectional laminate. Peeters et al. [279] used dry fiber placement and vacuum-assisted resin infusion to manufacture a Variable Stiffness panel with 50 % coverage ratio and internal ply drops, achieving 11.7 % higher buckling load and 15 % weight saving compared to a quasi-isotropic referenc laminate (Figure 2.23(b)).

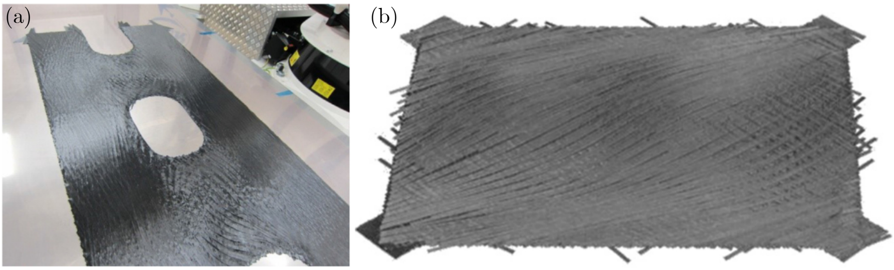

Figure 2.23: Variable Stiffness Panels: (a) Thermoset AFP laminate with central cut-out, reprinted from [277] with permission from Elsevier, (b) Dry fiber placement laminate, reprinted from [279] with permission from Elsevier

Wang et al. [198] compared unidirectional laminates with constant curvature variable stiffness layup on a coupon level and found slightly decreased tensile strength but 16.7 % increased bending strength. Blom adapted the principle of flat Variable Stiffness laminates to cylindrical and conical structures [186, 187, 190, 205]. The optimization of a variable stiffness cylindrical shell resulting in 17 % improvement in buckling load under longitudinal bending [190, 280].

To the authors' knowledge, manufacturing of thermoplastic Variable Stiffness Laminates or considerations of in-situ AFP manufacturing signature have not been investigated yet.

2.3.2 In-situ AFP technology demonstrators

While AFP represents the state of the art for the production of thermoset composite components, only a limited number of technology demonstrators and applications have been presented for in-situ AFP. Important recent developments are presented in this section.

A group of researches at the University of Limerick's Bernal Institute designed, manufactured and tested a full-scale wing box segment of an Airbus A320-sized aircraft using in-situ AFP (Figure 2.24 (a)) [281, 282]. Closed-section omega stringers were manufactured using an in-situ AFP winding process and inserted into a collapsible tooling [281, 282]. The stringers were joined to the skin during the first-ply layup. The skin design used in-situ AFP winding with fiber steering for a variable stiffness layup. The tapes were steered from 35 ° to 52 °, considering the minimal steering radius of 400 mm, determined in [219]. Elastic buckling was demonstrated in both simulation and full-scale test of the wingbox. The variable stiffness section of the skin showed significant gaps between steered tows [261]. Spreading of thermoplastic prepreg tape, as presented in section 2.2.3 was mentioned as a possible solution to overcome this issue.

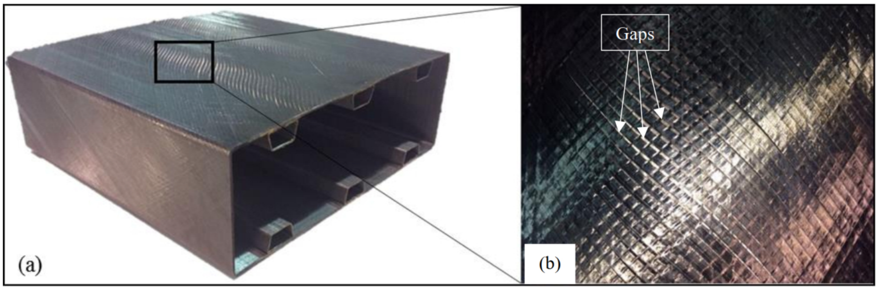

Figure 2.24: Thermoplastic wing box segment [261]: (a) wing box overview (b) detail view of steering-induced gap defects

Researchers at the German Aerospace Center (DLR) Institute of Structures and Design manufactured a full scale 8 m long and 4 m diameter fuselage half shell manufacturing demonstrator using in-situ AFP skin layup and subsequent ultrasonic and resistance welding for joining stringers and frames, respectively (Figure 2.25(left)) [283–286].

Recent work by Cetim showed an in-situ consolidated Krueger flap, manufactured using heated tooling and a thermoplastic tape winding process [287] (Figure 2.25(right)).

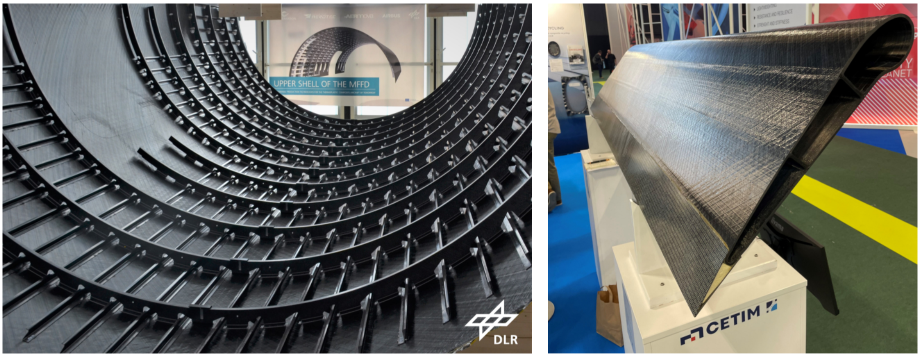

Figure 2.25: Clean Sky 2 in-situ AFP demonstrator components: (left) Multifunctional Fuselage Demonstrator upper shell [289], (right) Krueger wing flap [290]

Researchers at FIDAMC (Foundation for Research, Developement and Application of Composite Materials, Getafe, ES) demonstrated co-consolidation of thermoplastic stiffening elements and in-situ AFP skin layup in multiple publications [67, 166, 288]. Martín et al. [166] manufactured a component level fuselage section consisting of two press-consolidated omega stringers, a press-consolidated Z-shaped frame and in-situ AFP skin. The stiffening elements were inserted into a 180 °C heated tooling and joined to the skin during the first ply layup. In-situ AFP in plane shear strength (IPSS) reached 75 % of oven consolidated reference laminates. Zuazo et al. [288] similarly manufactured an upper wing shell demonstrator using in-situ AFP layup directly on T-Stringers inserted into a tooling.

2.4 Summary of the State of the Art

The analysis of the literature allows the following conclusions to be drawn. In-situ AFP has been in development for more than four decades. A large part of the research has focused on process optimization to achieve autoclave-level consolidation quality. While this has been achieved for unidirectional layup in some cases, manufacture of realistic quasi-isotropic laminates still presents a challenge to the technology. State of the art laser heating and process control- and monitoring systems as well as AFP-grade prepreg material have the potential to further advance the technology. Recent developments successfully investigated higher layup rates and process scaling for potential future full-scale applications. The in-situ AFP process represents a multi-factorial optimization problem, the solution of which, however, offers the prospect of far-reaching advantages for the production of large-scale composite primary structure components.

So far, only very limited research has been carried out on in-situ AFP for complex geometries. Comprehensive literature is however available on thermoset AFP for complex geometries. Complex geometries inevitably result in defects in the layup on the surface of the complex part. Layup strategies were developed for thermoset AFP to optimize and automate path planning on complex geometries. Depending on the strategy, gap and overlap defects, steering defects and fiber angle deviation have to be accounted for in the laminate. Numerous studies analyzed characteristics, interaction and mechanical impact of these defects for thermoset AFP. Limited work is available for thermoplastic AFP and in-situ AFP in particular.

Chapter 3

Research Aim and Outline

3.1 Research Gap

As detailed in Chapter 2, there is extensive literature on thermoset AFP for complex structures. For in-situ AFP, however, further work is required to investigate the impact of complex geometries on the resulting laminate composition and performance. Without the subsequent autoclave- or press consolidation, complex geometry layup presents a significantly greater challenge to in-situ AFP compared to thermoset AFP, as inevitable defects cannot be mitigated in a post-consolidation process. A detailed analysis of the defects and investigation of the resultant knockdown factors is thus required. In the literature, the impact of the geometry-induced steering- and gap-or overlap defects on the laminate composition and the resulting mechanical properties has not yet been investigated. Key research gaps include the quantification of steering-induced narrowing of consolidated tape width and deriving adjusted layup paths and quantifying the impact of steered layup and gap and overlap defects on mechanical properties of resulting in-situ AFP laminates. Such results are necessary to develop in-situ AFP process-specific layup strategies. While many of the basic correlations for geometry-dependent path planning and the resulting defect geometries can be adopted from thermoset AFP, the weighting of the parameters for the layup strategy considering in-situ AFP-specific defect signature is novel. This would be an important step in assessing the suitability of the in-situ AFP technology for complex structures and potential applications.

3.2 Research Aim and Objectives

The aim of this work is thus to investigate the impact of geometry-induced defects on in-situ AFP-manufactured laminates and to develop layup strategies that consider the process-specific defect signature. To this end, the following research objectives were derived:

1. Determine geometry-induced defect dimensions for relevant complex geometries.

2. Investigate steering defects with a particular focus on their impact on laminate level mechanical properties.

3. Investigate geometry-induced gap and overlap defects and their impact on laminate composition and mechanical properties.

4. Develop layup strategies considering the geometry-induced defect influence for in-situ AFP.

3.3 Outline of the thesis

This work is structured as follows: Firstly, in the following Chapter 4 the relevant materials, manufacturing and analysis methods are presented. In Chapter 5, layup strategies for relevant complex geometries are investigated to determine relevant defect geometries as a basis for the experimental design of the subsequent investigation of steering and gap and overlap defects. Furthermore, the interdependencies of layup strategy parameters and the resulting geometry-induced defects are determined as a basis for the layup strategy recommendations in Chapter 8. In Chapter 6 in-plane path curvature is investigated experimentally in terms of the resulting steering defects for varying process parameters and the impact on laminate level mechanical properties. Gap and overlap defects and their impact on the resulting laminate composition and mechanical properties are investigated in Chapter 7. Chapter 8 presents the conclusions, which can be drawn from both defect analysis chapters with regard to resulting layup strategies for in-situ AFP and the laminate quality, which can be expected from the process. Final conclusions and an outlook which addresses relevant topics for subsequent work are outlined. Additional information can be found in the appendix (Chapter 8.4).

Chapter 4

Methodology

This chapter presents the materials, manufacturing technology and analysis methods used in this research work. The chapter includes the Automated Fiber Placement and hot press facilities and respective manufacturing process parameters. The sample preparation procedure and analysis methodology to characterize the test laminates is described.

4.1 Material

Thermoplastic CF/LM-PAEK prepreg tape of different widths was used for the experimental work (Table 4.1). AFP-grade half-inch prepreg tape with 55 % fiber volume fraction by Suprem SA (Yverdon-les-Bains, Switzerland) was primarily used for the AFP experiments due to the good consolidation quality following in-situ AFP processing, as discussed in Section 2.1.2.

Extensive reference data was available for this material. Quarter-inch tape with similar specifications was used to analyze the impact of the tape width. 300 mm-wide prepreg tape by Toray Advanced Composites (Morgan Hill, United States) was used as a substrate for some of the experiments and served as a first ply for the laminates manufactured within this work.

Table 4.1: Thermoplastic prepreg materials

Material	Width [mm]	Thickness [mm]	Fiber volume fraction [%]	Fibers
Suprem $\frac{1}{2}''$ CF/LM-PAEK	12.7	0.19	55	AS7
Suprem $\frac{1}{4}''$ CF/LM-PAEK	6.35	0.13	55	AS7
Toray $12''$ CF/LM-PAEK	300	0.2	60	T700

4.2 Thermoplastic Automated Fiber Placement

The thermoplastic tape placement facility at DLR in Stuttgart was used for the manufacturing of all laminates, test specimens and demonstrator parts within the scope of this work.

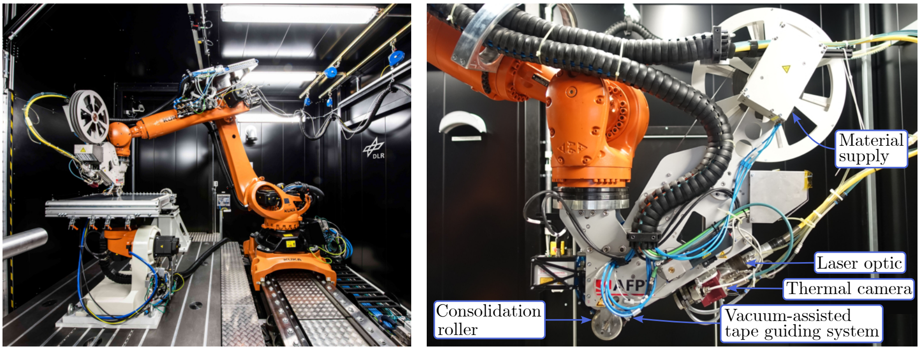
(a) Tape placement facility

(b) AFP end effector (MTLH)

Figure 4.1: Thermoplastic tape placement facility at DLR Stuttgart

The facility consists of a KUKA AG (Augsburg, Germany) Quantec KR210 R3100 ultra six-axis robot and a two-axis rotatable and tiltable KUKA DKP400 V5 positioner with a flat tooling, which can be heated up to 250 °C (Figure 4.1(a)). The Multi Tape Laying Head (MTLH) end-effector by AFPT GmbH (Dörth, Germany) is attached to the robotic arm and can process three half-inch tape spools simultaneously or one single spool of half-inch, quarter-inch or one inch prepreg tape (Figure 4.1(b)). A 6 kW LDF-series fiber-coupled near infrared diode laser by Laserline GmbH (Mülheim-Kärlich, Germany) was used as the heat source for the in-situ AFP process. The laser beam is delivered to the end-effector via fiber-optic cable. Depending on the track configuration of the end-effector, different laser optics are used, expanding the beam to a rectangular flat top intensity profile adjusted to the respective track width (Table 4.2). The surface temperatures of the incoming tape and the substrate are continuously monitored using an infrared sensor array (thermal camera). The temperature measurement is used to control the laser power in order to attain the specified target temperature.

Table 4.2: Laser optics used for varying track width configurations

Track configuration	Laser optic	Working distance [mm]	Spot dimension [mm^2]
$1 \times \frac{1}{2}''$	OTS-1	242	40 x 20
$1 \times \frac{1}{4}''$	OTS-1	195	43 x 11
$3 \times \frac{1}{2}''$	OTS-1	320	50 x 50

The laser angle is also continuously controlled using the temperature measurements to maintain the same temperature for both, the tape and substrate surface. Both, the laser power and the laser angle control systems can also be overwritten manually for special applications. Due to the position of the thermal camera with respect to the consolidation roller, the nip point is not visible in the thermal camera image. The nip point temperature, is defined as the hottest temperature measured by the thermal camera, assuming a thermal emissivity $\varepsilon_e = 1$.

A water-cooled 60 mm wide steel consolidation roller with a 5 mm thick, shore A 60 hardness silicone outer layer and a total diameter of 80 mm was used. The consolidation roller, heating- and temperature control system are attached to an extendable part of the end-effector, which can be actuated via a pneumatic cylinder. This enables level compensation and applies the consolidation pressure. A system pneumatic pressure combined with the weight force of the extendable part of the end-effector results in a consolidation force of 500 N at the nip point. A specially developed patented tape guiding system was used, which replaced the blowing nozzle with vacuum suction openings, allowing the tape to be positioned longer on the guiding system after the tape cut and increasing lateral positioning accuracy.

Table 4.3: AFP manufacturing parameters

Layup speed [mm/s]	125
System pneumatic pressure [bar]	6
Tool set temperature [°C]	20, 200
Nip point set temperature [°C]	470
Tape tension [N]	15

As presented in the literature section (2.1.2), an optimized parameter set was found for the utilized prepreg material and is used for the experimental work (Table 4.3). Two tool temperatures, an unheated room-temperature and a 200 °C heated configuration were used for the experiments.

Table 4.4: Consolidated tape widths

Prepreg tape	Tool temperature [°C]	Consolidated tape width [mm]
Suprem $\frac{1}{2}''$ CF/LM-PAEK	20	14.2
	200	15.0
Suprem $\frac{1}{4}''$ CF/LM-PAEK	20	7.6

The widening of the tape through the process varies depending on the process parameters. The consolidated tape width $w_{t,c}$ was determined experimentally for the relevant parameter sets (Table 4.3) and is listed in Table 4.4.

4.3 Hot pressing

For post-consolidation of laminates, two hot presses were used for different sized laminates. A Diefffenbacher GmbH (Eppingen, Germany) HPO 400 hot press was used for the larger sized laminates. A smaller Rucks Maschinenbau GmbH (Glauchau, Germany) KV330.00 hot press was used for the smaller laminates. The respective dimensions of the regular flat dies and process parameters are presented in Table 4.5.

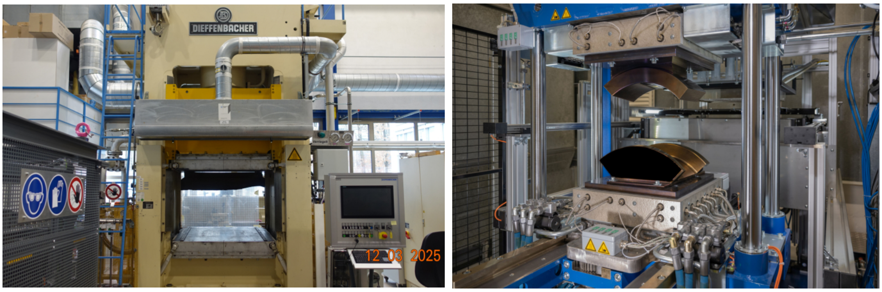
(a) Dieffenbacher HPO 400

(a) Rucks KV330.00

Figure 4.2: Hot press facilities at DLR Stuttgart

Table 4.5: Hot press consolidation process parameters

Process parameter	Dieffenbacher HPO 400	Rucks KV330.00
Die area [mm^2]	690 x 530	300 x 300
Consolidation temperature [°C]	365	365
Holding time [min]	30	30
Heating rate [K/min]	5	10
Cooling rate [K/min]	5	4
Pre-pressing pressure [bar]	2	2
Pressing pressure [bar]	15	15
Cooling pressure [bar]	15	15

4.4 Process Parameter Analysis

The first analysis of the consolidation quality can be carried out directly using the recorded process parameters. The AFP system provides time series data of relevant process parameters, which were exported as text files and processed using specially developed Python scripts.

The process parameters of the time series data relevant for this work were the tool center point coordinates, thermal camera measurements of incoming tape, substrate and the estimated nip point temperature, laser power, laser angle and tape tension. As discussed in section 2.1.1, the process temperature is the most relevant process parameter for the in-situ AFP process. A precise temperature measurement is also vital for the laser power control system, which uses the thermal camera measurements as input variables for its control algorithm. The AFPT MTLH end-effector uses a 168 x 128 pixel infrared sensor array which captures temperature data at a measurement frequency of 60 Hz and with an emissivity coefficient $\varepsilon_e = 1$. The measured temperature thus does not represent the real temperature but a repeatable reference value with an accuracy of ±2 %. This approach was selected, since it is was not the objective to measure the exact process temperature, but to analyze temperature deviations from the empirically optimized process parameter set. The recorded matrix of temperature values is evaluated row by row. For each row, the hottest pixels are deleted and an average value is calculated from a defined number of the next hottest pixels, which is output as the temperature for the respective row. The rows of the sensor array are divided into evaluation areas, as presented in Figure 4.3.

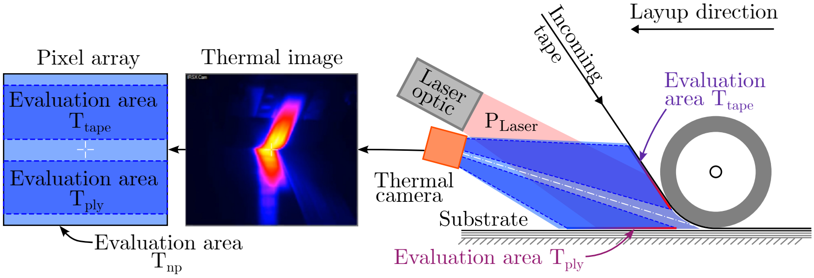

Figure 4.3: AFP end effector thermal camera temperature measurement principle

The hottest row of the tape temperature (T_{tape}) and ply temperature (T_{ply}) evaluation areas are defined as the tape temperature and ply temperature, respectively. The nip point temperature (T_{np}) is defined as the hottest row of the entire temperature array. These three temperature values are recorded as time series and are available for subsequent process parameter analysis. Due to the laser shadow and the pressure-induced deformation of the consolidation roller, the thermal camera cannot measure the temperature exactly at the nip point. The distance between the temperature measuring point and the tool center point (TCP), which is defined as the central contact point of the roller with the tool, was experimentally determined for the utilized end-effector and consolidation roller to be 7.755 mm in [291] and was considered in the process temperature analysis.

4.5 Ultrasonic Testing

An Evident (formerly Olympus, Tokyo, Japan) OmniScan MX2 with a 5L64-NW1 phased array probe was used for ultrasonic scanning of the laminates. A frequency of 5 MHz was selected because of its common use, providing comparability of the results with the literature. Depending on the tested laminate, a voltage of 40 V, 80 V or 115 V in combination with a gain between 0 dB and 3 dB was selected to achieve a back wall echo of 80-90 % full-screen height on an A-scan display without over-amplifying the front wall echo [292].

4.6 Optical 3D Scanning

A Carl Zeiss GOM Metrology GmbH (Braunschweig, Germany) ATOS 5 optical 3D scanning system was used for the detection of tape dimensions and layup paths. GOM Inspect 2020 software was used to process the generated image data.

4.7 Computed Tomography

Micro computed tomography (μCT) scans were performed using a high resolution μCT system v|tome|L 240/450 (Baker Hughes, Wunstorf). X-ray parameters 180 kV/160 μA, an exposure time of 334 ms and 1400 projections per sample were used to achieve a voxel size of 39 μm. Data analysis and visualisation were conducted using the commercial software package VGStudioMax 2024.4 (Volume Graphics GmbH, Heidelberg).

4.8 Microscopy

Microanalysis analysis specimens were embedded in epoxy resin and ground using a Struers ApS (Ballerup, Denmark) grinding and polishing system. A two step grinding process followed by a three step polishing process using 9, 3 and 0.25 μm diamond suspensions, respectively, was used for the specimen preparation. Micrograph images were taken using a Keyence Corporation (Osaka, Japan) VHX-5000 digital microscope at 500x magnification.

4.9 Mechanical Testing

Laminate level tensile and compressive tests were carried out according to AITM 1-0007 A2 [293] and AITM 1-0008 A2 [294], respectively. Water jet cutting was used for preliminary sizing of the specimens, with a specimen diamond saw used to realize the final dimensions. The surface of the specimens was plasma activated and fit with 1.5 mm glass fiber-reinforced epoxy end tabs. Tensile specimen dimensions were 250 mm by 22 mm with 50 mm end tabs. The specimens were tested until final failure using shear loading at 270 bar hydraulic clamping pressure, a rate of 2 mm/min and a ZwickRoell (Ulm, Germany) 200 kN material testing machine with hydraulic clamping system and 250 kN load cell. Digital Image Correlation (DIC) was used for strain measurement (Section 4.10). The dimensions of each individual specimen were measured and used for the calculation of ultimate tensile stress σ_{tu} and modulus E_t following:

$$\sigma_{tu} = \frac{P_u}{t_n \cdot w} \tag{4.1}$$

$$E_t = \frac{\Delta\sigma}{\Delta\epsilon} \tag{4.2}$$

where P_u was the ultimate load, t_n was the specimen thickness, w was the specimen width and $\Delta\sigma$ and $\Delta\epsilon$ were the stress and strain differences at 10 % and 50 % of the ultimate strength, respectively.

Compressive test specimen dimensions were 152 mm by 22 mm with 65 mm end tabs and 22 mm free length. A Hydraulic Compression Test Kit for Composites (HCCF) by ZwickRoell was used for the tests. DIC was used for strain measurements of the front and side of the free length, while strain gauges were used for the back side of the free length, which was not accessible with DIC. The surface of the sample was roughened with fine sandpaper and then cleaned with isopropyl alcohol as preparation for strain gauge application. Strain gauges were attached using General purpose cyanoacrylate (type CN) adhesive for strain gauges by Tokyo Measuring Instruments Laboratory Co., Ltd. (Tokyo, Japan). Linear standard strain gauges with 3 mm measuring grid (type 1-LY21-3/120) by Hottinger Brüel & Kjaer GmbH (Darmstadt, Germany) were used. In order to track the failure mode, damage initiation and strain fields using DIC, an anti-buckling device was not used. The compressive specimens were tested until final failure using combined loading (shear loading at 50 bar hydraulic pressure and end-loading), a rate of 0.5 mm/min and a ZwickRoell 200 kN material testing machine with 250 kN load cell. The ultimate compressive strength σ_{cu} was calculated following:

$$\sigma_{cu} = \frac{P_u}{t_n \cdot w} \tag{4.3}$$

where P_u was the ultimate load, t_n was the specimen thickness and w was the specimen width. The compressive modulus E_c was calculated following:

$$E_c = \frac{\Delta\sigma}{\Delta\epsilon} \tag{4.4}$$

where $\Delta\sigma$ and $\Delta\epsilon$ were the stress and strain differences at 10 % and 50 % of the ultimate strength, respectively.

Five-point-bending testing, also referred to as double beam shear test, following ISO-19927 [165] was used to determine interlaminar shear strength (ILSS). As discussed in Section 2.1.2, five-point-bending testing, as opposed to three-point bending testing, results in relevant in-plane shear failure modes for ductile thermoplastic specimens. A span-to-thickness ratio of 5 and 6 mm diameter cylindrical supports were used. The resulting specimen dimensions were 40 mm by 20 mm. The specimens were cut from the laminates using water jet cutting. DIC was used for strain measurement and detection of delamination and failure modes. The specimens were tested up to an advanced delamination state using a ZwickRoell 100 kN material testing machine with a 100 kN load cell and a crosshead speed of 0.5 mm/min. The interlaminar shear stress τ was calculated following:

$$\tau = \frac{33 \cdot P}{64 \cdot w \cdot t_n} \tag{4.5}$$

Maximum shear strains were extracted from DIC strain field analysis of virtual measurement surfaces in the principal shear regions at each loading step. The crack initiation was defined as the point of maximum acceleration of the shear strain rate.

Flexural stiffness and strength were determined using a four-point-bending test following ASTM D7264 [295]. A span to thickness ratio of 32 was used, resulting in a support length of 70 mm and specimen dimensions of 92 mm by 13 mm. Support and loading noses of 6 mm diameter were used. DIC was used for strain measurement. The specimens were tested until failure using a ZwickRoell 100 kN material testing machine with a 100 kN load cell and a crosshead speed of 1 mm/min. The maximum strain at the outer surface of the specimen, occurring at mid-span was calculated following:

$$\varepsilon_b = \frac{4.36 \cdot \delta \cdot t_n}{L^2} \tag{4.6}$$

where δ was the mid-span deflection of the specimen which was measured using DIC analysis (Figure 4.4), t_n was the specimen thickness and L was the support span (70 mm). The maximum stress occurring at mid-span of the specimen can be calculated following

$$\sigma_b = \frac{3 \cdot P \cdot L}{4 \cdot w \cdot t_n^2} \tag{4.7}$$

where P is the applied force and w is the specimen width. The flexural modulus of elasticity was calculated in the strain range between 0.001 and 0.003 with the closest available data points following:

$$E_b = \frac{\Delta\sigma}{\Delta\varepsilon} \tag{4.8}$$

where σ is the stress at the outer surface and ε is the maximum strain at the outer specimen surface. $\Delta\sigma$ and $\Delta\varepsilon$ are the difference in flexural stress and strain between the two selected points, respectively.

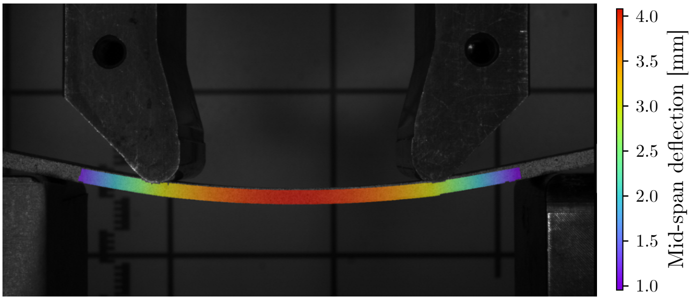

Figure 4.4: Four point bending DIC deflection analysis

4.10 Digital Image Correlation

Before testing, the side edges of all specimens and the front-facing surfaces of the free lengths of tensile and compressive specimens were coated with white paint and sprayed with a pattern of black speckles as reference for DIC. The sufficiently small size of the speckles, which is required to achieve an adequate resolution to detect cracks and delaminations, was defined as half of the layer thickness of 125 μm. A mean speckle size of 50 μm was achieved.

A Q400 DIC measurement system by LIMESS Messtechnik & Software GmbH (Krefeld, Germany) was used to record the tests at a framerate of 5 fps. The crosshead displacement and load were transferred from the material testing machine and synchronized with the DIC measurement system image data. The strain measurements for the respective evaluation of the experiments was determined by introducing virtual measurement surfaces in the relevant areas of the specimens surface. For tensile and compressive specimens, the virtual measurement surfaces were oriented in the center of the free length. The virtual measurement surfaces for shear strain analysis in five-point-bending tests was placed in the first principle shear region and evaluated in terms of the maximum shear strain at any loading step [106]. Figure 4.5 shows the experimental setup with lighting for the four test types.

(a) Tensile test setup (b) Compressive test setup

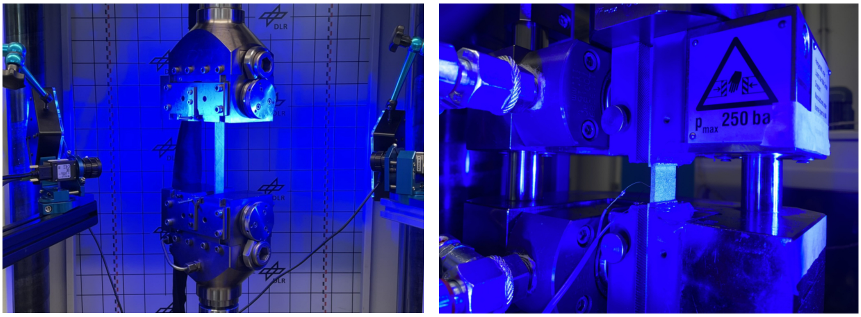

(c) Five-point-bending test setup (d) Four-point-bending test setup

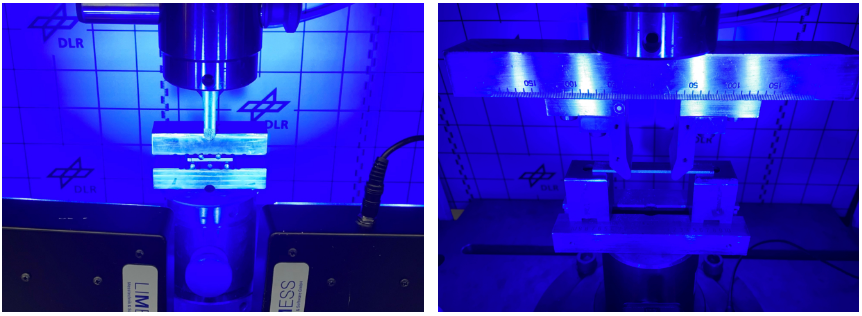

Figure 4.5: Mechanical test setups with DIC

4.11 Statistical Methods

For all employed statistical tests, a significance level of 0.05 was chosen. The distribution of the mechanical strength and modulus data sets was validated as normally distributed using the Shapiro-Wilk test. Lavene's Test was subsequently used, to assess the equality of the variances of the compared datasets. The statistical significance was then determined using a t-test for the comparison of two parameter set groups, while a one way ANOVA was used to determine the statistical significance of three and more sample group means, followed by Tukey's range test for pair-wise comparison of the parameter set groups in order to identify which group means were significantly different. The Tukey's range test was chosen over a t-test following one way ANOVA to avoid type I error due to multiple testing. The statistical analysis and data visualization was carried out by means of specially programmed Python scripts using the packages NumPy, pandas, statsmodels, SciPy, scikit-learn, Matplotlib and seaborn.

Chapter 5

Geometry and Analysis of Layup paths

This chapter presents a systematic derivation of geometry-induced defects, as defined in the literature review (Section 2.2) for relevant potential applications of the in-situ AFP process and was published in [296]. The triangular correlation between the three defect types steering, gap and overlap defects and angle deviation, resulting from complex geometries and applied layup strategy is demonstrated. The derived defect geometries are used as the basis for the experimental design in the following chapters. To this end, three geometries from current research projects are employed as case studies: A Variable Stiffness Panel structure as introduced in Section 2.3.1, which is a two-dimensional academic representation of a stiffness-optimized structure and is well suited for demonstrating geometry-induced defects on a laminate level; a hydrogen tank structure which creates regular defect patterns due to its double-curved but rotationally symmetrical and closed geometry; and a complex double-curved fuselage section which can be used to visualize the effect of free-form surfaces. The Variable Stiffness Panel is investigated analytically using a specially developed Python script. The hydrogen tank structure and fuselage section are analyzed using the commercial tape placement software VERICUT Composites Programming (CGTech, Irvine, California).

5.1 Variable Stiffness Panels

A parametric Python script for constant curvature Variable Stiffness Panels was developed based on analytic functions, allowing for an exact calculation of defect sizes for a wide range of input factors. A brief derivation of the analytic functions is provided below. Based on the Python algorithm, a parameter study was carried out to demonstrate the correlations between layup strategy and resulting defects and to find Variable Stiffness Panel configurations suitable for the in-situ AFP process.

5.1.1 Analytic algorithm for Variable Stiffness Panel analysis

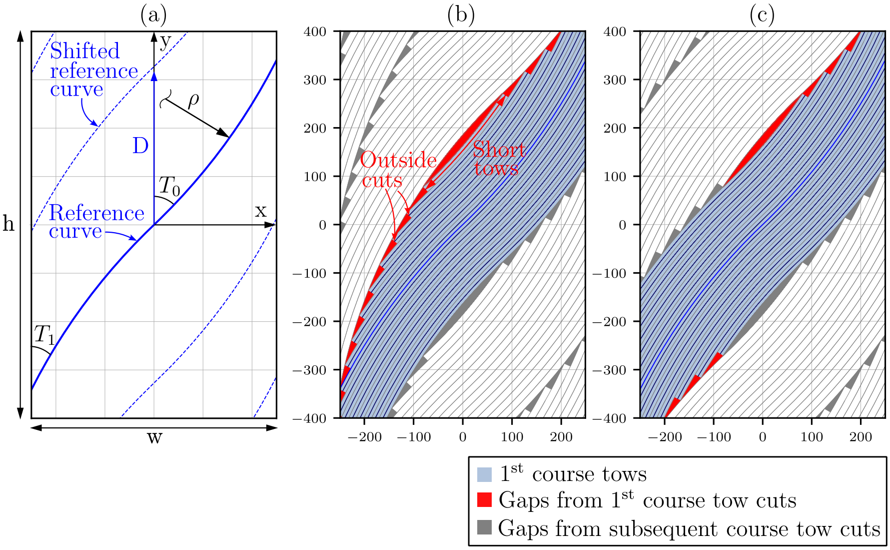

Figure 5.1: Constant curvature Variable Stiffness Panel design with 0 % coverage ratio: (a) Reference curve definition, (b) One-sided tow cuts [188, 192], (c) Tow cuts on the inside radius of the steered course

Constant curvature flat Variable Stiffness Panels can be defined by the parameterization given in Equation 2.6. Using the trigonometric identity $sin^2(t) + cos^2(t) = 1$ and substituting the equations gives the form:

$$y(x) = \begin{cases} \sqrt{\rho^2 - (x - \rho \cdot cos(T_0))^2} - \rho \cdot sin(T_0) & \text{if } x < 0 \\ -\sqrt{\rho^2 - (x + \rho \cdot cos(T_0))^2} + \rho \cdot sin(T_0) & \text{if } x \geq 0 \end{cases} \tag{5.1}$$

where T_0 is a constant that is defined as the angle between the y-axis and the reference curve $y(x)$ at the origin and ρ is the steering radius of the constant curvature reference curve (Figure 5.1(a)). The angle T_0, steering radius ρ and laminate width w determine the angle T_1 at the lateral boundaries of the laminate. This constant curvature reference path definition was also used in [188, 192]. The reference curve defines the course of the initial course of parallel tows. This can be viewed as a course of simultaneously placed tows using multi-tow layup or as individually placed tows which are placed in parallel. Figure 5.1(b) shows 16 parallel half-inch tows. The reference curve is shifted in the y-direction by the shifting distance D to create the subsequent courses of parallel tows. In order to avoid excessive overlaps, tow-cuts are required at the intersection of course-boundaries. Here it is important to note that while the reference curve lies in the middle of the grouped simultaneous tows, i.e. between tows 8 and 9, the order in which to cut tows is typically from one side of the group, i.e. "one-sided" beginning at tow 1 or 16. This has previously been promoted in studies such as by Fayazbakhsh [192]. For a 0 % coverage ratio (gap design) strategy, this is presented in Figure 5.1(b). With a one-sided approach, tows are cut at the upper boundary of each course at the intersection with the lower boundary of the subsequent course. This tow cut strategy however leads to two disadvantageous effects for AFP layup. Firstly, the tows are cut, both at the inside and outside boundary of the steered course. Outside cuts, however, were shown to lead to tow-straightening and deviation from the intended layup path [186, 215]. Secondly, this strategy leads to very short tows at the upper boundary of the course which can lead to conflict with the minimum cut length capabilities of the AFP end effector (Figure 5.1(b)).

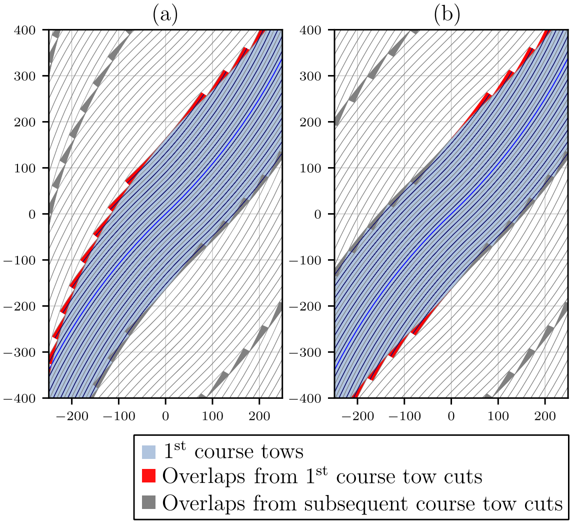

Figure 5.2: Constant curvature Variable Stiffness Panel design with 100 % coverage ratio: (a) One-sided tow cuts, (b) Tow cuts on the inside radius of the steered course

A novel strategy is suggested in this work, cutting tows only at the inside radius of the steered course (Figure 5.1(c)). In the example presented in Figure 5.1 with $T_1 < T_0$ tows are thus cut at the lower course boundary for $x < 0$ and at the upper course boundary for $x > 0$. Tow cuts at the outside radius are avoided and the minimum tow length is considered as each tow is only cut or started once on the laminate. The same principle can also be applied to a 100 % coverage ratio (overlap) design. A 100 % coverage ratio one-sided tow cut laminate representation and a laminate with the novel strategy of tow cuts on the inside radius of the steered course is presented in Figure 5.2 (a) and (b), respectively.

An analytical Python algorithm was developed to generate constant curvature Variable Stiffness Panel designs for the layup strategies presented above. The algorithm calculates resulting steering effects, angle deviation and gap or overlap defect dimensions for varying reference curve steering radii, tape width, number of parallel tows and further input parameters. A comprehensive list of input variables and calculated results is presented in Figure 5.3. A detailed description of the Python algorithm is presented in Appendix A2.

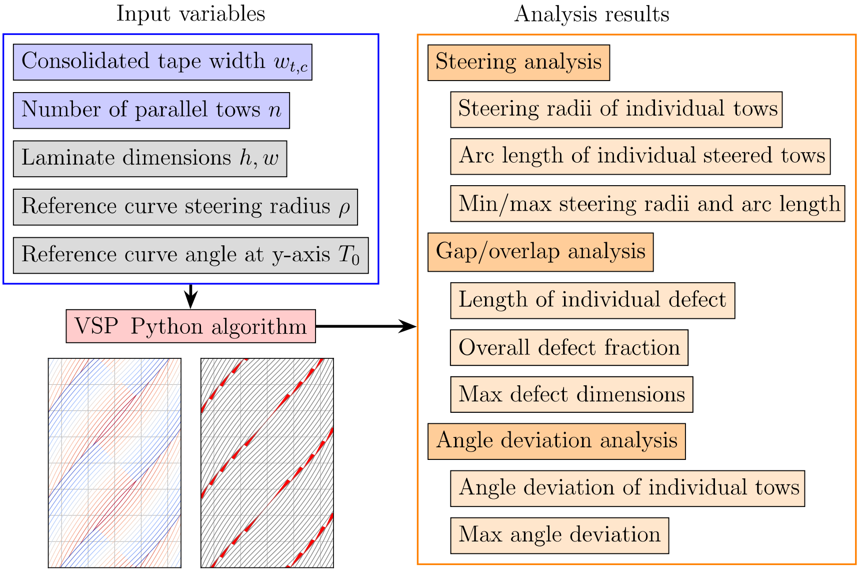

Figure 5.3: Variable Stiffness Panel Python algorithm - Input parameters and analysis results

5.1.2 Results of Variable Stiffness Panel analysis

The panel dimensions and reference curve geometry are determined by the stiffness optimization of the Variable Stiffness Panel design, whereas the AFP layup strategy-specific parameters tape width and number of parallel tows are chosen as part of the AFP design for manufacturability. A parameter study was thus carried out for fixed laminate dimensions ($h = 800\ mm$, $w = 500\ mm$) and reference curve geometry ($T_0 = 46\ °$, $\rho = 1250\ mm$) while varying consolidated tape width and the number of parallel tows to compare the resulting angle deviation, steering and gap and overlap defects.

Figure 5.4 illustrates the impact of the tow cutting strategy on the angle deviation. The example heat map plots of the angle deviation for 16 parallel tows and 14 mm width of individual tows show significantly larger angle deviation (a maximum value of 14.1 °) on the left hand side of the one-sided tow cuts plot (Figure 5.4(a)) compared to the tow cuts at the inside radius (Figure 5.4(b)), reaching a maximum of 6.6 °. Figure 5.5 presents the corresponding parameter plot for varying number of parallel tows and varying width of individual tows.

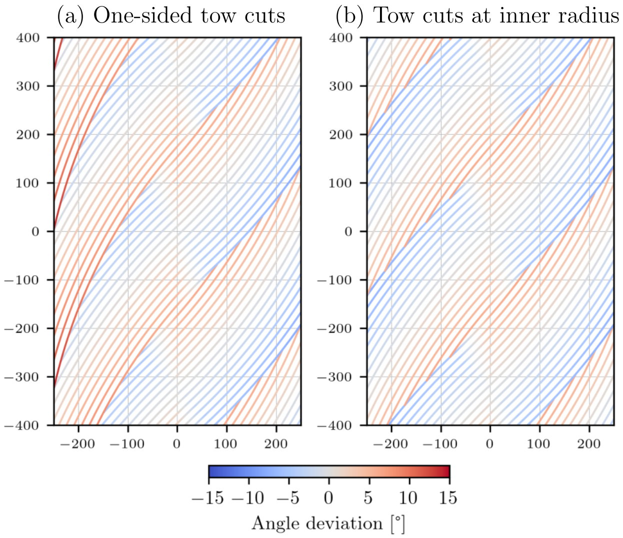

Figure 5.4: Variable Stiffness Panel angle deviation analysis: (a) One-sided tow cuts, 16 parallel tows, 14 mm width of individual tows (b) Tow cuts at inner radius, 16 parallel tows, 14 mm width of individual tows

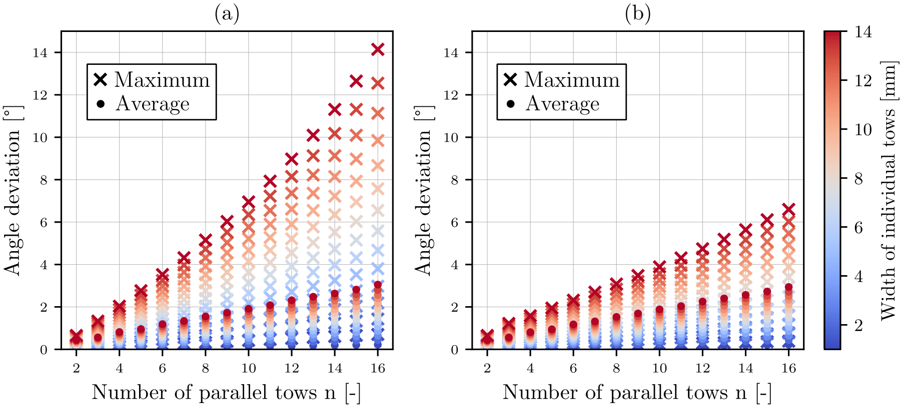

Figure 5.5: Maximum and average angle deviation for Variable Stiffness Panels with varying number of parallel tows and tape width: (a) One-sided tow cuts, (b) Tow cuts at inside radius

The maximum and average angle deviation is illustrated for the respective Variable Stiffness Panels with (a) one-sided tow cuts and (b) tow cuts at the inner radius. Both, the number of parallel tows and the width of individual tows lead to an increase in maximum angle deviation as they each increase the course width. The wider the course, the farther away from the reference curve are the tows at the edges of the course. This results in larger angle deviation, which primarily affects the maximum angle deviation values. The average angle deviation, however, remains at the same level for both tow cut strategies. Figure 5.6 shows steering radii of individual tows for an example Variable Stiffness Panel with 16 parallel tows and 14 mm tow width.

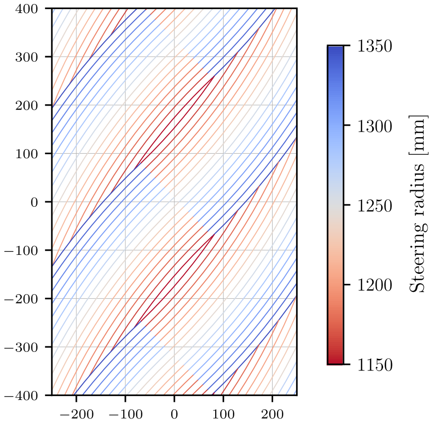

Figure 5.6: Steering visualization of Variable Stiffness Panels with tow cuts on the inside radius, 14 mm width of individual tows and 16 parallel tows

For constant curvature Variable Stiffness Panels, there is a direct linear correlation between steering radius of the individual tow, the reference curve steering radius and the lateral distance between the respective tow and the reference curve, which is illustrated in the corresponding parameter plot in Figure 5.7. Both, the number of parallel tows and the width of individual tows results in a linear increase of the steering radius on the outer edge of the course and a decrease on the inner edge of the course starting from the reference steering radius of 1250 mm. The largest number of parallel tows in combination with the largest width of individual tows thus results in the largest deviation from the reference curve steering radius in positive and negative direction.

Figure 5.8 shows two example plots of different Variable Stifness Panel configurations with 100 % coverage ratio and the resulting overlap defect pattern. 16 parallel tows in Figure 5.8(a) result in significantly smaller individual overlap defects and lower defect fraction of the entire laminate area compared to 2 parallel tows in Figure 5.8(b).

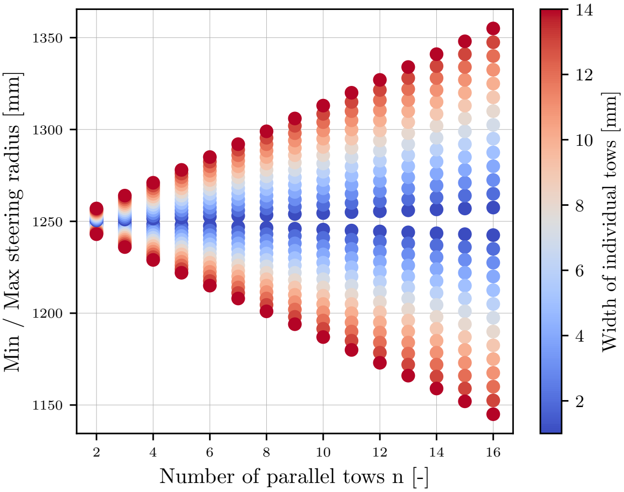

Figure 5.7: Variable Stiffness Panel analysis of minimum and maximum steering radii of individual tows for varying number of parallel tows and tape width

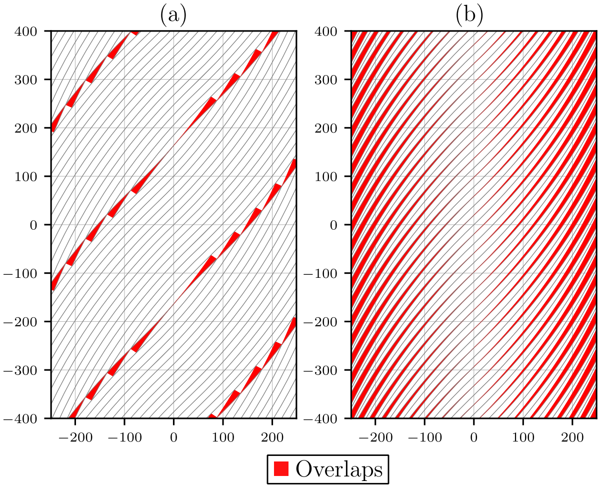

Figure 5.8: Overlap defect visualization of Variable Stiffness Panels with tow cuts on the inside radius and 14 mm width of individual tows: (a) 16 parallel tows, (b) 2 parallel tows

The associated parameter plot (Figure 5.9) emphasizes that the number of parallel tapes has a major influence, both on the proportion of defects in the total area (Figure 5.9(a)) and on the length of the defects (Figure 5.9(b)). For two parallel tows, a defect fraction of 22 % and maximum defect length above 500 mm can be observed.

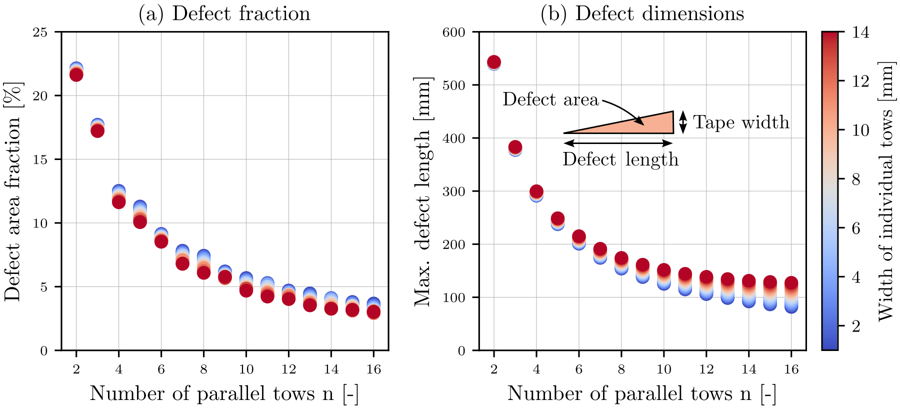

Figure 5.9: Variable Stiffness Panel defect analysis for varying number of parallel tows and tape width: (a) Area fraction of overlap defects, (b) Maximum length of overlap defects

The width of individual tows plays a less important role for the defect area and dimensions. The same effect can be observed for 0 % coverage ratio (gap configuration) and one sided tow cuts, as well.

As discussed in section 2.2.3, through thickness staggering of defects can lead to a reduction in the resulting negative effects. The gap defects of each subsequent ply should thus be shifted as far away from the previous ply of the same orientation, as possible. To keep the local fiber angle consistent with the reference curve, it makes sense to carry out staggering of constant curvature Variable Stiffness Panels in the same direction as the shifting distance D; in this case the y-direction. The staggering factor is typically expressed as a proportion or multiple of the consolidated tape width. For standard AFP laminates, often a staggering factor of 0.2 to 0.5 is used, in order to avoid super-positioning of tape boundaries of plies of the same orientation. For Variable Stiffness Panels, the position of gap and overlap defects has to be taken into account, as well, to determine the optimum staggering factor. For a Variable Stiffness Panel with multiple Variable stiffness plies of the same orientation, the optimum staggering factor S to achieve the widest possible spacing of the defects can be calculated by dividing the shifting distance D by the number of Variable Stiffness plies of the same orientation. Depending on the number of parallel tows and Variable Stiffness plies of the same orientation, an additional staggering factor has to be added to avoid super-positioning of tape boundaries. Figure 5.10(a) shows an example plot of staggered overlap defects of a Variable Stiffness Panel with 16 parallel tows, 14 mm width of individual tows and 4 Variable Stiffness plies of the same orientation, which produces the ply stacking sequence $[\langle 23.5|46|23.5\rangle]_4$. This notation describes the fiber orientation of the variable stiffness ply by the local fiber angle at the left edge, at the vertical symmetry axis and at the right edge of the panel, respectively. The staggering results in an even distribution of the overlap defects over the laminate. The defects are shifted in the y-direction by the staggering factor S. For the example presented, a large distance between the defects is possible. As the ratio of the number of parallel tapes to the tape width decreases, the defects move closer together or can no longer be spatially separated at all. Since, for reasons of symmetry, all effects up to this point could be analyzed using the positive Variable Stiffness orientation, only this side has been considered so far. Realistic Variable Stiffness Panels, however, have a symmetric stacking sequence. The overlap defect pattern of the corresponding symmetric laminate is shown in Figure 5.10(b). The addition of the corresponding mirrored ply to each Variable Stiffness ply results in the ply stacking sequence $[\pm\langle 23.5|46|23.5\rangle]_{2S}$. Inevitably, this results in crossing-points of defects. The sectional views however illustrate, that in most cases there are three or more layers between the superimposed defects. Furthermore, many Variable Stiffness Panel designs also contain regular plies with straight layup paths, which can be used to further increase through-thickness separation of defects.

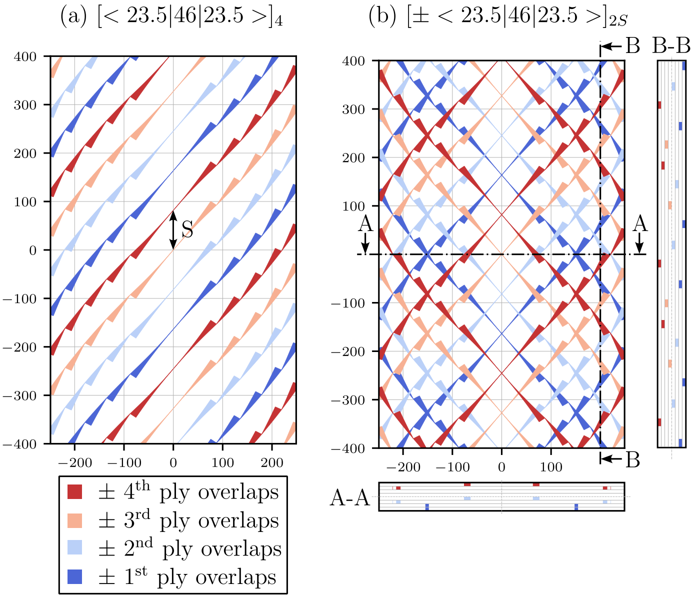
(a) $[< 23.5|46|23.5 >]_4$ (b) $[\pm < 23.5|46|23.5 >]_{2S}$

Figure 5.10: Staggered plies and resulting overlap defect pattern of a Variable Stiffness Panel with 16 parallel tows and 14 mm width of individual tows: (a) Positive ply angle orientation, (b) Positive and negative ply angle orientation and sectional views A-A at y=0 mm and B-B at x=200 mm

5.1.3 Summary of Variable Stiffness Panel analysis

There is an infinite number of theoretical parameter combinations for Variable Stiffness Panel design. Usually, however, laminate dimensions and reference curve geometry are predetermined, following stiffness optimization design. For a given set of geometric boundary conditions and stiffness-optimized reference curve, correlations can be derived with regard to the selected AFP layup strategy parameters and the resulting defects. Tow cuts at the inner radius of a course were identified as a usefull strategy with regard to AFP-manufacturability and limiting angle deviation at the laminate edge regions, compared to one-sided tow cuts, as presented in the literature. Using a larger number of parallel tows results in smaller individual gap or overlap defects and a smaller overall area-related defect fraction. On the other hand, a larger number of parallel tows, particularly in combination with using wider tapes, increases the angle deviation and can decrease the steering radius of the individual tows.

The developed Python algorithm can predict exact defect positions and dimensions and can be used as a tool in the decision making process of AFP layup parameter choice.

5.2 Hydrogen tank structure

Composite hydrogen tank structures are typically manufactured using thermoset filament winding processes. The design consists of continuous geodesic layup paths covering the cylindrical and dome section of the tank and additional hoop layers, reinforcing the cylindrical section of the tank (Figure 5.11(left).

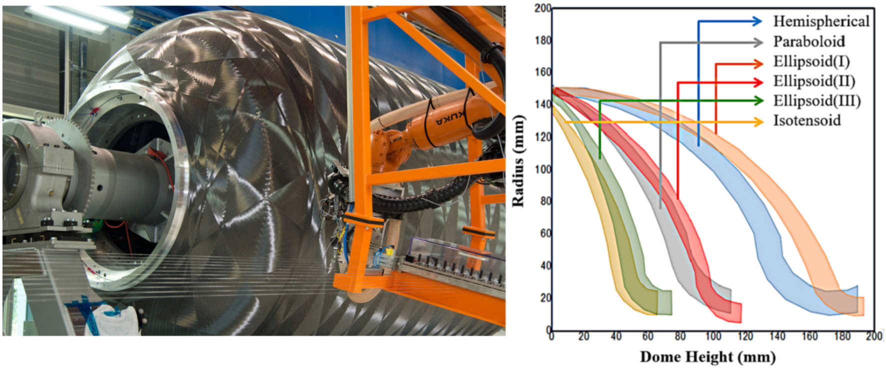

Figure 5.11: Filament wound composite pressure vessels: (left) Example tank structure with geodesic winding pattern [297], (right) Dome thickness profiles for filament wound composite pressure vessels, reprinted from [298] with permission from Elsevier

While this technology is well-established for manufacturing composite pressure vessels, it does present some inherent design limitations. The process relies on tension to apply the filament onto a convex surface, requiring geodesic paths as it has only negligible friction-based steering capabilities. The continuous winding principle, without cutting, results in a laminate thickness buildup towards the pole of the dome (Figure 5.11(right) [298]), exceeding the strength requirements in the pole region and leaving lightweight construction potential unutilized.

Filament winding composite tank designs usually follow the assumption of monotropic material properties (strength and stiffness properties only in fiber direction), neglecting strength and stiffness properties transverse to the fiber direction, also referred to as Netting Theory [299]. This design principle results in isotensoidal dome geometries. For isotropic materials, however, a spherical dome geometry theoretically would result in a factor of two lighter structure compared to an isotensoid of the same material [299]. AFP's tow cutting and restarting capability allows for constant laminate thickness of dome structures and the steering capability enables non-geodesic paths, as well as ply orientations other than meridians close to the pole of the dome. It could thus be beneficial to attempt to achieve quasi-isotropic laminate properties to leverage the weight advantages of a spherical dome structure. Boeing and NASA manufactured a 5.5 m full size pressure tank using a thermoset AFP with non-geodesic layup paths and spherical dome sections (Figure 5.12) [300]. With the increased design space of AFP, however, come additional challenges, as introduced in Section 2.1 and 2.2. In order to utilize the advantages of AFP over filament winding, sufficient laminate quality must be ensured. Inherent defects such as gap or overlap defects must not outweigh the advantages of more isotropic laminate properties. This section aims to quantify geometry-induced AFP defects for realistic composite tank structures as a second use-case for in-situ AFP manufacturing signature of complex geometries.

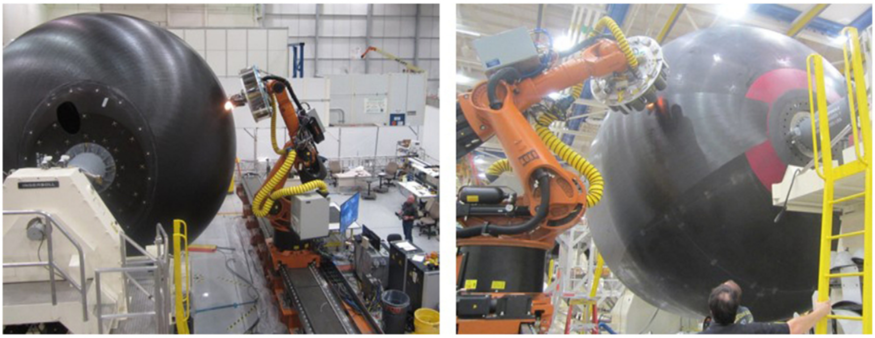

Figure 5.12: NASA and Boeing thermoset AFP composite tank, reprinted from [300] with permission from Elsevier: (left) thermoset AFP process, (right) 0 ° ply layup

5.2.1 Tape placement simulation for hydrogen tank geometry analysis

The commercial tape placement software VERICUT Composites Programming (VCP) (CGTech, Irvine, California) version 9.3.2 was used for simulating AFP layup with different strategies on composite tank geometries. A spherical dome with polar opening and attached cylindrical section was chosen as the tank geometry. The dimensions were selected on the basis of current projects, which ensures their application-related relevance. The dimensions are presented in Table 5.1. The polar opening is scaled linearly with the tank diameter.

Table 5.1: Composite tank geometries

Diameter [mm]	Polar opening [mm]
1700	425
1000	250
600	150

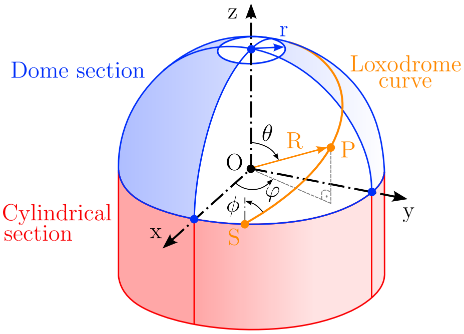

Figure 5.13: Spherical coordinate system of tank geometry and loxodrome reference curve definition

In order to achieve the quasi-isotropic laminate properties, as discussed in the previous section, a fixed angle layup strategy was chosen. For each Point P on the surface of the tank, the orientation of the reference curve is determined with respect to a projection of the z-axis onto the surface, also referred to as meridian and the angle ϕ. This results in loxodrome reference curves, spiraling towards the pole of the tank dome. For the spherical coordinate system presented in Figure 5.13, the loxodrome reference curves can be defined in relation to the colatitude angle θ following:

$$x(\theta) = R\sin(\theta)\cos(\alpha\theta) \tag{5.2}$$

$$y(\theta) = R\sin(\theta)\cos(\alpha\theta) \tag{5.3}$$

$$z(\theta) = R\cos(\theta) \tag{5.4}$$

where R is the radius of the spherical dome, α is the gradient of the loxodrome $\alpha = \cot(\phi)$, and ϕ is the angle between the loxodrome and the meridians. The local geodesic path curvature of the loxodrome reference curve can be calculated following [301]:

$$k(r) = \frac{1}{R\tan(\theta)}\cos(\phi) \tag{5.5}$$

The steering radius, which is the inverse of the geodesic curvature is thus calculated analytically using Equation 5.5. Both the angle deviation and the gap defects are investigated using VCP layup analysis tools. While the analytical Python script for the Variable Stiffness Panel analysis calculated exact defect dimensions, VCP puts out numerically determined layup paths and defect values and frequently produces undesired artifacts. Figure 5.14 shows the systematic underestimation of gap defect areas in VCP. The error increases with increasing opening angle of the triangular defects. In this case the defect area was underestimated by 6 %. However, the deviation is considered to be sufficiently small in comparison to the layup strategy influences.

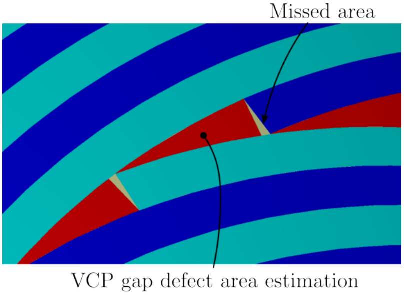

Figure 5.14: VCP gap defect misscalculation

For the gap and overlap analysis defect surfaces were exported from VCP and imported into the CAD software CATIA V5-6R2017 (Dassault Systèmes, Vélizy-Villacoublay, France), where artifacts were removed and surfaces were trimmed in order to investigate gap defects only on the hemispherical section between the polar opening and the transition with the cylindrical section (Figure 5.15). The length of the individual gap defects and the total gap defect area of the ply was measured using the measure tool in CATIA. The fraction of gap or overlap defects was calculated as the quotient of total defect area A_{defect} and the area of the spherical tank dome with polar opening A_{dome} (Equation 5.6):

$$\alpha_{defect} = \frac{A_{defect}}{A_{dome}} \tag{5.6}$$

where the area of the spherical tank dome with polar opening A_{dome} can be calculated following Equation 5.7:

$$A_{dome} = 2\pi R\sqrt{R^2 - r^2} \tag{5.7}$$

where R is the radius of the spherical dome and r is the radius of the polar opening.

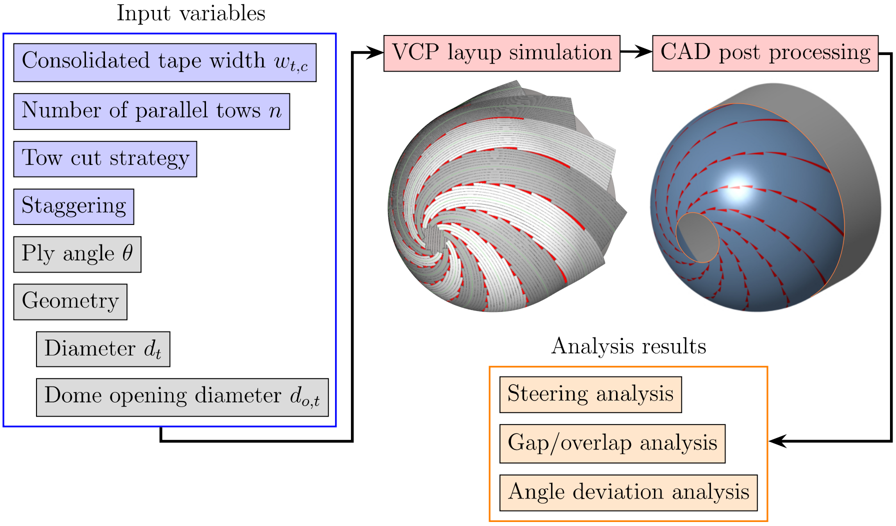

Figure 5.15: VCP tank layup simulation and analysis

The hydrogen tank is a closed surface and thus an incompatibility of tape width and dimensions of the geometry can not be placed outside of the trimmed area. In order to avoid resulting additional gaps influencing the gap and overlap analysis, the tape width is slightly adjusted in order to correspond to the tank dimensions. This practice is commonly used in thermoset AFP, essentially distributing small gaps throughout the ply in order to adhere to boundary curves. For 14 mm tape width and a tank diameter of 1000 mm, the theoretical number of tapes of a 45 ° ply is 158.67. Using a rounded number of 158, the resulting tape width is 14.06 mm. This small difference is negligible compared to the in-situ AFP process-induced tolerance of the consolidated tape width. 14 mm and 7 mm consolidated tape widths were investigated in the parameter study, representing consolidated tape widths of typically used commercially available half-inch (12.7 mm) and quarter-inch (6.35 mm) prepreg tape materials. As for the Variable Stiffness Panel analysis, between 2 and 16 parallel tows were investigated as layup strategies.

5.2.2 Results of hydrogen tank geometry analysis

A parameter study was carried out for the tank geometries presented in Table 5.1, fixed angle reference curves and varying consolidated tape width as well as varying number of parallel tows to compare the resulting angle deviation, steering and gap and overlap defects.

Fixed angle reference curves by definition do not deviate from the target angle. Parallel offset of the reference curve to layup multiple parallel tows, however, results in angle deviation, similar as in Variable Stiffness Panels.

(a) 1000 mm tank diameter (b) 1700 mm tank diameter

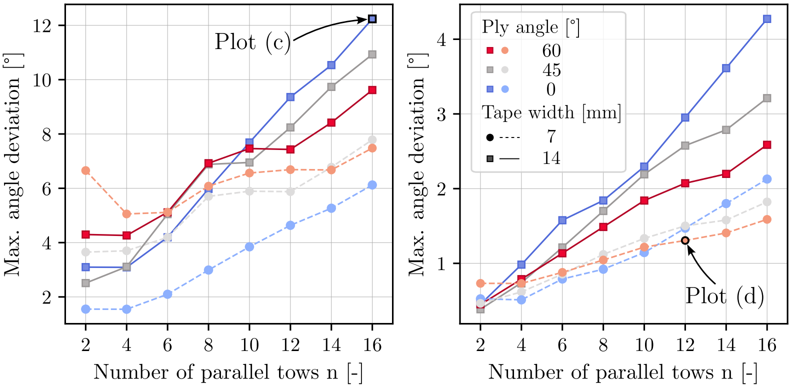

(c) Angle deviation plot (d) Angle deviation plot

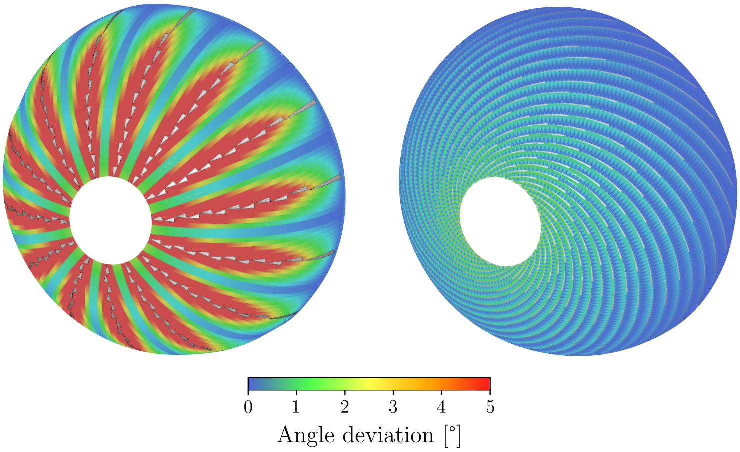

Figure 5.16: Angle deviation analysis for fixed angle layup on spherical domes with varying number of parallel tows and tape width (a) Maximum angle deviation for 1000 mm diameter tank, (b) Maximum angle deviation for 1700 mm diameter tank, (c) Example angle deviation plot of 1000 mm diameter tank 0 ° ply, 16 parallel tows and 14 mm tape width, (d) Example angle deviation plot of 1700 mm diameter tank 60 ° ply, 12 parallel tows and 7 mm tape width

The extend of the angle deviation is determined by the lateral distance from the reference curve and the radius of the spherical dome. Larger tape width and larger number of parallel tows thus lead to an increase in maximum angle deviation. The increase in angle deviation with increasing number of parallel tows can be observed for all investigated ply angles and the two tank diameters 1000 mm and 1700 mm in Figure 5.16 (a) and (b), respectively. At the same time, the larger tape width of 14 mm also results in larger angle deviations than the smaller 7 mm tape width. The second influencing factor is the tank diameter. Smaller diameters and thus larger normal surface curvatures result in larger angle deviation, as the meridians of equal angular distances are closer together. The largest angle deviation in the presented plot is thus the configuration with the largest number of parallel tows (16) and largest tape width (14 mm), combined with the smallest tank diameter (1000 mm). The angle deviation plot of this parameter set is presented in Figure 5.16(c). The plot shows no significant angle deviation close to the reference curve in the center of the courses but very large deviation of up to 12 ° at the lateral edges of the courses, where tows are cut to avoid overlapping. In contrast, Figure 5.16(d) shows an example plot of a less severe parameter set with larger tank diameter, lower number of parallel tows (12) and smaller tape width (7 mm), resulting in a maximum angle deviation of only 1.3 °. At low numbers of parallel tows (2 and 4 parallel tows), only every second or third course reaches the polar opening, which leadst to unstable path calculation near the polar opening and inconsistent angle deviation results, particularly for the 1000 mm tank diameter.

As tows are cut on both sides ot the course for layup of multiple parallel tows in one course, typically only the two central tows of each course reach the polar opening of the tank, where the most severe geodesic curvature occurs. The curvature deviation from the reference curve is therefore small and thus the reference curve approximates the geodesic curvature of the tapes with sufficient accuracy. The geodesic curvature of reference curves with different gradient angles is shown in Figure 5.17 and was calculated using Equation 5.5. The curves only vary by the constant factor $\frac{\cos(\phi)}{R}$, which determines the initial gradient of the curve. Both, smaller tank diameters and thus sphere radii R, as well as smaller gradient angles ϕ of the loxodrome curves, thus result in steeper curves.

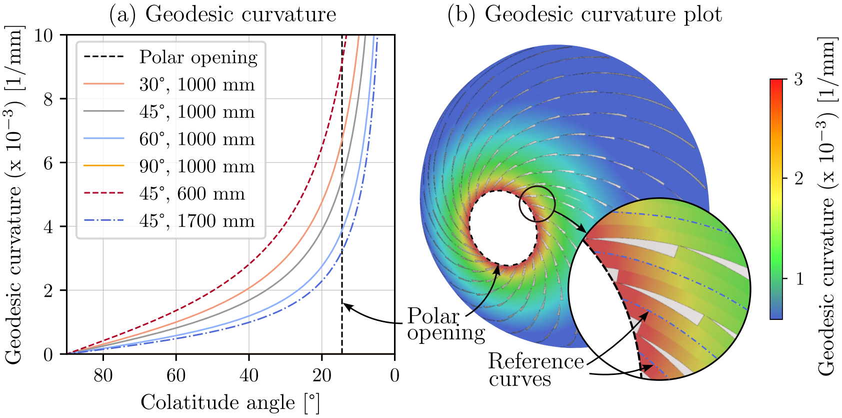

Figure 5.17: Geodesic curvature of loxodrome curves on spherical tank domes (a) Analytical plot of geodesic curvature, (b) Example plot of 1700 mm tank 45 ° ply with 14 mm tape width and 12 parallel tows

The resulting geodesic curvature at the polar opening, which is at 75.48 ° colatitude angle for the tank geometries investigated in this work, determines the maximum geodesic curvature on the tank geometry. An example plot with 45 ° gradient angle loxodrome reference curves and 1700 mm tank diameter is presented in Figure 5.17(b). The maximum geodesic curvature of $3 \cdot 10^{-1}$ mm^{-1} (333 mm steering radius) occurs in the tows close to the reference curves, as the other tows were already dropped approaching the pole of the dome.

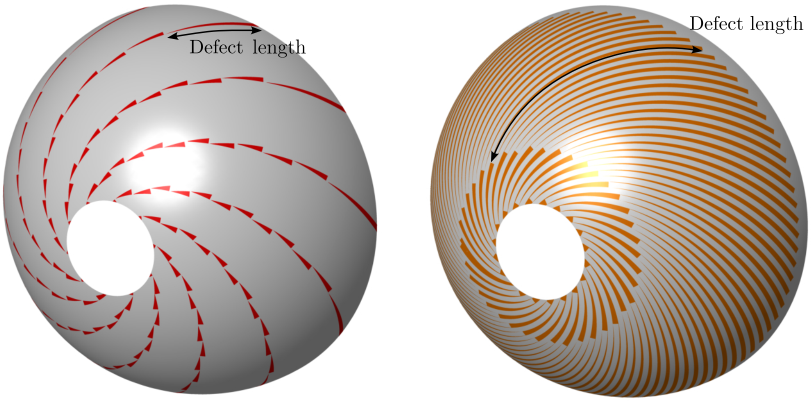
(a) 45° gap defects, 16 parallel tows

(b) 45° gap defects, 2 parallel tows

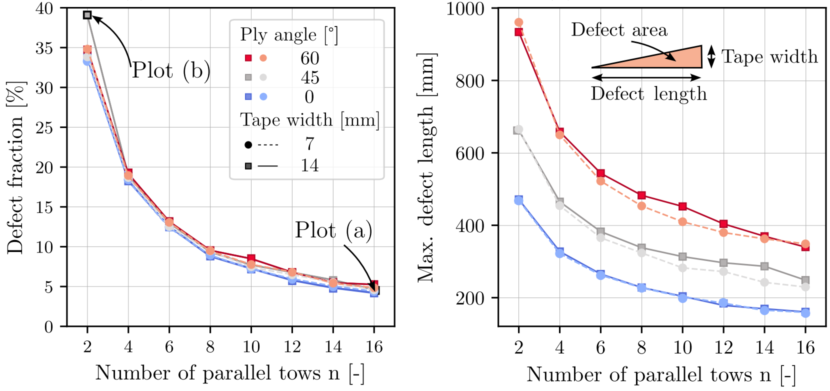
(c) Defect fraction

(d) Defect dimensions

Figure 5.18: Hydrogen tank geometry gap defect analysis for 1000 mm diameter, varying ply angles, number of parallel tows and tape width: (a) Example gap defect plot of 45 ° ply, 16 parallel tows and 14 mm tape width, (b) Example gap defect plot of 60 ° ply, 2 parallel tows and 14 mm tape width (c) Area fraction of gap defects, (d) Maximum length of gap defects

With regard to gap and overlap defects, similar correlations can be recognized for spherical tank geometries as for Variable Stiffness Panels. The width of the defects is determined by the tape width. The number of parallel tows has a large impact on the length of the individual defects and the area-related defect fraction. Example plots of a 45°-ply with 14 mm width of individual tows, 16 and 2 parallel tows are presented in Figure 5.18(a) and (b), respectively. The corresponding parameter plot shows, that the tape width has a comparatively small influence on the overall area-related defect fraction (Figure 5.18(c)) and the dimensions of the individual defects (Figure 5.18(d)). An increase in the number of parallel tows, however, results in a significant decrease in overall defect fraction and length of the individual defects. The example plot with 16 parallel tows (a) has a total defect fraction of 5 %, whereas the example plot (b) with only 2 parallel tapes reaches a defect fraction of close to 40 %. The length of the defects is also influenced by the ply angle, with larger ply angles resulting in longer defects.

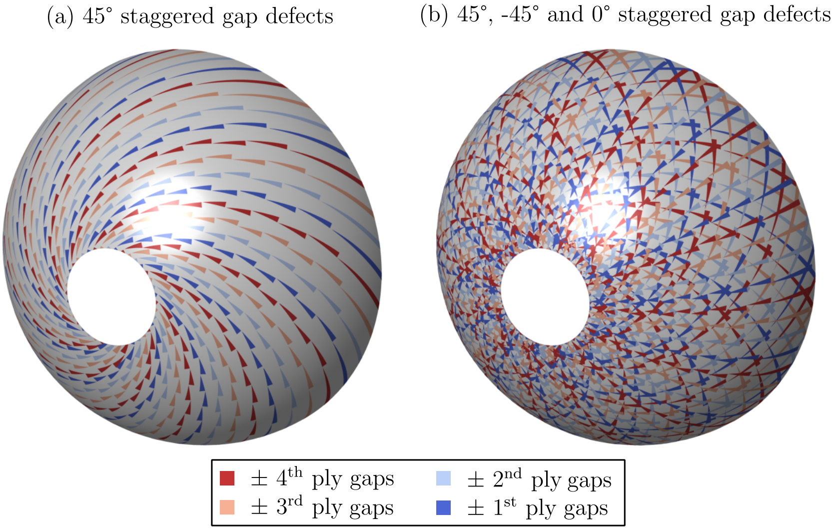
(a) 45° staggered gap defects

(b) 45°, -45° and 0° staggered gap defects

Figure 5.19: 1000 mm diameter spherical dome section gap defect staggering analysis with 16 parallel tows and 14 mm tape width: (a) 45° staggered gap defects, (b) 45°, -45° and 0° staggered gap defects

While the linear staggering factor S was used to offset defects of plies of the same orientation for Variable Stiffness Panels, for rotationally symmetrical tank structures, an angular shift is used to avoid through-thickness super-positioning of defects. Figure 5.19(a) shows an example plot of the resulting gap defect pattern of four evenly distributed 45° plies. The concentrically converging courses result in a decrease in circumferential distance of defects towards the pole. As can be observed in Figure 5.19(b), adding staggered -45° and 0° plies results in a high defect concentration with numerous defect crossing-points and a complex polar-angle-dependent defect pattern.

5.2.3 Summary of hydrogen tank geometry analysis

A methodology was presented to develop fixed angle layup strategies for spherical tank geometries, taking advantage of AFP tow cutting and steering capabilities. An analysis method for the resulting geometry-induced defects was introduced and relevant example geometries and layup strategies were investigated in a parameter study. Similar correlations as for Variable Stiffness Panels were observed between the layup strategy parameters tape width and number of parallel tows and the resulting emphasis of the defect types. Larger numbers of parallel tows lead to smaller gap or overlap defects and lower defect fraction but increased steering and angle deviation defects. In contrast to Variable Stiffness Panels, the rotationally symmetrical geometry, however, leads to an accumulation of all three defect types angle deviation, steering defects and gap or overlap defects towards the pole or polar opening of the dome.

5.3 Complex fuselage section

The complex fuselage section was derived from the upper shell of a generic unmanned aerial vehicle [302]. It has a length of 8060 mm and a double curved geometry with a central cutout (Figure 5.20). A layup strategy was developed for the complex geometry, demonstrating resulting geometry-induced defect patterns.

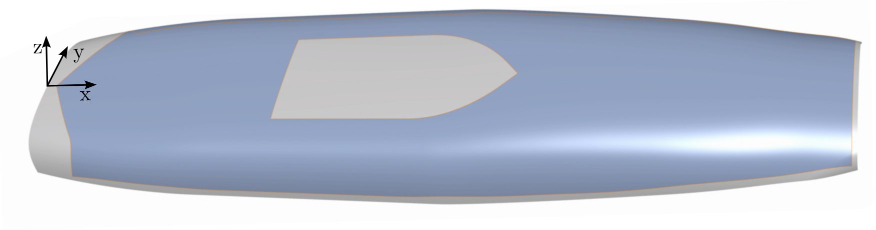

Figure 5.20: Complex fuselage geometry with boundary curve and central cutout

5.3.1 Tape placement simulation for complex fuselage geometry analysis

A similar layup simulation methodolgy was employed, as for the hydrogen tank analysis. Fixed angle reference curves of the orientation 0 °, ±45 ° and 90 ° with respect to the x-axis of the geometry's global coordinate system represent the standard procedure in the aircraft industry for composite design. Due to the comparably small double curvature and large dimensions of the geometry, only half-inch tape width was considered. A generic quasi-isotropic ply stacking sequence $[45°/0°/-45°/90°]_{2S}$ was used for the layup simulation. The starting point and number of parallel tows was varied to achieve a suitable design, with few geometry-induced defects.

5.3.2 Results of complex fuselage geometry analysis

Contrary to Variable Stiffness Panels, where the start point is defined as the center point of the panel or rotationally symmetrical structures, where the start point only results in an angular displacement of the reference curve, the start point and first reference curve play an important role for non-symmetrical double curved geometries. Depending on the position, the reference curve can take on different shapes.

The comparatively low curvature at the center of the geometry allows a large number of parallel tapes without defects occurring. In order to make the most use of this effect, the start point was placed in the center of this region with low double-curvature to enable the largest possible number of parallel tows. It was possible to plan the 90 ° ply with only one reference curve and parallel tows for the entire ply without major defects. For the 0 ° plies, in the central flat section of the part surface, up to 64 parallel tows were used, while in the more curved areas, 16 parallel tows were used. Similarly, for the 45 ° plies, up to 160 parallel tows could be used, without major steering or angle deviation defects. Staggering, to avoid through-thickness superimposition of defects was carried out as a linear shift of the starting points, perpendicular to the respective reference curve orientation. The shifting distance consisted of the consolidated tape width divided by the number of plies of the same orientation to avoid superimposition of tow boundaries and the minimum number of parallel tows divided by the number of plies of the same orientation to offset gap defects. A list of the start points and a full analysis of angle deviation and steering radii is presented in Appendix A3.

Figure 5.21(a) shows the first 45 ° ply with the large section of 160 parallel tows in the center of the laminate and fewer parallel tows in the more curved sections of the geometry. The corresponding angle deviation distribution is presented in Figure 5.21(b). As the geodesic path curvature is uncritical for this geometry, the angle deviation becomes the limiting factor for the number of parallel tows. Whenever the deviation exceeds a limit of 3 °, a new reference curve is generated for the next set of parallel tows. The resulting gap defect pattern of the four 45 ° plies is presented in Figure 5.21(c). The opening angle, and thus the aspect ratio of the triangular defects corresponds to the respective angle deviation at the edges of the two sets of parallel tows, which are adjacent to the defect. The opening angle equals the sum of the two angle deviations. The gap defects are thus shorter in the areas with larger angle deviation and reach very small opening angles in areas with low angle deviation in the center of the laminate. As the staggering distance is determined by the areas with the fewest parallel tows, the defects are evenly distributed in these sections, whereas in areas with more parallel tows, larger spacing is observed between the defect stacks. Figure 5.21(d) finally shows the resulting gap defect pattern of all plies. The defect concentration increases towards the most complex section of the geometry on the right hand side of the plot. While the pattern was rotationally symmetrical for the hydrogen tank geometries, an irregular pattern wass observed for the complex fuselage geometry. The distance between the defects is however determined by the chosen staggering strategy.

(a) 1st 45° ply parallel layup sections

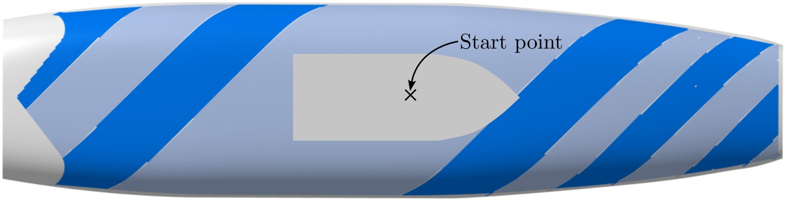

(b) Angle deviation of 1st 45° ply

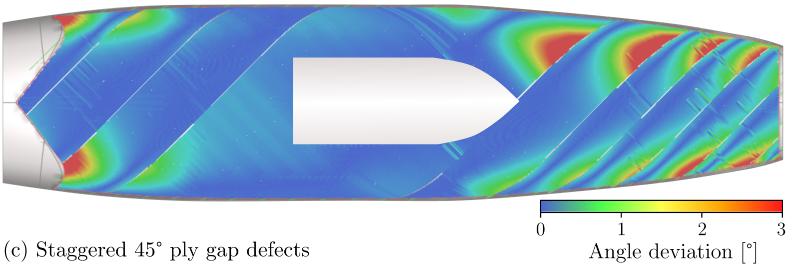

(c) Staggered 45° ply gap defects

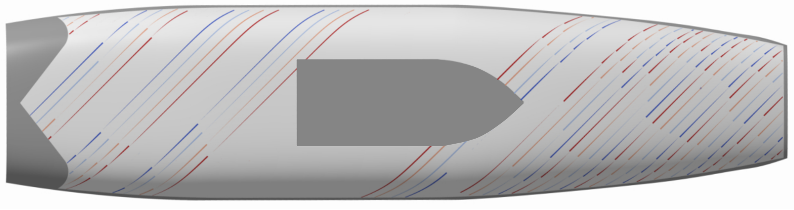

(d) Staggered 0° and ±45° ply gap defects

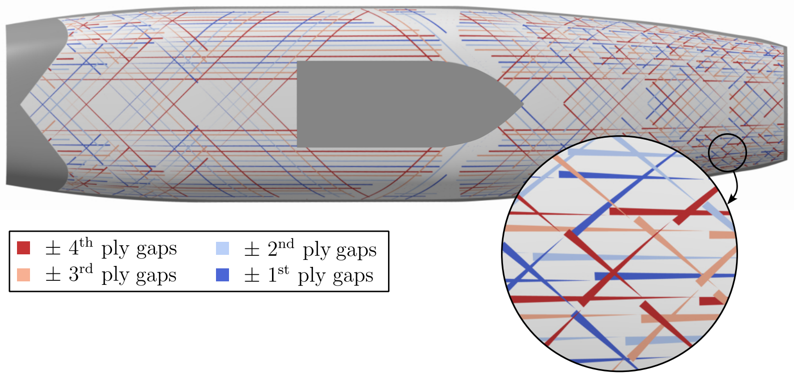

Figure 5.21: Complex fuselage geometry layup analysis result: (a) 1st 45 ° ply parallel layup analysis, (b) 1st 45 ° ply angle deviation analysis (c) Staggered 45 ° ply gap defects, (d) Staggered 0 ° and ±45 ° ply gap defects

5.3.3 Summary of complex fuselage geometry analysis

A layup strategy was presented for a complex fuselage geometry. The resulting geometry-induced defects were analyzed. Further effects in comparison to rotationally symmetrical structures were demonstrated. Starting points play an important role in asymmetrical double-curved structures, as they can determine the number of parallel tows, that be can be used in a ply without exceeding defect constraints. The gap or overlap defects pattern was found to depend on the local curvature of the geometry, the number of parallel tows and the staggering strategy. A correlation was observed for the local angle deviation and the aspect ratio of the triangular gap or overlap defects. Large angle deviations at the edges of neighboring sets of parallel tows resulted in larger aspect ratio of triangular defects.

5.4 Experimental validation of layup path analysis

In order to validate the simulative investigations of the previous sections, an experiment was carried out to produce a double-curved laminate and compare the resulting defects with simulation results. A double-curved spherical non-heatable steel tooling representing a section of a hydrogen tank dome was provided as part of a research project and could be used to manufacture the validation laminate.

5.4.1 Manufacture of validation laminate

The tank section tooling had a spherical surface with radius $R = 1034$ mm and a side length of $a = 700$ mm. A layup simulation for a corresponding dome geometry was created for 0 °, 45 ° and -45 ° ply orientation, 8 parallel tows and 0 % coverage ratio (gap design). The tank section was positioned halfway between the pole and the edge of the sphere (Figure 5.22(a)).

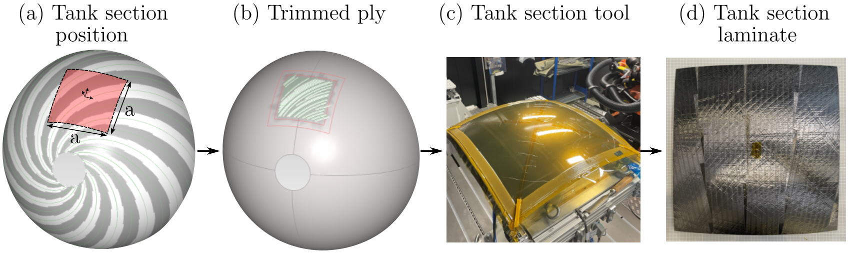

Figure 5.22: Tank section laminate: (a) Laminate positioning on tank surface, (b) Trimmed example ply on tank surface, (c) Tank section tool with polyimide film first ply, (d) Trimmed tank section laminate

The center point of the tool section was thus positioned at $\theta = \frac{\pi}{4}$ and the z-axis of the tool was radially oriented, while x- and y-axis were oriented tangentially to the sphere surface in parallel and perpendicular orientation to the meridian passing through the center point of the tooling, respectively. The plies were subsequently trimmed using boundary curves that took into account the lead-in length and minimum cut length of the AFP facility (Figure 5.22(b)). The tool was placed on the two-degree-of-freedom tool system of the AFP facility (Figure 5.22(c)). The double-curved first ply substrate was realized using a vacuum-assisted setup without breather fabric. 25 µm polyimide film with diagonal cuts and subsequent joining with polyimide adhesive tape on the tool-facing side of the polyimide film was draped onto the steel tooling. This allowed an almost wrinkle-free first ply. Suprem AS7/LM-PAEK half-inch prepreg tape with 60 % fiber-volume-fraction was used for the validation laminate. The consolidated tape width was determined in a preliminary test for parallel geodesic layup to be 15.5 mm. An 8-ply laminate was manufactured with the ply stacking sequence $[0°/45°/90°/-45°]_S$ (Figure 5.22(d)). While the 90 ° ply would not be found in a realistic spherical dome section, it was added to this validation laminate for reasons of symmetry. The 8 parallel tows were manufactured as 8 individual single-tow courses.

5.4.2 Results of validation laminate analysis

The manufactured laminate showed good agreement with the simulation. Figure 5.23(a) and (b) show the simulated gap prediction and manufactured result of the first 0 ° ply, respectively. For the given surface curvature and layup strategy, no noticeable steering influence could be detected for the 0 ° ply. The predicted triangular gap defects following tow cuts were accurately reproduced in the validation laminate. In the first ply, the triangular gaps can be clearly recognized due to the color contrast of the underlying polyimide film and the prepreg material. Figure 5.23(c) and (d) show the comparison of the VCP steering analysis and manufactured ply of the following 45 ° ply, respectively. The simulation analysis show the increase in geodesic curvature (decrease of local steering radius) towards the pole of the dome. Due to the chosen layup direction, starting the tows on the pole-facing side, steering defects occured towards the center of the laminate and exacerbated in the further course of the paths. This suggests an influence of the arc length of the curved path in addition to the mere local curvature influence. As can be observed from Figure 5.23(d), triangular gap defects were still accurately produced in the 45 ° ply. Towards the center of the laminate, however, additional longitudinal gap defects arose between the individual tows. Furthermore tow straightening and even compensatory steering in the opposite direction of the intended curved path can be observed at the end of the tracks, before the tow cuts.

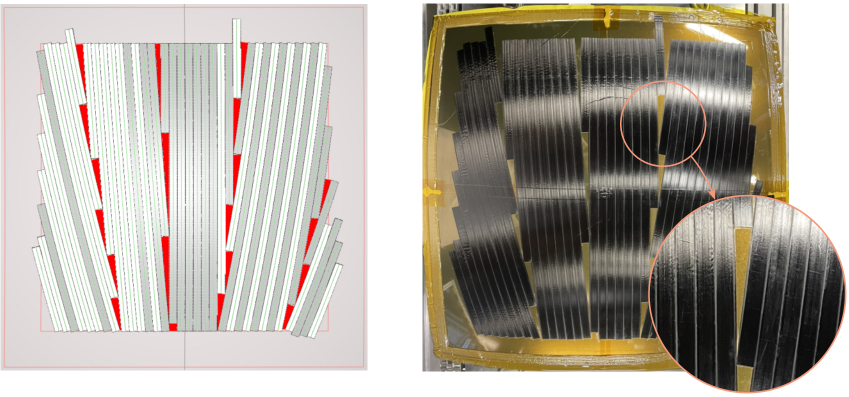

(a) VCP gap defect analysis of 0° ply

(b) Manufactured 0° ply

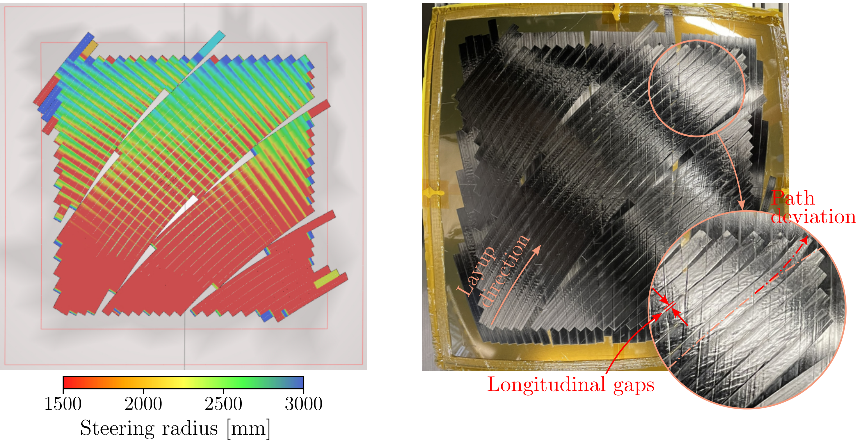

(c) VCP steering analysis of 45° ply

(d) Manufactured 45° ply

Figure 5.23: Comparison of VCP defect simulation and experimental result: (a) VCP gap defect analysis of 0 ° ply, (b) Experimental result of 0 ° ply with gap defects, (c) VCP steering analysis of 45 ° ply, (d) Experimental result of 45 ° ply with gap and steering defects

5.4.3 Summary of validation laminate analysis

The validation laminate experiment successfully demonstrated the manufacturability of the simulation-derived layup paths using in-situ AFP. The Predicted triangular gap defects were accurately reproduced in the validation experiment. Steering defects were observed after a finite length of the steered paths. Narrowing of steered tows was also detected, which resulted in longitudinal gaps between the tows. Tow cuts at the end of steered paths resulted in a lateral deviation from the track in the opposite direction.

5.5 Conclusion

The three geometries: constant curvature Variable Stiffness Panel, spherical hydrogen tank and complex double-curved fuselage section were analyzed with regard to layup strategies and their impact on the resulting geometry-induced defects. The correlation between the geometry, layup strategy and resulting angle deviation, steering and coverage defects was demonstrated for all three applications. For a given reference curve, a larger number of parallel tows generally results in larger angle deviation and more critical steering radii, but lower area-related coverage defect fraction and smaller individual defects. One possible strategy to solve this optimization problem could be, to develop allowable limits for steering radii and angle deviation and to maximize the number of parallel tows, without exceeding these limits. For thermoset AFP, a typcial industry requirement is a maximum value of ± 3 ° angle deviation [303]. The second boundary condition for allowable steering radii is highly process-dependent and will be subject of the following Chapter 6.

The simulation results of this chapter show a wide range of steering radii reaching minimum values of up to 500 mm for the complex fuselage section and 100 mm for spherical dome geometries. Gap and overlap defects dimensions also vary greatly depending on geometry and layup strategy. While the width of the triangular defects is determined by the consolidated tape width, the maximum length ranged between 100 mm for Variable Stiffness Panels and up to several meters for the complex fuselage geometry. The opening angles of the triangular defects typically correspond to the angle deviations at the boundaries of the parallel sets, intersecting at the defect position. The ±3 ° boundary condition would thus result in a maximum defect opening angle of 6 °. Staggering of plies of the same orientation to avoid through-thickness superimposition of defects results in an even distribution of defects of the same orientation. For larger numbers of parallel tows, defect spacing of multiple tape widths can be realized, while lower number of parallel tows result in more overlapping defects. For double-curved geometries, the defect pattern varies over the course of the surface. Spherical tank dome geometries lead to larger concentration of defects and crossing-points of defects of varying orientation towards the pole. For complex free-form geometries, defect patterns similarly accumulate in the most curved areas.

The validation experiment showed good agreement of the predicted gap defect positions. The steering defects did not occur in the areas with the strongest geodesic curvature but occured after a certain length of the steered track, which needs to be considered in the steering investigation. Over the course of the steered tracks, the consolidated tape width decreased, resulting in longitudinal gaps between the tows, as it was also observed in the literature (Figure 2.24 [261]). Parallel paths can therefore not be assumed in the case of strong geodesic path curvature.

Chapter 6

In-plane path curvature

This chapter presents an investigation of in-plane path curvature (steering) and resulting defects for in-situ AFP. The content of this chapter was published in [304, 305] and [306]. As shown in the literature review (Section 2.2.2), the focus of other published works has been the definition of critical steering radii to avoid in- and out-of-plane defects. Both the experimental studies and the modelling approaches assume stationary curvature states and neglect the transient section from straight to curved paths. This assumption would result in an even distribution of defects on constant curvature layup paths and higher frequency or greater magnitude defects in sections with larger curvature for varying curvature layup paths. While this is valid for thermoset AFP, where wrinkles form after the consolidation roller has passed as a function of tape buckling following compressive stress and tackiness of the prepreg material, in thermoplastic AFP, full consolidation is achieved in the process. All occuring defects thus form in front of- or right at the nip point and are a function of the accumulated curvature up to the current point of the additive process. The validation laminate analysis in the previous Chapter 5 accordingly showed defects not in the most curved sections of the layup path, but after a certain arc length of curved layup path had been passed.

While dimensional changes of the consolidated tape and deviation from the intended layup path following steering were reported, a detailed analysis of the onset and progression of these effects is required. Furthermore, laminate level mechanical properties are needed to quantify the influence of steering defects. This chapter thus aims to address these research gaps.

The simulatively derived geodesic curvatures (steering radii) from the previous Chapter 5 were used as the basis for an experimental parameter study. Resulting steering defects, as well as dimensional changes of the consolidated tape and layup path deviations following steering were analyzed and quantified. A correlation between geodesic curvature and arc length was developed with regards to the onset of steering defects. The usability of sub-critical steering radii for in-situ consolidated laminates was validated using mechanical test on coupon level. An empirical model was developed to predict the onset of out-of-plane steering defects and dimensional changes of the consolidated steered tape. Optimized layup strategies can be derived from this model achieving steered plies with minimal defects. This allows for an expansion of the design space by allowing steering radii which in the literature were considered too small for a specified arc length.

6.1 Analytical considerations for geodesic curvature and in-situ AFP

Steering models presented in the literature typically investigated solely steered paths, without considering the transition area from straight lead in section to steered section of a layup path, assuming infinite steering arc length. This approach, assuming an infinite steering radius and constant strain over the entire steered path is visualized in Figure 6.1(a).

Assuming equal proportions of tensile and compressive strain, the compressive strain at the inner edge of the tape ε_c can be calculated following Equation 6.1 [198, 200]:

$$\varepsilon_c = \frac{w_t}{R + \frac{w_t}{2}} = \frac{1}{\frac{1}{K_g w_t} + \frac{1}{2}} \tag{6.1}$$

where w_t is the tape width and K_g is the geodesic curvature. In this work, a novel approach is suggested, considering the progressive increase of steering-induced stresses and strains beginning with a straight lead-in section and subsequent constant curvature steering radius section. Figure 6.1(b) shows the progressive increase of the steering-induced length difference $\Delta l(\alpha_{arc})$ over the course of the steered path. Using the local tape width parameter ρ_w, ranging from 0 to w_t, as introduced by Zenker [200], the progressing length difference can be calculated following:

$$\Delta l(\alpha_{arc}, \rho_w) = (R + \frac{w_t}{2})\alpha_{arc} - (R + \frac{w_t}{2} - \rho_w)\alpha_{arc} = \rho_w \alpha_{arc} \tag{6.2}$$

where α_{arc} is the arc angle in radians. The strain distribution, resulting from the progressing length difference depends on the deformation of the tape. As the preliminary results indicate an increase in stress over the course of the steered path, not all the length difference is absorbed by local strain in the form of deformation of the tape. Three extreme cases are considered below, whereby the actual deformation likely corresponds to a combination of the three cases: No tape deformation, complete bending deformation and complete shear deformation.

If no deformation of the consolidated tape occurs, the entire length difference is passed forward towards the incoming tape. Under the further assumption of a linear elastic stress-strain relationship, the compressive stress increases linearly over the course of the steered path. The strain can be calculated as the quotient of the length difference and the free length of the incoming tape between the consolidation roller and the tape guiding system (l_f). Taking into account the initial condition of constant tape tension σ_0, the following stress distribution can be deduced:

$$\sigma(\alpha_{arc}, \rho_w) = \sigma_0 - \frac{\rho_w \cdot \alpha_{arc}}{l_f} E_c \tag{6.3}$$

where E_c is the linear elastic compressive modulus of the tape and the initial stress resulting from the tape tension can be calculated as:

$$\sigma_0 = \frac{F_t}{w_t \cdot t_t} \tag{6.4}$$

where F_t is the tape force and t_t is the tape thickness. While the resulting stress distribution depends on the magnitudes of initial tape tension, geodesic curvature and compressive modulus, the overall effect remains the same and is visualized in Figure 6.1(c).

(a) Constant curvature strain

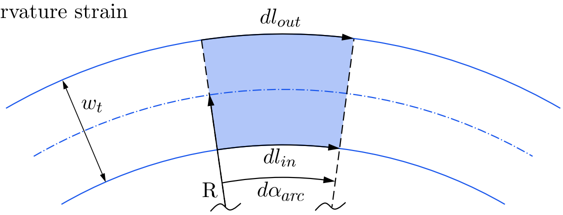

(b) Progressing length difference

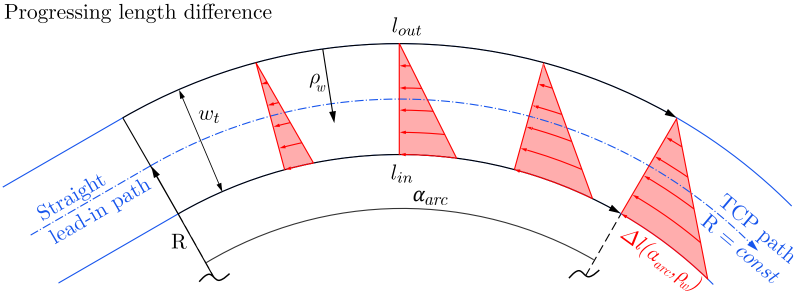

(c) Progressing stress distribution

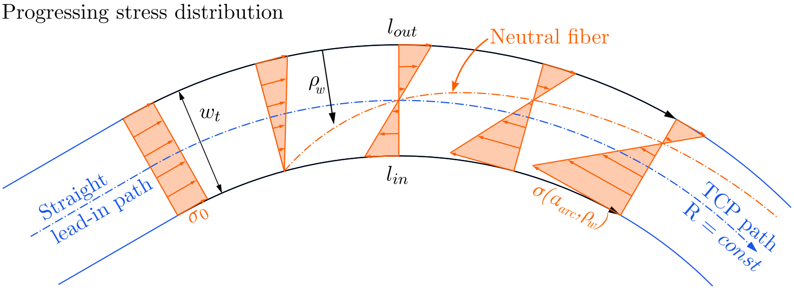

Figure 6.1: Analytical derivation of stress distribution of constant curvature steered path with straight lead-in: (a) Constant curvature strain [198, 200], (b) Progressing length difference, (c) Progressing stress distribution from combined tape tension and steering

(a) Bending deformation mode

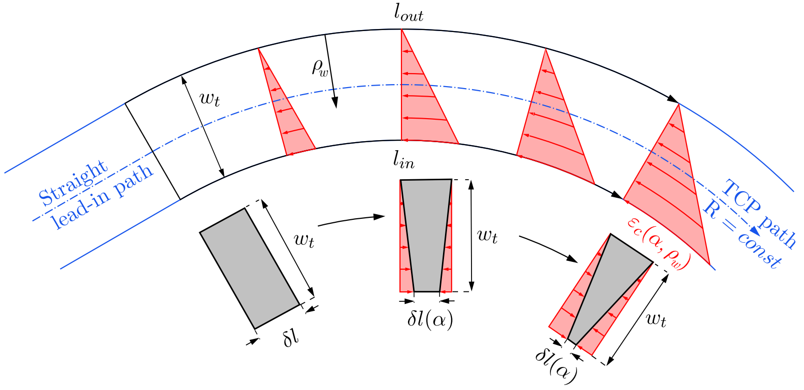

(b) Shear deformation mode

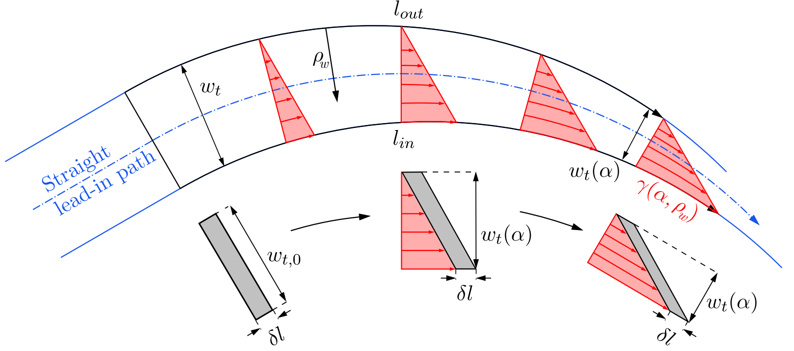

Figure 6.2: Steering stress-induced tape deformation modes

The initial state of uniform tensile stress across the tape width is progressively superimposed with the steering-induced compressive stress. At the inner edge at some point, the compressive stress exceeds the tensile tape tension. With further increase in compressive stress, the neutral fiber moves towards the outer edge of the tow. While tensile stress results in a normal force towards the consolidation roller, the compressive stress results in a normal force in the opposite direction allowing the tape to bend away from the consolidation roller.

The second extreme case of complete bending deformation is presented in Figure 6.2(a). In this case, the entire length difference is absorbed by compressive strain in the form of in- and out-of-plane fiber undulations. The tape width theoretically remains constant.

In the third extreme case of complete shear deformation (Figure 6.2)(b), the inner and outer tape edges remain at the same length and no undulations occur. This deformation mode results in a shear-induced narrowing of the tape. The shearing deformation mode is utilized as the key enabling factor for defect-free layup of very small steering radii in the Continuous Tow Shearing technology using a translational instead of rotational path movement and dry fiber tape in combination with a specified lead section allowing for longer relative shearing of the tape [195]. For the thermoplastic AFP process, only a very short lead section in front of the consolidation roller is available and is accompanied by a superposition of bending and shear stresses. In order to quantify the weighting of the actual deformation modes present, experimental steering tests were carried out and evaluated in the following sections.

6.2 Experimental Analysis of in-plane curvature

An initial set of of steering experiments was carried out to quantify in-plane curvature effects and mechanisms in in-situ AFP. A wide range of steering radii was investigated to achieve a principle understanding of the steering mechanisms and defect formation.

6.2.1 Methodology

Mechanically fastened wide prepreg tape in 90 ° orientation joined with polyimide adhesive tape on the tool-facing side, producing a full first layer was used as a first ply. It was clamped across the entire width in 90 ° direction on both sides under a bar and placed under slight pre-tension using toggle levers. A subsequently placed 0 ° ply of Suprem CF/LM-PAEK half-inch tape completed the substrate for the initial steering experiments. Individual steering tracks with one tow track configuration using the same half-inch material were placed on the substrate starting with a 150 mm 0° straight lead-in path and subsequent steering radii of 2000 mm to 800 mm in 200 mm increments and 800 mm to 200 mm in 50 mm increments. The standard unheated tool AFP process parameter set (Table 4.3) was used for the experiments. One track was produced for each individual radius. In a second experiment 22 samples were manufactured for a steering radius of 1200 mm in order to analyze the variability of the results. The results were analyzed using visual inspection, profilometry, microsections, caliper measurements of the resulting consolidated tape width and arc length measurement, using a flexible ruler.

6.2.2 Results and discussion

The progression of an example track with straight lead in path and 800 mm steering radius is presented in Figure 6.3. The steered section of the track starts at Position 0. For the first few centimeters of the steered path, no defects could be observed (Position 1, Figure 6.3(d)). The corresponding thermal camera image showed no steering influence (Figure 6.3(b)). In-plane and slight out-of-plane undulations were observed starting at Position 1. At Position 2, the inside edge of the tape started to detach from the consolidation roller, as can be observed in the thermal camera image in Figure 6.3(c). Shortly after, at Position 3, the first out-of-plane wrinkle occured (Figure 6.3(e)). This defect looks similar to a ”sheared fiber” defect, as presented in the thermoset AFP literature (Figure 2.16(b)-(c)) [207].

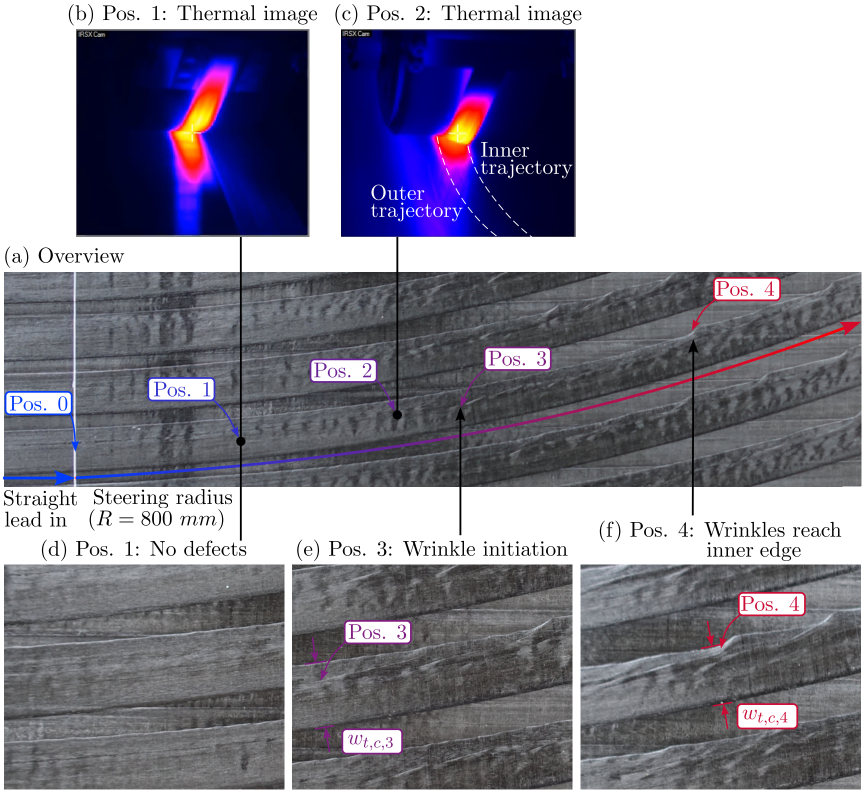
(b) Pos. 1: Thermal image (c) Pos. 2: Thermal image

(a) Overview

(d) Pos. 1: No defects (e) Pos. 3: Wrinkle initiation (f) Pos. 4: Wrinkles reach inner edge

Figure 6.3: Steering experiment example image with steering radius 800 mm

This wrinkle continued in layup direction until it reached the inner radius at Position 4 (Figure 6.3(f)). Up to this point, the consolidated tape width steadily decreased. As the wrinkle reached the inner edge of the tape, the tape width increased sharply. Out-of-plane wrinkle defects periodically formed after this point and ran towards the inner edge of the tape. The arc length from Position 0 to Position 3 was defined as the critical arc length l_{crit}, as this marks the position of out-of-planes defect initiation. The consolidated tape width measurements at Positions 0, 3 and 4 were labeled $w_{t,c,0}$, $w_{t,c,3}$ and $w_{t,c,4}$, respectively. A similar steering progression and sequence of defects was observed for all steering radii, but with varying arc lengths. The critical arc lengths for all steering radii are presented in Figure 6.4(a). A proportional correlation was observed between the steering radius and the respective critical arc length. A larger steering radius allowed for a longer defect-free arc length layup. The respective variance plot of the second experiment with multiple iterations of the same 1200 mm steering radius is shown in Figure 6.4(b). The large variance indicates a large fluctuation of the critical arc length which is two orders of magnitude larger than the assumed measurement accuracy of 1 mm.

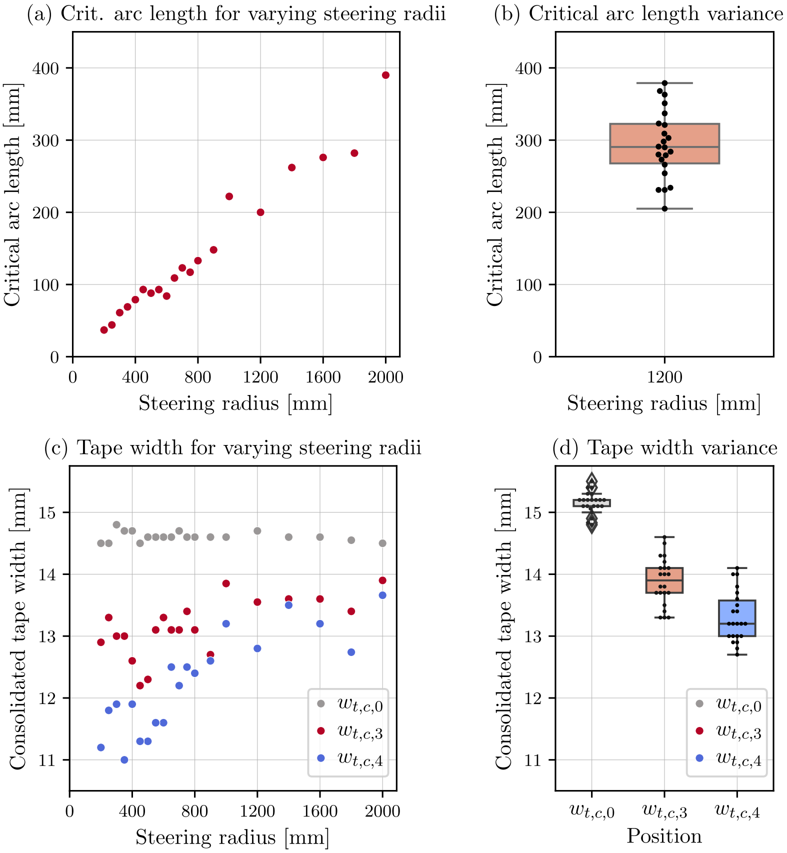

Figure 6.4: Preliminary steering critical arc length and tape width measurement results

The definition of the critical arc length, however, depends on the subjective classification of out-of-plane wrinkle defects, which adds additional inaccuracy. Figure 6.4(c) presents the consolidated tape width measurements at the start of the steering radius ($w_{t,c,0}$), out-of-plane wrinkle initiation ($w_{t,c,3}$) and at the position where the wrinkles reached the inner edge of the tape ($w_{t,c,4}$) for varying steering radii. As expected, the consolidated tape width prior to the steered section remained constant for all investigated radii. In the associated variance plot (Figure 6.4(d)) for constant 1200 mm steering radius, the consolidated tape width prior to the steered section exhibits the smallest variation with a standard deviation of 0.17 mm. A standard deviation about twice as high can be observed for both consolidated tape width measurements in the steered section. Despite the larger deviation, a correlation between the consolidated tape width and the steering radius can be observed. Smaller steering radii led to smaller consolidated tape widths. This steering-radius-dependent narrowing effect was about three times as large for the width at Position 4 as opposed to Position 3.

The process temperature of all steered tracks was analyzed using the thermal camera integrated into the ATP system's data monitoring system. While the thermal camera employs a emission coefficient $\varepsilon_e = 1$ and does not measure the exact nip point temperature, deviations from the optimal set point temperature of 470 °C can be observed. The heatmap of an example steering ply with radius 1200 mm (Figure 6.5(a)) shows an even temperature distribution after the transient track start section. With the current temperature control system, the fastest way to reach the target nip point temperature is to briefly overshoot the target temperature.

(a) R=1200 mm steering ply heatmap

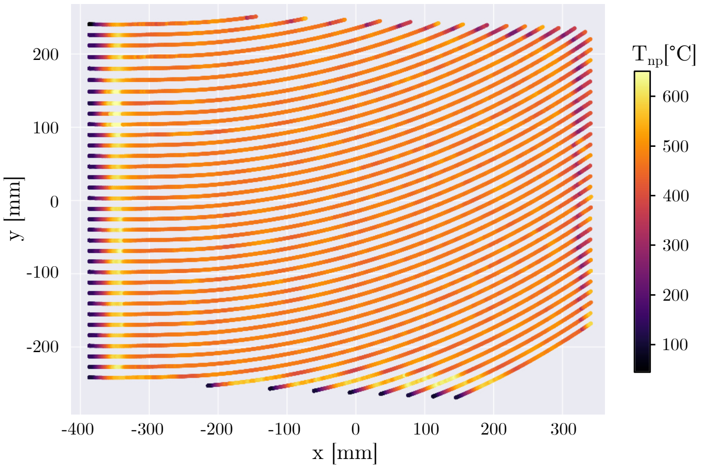

(b) 0° reference ply temperature curves (c) R=1200 mm steering temperature curves

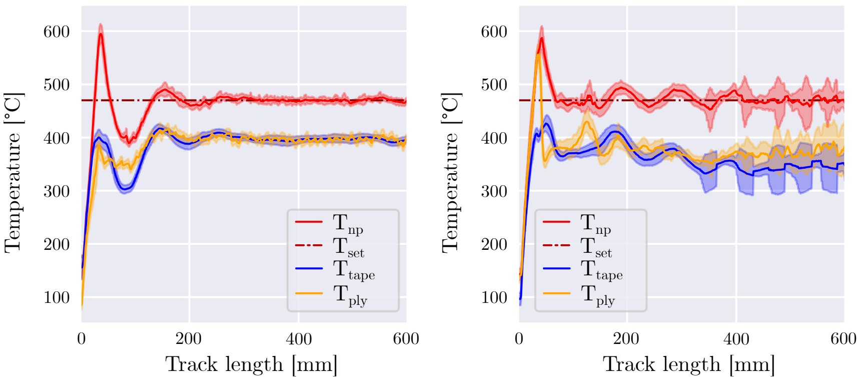

Figure 6.5: Heatmap and average track temperature curves of steering and straight reference experiments as measured by thermal camera at thermal emissivity $\varepsilon_e = 1$

Preferentially, those sections are placed outside the trimming area of the final laminate. A more detailed look at the average temperature curves over the track length in a direct comparison of straight reference tracks (Figure 6.5(b)) and curved tracks (Figure 6.5(c)) shows the influence of the curvature on the process temperatures. While the temperature control system achieved near-perfect match of tape and ply temperatures and close adherence to the target temperature, larger deviations were observed in the steering temperature curves. The presented steering dataset with the steering radius 1200 mm showed an increase in the temperature variance after the critical arc length of around 300 mm. The concomitant severe out-of-plane wrinkle defects led to recurring fluctuations in the tape temperature which aggravated the temperature control. The out-of-plane wrinkles, strong fluctuations in the consolidated tape width and uncontrollable process temperature occurring at arc lengths above the respective steering-radius-dependent critical arc length make these track sections unusable for in-situ consolidated laminates.

6.3 Impact of sub-critical steering radii on in-situ consolidation laminate properties

Laminates with steered plies were manufactured and tested in order to investigate the impact of in-plane path curvature on the consolidation quality of in-situ AFP laminates. The steering radius and arc length was varied to account for different stages of the curvature influence and to investigate the hypothesis that curved paths can be used up to the respective critical arc length. The relevant process parameters were recorded during laminate production using the data monitoring system. The consolidation quality was then examined using ultrasonic testing and microsection samples. Finally, the mechanical properties were determined using four-point-bending and five-point-bending tests. As discussed in Section 2.1.3 three-point-bending tests (ILSS) are typically used in the literature for determining interlaminar shear strength, but the values for thermoplastics are only of limited value. To this end, four- and five-point-bending tests were selected to assess the impact of in-plane path curvature on the consolidation quality of in-situ manufactured laminates. The properties of flexural strength and interlaminar shear strength which are superimposed in the results of the three-point-bending test were thus factored out to individual test methods, each of which could quantify one of the two stress states in isolation to obtain a more nuanced result of the mechanical properties.

6.3.1 Methodology

Mechanically fastened wide prepreg tape in 0 ° orientation on an unheated aluminum tooling (20 °C) was used as the first ply for all laminates with polyimide adhesive tape joining of the 300 mm wide bands to achieve a full layer. A smaller steering radius of 1250 mm and a larger radius of 2500 mm were chosen for the experiment. For each steering radius, a shorter and longer arc length resulted in the four steering parameter sets. The longer arc length was selected to remain just below the respective critical arc length for the given steering radius. Ten steering plies of alternating path curvature with 50 % staggering of subsequent plies of the same direction of curvature were layed up on the first ply prepreg layer using half-inch prepreg tape and the optimized process parameters as introduced in Section 4.2. The layup paths were planned in such a way that they ran tangentially at 0 ° at the position of the sample center (Figure 6.6).

The lateral track spacing was set to yield neither gaps nor overlaps between the individual tracks at the position of the sample centers. While this led to gaps or overlaps outside the sample sections, it enabled the required minimum number of identical samples with the same ply stacking sequence due to the same local path curvatures. Finally, for reasons of symmetry, a further 0 ° ply was added resulting in the ply stacking sequence $[0/(-\theta/+\theta)_5/0]$, where the local fiber angle is a function of the 0 °-distance from the symmetry plane of the specimens (y_0) and the steering radius (R). The local fiber angle can be calculated following:

$$\theta_f(R, y_0) = \sin^{-1}(\frac{y_0}{R}) \tag{6.5}$$

For the investigated five and four-point-bending specimens, the maximum distances from the symmetry plane were 20 mm and 46 mm resulting in a maximum local fiber angle of ±0.9 ° and ±2.1 °, respectively. The specimens thus had an almost unidirectional ply stacking sequence and at the same time took into account any influences of the steering on the consolidation quality.

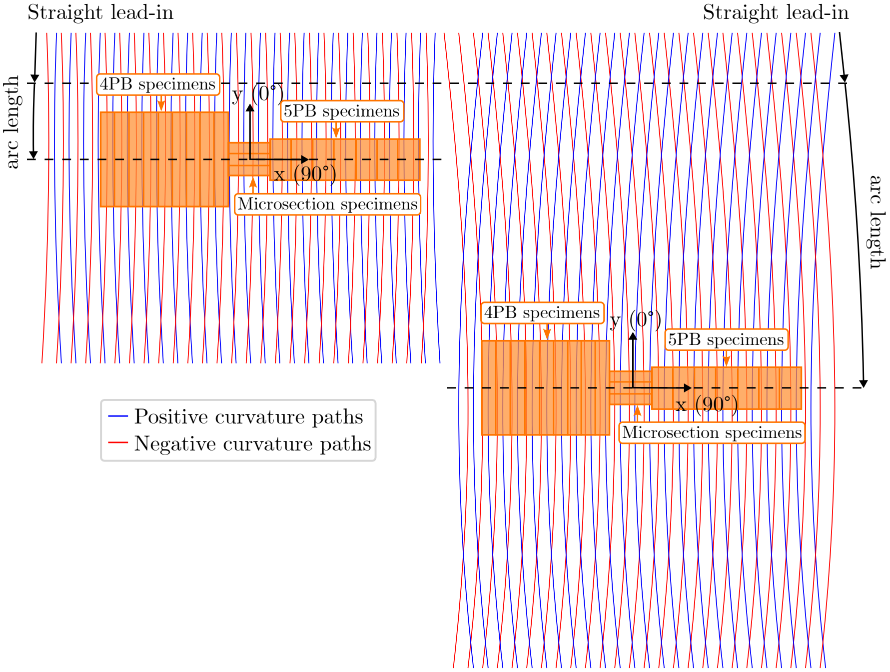

Figure 6.6: Steering laminate design with example layup paths and specimen positions

Table 6.1: Experimental design of steering laminates

Specimen label	Steering radius	Arc length
R2500-A300	2500 mm	300 mm
R2500-A75	2500 mm	75 mm
R1250-A150	1250 mm	150 mm
R1250-A75	1250 mm	75 mm
UD Ref	-	-

A unidirectional laminate with the stacking sequence $[0]_{12}$ was manufactured as reference for the steering specimens. The experimental design of the steering laminates is summarized in Table 6.1. Ultrasonic scanning was used as an initial assessment of the consolidation quality. Microsection and mechanical test specimens were subsequently extracted from the laminates at positions marked in Figure 6.6 using water jet cutting. Mechanical tests were carried out as presented in the Methodology section using DIC for strain and crack initiation measurements.

6.3.2 Results and Discussion

The process temperature analysis showed consistent and even nip point temperature throughout the steering plies. The median nip point temperatures of all plies were calculated for the areas of the mechanical test specimens and are summarized in Table 6.2.

Table 6.2: Median and standard deviation of nip point temperatures over all plies in areas of mechanical test specimen positions

Specimen label	4PB T_{np} [°C]	5PB T_{np} [°C]
R2500-A300	470.9 ± 6.6	470.8 ± 6.3
R2500-A75	468.0 ± 33.6	466.4 ± 10.4
R1250-A150	475.9 ± 7.3	477.8 ± 7.2
R1250-A75	470.5 ± 10.2	468.3 ± 5.7
UD Ref	469.5 ± 15.9	466.2 ± 10.8

Larger variances were observed in the 75 mm arc length specimens compared to the longer arc length specimens which was likely due to the close proximity to the transient effects at the track starts. A slightly elevated median process temperature was found in the R1250-A150 specimen area. This sublaminate comprised the most critical steering state with the smallest radius and the longest arc length of the configurations investigated. Overall, however, no statistically significant difference between the nip point temperatures of the specimen groups could be determined.

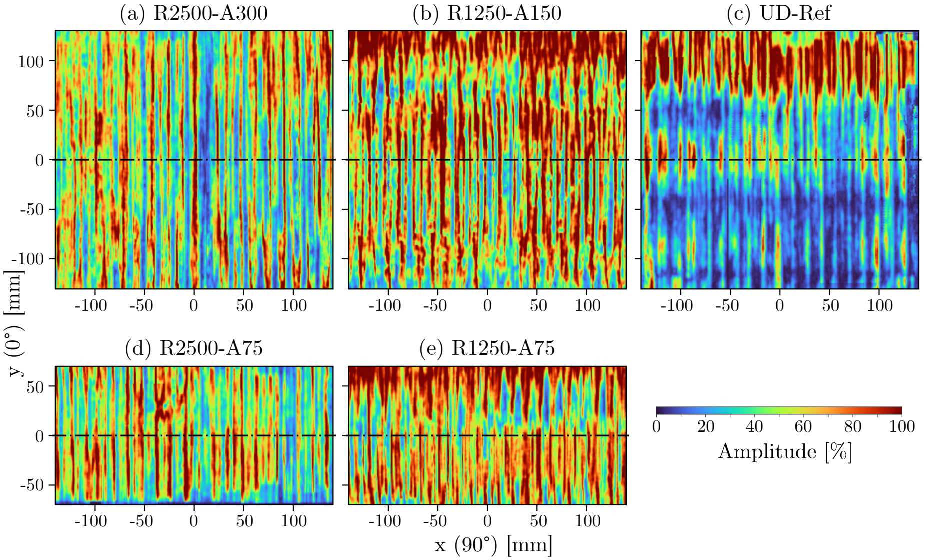

Figure 6.7: Steering laminate ultrasonic C-Scan backwall results

Figure 6.7 presents the ultrasonic C-scan test results with the gate adjusted to the backwall of the trimmed sublaminates with different steering radii and arc lengths. Longitudinal patterns oriented in the 0 °-direction were observed in all sublaminates. The patterns likely arose from porous sections at tape boundaries. The largest area of high amplitude backwall echo was observed in the R1250 sublaminates (Figure 6.7(b) and (e)) indicating the best match of layup path spacing and consolidated tape width in the measured sections of the laminate. The unidirectional reference laminate unexpectedly yielded large sections of low amplitude backwall echo (Figure 6.7(c)).

Example micrographs taken from the center of the sublaminates at x=0 mm and y=0 mm are presented in Figure 6.8. The microsection of the unidirectional laminate showed overall good consolidation and only smaller scattered intralaminar pores (Figure 6.8(a)). The tape boundaries can be recognized as matrix-rich lines and did not show any noticeable pores. Similarly well-adjusted tow-to-tow boundaries were observed in the four steering sublaminates (Figure 6.8(b)-(e)) with the exception of the R2500-A300 sample which showed gaps in some of the plies indicating overestimation of the consolidated tape width. For the advanced arc length, a greater fluctuation in the consolidated tape width is to be expected, as undulations occur on the inner track even before the critical arc length is reached. However, no porosity resulted from tape boundaries due to near-0 ° orientation of all plies allowing for smooth merging of the plies with fibers of the same orientation. The R1250 specimen sublaminates show pronounced intralaminar porosity in lower plies, most noticeably in ply 4.

(a) UD-Ref

(b) R2500-A300

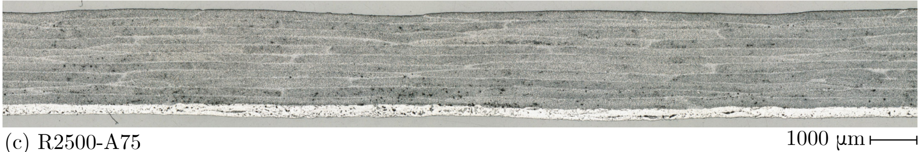

(c) R2500-A75

(d) R1250-A150

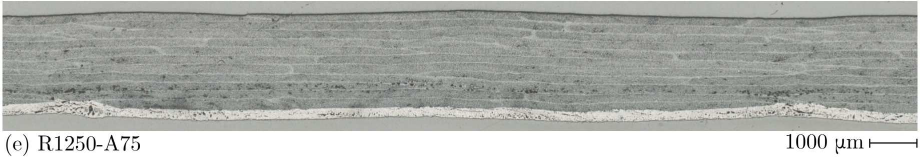

(e) R1250-A75

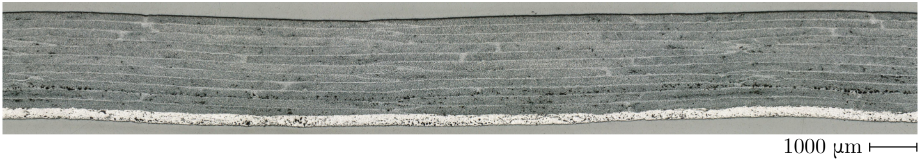

Figure 6.8: Steering laminate microsections

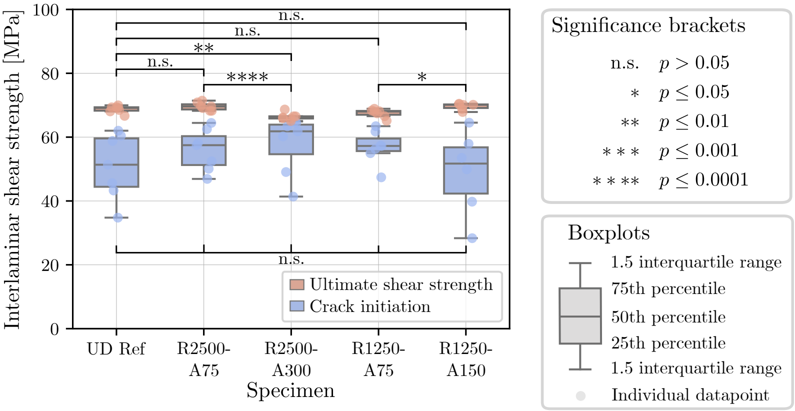

Figure 6.9: Five point bending test results

Although the laminates exhibited a relatively strong warpage due to their mainly unidirectional ply stacking sequence, the flatness of the individual mechanical specimens was not critical due to their orientation in the 0° direction and the relatively small dimensions.

The mechanical test results of the five-point-bending specimens are summarized in Figure 6.9. Initially, all four steering specimen groups were compared to the unidirectional reference. The specimen groups of the same steering radius and different arc length were then compared with each other to quantify the impact of progressed steering. Normality and comparability of variances were validated for all compared parameter sets using the Shapiro-Wilk test and Levene's Variance test, respectively. The results of the statistical analysis following independent t-test or one way ANOVA and Tukey's range test for two or three and more parameter groups, respectively, are indicated in the respective figures using significance brackets. Due to the large variances, no statistically significant difference could be determined for the crack initiation results. The ultimate interlaminar shear strength analysis on the other hand achieved very reproducible results with consistently low variance of approximately 1 MPa standard deviation for all specimen groups. No statistically significant difference was observed between the unidirectional reference and any of the steering groups, except for the R2500-A300 set, which showed a 4.3 % strength decrease compared to the reference. This correlated with the slightly sub-optimal consolidated tape width adjustment of this specimen set and the resulting gaps between tows, as observed in the microsection analysis. The comparison within the respective steering radius groups yielded a similar 5 % strength decrease between the R2500-A75 and R2500-A300, which can be explained by the slight gap defects in the longer arc length specimens, as well. For the R1250 specimens, a slight 3.1 % increase was determined between the A75 and A150 specimens. The effect, however, has a larger p-value of 0.02 (Tukey's range test) indicating lower statistical significance.

The four-point-bending strength and modulus test results are presented in Figure 6.10(a) and (b), respectively. Normality and comparability of variances were successfully validated for all compared parameter sets using the Shapiro-Wilk test and Levene's Variance test, respectively. The comparison of median ultimate strength results showed no statistically significant effects except for the R2500-A75 sample set, which achieved an 18.4 % larger bending strength than the unidirectional reference. A slight reduction was observed in the bending modulus results for both longer arc length sample sets with 3.5 % decrease for the R2500 samples and 10.0 % for the R1250 sample set. This effect is likely caused by the undulations due to the progressed steering effects resulting in lower tensile and compressive stiffness of the stressed layers.

The results presented in this section show that sufficient consolidation quality can be achieved using steering radii up to the critical arc length. It is, however, important to accurately predict the steering-induced tape geometry changes to achieve the best possible match of tow-to-tow spacing and consolidated tape width to avoid defects. This is addressed in the following section.

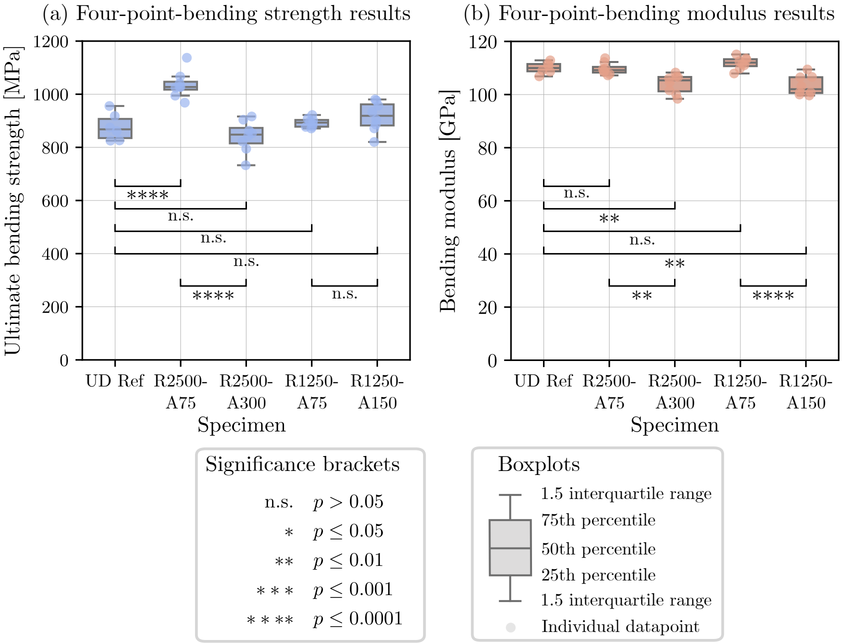

Figure 6.10: Four point bending strength and modulus results

6.4 Development of an optimized steering layup strategy

With the successful demonstration of the critical arc length principle, the next step is to develop a layup strategy that takes into account the steering-induced geometric changes in the consolidated tape dimensions and thus enables complete surface coverage, without critical defects and longitudinal tow-to-tow gaps. To this end high-resolution geometric measurement data of steered tracks was generated in a further experimental series in order to build an empirical model. The factorial design was extended to also include quarter-inch tape.

6.4.1 Methodology

Hot press-consolidated laminates were used as substrates as the smooth surface allowed for increased detectability of consolidated tape edges using the optical 3D measuring system. A [45/-45/90/0/-45/45/0/90/-45/45] ply stacking sequence and Toray 300 mm CF/LM-PAEK prepreg tape was used for the substrate laminates. The standard process parameters, as presented in Chapter 4 were used for hot pressing. Both, half-inch and quarter-inch Suprem CF/LM-PAEK prepreg tapes were used for the steering experiments. 65 mm straight lead in paths followed by constant steering radii between 1500 mm and 250 mm were investigated using the standard unheated tooling AFP process parameter set, as presented in the methodology section. The 250 mm radius was only investigated for quarter-inch tape, since the preliminary steering experiment did not yield any meaningful results for such a small steering radius with half-inch tape. Large steering radii above 2500 mm, on the other hand, were only investigated for half-inch tape since these curvatures are uncritical for quarter-inch tape. An overview of the investigated radii for the respective tape widths is presented in Table 6.3.

Table 6.3: Iterations of steering radii and respective tape width

R [mm]	$\frac{1}{2}$ inch tape iterations	$\frac{1}{4}$ inch tape iterations
4000	3	-
3500	3	-
3000	3	-
2500	3	6
2250	-	6
2000	3	9
1750	-	9
1500	9	9
1250	6	9
1000	11	9
750	6	9
500	6	9
250	-	6

The critical arc length (l_{crit}) was measured for all manufactured steering tracks. A detailed surface scan was produced of each laminate using the optical 3D scanning system. Curves were carefully constructed lengthwise along both edges of each tape up to the position where the first out-of-plane defect reached the inner tape edge, using the GOM Inspect software. Unlike the onset of the first out-of-plane defect (Position 3), this point can unequivocally be determined from the data and was thus used for this investigation. Because of the flattened edge shape shown in Figure 6.11(a), the true position of the edge was ambiguous.

Therefore, the point of maximum curvature, which can be detected automatically with the evaluation software was defined as the tape edge. The coordinates of the curves were subsequently exported as text datasets. Tape width and tape center were calculated using a MATLAB script. For each point of the inner radius curve, the outer radius points were iterated and their respective distances were calculated. The local tape width equals the minimum of all calculated distances, as shown in Figure 6.11(b). The local tape center point was subsequently calculated by adding half of the local tape width vector to the inner radius point.

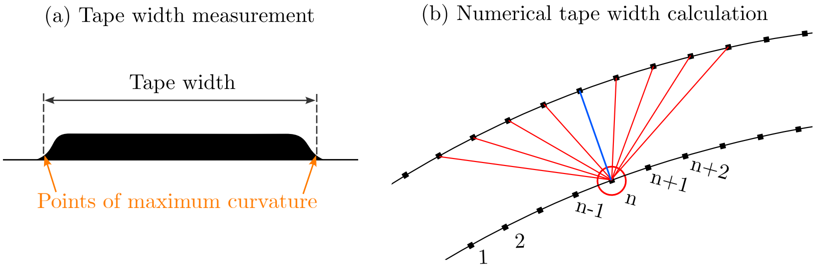
(a) Tape width measurement

(b) Numerical tape width calculation

Figure 6.11: Optical 3D scan analysis of steering experiments

The obtained geometry data was projected onto the global coordinate system of the tape placement facility using a python script, whereby the tracks with the same radius were superimposed at the same position to analyze the variance of steered tracks. The tape geometry data was then compared with the CAD-derived theoretical path planning data and the real Tool Center Point (TCP) data recorded from the facility's data acquisition system. The calculated average curves of the inner and outer tape edges were fitted over multiple steering radii using bivariate spline functions (SciPy 1.15.1 SmoothBivariateSpline). From the spline functions, a model was developed to select the optimum radius and y-direction shift of the subsequent track so that the distance between the outer tape edge of the existing track and the inner tape edge of the following track was minimal, or vice versa. In order to limit the solution space constant x-coordinates of the steering start points were defined as boundary condition, in addition to the constant geodesic curvature. This facilitated the layup strategy with track starts as in the established parallel layup strategy. Moreover, the optimization potential through x-direction shift was found to be negligible. The radial distance between tape edges integrated over the valid arc length was used as the optimization variable. The solution was determined numerically, beginning with a nominal start steering track and iteratively calculating the subsequent optimized steering track. The principle was validated for half and quarter-inch example plies with 1500 mm reference start radius. Straight 65 mm lead-in paths and 120 mm track ends were added to the steered paths. The example plies were layed up on hot-pressed substrate laminates using the same process parameters as in the prior steering experiments. The results were analyzed in conclusive optical 3D scans.

6.4.2 Results and discussion

The out-of-plane defect analysis of the manufactured steering experiments is presented in Figure 6.12. The measured onset of out-of-plane defects is plotted over the arc length (l_{crit}) in Figure 6.12(a) and in relation to the arc angle α_{arc} in Figure 6.12(b). For steering radii larger than 1500 mm and 2000 mm for quarter-inch and half-inch tape, respectively, not all steering tracks resulted in out-of-plane defects within the investigated arc length. For 3500 mm and above no out-of-plane defects were observed for half-inch tape. Similarly, for quarter-inch tape no out-of-plane defects were found for 2000 mm and larger radii. These steering radii can be considered non-critical for the respective tape width. To this end, only steering radii with consistently occurring defects were taken into account in the statistical analysis. A linear regression led to similar root mean square error (RMSE) evaluation results as higher degree polynomial or spline fits, confirming the linear correlation between steering radius and critical arc length found in the initial steering experiments. When plotting the linear curve fits analysis (Figure 6.12(b)), the curves indicated a constant arc angle limit at which defects occur independent of the steering radius. Average arc angles of 0.22 rad and 0.28 rad were observed for half-inch and quarter-inch tape, respectively. The visualized inter-quantile range of 90 % demonstrates the large variance in the onset of defects. The 5 % percentile is suggested as a upper arc angle limit, to avoid nearly all out-of-plane defects.

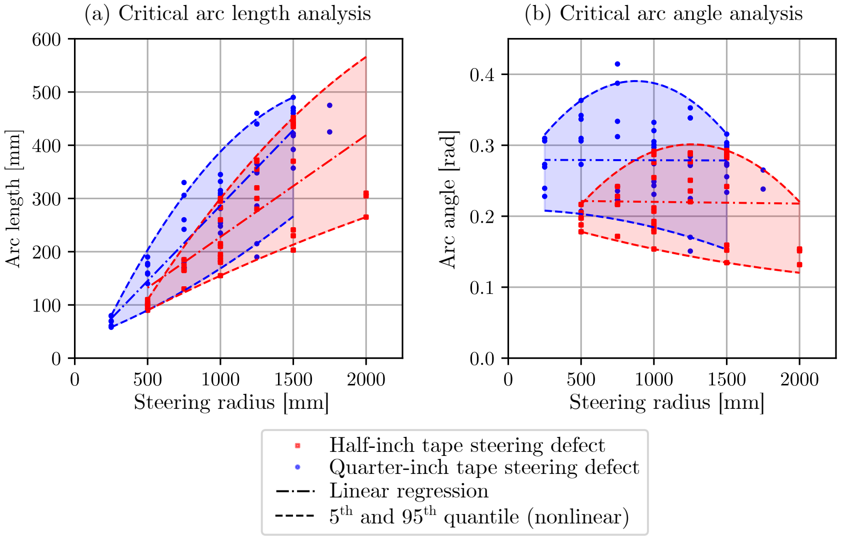

Figure 6.12: Critical arc length and arc angle analysis for onset of out-of-plane defects with hot-pressed substrate

One of the resulting panels with half-inch steered tracks and straight reference tracks is presented in Figure 6.13(a). For the half-inch material the tape edge analysis of all straight reference tracks projected onto the same x and y-position (Figure 6.13(b)) showed a slight fluctuation in the consolidated tape width at the beginning of the track due to the transient power response of the temperature control system. An average consolidated tape width of 14.47 mm with a standard deviation of 0.22 mm was determined in the quasi-stationary parts of the tracks between 100 mm and 300 mm track length.

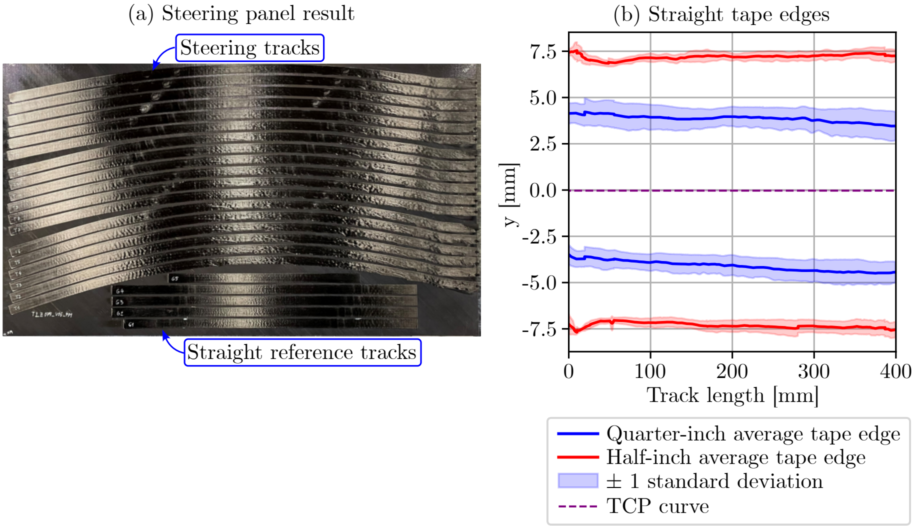

Figure 6.13: Resulting steering panel and analysis of straight half-inch reference tracks

For the quarter-inch tape an average consolidated tape width of 8.48 mm and a standard deviation of 0.27 mm was observed. This amounts to a more than twice as large proportional increase in consolidated tape width for quarter-inch material, 33.5 % compared to 13.9 % for half-inch tape and similarly higher width variance.

Figure 6.14 presents measured tape edge, TCP and path planning (CAD) data of the half-inch tracks with straight lead in sections and steering radii 1000 mm, 1250 mm and 1500 mm.

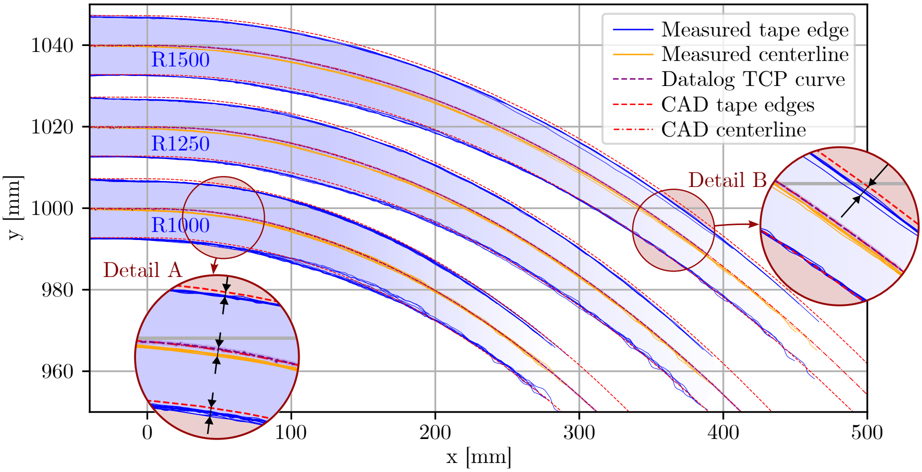

Figure 6.14: Optical 3D scan analysis results for superimposed 1500 mm, 1250 mm and 1000 mm steering radii with half-inch tape

The individually measured tape edges and calculated centerlines of each track were projected onto the same reference position to visualize the variance in the resulting consolidated tape geometries. The CAD-derived track centerlines matched the real TCP curve, recorded from the facility's data acquisition system perfectly, indicating a good match between the planned and executed path curve without point deviations by the robot. The theoretical CAD tape edges were generated as parallel lines to the CAD centerline with a distance of half the consolidated tape width of the straight tracks, representing the complete bending deformation mode. For a better visualization of the effects, a different X and Y-axis scaling was selected, which is why the parallel lines appear to converge. While the steering radius began at $x = 0$ mm, a deviation of the measured tape edges from the CAD tape edges was observed before the start of the steering radius in the straight lead-in section. Detail view A shows a shift of the measured tape edges and centerline compared to the CAD reference towards the inside of the steered track, while the tape width remained constant. Detail view B at a further-progressed steering arc length, on the other hand, shows a narrowing of the consolidated tape width. While the measured inner edge followed the CAD tape edge, the outer edge was shifted inwards towards the centerline. Furthermore, the inner edges showed clear undulations, which contributed to a greater variance of the measured inner edge.

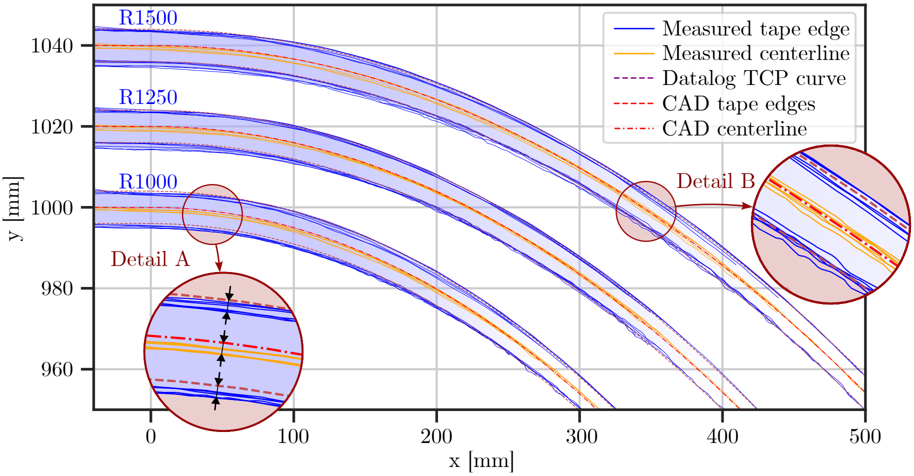

Figure 6.15: Optical 3D scan analysis results for superimposed 1500 mm, 1250 mm and 1000 mm steering radii with quarter-inch tape

The analogous analysis of the quarter-inch radii is shown in Figure 6.15. As observed in the straight quarter-inch width analysis, there was a larger variance in the tape edge positions of the steered quarter-inch tracks. This could also be due to the lower directional stability of the thinner and narrower tapes and aggravated tape guiding with the vacuum-assisted tape guiding system. While detail view A shows a similar shift of the tape towards the inside of the steered track at the beginning of the steering radius, the narrowing and deviation of the outer tape edge from the theoretical CAD curve was not recognizable.

Figure 6.16 presents the developed empirical model for predicting the consolidated tape edges of steered tracks, enabling the selection of optimal steering radii to minimize steering-induced gaps between tracks. The measured tape edge data was extended to a third dimension representing the steering radius, allowing for bivariate spline fits to be generated for both the outside and inside tape edges based on half-inch tape datasets with steering radii of 1000 mm, 1250 mm, and 1500 mm (Figure 6.16(a) and (b)).

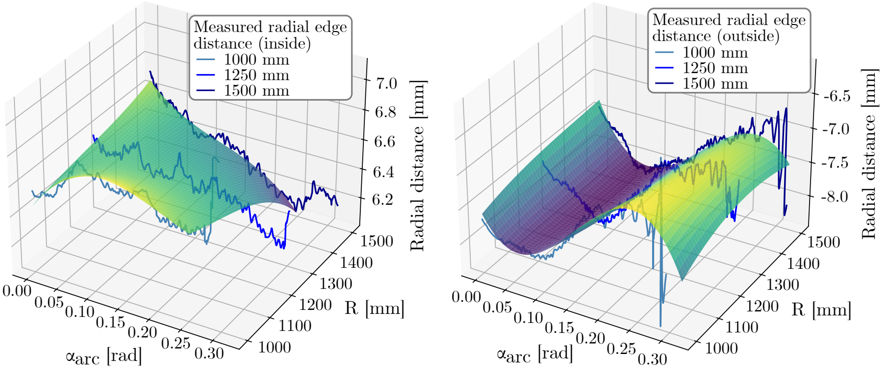
(a) Outside edges bivariate spline fit

(b) Inside edges bivariate spline fit

(c) Outside edges fit cartesian coordinates

(d) Inside edges fit cartesian coordinates

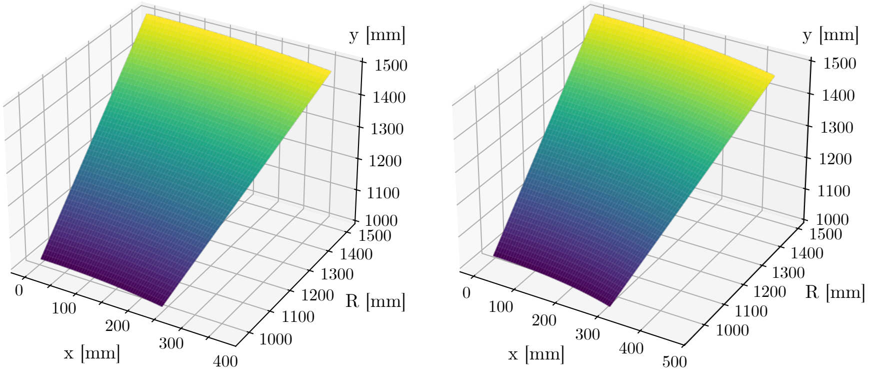

Figure 6.16: Bivariate spline fits for average track edges of 1500 mm, 1250 mm and 1000 mm steering radii with half-inch tape

Table 6.4 presents the fitting parameters of the resulting bivariate splines. The complete set of knot vectors and B-spline coefficients is attached in Appendix A4. The smoothing factors were chosen empirically to balance overfitting and underfitting. The residuals had standard deviations of 0.04 mm to 0.1 mm and maximum values of 0.15 mm to 0.38 mm, indicating a good fit as these values are within the width variance of the straight reference tracks.

Table 6.4: Bivariate spline fitting parameters and residuals

	Half-inch spline fit		Quarter-inch spline fit	
	Outside edges	Inside edges	Outside edges	Inside edges
Smoothing factor s	1000	1000	1000	1000
Degrees k_x, k_y	3	3	3	3
Mean residual [mm]	0.00 ± 0.04	0.00 ± 0.08	0.00 ± 0.10	0.00 ± 0.08
Max residual [mm]	0.15	0.34	0.38	0.28

Transforming these lateral distance fits into the cartesian coordinate system yielded three-dimensional spline functions capable of predicting the outer and inner edges of steered tracks (Figure 6.16(c) and (d)).

As described in the methodology section, the empirical optimization algorithm used the radial distance between the outer edge curve of the reference track and the inner edge curve of the subsequent track integrated over the valid arc length as the optimization variable. The results of this optimization approach are visualized in Figure 6.17. For reference the subsequent radius of the parallel layup strategy, which corresponds to the reference radius plus the consolidated tape width and the shifted strategy with the same radius as the reference radius and optimized y-shift were added in the plots. A linear correlation was found not only for the parallel and shifted layup strategy, but also between the reference input radii and the fitted subsequent track radius for half-inch and quarter-inch tape in Figure 6.17(a) and (c), respectively. A constant radius decrease of 22.5 ±1.5 mm and 19.9 ±1.1 mm was found for the fitted radii of half-inch and quarter-inch steering-optimized layup strategy, respectively.

The average radial curve differences between the reference outside edge and the inside edge of the respective layup strategy is presented in Figure 6.17(b) and (d) for half-inch and quarter-inch tape, respectively. For both tape widths, the steering-optimized layup strategy achieved less than half of the parallel strategy average radial distance. While for half-inch tape, the steering-optimized strategy yielded only small advantages compared to the shifted strategy, for quarter-inch tape another significant improvement was found with average radial curve deviation of less than 0.1 mm.

The optimization examples for a half-inch and quarter-inch plies with 1500 mm reference radius are shown in Figure 6.18. The optimized steering curves were created for an arc angle of 0.2 rad and 0.25 rad for half-inch and quarter-inch tape, respectively, taking into account the critical arc angle results. The resulting tape edge prediction shows negligible curve deviation of the outer tape edges and fitted inner tape edges (Figure 6.18(a) and (c)).

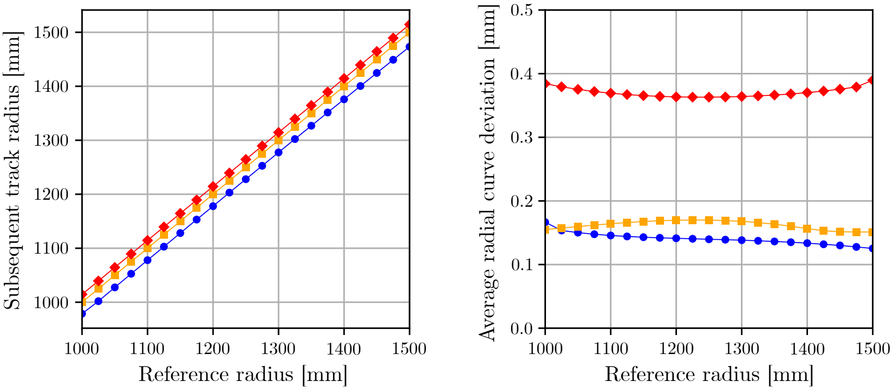

(a) Half-inch inside edge fit for outside edge ref.

(b) Half-inch curve fit evaluation

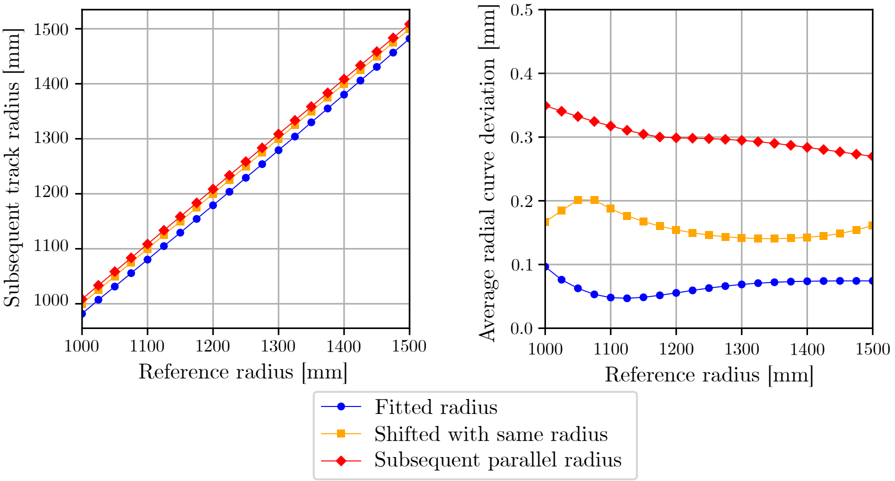

(c) Quarter-inch inside edge fit for outside edge ref.

(b) Quarter-inch curve fit evaluation

Figure 6.17: Steering radius match and evaluation of curve fits

The resulting manufactured steering plies are presented in Figure 6.18(b) and (d). Due to the large variation in the critical arc length, some tracks showed shear defects and pronounced undulations at the inner tape edges, resulting in small gap defects. This effect was more pronounced in the half-inch steering ply than in the quarter-inch ply. At the tape cuts at the right-hand side of the laminate, tow straightening was detected as expected.

The residual defects are visualized in Figure 6.19. Deviations from optimum surface coverage were particularly noticeable in the tow cuts area resulting from the tow straightening and transient process parameters resulting in narrower consolidated tape width. Smaller residual gap defects were also observed at the inner edges due to in-plane undulations occurring below the critical arc length. These residual gaps are visualized in the section views

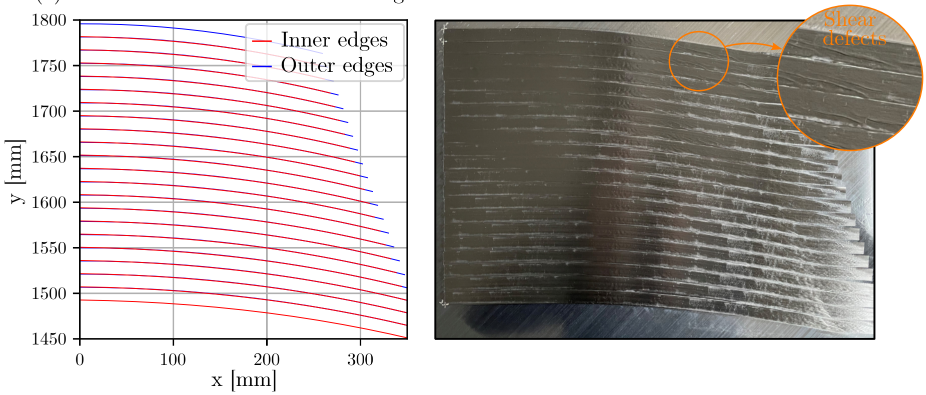
(a) Half-inch fitted inner and outer edges

(b) Half-inch manufactured ply

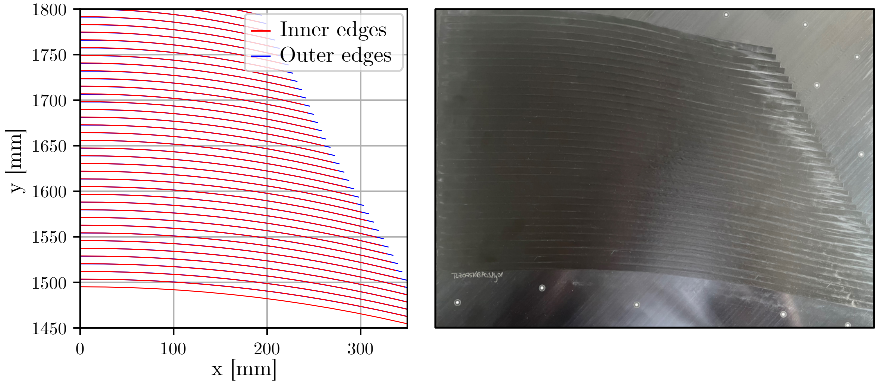
(c) Quarter-inch fitted inner and outer edges

(d) Quarter-inch manufactured ply

Figure 6.18: Optimized example steering plies and manufactured validation plies

A-A' and B-B' for half and quarter-inch, respectively. They could be avoided by further reducing the utilized arc angle. Overall, the gap defects could be reduced to a minimum for both tape widths with the optimized layup strategy compared to conventional parallel layup.

The presented results demonstrate the methodology of a steering-optimized ply for a very specific material, machine a process parameter combination. The algorithm can, however, easily be trained with empirical data from any machine and material setup. Using a wider range of steering radii could potentially increase the accuracy of the spline fit and resulting layup paths. The present algorithm is valid for constant curvature layup paths. Without boundary condition of constant geodesic curvature, an even better fit could potentially be achieved, however, at the cost of a significantly more complicated layup strategy. Future work could elaborate on the presented results, investigating non-constant curvature steering. This could expand the design space to non-constant curvature applications such as linear variation reference curves or double-curved dome geometries.

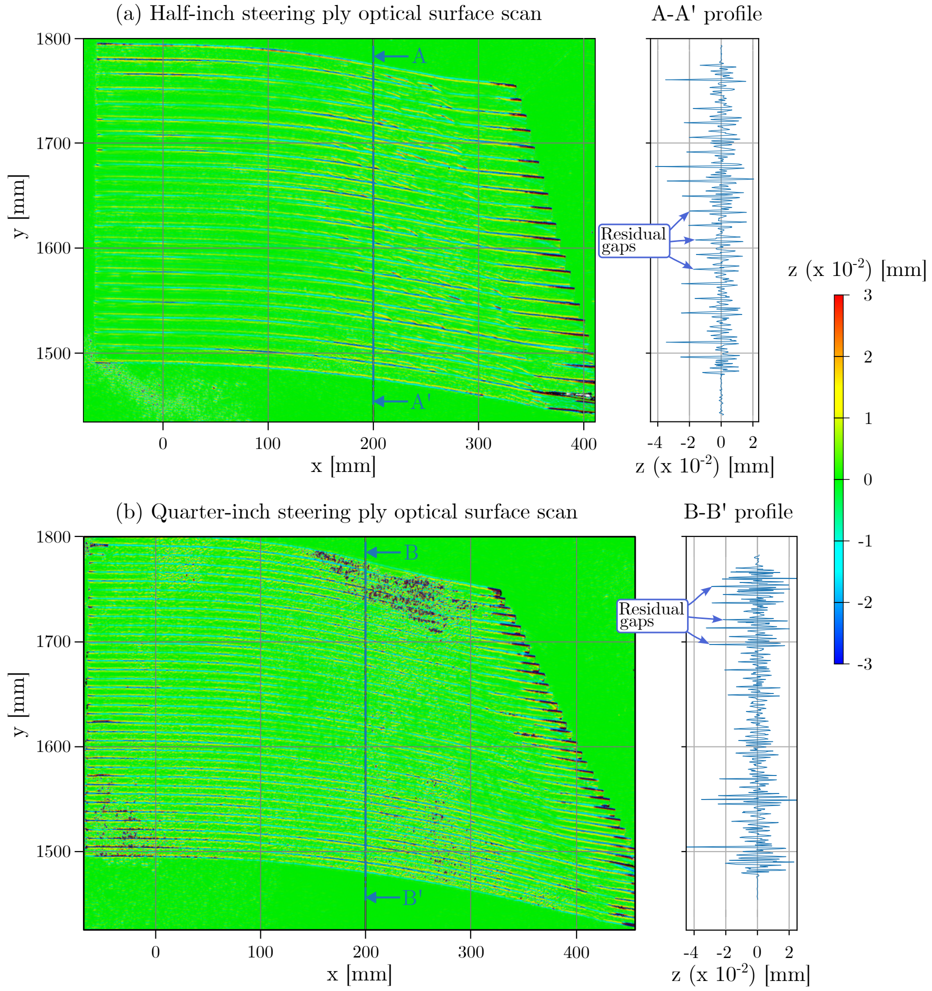
(a) Half-inch steering ply optical surface scan

(b) Quarter-inch steering ply optical surface scan

Figure 6.19: Optical 3D scans of steering plies

6.5 Conclusion

This research presents a comprehensive investigation of the impact of constant geodesic curvature (steering) on in-situ AFP-manufactured laminates. A novel concept of critical arc length was developed for steered layup in-situ AFP. Steering radii that were previously considered too critical in the literature were shown to be usable up to a radius-dependent arc length using the concept of critical arc length for in-situ AFP. The interlaminar mechanical properties, which are considered the most critical properties for the in-situ AFP process, were investigated using coupon level mechanical tests. Only very small interlaminar shear strength and bending strength effects were found for steering laminates compared to unidirectional reference. For bending modulus, however, up to 10 % stiffness decrease was found for steering specimens with near-critical arc lengths, due to steering-induced fiber undulations resulting in larger flexural compliance of the specimens.

The steering-induced geometry changes of the tapes were mapped in an empirical model and implemented in a path planning algorithm for constant curvature steering without gap or overlap defects. The methodology was successfully validated for half-inch and quarter-inch tape and can be used for other process parameters and machine-material combinations by training the model with the respective test data.

The combination of the critical arc length concept and the optimized path planning algorithm presents a design space for the application of curved paths using in-situ AFP with high laminate quality. The envelope for the usable steering design space for half-inch and quarter-inch material was determined for the investigated material process parameters and machine combination. Greater degrees of freedom were found for quarter-inch material. This data can be used as a basis for the in-situ AFP process-optimized design for manufacturability of target components.

Future work should investigate further mechanical properties of steering laminates. The model could also be extended to variable curvature to evaluate components such as dome structures, which were explored from a path planning perspective in Section 5. Lastly, the fiber straightening following tape cut at track ends and the transient start and end section require further improvement of the process control algorithms to achieve sufficient layup quality in those sections and enable track starts and ends within the usable laminate.

Chapter 7

Structural Impact of Gap and Overlap Defects

This chapter presents an investigation of geometry-induced gap and overlap defects on in-situ AFP laminates. As detailed in the literature review (Section 2.2.3), there are no publications on realistic, i.e. non-parallel, gap defects for in-situ AFP yet.

Based on the gap and overlap defect patterns derived in Chapter 5, an experimental design with realistic triangular, staggered defects was developed. In-situ AFP laminates with both half-inch and quarter-inch tapes were compared to hot-press consolidated laminates in terms of laminate composition in the defect areas and resulting mechanical properties.

The work presented in this chapter was published in the journal papers ”In-situ automated fiber placement gap defects filled by fused granular fabrication” [307] and ”Effect of geometry-induced triangular gap and overlap defects on in-situ AFP-manufactured structures” [308].

7.1 Experimental design

A total of seven laminates were manufactured as part of this study. Half-inch and quarter-inch tape, as introduced in Section 4.1, were utilized to compare the impact of different triangular defect widths. A room temperature tooling configuration (RT) with a tool temperature of 20 °C was compared with a heated tooling configuration (HT) with 200 °C tool temperature to assess the impact of gap and overlap defects for different in-situ consolidation-optimized manufacturing parameters. Sections of the various laminates were hot pressed (HP) to provide insight into the severity of gap and overlap defects between in-situ AFP and standard thermoplastic manufacturing processes.

From the collection of laminates, specimens with gaps (G) or overlaps (O) and reference specimens without defects (R) were produced. An overview of the various configurations with the respective parameters and specimen labels is presented in Table 7.1. Tensile and compressive test specimens were chosen to assess the impact of defects on the mechanical properties of the laminate. Due to the long nature of the samples, tensile specimens considered multiple defects within a single sample. Compressive testing, on the other hand, prioritizes the matrix-dominated failure modes which are more critical for in-situ AFP laminates. Furthermore, compressive tests are sensitive to defect-induced out-of-plane undulations, impaired consolidation and porosity in the defect areas.

Table 7.1: Factorial design of gap and overlap defect laminates

Tape width [inches]	**Process**	**Type**	**Laminate**							**Designation**
			1	2	3	4	5	6	7	
$\frac{1}{2}$	RT	Gaps	x						x	G-1/2-RT
	RT	Reference	x							R-1/2-RT
$\frac{1}{2}$	HT	Gaps		x						G-1/2-HT
	HT	Overlaps			x					O-1/2-HT
	HT	Reference		x						R-1/2-HT
$\frac{1}{2}$	HP	Gaps				x			x	G-1/2-HP
	HP	Reference				x				R-1/2-HP
$\frac{1}{4}$	RT	Gaps					x			G-1/4-RT
	RT	Reference					x			R-1/4-RT
$\frac{1}{4}$	HP	Gaps						x		G-1/4-HP
	HP	Reference						x		R-1/4-HP

Laminate design

Mechanically fastened wide prepreg tape joined with polyimide adhesive tape was used as the first ply for all laminates. It was clamped across the entire width in 90° direction on both sides under a bar and placed under slight pre-tension using toggle levers. Straight layup paths were used to approximate the triangular defect patterns as observed in VSP or double-curved geometries with converging and curved courses. The slight curvature of the triangles was neglected and approximated with sufficient accuracy using idealized triangles. For reference, a typical defect pattern of the bottom left (third) quadrant of a VSP with gap defects and $[\langle 23.5|46|23.5\rangle]_4$ layup sequence is shown in Figure 7.1(a), as derived in Chapter 5.

While the laminate design would ideally contain both positive and negative orientations of the plies with defects, this would result in a different defect pattern for each specimen on the laminate and thus would not allow for a minimum number of identical samples. For this reason, only the positive orientation of the defect plies is taken into account by replacing the +45°

layers in a 16-ply quasi-isotropic laminate. A triangular defect shape with an opening angle of $\gamma_{defect} = 12\,^\circ$ was chosen for the laminate design, as observed in Chapter 5 for realistic layup strategies of application-related VSP and double-curved geometries. The triangular gap defects were implemented by replacing the +45 ° plies with ⟨39|51⟩ plies, where the top left and bottom right side of the ply were realized using 39 ° and 51 ° layup paths, respectively. Both orientations meet at the first main diagonal of the ply and the gap defects automatically emerge following a 0 % coverage tow cutting strategy. Track starts were used at the tow cut positions as they enable greater positioning accuracy and consolidation close to the defect compared to track ends where no tape tension for lateral tape guiding is applied after the tape cut and only the upper surface of the tape is heated after the tape fold-down. A similar design with 12 ° triangular defect opening angle was used by Falcó et al. [239–241]. The resulting laminate ply stacking sequence is therefore $[0/\text{-}45/90/\langle 39|51\rangle]_{2S}$, where the first ply for all laminates was realized as mechanically fastened wide prepreg tape joined by adhesive tape on the tool-facing side to achieve a full layer for the laminate. The width of the triangular defects is determined by the consolidated tape width which was determined experimentally for the various tool temperatures and prepreg tapes while producing the test laminates in Chapter 4 (Table 4.4).

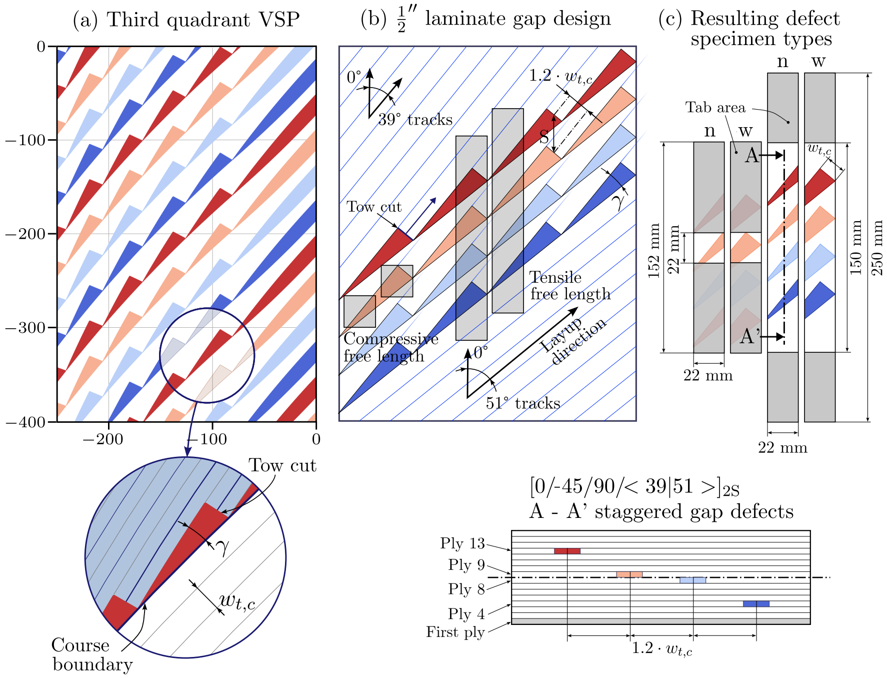

(a) Third quadrant VSP

(b) $\frac{1}{2}''$ laminate gap design

(c) Resulting defect specimen types

Figure 7.1: Derivation and design of defect laminates and resulting tensile and compressive specimens

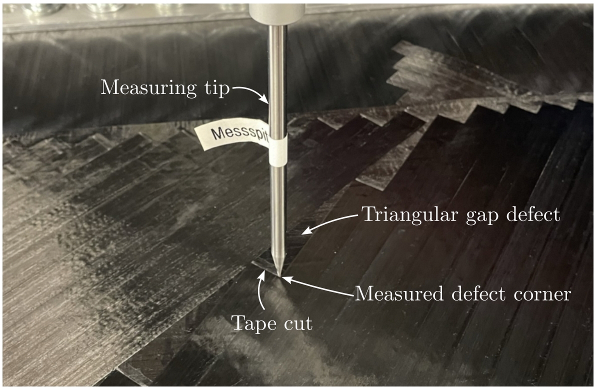

Figure 7.2: Measurement of triangular defect positions

The four defect plies were staggered using a staggering factor perpendicular to the layup direction of the 39 ° layup paths of 1.2 times the consolidated tape width. While the 0.2 component of the staggering factor was used to avoid superimposing tape boundaries of same-orientation plies, the additional factor 1 yielded an offset of gap defects in the y-direction, which corresponds to VSP and double curved geometry staggering strategies. A schematic drawing of the design for half-inch defect laminates with 0 % coverage ratio is shown in Figure 7.1(b).

The defect positions were measured using the measuring tip of the end effector after the completion of each defect ply and compared with the intended positions from the laminate design (Figure 7.2). The finished AFP and HP laminates were trimmed using water jet cutting and analyzed with water-coupled ultrasound. The entire process chain is visualized in Figure 7.3. Tensile and compressive test specimens based on AITM 1-0007 and AITM 1-0008 (Chapter 4) were positioned on the laminate in such a way, that one specimen type contained the wide portion (w) of the triangular defects while the other type contained the narrow portion (n) of the defects, as the standardized specimen width of 22 mm did not allow for the consideration of the entire defects within one sample width. Similarly, the 22 mm free length of the compressive specimens allowed for only one partial defect in the free length section of the specimens, while all four staggered defect rows where accommodated in the free length of the tensile specimens. The resulting specimen design with a cross section of the free length and staggered defects is presented in Figure 7.1(c). From each laminate, eight tensile and compressive specimens were extracted, respectively. Water-jet cutting was used to accurately extract the specimens at the intended defect position using a 1 mm oversize. After applying the end tabs to several samples next to each other, the samples were cut to the final width of 22 mm using a sample saw, so that no influence of the edges by water jet cutting was to be expected.

Additionally, reference tensile and compressive specimens were positioned in the defect free

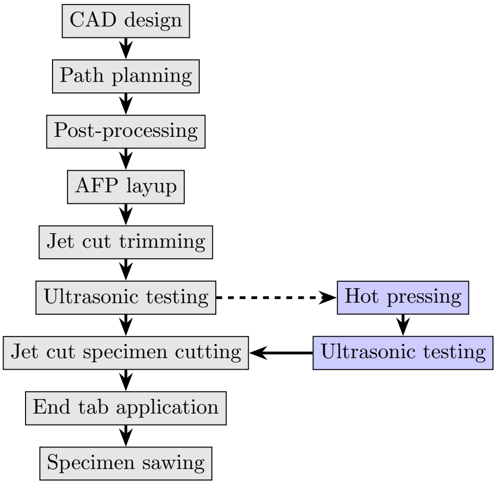

Figure 7.3: Defect specimen manufacturing process steps

$[0/\text{-}45/90/39]_{2S}$ and $[0/\text{-}45/90/51]_{2S}$ sections of the laminates, respectively. Selected tensile and compressive specimens were analyzed using CT-scanning before and after the mechanical test. Microsection specimens were extracted from all defect rows for visual analysis of the defect areas.

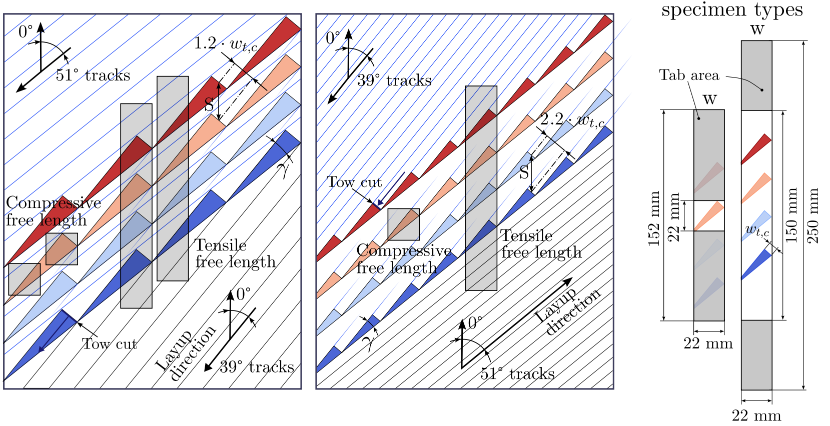
(a) $\frac{1}{2}''$ laminate overlap design (b) $\frac{1}{4}''$ laminate gap design (c) Resulting $\frac{1}{4}''$ defect specimen types

Figure 7.4: Overlap and quarter-inch gap defect laminate design

Overlaps could be generated using slightly longer tracks with a later tape cut position in order to achieve 100 % coverage ratio. However, the resulting triangular overlap would have the opposite orientation of the respective gap defects. In order to maintain the same position of the defects, the orientation of the layup paths was swapped instead (Figure 7.4(a)). The defect plies were thus created from 39 ° tracks on the top left-hand side and 51 ° tracks on the bottom right-hand side. All other parameters remained constant, as presented in Figure 7.4(a).

The quarter-inch gap defect laminates were designed analogous to the half-inch gap defect laminates. The smaller consolidated tape width of 7.6 mm compared to 14.2 mm of the (RT) half-inch laminates, however, results in narrower and shorter triangular defects, which almost fit on the width of a specimen. Therefore, only one tensile and compressive (w) defect type was required for quarter-inch laminates, respectively. In addition to the smaller individual defects, the quarter-inch width enabled a larger staggering factor. For comparability with the half-inch specimens, a staggering factor of 2.2 times the consolidated tape width was chosen for the design.

7.2 Results and discussion

The following section presents the results of the gap and overlap defect experiments. The results are presented in the order of the process chain, starting with the process data analysis, continuing with the non-destructive testing and ending with the mechanical test results. The various analysis results are correlated with each other in order to achieve a detailed analysis of the experimental test data and to obtain a complete picture of the defect influences.

7.2.1 Process Temperature

The process temperature data of all plies was analyzed for all manufactured laminates in order to identify and quantify influences of the gap and overlaps on the process window. While the thermal camera measurements with the emission coefficient $\varepsilon_e = 1$ do not measure the exact nip point temperature, deviations from the optimal set point temperature of 470 °C can be observed. For standard laminates, the start and end sections of the tracks are preferentially placed outside the trimming edge since these transient sections are harder to control with regard to the process temperature and the positioning accuracy. As the triangular gap and overlap defects are caused by starting or ending tracks, the transient start or end sections of the tracks are, however, inevitably present in the center of the laminate. Figure 7.5(a) shows an example heatmap of the nip point temperature of ply 4 from laminate 1 (G-1/2-RT) with the two layup orientations 39 ° and 51 ° and the resulting gap defect positions. The tracks within the trimming edge show a relatively even temperature distribution. The start and end sections outside the trimming edge and the gap defect positions, however, show deviations from the set point temperature. Figure 7.5(b) presents density histograms of the temperature distribution for all plies of the four in-situ consolidated laminates without the transient start and end sections of the tracks. All four laminates achieve mean temperature values with less than 1 °C deviation from the set point temperature. The quarter-inch laminate, however, shows significantly larger variance in the temperature data, indicating a greater fluctuation in the nip point temperature in the steady-state portion of the laminate. Figure 7.5(c) and (d) show the average nip point, tape and ply temperature curves with standard deviation error bands of the transient start and end sections of all tracks derived from the example ply in Figure 7.5(a), respectively.

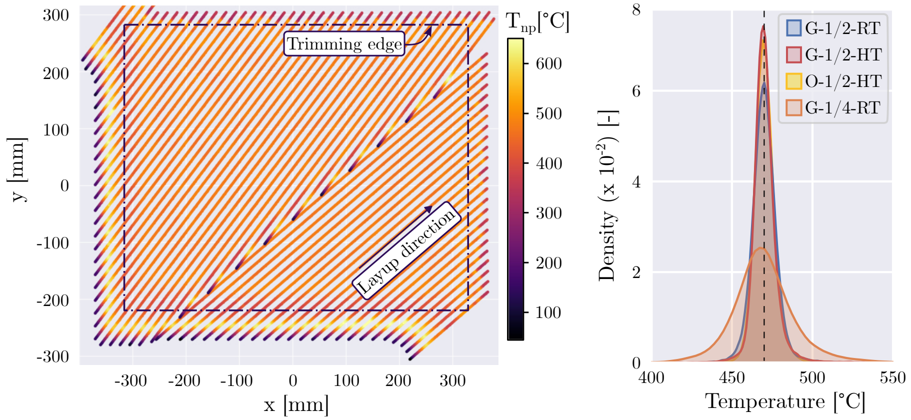

(a) Nip-point temperature heatmap G-1/2-RT Ply 4

(b) Temperature histogram

(c) Track start temperature curves G-1/2-RT Ply 4

(d) Track end temperature curves G-1/2-RT Ply 4

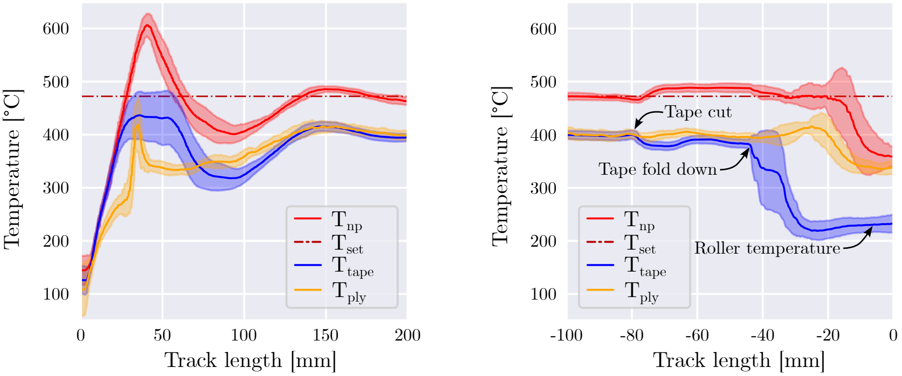

Figure 7.5: Heatmap and average track temperature curves of gap ply as measured by thermal camera at thermal emissivity $\varepsilon_e = 1$

With the currently implemented laser power control system, the best way to quickly reach the set point temperature is to introduce a short temperature peak before converging to the target temperature. Without this overreaching, an even longer distance would be required to match the ply and tape temperature and to reach a stationary nip point temperature of 470 °C. The temperature curves for tape, ply and nip point temperature are very reproducible in the track length direction. Reaching the desired temperature is, however, far from step-like when observed over the full track length, with peaks and drops owing to specific events. For the track start temperature curves, the greatest variance occurs in the tape temperature measurements around the local temperature maximum at approximately 40 mm track length, reaching a maximum standard deviation of 68 °C (Figure 7.5(c)). The short time at the temperature exceeding the optimal range could have a small degrading effect, which is likely negligible, as discussed in Section 2.1.1. Following the local maximum, the measured nip point temperature drops to approximately 400 °C. As discussed in Section 2.1.3, recent work at the DLR showed that a measured nip point temperature of 410 °C yielded slightly lower shear strength than 470 °C samples although a significantly greater drop was noticed below 400 °C [56].

The track end temperature curves do not show any significant excess temperature (Figure 7.5(d)). The uniform progression of the temperature curves ends with the tape cut, which is accompanied by a total loss of tape tension, allowing the tape to move more freely in the tape guiding system. The vacuum-assisted tape guiding system (Section 4.2, Figure 4.1) holds the tape in contact with the guiding system for longer than a regular tape guiding system. However, after passing the suction openings, the cut tape eventually folds down due to the bending moment introduced by the consolidation roller. After the tape fold down the measured tape temperature corresponds to the surface temperature of the consolidation roller, as the tape is no longer in the relevant thermal image area. Furthermore, for the last 45 mm of the track the laser can no longer heat the joining surfaces of ply and tape but only the top surface of the folded-down tape. The joining interface of the track ends is thus subject to uncontrolled cooling, which leads to sub-optimal consolidation. To this end, track starts were chosen at the defect positions, as discussed in the methodology section of this Chapter.

7.2.2 Positioning Accuracy

One of the critical challenges in the investigation of planned defects is the exact tracking of defect positions over the process steps of sample production. In the process chain from virtual path planning to the finished sample, the actual AFP process is subject to the greatest geometric tolerance with regard to the resulting defects. The layup accuracy depends on the accuracy of the robotic system, geometrical tape tolerances, the AFP process and end effector accuracy. The robotic system consists of the robot with a position repeatability of ±0.08 *mm* [309] and the two-axis positioner with position repeatability of 0.009 ° of both axes [310]. However, the absolute position accuracy of the robotic system depends on the calibration, payload and environmental conditions and is around 1-3 mm [311]. Additionally the AFP process itself adds significant inaccuracy to the defect positions. Depending on the process parameters nip point temperature, consolidation pressure, layup speed and prepreg material composition, the resulting consolidated tape dimensions vary, specifically at the start and end of a track, where the process control is aggravated. The tape guiding system is designed to allow for the smallest possible lateral deviation. After the tape cut, however, the tape tension is released and the tape can move relatively freely in lateral direction after leaving the tape guiding system. Furthermore, residual stress in the prepreg tape can lead to lateral deviation from the intended layup path. This is especially relevant for the triangular gap and overlap defects, which are typically created at the end of a track via tape cuts at the intended position. The lengthwise deviation (in layup direction) is even harder to control, than the lateral deviation, as it depends on prefeed, tape tension and cut timing parameters of the end effector. These parameters were iteratively optimized for the most accurate position of the defects. The converging of the layup paths in a 12 ° angle at the position of the defects causes the tolerances in tape width and length direction both to influence the geometry of the triangular defects. Measuring the individual triangular defects after completion of each ply with defects in the AFP process helped to understand the geometric variance in the AFP process. Figure 7.6 shows the measured corner point data of all triangular defects of the first three half-inch laminates projected onto one single reference defect geometry. An elliptical 95 % confidence interval was fitted to each point cloud. A 2.5 times larger standard deviation of 2-3 mm can be observed in the layup direction (u) as opposed to the width direction (v). This confirms the hypothesis that the layup accuracy in the layup direction is lower than in the width direction due to the effects described above. Furthermore, the median corner values indicate overall 5.6 % shorter and 4.4 % narrower triangular defects compared to the theoretically planned dimensions.

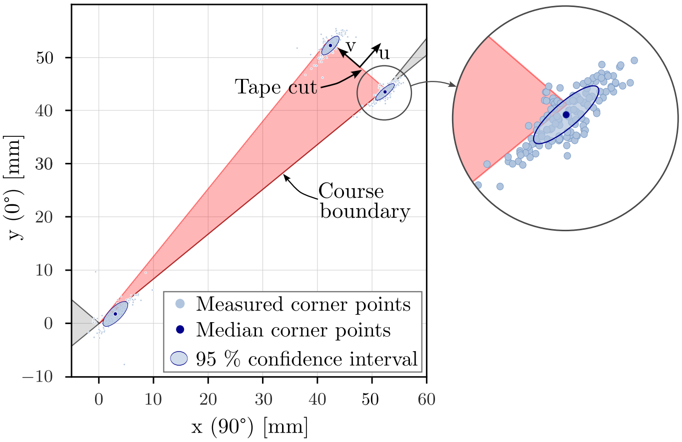

Figure 7.6: Measured corner points of half-inch triangular defects compared to the reference geometry

7.2.3 Ultrasonic Testing

The results of the ultrasonic scans of the in-situ consolidated laminates are shown in Figure 7.7. C-Scans with the gate adjusted to the backwall are presented for the left halves of the laminates, whereas internal echo images are shown for the right laminate halves, respectively.

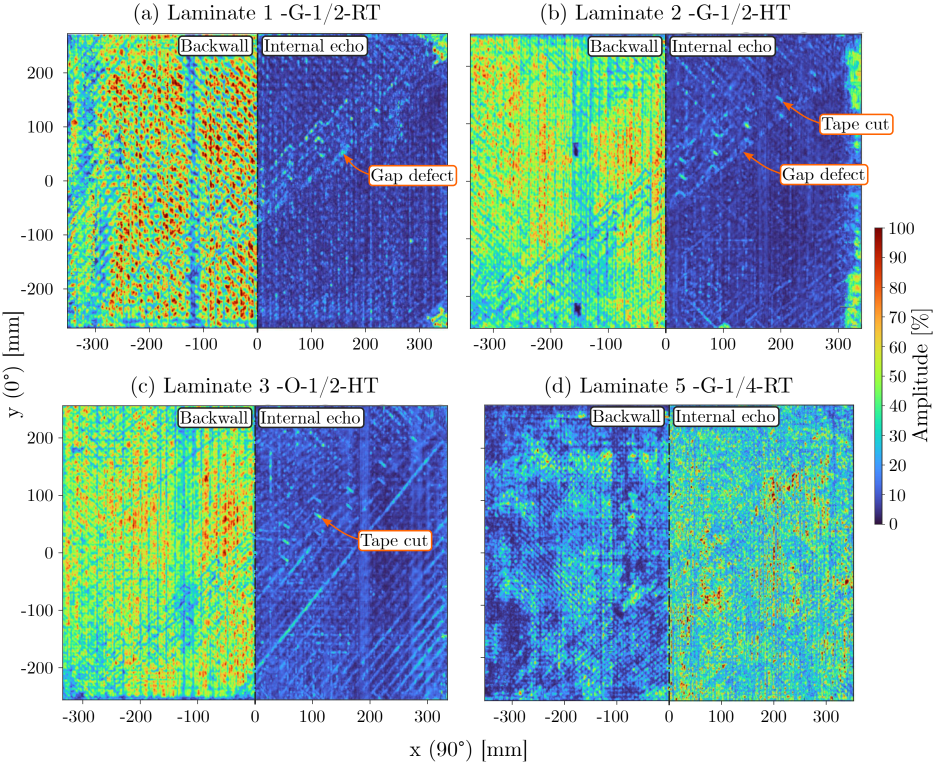

Figure 7.7: Ultrasonic C-Scan backwall and internal echo test results of in-situ consolidated defect laminates

The three half-inch laminates presented in Figure 7.7(a)-(c) have diagonally and orthogonally cross-shaped patterns, as typically found in in-situ AFP quasi-isotropic laminates as part of the in-situ AFP process signature [106]. These crossing lines of low amplitude back wall signal are caused by small pores at the lateral edges of the tracks. Vertical stripes of low amplitude signal can be observed at the position of the polyimide adhesive tape, which was used to join the wide prepreg tape on the tool-facing side for the first ply. The adhesive residue likely influences the ultrasonic back wall signal. The four rows of triangular defects that run along the first main diagonal of the laminates can be surmised as areas with lower overall back wall amplitude but do not show a very clear signature in the scan. The internal echo analysis shows a clear reflection of the edges of the triangular defects. In the case of the HT laminates 2 and 3, the short sides of the triangular defects resulting from porosity at the tape cut position are mainly visible for both gaps and overlaps from the internal echo analysis. While for both gap defect laminates (Figure 7.7(a) and (b)) the triangular gap areas can be recognized in the internal echo images, only the short edge of the defects is visible in the overlap internal echo image (Figure 7.7(c)), indicating lower overall porosity introduced by overlap defects. The in-situ consolidated quarter-inch laminate (Figure 7.7(d)) shows a consistently low back wall signal over the entire surface. Half the tape width leads to a doubling of the tape boundaries and thus to a larger number of potential pore sources and a closer diagonal and orthogonal pore pattern. However, hardly any areas with significant backwall echo can be recognized. The internal echo analysis showed distributed small areas of strong signal, unrelated to the triangular gaps, which indicates poor consolidation overall.

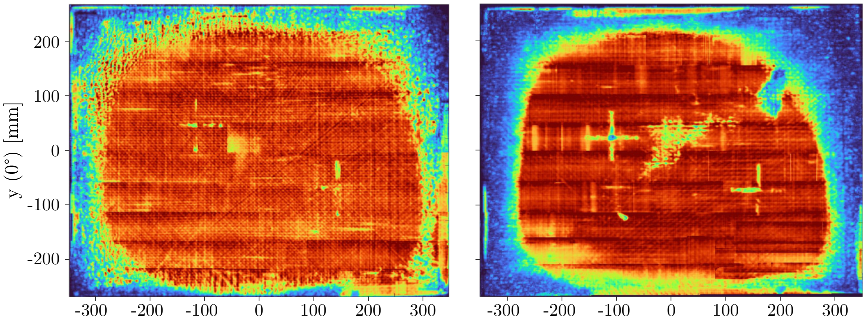
(a) Laminate 4 - G-1/2-HP

(b) Laminate 6 -G-1/4-HP

(c) Hot pressed section from Laminate 7 - G-1/2-HP

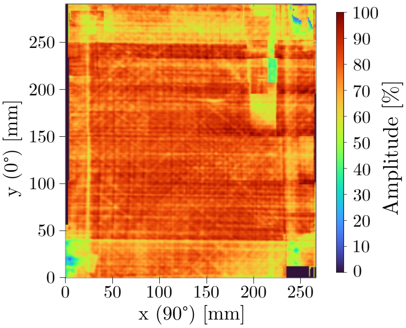

Figure 7.8: Ultrasonic C-Scan backwall test result of hot pressed laminates

The hot pressed laminates (Figure 7.8) achieved very high amplitude signal in the center of the laminates. The light pattern shows the 39 ° and 51 ° tracks of the defect plies. However, the edge areas of laminate 4 and laminate 6 (Figure 7.8(a) and (b)) show poor signal. This is probably due to too low press consolidation pressure in the edge areas, due to decreasing laminate thickness in those sections. No specimens were extracted from these regions. Furtherore, two crosses can be observed in each of the two laminates, which were created by polyimide adhesive tape used as a position reference. The quarter-inch hot pressed laminate (Figure7.8(b)) shows an area of decreased back wall signal in the center of the laminate. However, no internal echo was observed in this area.

In order to investigate the problems with consolidation in the edge area of the hot pressed laminates, an additional 300 mm by 300 mm panel from laminate 7 was hot pressed and analyzed using ultrasonic scanning (Figure 7.8(c)). The laminate showed a much more consistent high amplitude backwall echo over the entire surface. The consistent laminate thickness allowed for a more even pressure distribution and resulting consolidation as opposed to the full laminates 4 and 6 which included the AFP edge region with lower laminate thickness.

7.2.4 Microsectioning

The micrograph specimens inherently represent random samples of the laminate composition. Although a large number of samples was analyzed, they only cover a small part of the laminate area. Figure 7.9 presents selected micrographs of half-inch gap and overlap defects. For reference, the relevant plies are shaded in color. Schematic reference images with the sectional view in relation to the defect are shown for orientation. The RT specimens presented in Figure 7.9(a) show a composition that is characteristic of the in-situ AFP process. The gap defects in ply 8 result in a very smooth transition over the tow drop areas, which is likely due to the equal ply angle of the subsequent ply 9. This is in accordance with the work by Peeters et al. [263], that found no porosity defects if the subsequent ply was oriented parallel to the ply which contained the ply drop. Gaps in ply 4 with subsequent 0 ° ply, however, result in characteristic triangular pores following the tow drop. Gap defects in ply 13 with the subsequent 90 ° ply result in either smooth transition zones or triangular pores. Within the available samples, no correlation between the layup orientation (ascending or descending roller) as reported in [263] could be found. The samples either had smooth transition zones or triangular pores on both sides of the gap defects, respectively. At all gap defect edges, the discontinued plies are compacted more strongly towards the gap defect. This appears to be the case for both, ascending and descending roller side of the defects.

The HT specimens (Figure 7.9(b)-(c)) show slightly higher intralaminar and interlaminar porosity than the RT specimens. This is partly due to the tape width not being optimally adjusted, as can be seen from the pronounced pores in Figure 7.9(b) plies 2 and 15, in the center of the micrograph, resulting from longitudinal gaps between the tapes. Ply 8 also shows such a gap, however the subsequent ply 9 with the same orientation results in perfect compensation of the defect. The porosity at the edges of the defects is analogous to the RT samples. If the orientation of the subsequent ply is the same, a perfect transition is created in the defect area.

(a) G-1/2-RT

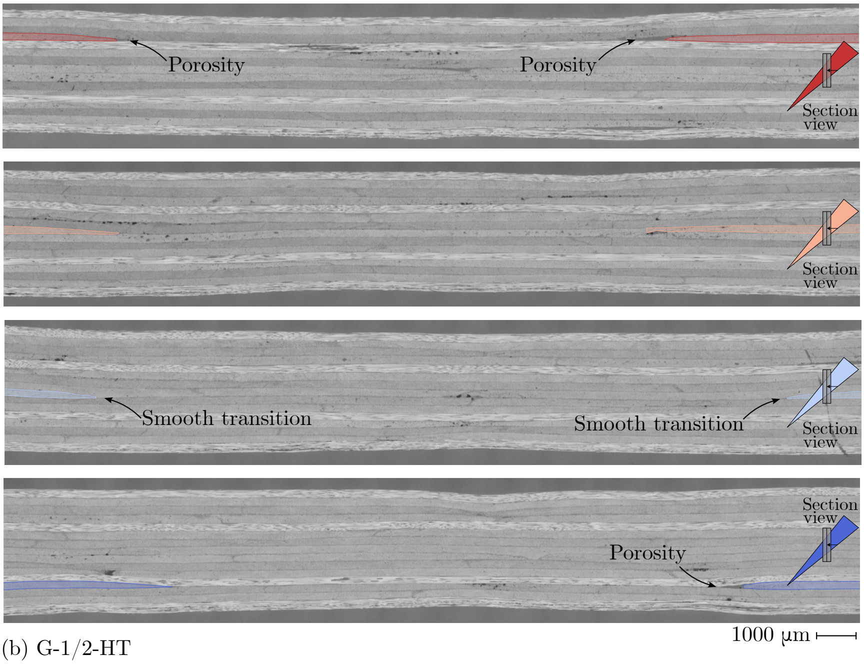

(b) G-1/2-HT

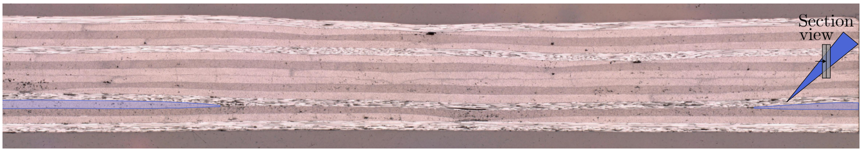

(c) O-1/2-HT

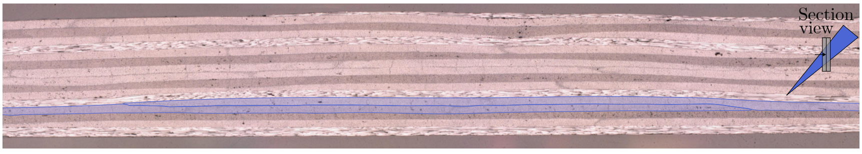

(d) G-1/2-HP

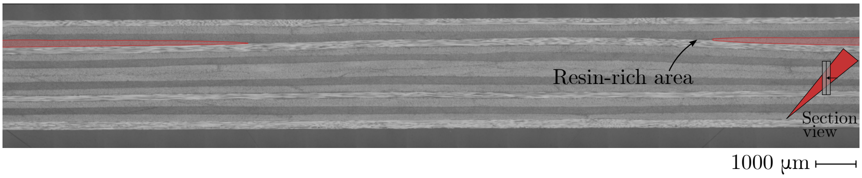

Figure 7.9: Half-inch gap and overlap defect microsection results

If the orientation is different, triangular pores are formed at the discontinued plies in some cases. Overall, however, the pores are less pronounced at the discontinued plies than at longitudinal gaps between individual tapes.

(a) G-1/4-RT

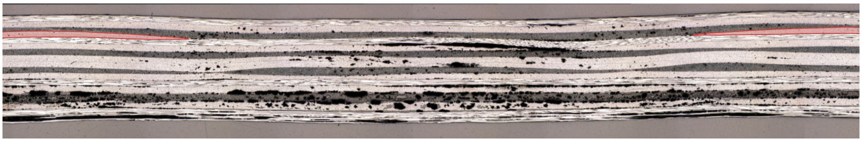

(b) G-1/4-HP

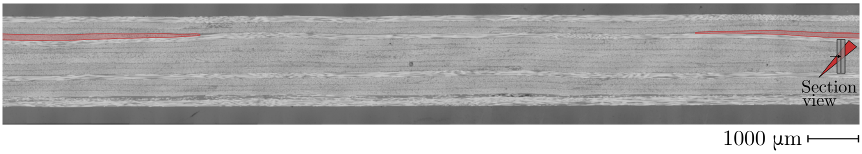

Figure 7.10: Quarter-inch gap defect microsection results

In contrast to gap defects, no pores were detected for overlaps at the edges of the overlapping layers in the examined micrograph samples (Figure 7.9(c). Even subsequent 0 ° plies, which are critical for gap defects, did not result in pores for overlaps. As expected, overlaps result in a slight local thickness increase with a measured median value of 7.2 %, whereas gaps lead to a local thickness decrease with a median value of -8.4 %. All HT specimens show characteristic vertical microcracks passing through single layers.

Figure 7.9(d) shows a representative reference specimen with gap defects from the well-consolidated center area of the hot pressed laminate. The micrograph shows perfect consolidation without any visually detectable porosity. As reported in the literature, small triangular resin rich areas can be observed at the edges of the discontinued plies. Both the top and the bottom surface of the laminate are perfectly even and the unevenness caused by the defects have been moved to the center of the laminate as slight undulations.

Figure 7.10 shows quarter-inch gap microsection results. The in-situ consolidated laminate (Figure 7.10(a)) shows significant interlaminar and intralaminar porosity and large delaminated areas, which indicate flawed process parameters or material-related problems. The hot pressed reference specimens again show no visible porosity, triangular resin rich areas at the gap defect edges and even top and bottom surfaces with undulations moved towards the center of the laminate.

7.2.5 Computed Tomography

Computed tomography scans were taken in order to obtain a three-dimensional visualization of the defects to supplement the two-dimensional spot test micrograph samples. The first CT specimen, extracted from laminate 7 contained three half-inch gap defects (G-1/2-RT) as presented in Figure 7.11(a). Figure 7.11(b) and (c) show extracts of the CT image stacks in the xz scan plane of ply 4 and 8, respectively.

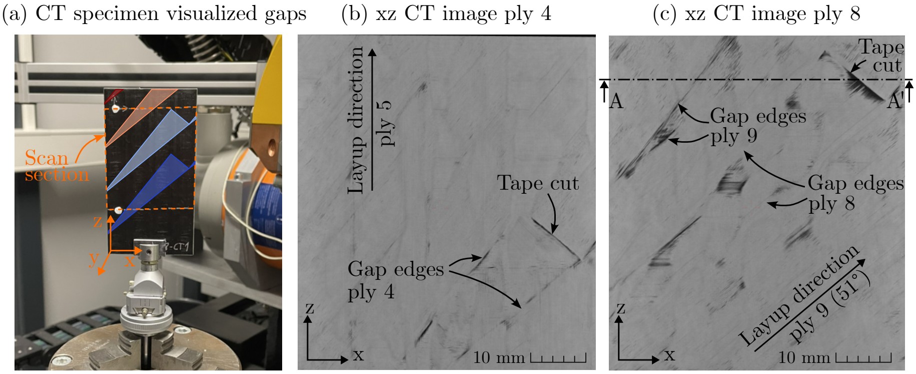
(a) CT specimen visualized gaps (b) xz CT image ply 4 (c) xz CT image ply 8

(d) xy CT image (A-A')

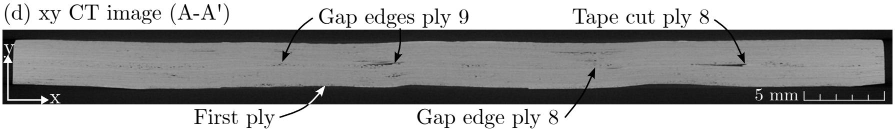

Figure 7.11: Computed Tomography RT half-inch gap defect images

The contours of the gap defect in ply 4 can be recognized as slight pore areas. Ply 3 previously deposited in a 90° direction and the subsequent 0° ply 5 can be surmised in the gap area as a 90° crossply pattern, indicating good contact in the majority of the defect area. The gap defect in ply 8 (Figure 7.11(c)) represents a special case, as the symmetrical layer structure results in the subsequent ply 9 being deposited in the same orientation. The lower edge of the gap in ply 8 thus runs in the same orientation (51°) as the following ply 9, while the upper edge of the gap is at a 12° angle to ply 9. This explains the perfect merging of the lower edge of the gap, whereas porous areas can be observed at the upper edge and the end face with the tape cut, where the plies meet at a 12° or 90° angle, respectively. Figure 7.11(d) shows a CT image in the xy plane, the position of which corresponds to the sectional view A-A' in Figure 7.11(c). The two sliced gap defects in plies 8 and 9 are clearly recognizable due to the discontinued plies and the accompanying pores. Interestingly, the gap defects have a more pronounced effect on the waviness of the underside of the laminate than on the top side. While other areas of accumulated smaller pores can be observed in the laminate, the most significant porosity is observed in the triangular voids at the tape cut in ply 8 and right-hand gap edge in ply 9.

Figure 7.12 shows a summarized analysis of the remaining CT scans, which were obtained from pre-test tensile specimens. The porosities in the area of the respective defect areas were merged and highlighted in color in the visualizations. The color coding corresponds to the colors of the laminate design (Figure 7.1). For the half-inch gap defect specimens (Figure 7.12(a)-(b)) porosity is primarily observed at the edges of the defects. The largest pore clusters tend to be on the tape cut side and the narrow sides (n-specimens) of the triangles.

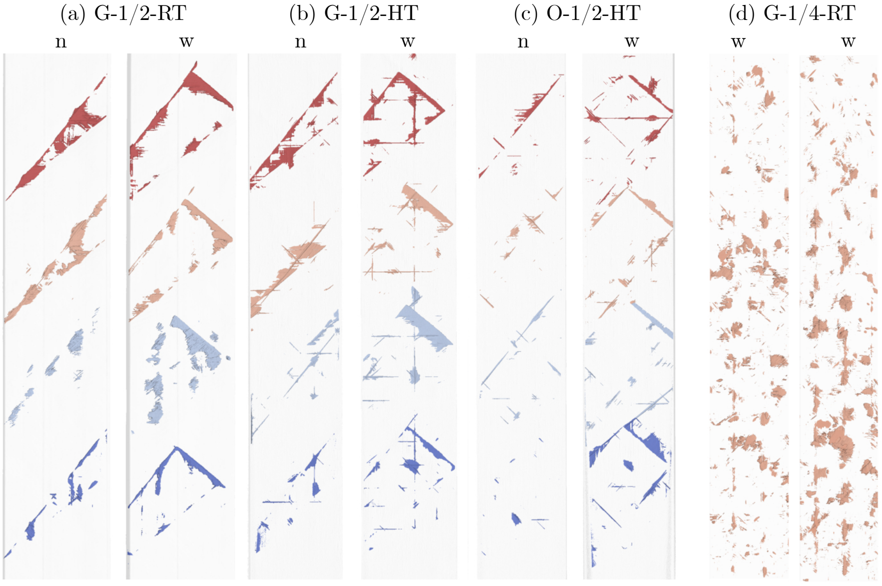

Figure 7.12: Compiled computed tomography results of tensile specimens before testing

As observed in the CT section view analysis (Figure 7.11), the lower edges of the gap defects in ply 8 (light blue coloring) show close to no detectable porosity, as the subsequent ply runs in the same orientation and merges well with the defect edge. No significant difference in gap-defect-induced porosity can be observed between the RT and HT configurations. Both HT specimen configurations (Figure 7.12(b)-(c)), however, show a slight additional cross-ply pattern, indicating slightly less optimally adjusted consolidated tape width in these laminates, compared to the RT laminate, as similarly observed in the microsection results. While the pores are inside the triangular defect contours in the gap defect specimens, they are primarily outside the defect contour in the overlap specimens (Figure 7.12(c)). Significantly less overall defect-induced porosity was observed in the overlap specimens, compared to the gap defect specimens, which is consistent with the micrograph examinations. This is particularly noticeable on the narrow side of the defects, where bridging effects result in clear pore areas in the gap specimens, whereas almost no porosity can be observed on the narrow side of the overlap samples. The quarter-inch specimens (Figure 7.12(e)) have such a high general proportion of pores, that no correlation between gap defects and porosity could be observed.

7.2.6 Tensile Testing

87 out of 102 tensile specimens yielded valid test results. 15 specimens were rejected due to invalid failure modes at the interface between specimens and end tabs or incorrect data

recording of the DIC system. Despite plasma activation of the specimen and end tab surfaces prior to adhesive joining and careful specimen preparation the most frequent cause of faults was detachment of the end tabs. The 150 mm free length of the specimens led to a large image section of the DIC cameras, resulting in a resolution that was too low for evaluating the strain fields. However, the visual analysis of the DIC image data allowed conclusions to be drawn about the failure modes of the individual parameter set groups. The stress-strain curves derived from virtual DIC strain gauges and failure modes of the reference specimens without defects are presented in Figure 7.13 as a baseline for the subsequent defect specimen analysis. The failure modes and locations as observed from the side view DIC recordings are shown schematically on the free length of a tensile specimen in Figure 7.13(c). Due to the length of the samples, multiple fracture positions were often observed during the tensile tests, in which cases the most severe position, or the position which showed the most severe pre-fracture damage was selected as the effective failure position. For each parameter set, a representative set of pre- and post-fracture side view DIC images is presented.

The RT and HT in-situ consolidated specimens showed interlaminar damage in the form of matrix cracks and delamination prior to final failure, whereas the HP specimens showed no damage prior to final failure. More significant delaminations were observed in the RT specimens in comparison to the HT specimens, which showed only very slight delamination, often at the positions of changes in the laminate thickness. At failure, explosive delamination failure modes were observed in both RT and HT specimens. HP specimens, on the other hand, failed via angled cracks and final fiber breakage, with sublaminates remaining intact. All reference specimens showed very consistent failure modes within the respective parameter set group. In contrast to the half-inch specimens, the quarter-inch specimens showed a clear difference in tensile strength between in-situ and hot pressed configuration (Figure 7.13(d)). Even more pronounced pre-fracture delamination of the RT specimens was observed, which can be explained by the poor consolidation as indicated by the ultrasonic, microsectioning and computed tomography results. Quarter-inch hot pressed reference samples again showed no visible cracks prior to final failure. The failure locations were distributed over the entire free length for the RT specimens and more pooled towards both sides of the free length for HT and HP specimens.

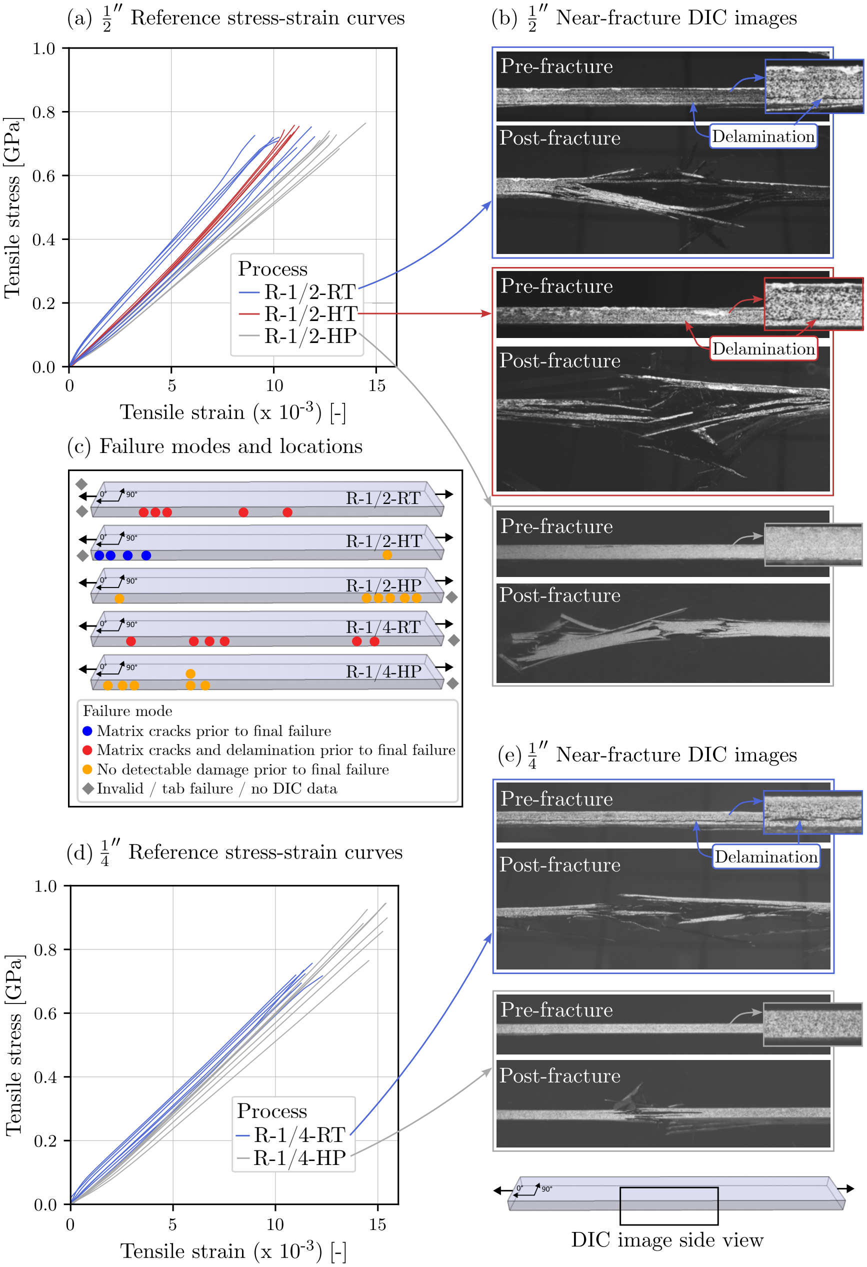

(a) $\frac{1}{2}''$ Reference stress-strain curves

(b) $\frac{1}{2}''$ Near-fracture DIC images

(c) Failure modes and locations

(d) $\frac{1}{4}''$ Reference stress-strain curves

(e) $\frac{1}{4}''$ Near-fracture DIC images

Figure 7.13: Reference specimen tensile test results

(a) Gap stress-strain curves (b) Failure modes and locations

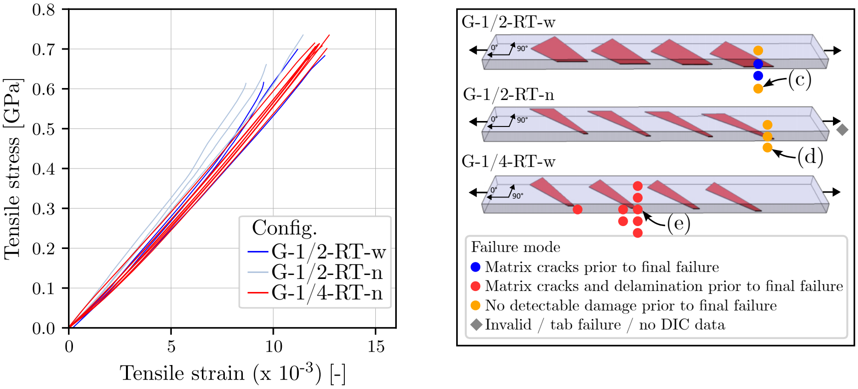

(c) G-1/2-RT-w near fracture DIC images (d) G-1/2-RT-n near-fracture DIC images

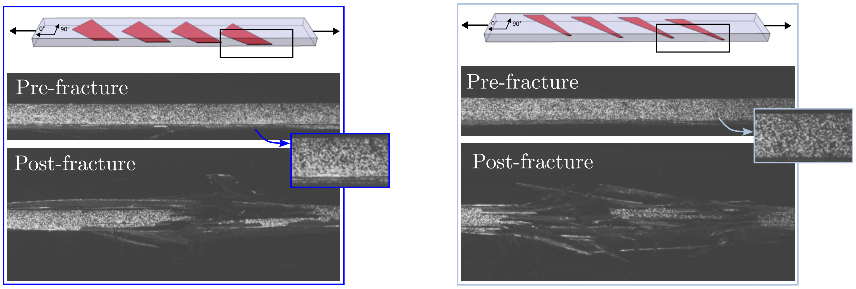

(e) G-1/4-RT-w near-fracture DIC images

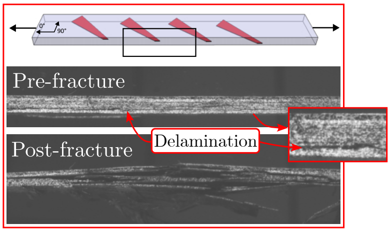

Figure 7.14: Room temperature gap specimen tensile test results

Figure 7.14 presents RT-configuration stress-strain curves and representative failure mode images of the three tested gap defect configurations. While the reference RT specimens all showed damage prior to final failure, this was not the case in the RT gap defect specimens. The evaluation of the failure modes and positions (Figure 7.14(b)) revealed that all specimens failed in the free length portion, in proximity to the defects. 50 % of the half-inch coupons which contained the wide portion of the triangular gaps (G-1/2-w) showed matrix cracks prior to final failure, while the other 50 % showed no pre-fracture defects. The specimens containing the narrow portion of the triangular gap defects (G-1/2-n) all failed without observable pre-fracture damage. However, half of the quarter-inch specimens showed matrix cracks and half had significant delamination prior to final failure, which again can be explained by the poorer consolidation quality achieved for the quarter-inch laminates. Representative example pre- and post-fracture DIC images are shown in Figure 7.14 (c)-(e).

(a) Gap/overlap stress-strain curves (b) Failure modes and locations

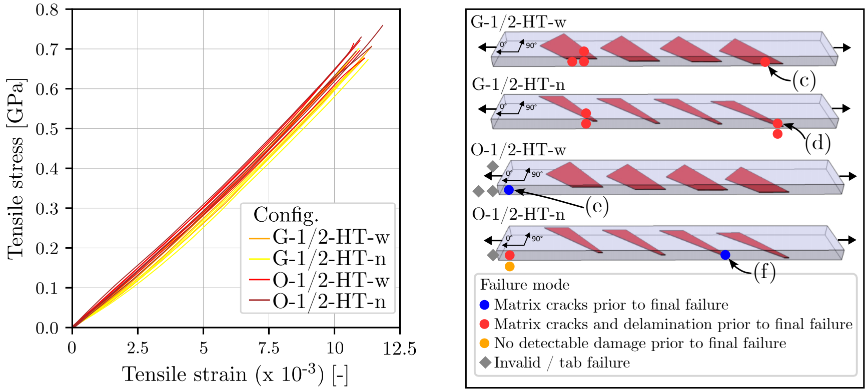

(c) G-1/2-HT-w near-fracture DIC images (d) G-1/2-HT-n near-fracutre DIC images

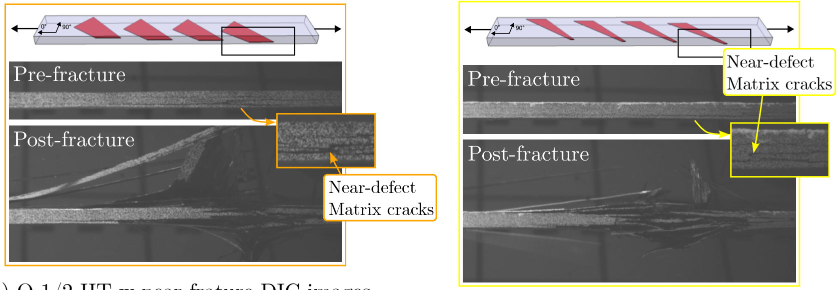

(e) O-1/2-HT-w near-frature DIC images (f) O-1/2-HT-n near-fracture DIC images

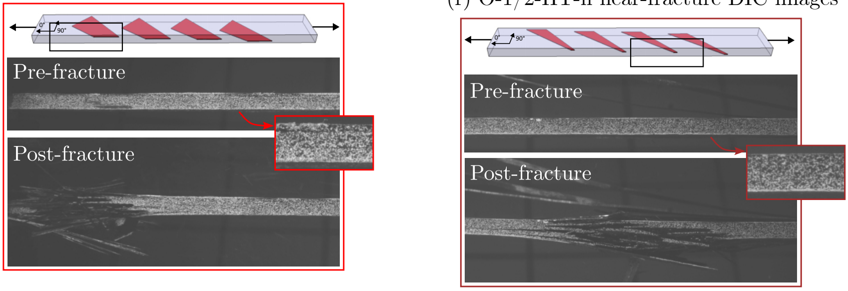

Figure 7.15: Heated tooling gap and overlap specimen tensile test results

Figure 7.15 presents HT-configuration stress-strain curves and representative failure mode images of the tested gap and overlap defect configurations. There is a clear difference in the failure modes between gap and overlap defect samples. While the gap defect specimens all failed in the free length area near the gap defects, the overlap specimens with one exception all failed outside the defect area (Figure 7.15(b)). Furthermore, all gap defect specimens showed pre-failure damage with larger cracks and delamination, while overlap specimens only showed smaller matrix cracks or no damage at all prior to final failure. Compared to the reference samples with continuous cracks and delaminations along the top and bottom ply boundaries, the matrix cracks were more localized and arose at the location of the gap defects (Figure 7.15(c)-(d)). For the overlap defects, no damage, or only slight horizontal cracks could be observed prior to final failure (Figure 7.15(e)-(f)).

(a) Gap stress-strain curves

(b) Failure modes and locations

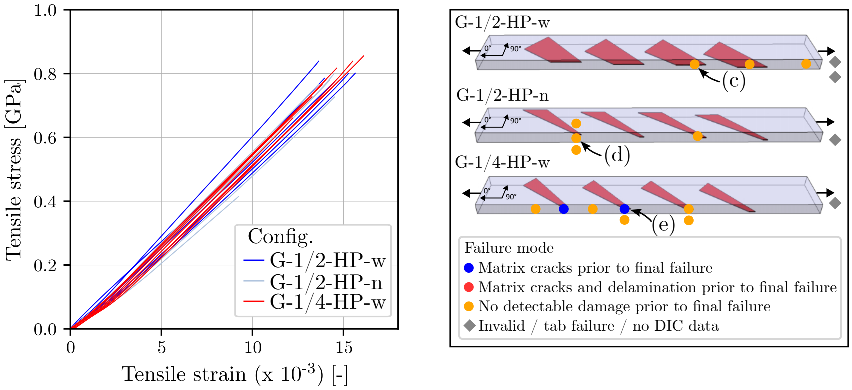

(c) G-1/2-HP-w near fracture DIC images

(d) G-1/2-HP-n near-fracture DIC images

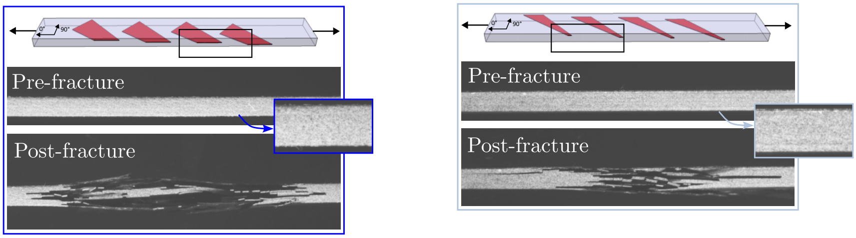

(e) G-1/4-HP-w near-fracture DIC images

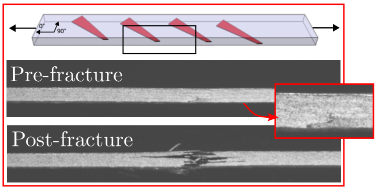

Figure 7.16: Hot pressed gap specimen tensile test results

Figure 7.16 presents HP-configuration stress-strain curves and representative failure mode images of the tested gap defect configurations. Half-inch gap defect specimens showed no damage prior to final fracture and the same failure mode as the reference samples without defects. In

25 % of the quarter-inch gap defect specimens, matrix cracks were observed prior to final failure. Compared to the HP reference specimens, failure positions were located more in the location of the gap defects.

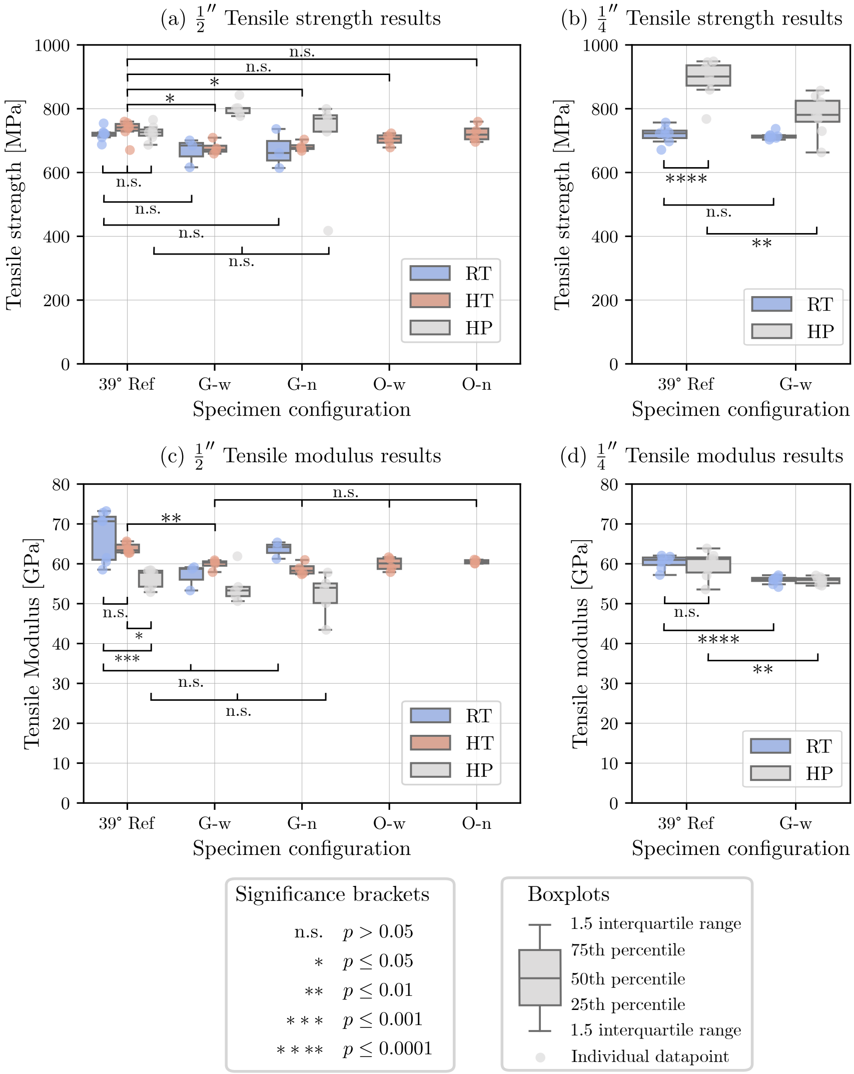

Figure 7.17: Tensile strength and modulus results of reference, gap and overlap defect specimens

The tensile strength and modulus results of all tested specimen configurations are presented in Figure 7.17. Initially, the reference RT, HT and HP results were compared with each other in order to quantify the influence of the different manufacturing processes. The defect specimens were then compared with the respective reference specimens within one of the three manufacturing processes. Normality and comparability of variances were validated for all compared parameter sets using the Shapiro-Wilk test and Levene's Variance test, respectively. The results of the statistical analysis following independent t-test or one way ANOVA and Tukey's range test for two or three and more parameter groups, respectively, are indicated in the respective figures using significance brackets.

Significantly different mean deviations were observed between reference specimen strength results from the 39 ° and 51° section of the laminates. The 39 ° reference specimens achieved higher strength results as the fibers were oriented more in the direction of the tensile stress. To this end the reference samples of the 39 ° section were used in all evaluations of the tensile tests as a conservative assumption.

Overall, the comparison of tensile strength results within the three processing condition groups RT, HT and HP revealed little impact of gap and overlap defects. No statistically significant difference was observed between the RT, HT and HP half-inch reference specimens (Figure 7.17(a)). Half-inch and quarter-inch RT specimens achieved the same median strength of 721 MPa, respectively. The quarter-inch HP reference specimens, however, reached a 24.6 % strength increase over the other reference specimens (Figure 7.17(b)). One possible explanation could be the lower overall laminate thickness due to the lower tape thickness of the quarter-inch tape, leading to better hot pressing consolidation results. No statistically significant effect was found comparing RT gap defect specimens with reference results for both tape widths. In the subset of half-inch HT specimens, overlap defects did not achieve a statistically significant change in relation to the reference specimens. Gap defect specimens, however, led to a slight statistically significant tensile strength decrease of 9.4 % and 8.6 % for the wide and narrow gap defects, respectively. The hot pressed half-inch and quarter-inch specimens achieved tensile strength results at the same level as the half-inch reference.

The tensile modulus results also showed only a minor influence of the gap and overlap defects. No statistically significant difference was found between the half-inch RT and HT reference samples (Figure 7.17(c)). However, a 18.3 % modulus decrease was observed between the RT and HP half-inch reference specimens, while no statistically significant difference was found in the quarter-inch specimens of the same RT and HP groups. This result again implies a better consolidation of the hot-pressed quarter-inch laminate compared to the half-inch laminate. Due to the large variance in the RT and HP results, no statistically significant difference could be determined between the respective reference and gap defect specimen groups. The HT half-inch configuration, however, due to smaller variance showed a 5-8 % modulus decrease of all defect specimen groups, compared to the HT reference. No statistically significant difference was found between the different HT defect configurations, though. Similarly, for both RT and HP quarter-inch tensile modulus configurations, a 8 % modulus decrease was observed between reference and gap defect specimens, respectively.

7.2.7 Compression Testing

The combined loading force application principle in the compressive tests avoided the end tab detachment issue of the tensile tests. The compressive specimens' smaller free length of 22 mm enabled a higher effective resolution of the speckle patterns and a detailed evaluation of the strains fields with the DIC system was thus possible. The stress-strain curves and failure modes of the half-inch reference specimens without defects are presented in Figure 7.18 as a baseline for the subsequent defect specimen analysis. The average strain was calculated from virtual DIC strain gauge measurements on the front and physical strain gauge measurements on the back of the specimen free length. Premature detachment of strain gauges, delamination and buckling of top and bottom layers led to diverging strain curves, particularly towards the final failure of the specimens (Figure 7.18(a)).

As expected, a larger impact of the manufacturing process on ultimate compressive strength was observed, than on ultimate tensile strength values. HP reference specimens achieve the highest compressive strength results, followed by HT and RT reference values. The 10 % bending strain limit of the compressive test standard to validate the compressive failure mode (no Euler Buckling) was exceeded by the majority of the tested specimens (Figure 7.18(c)). This was expected because the ply stacking sequence with 39 ° instead of 45 ° plies deviates from an ideal quasi-isotropic structure as it does not have a balanced and symmetrical structure. An anti buckling device was omitted in order to be able to analyze the failure modes by means of DIC and to be able to evaluate the influence of the defects. Furthermore, the ASTM-D6641 test standard states that larger bending of 30 % to 40 % may have no significant impact on compressive strength results [312]. As it was not the objective to calculate the compressive strength, but to determine the influence of gap and overlap defects on compressive properties of realistic laminates these results are still considered within this work. Furthermore, similar bending influence magnitudes were observed between the tested parameter sets and allowed to compare the results in this study. However, the compressive test results do not represent compressive strength and modulus values in the sense of the test standard and cannot be used outside the context of this work.

(a) $\frac{1}{2}''$ Reference stress-strain curves

(b) Failure modes and locations

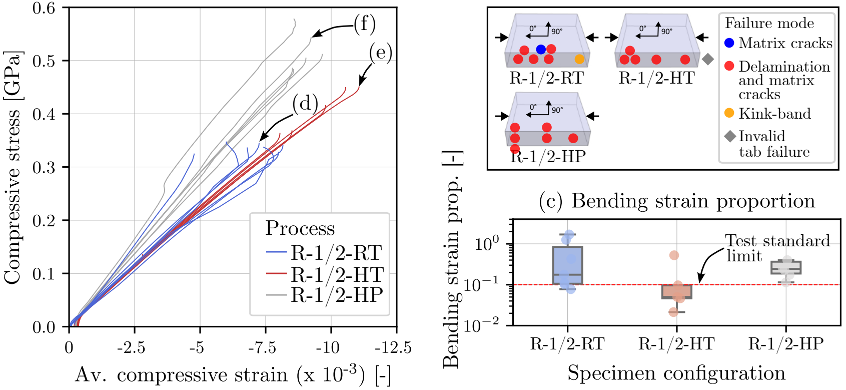

(c) Bending strain proportion

(d) R-1/2-RT near-fracture DIC images

(e) R-1/2-HT near-fracture DIC images

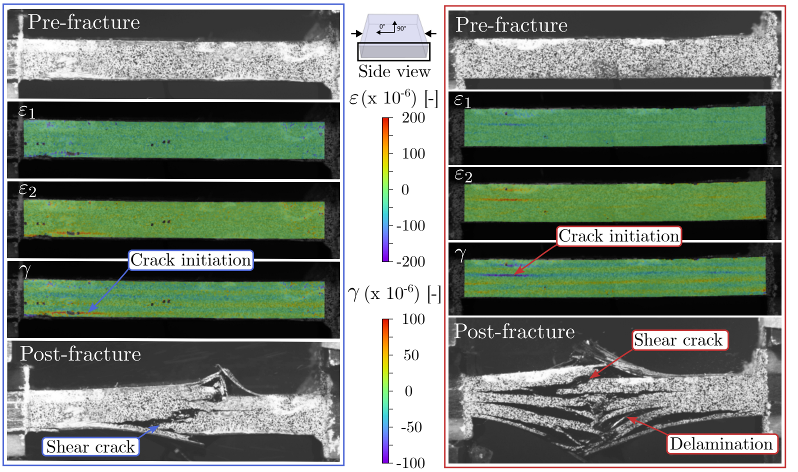

(f) R-1/2-HP near-fracture DIC images

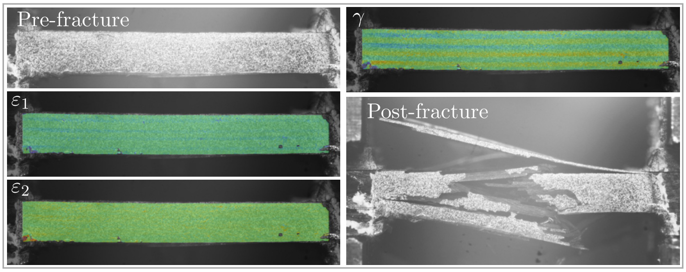

Figure 7.18: Reference half-inch specimen compressive test results

The failure modes and locations as observed from the side view DIC recordings are shown schematically on the free length of a compressive specimen in Figure 7.18(b). Both failure modes and locations were often ambiguous and multiple locations and a combination of failure modes were observed. In such cases, the prevalent failure mode and the location of pre-fracture damage or most severe damage were chosen as mode and location, respectively. As indicated by the schematic failure mode representation, delamination and buckling of the sublaminates was the prevalent failure mode in all reference specimens. In the RT specimen group, one specimen failed in a kink-band failure mode and one specimen failed with the failure mode through-thickness matrix shear cracking. A combination of through-thickness matrix shear cracking and subsequent delamination as presented in the example plot in Figure 7.18(d) was also frequently observed and labeled as delamination failure. The HT specimens similarly often showed combinations of through-thickness shear cracking and delamination as presented in Figure 7.18(e). The strain-field analysis of the in-situ consolidated specimens shows local areas of increased principal strain 2 (ε_2) and shear strain (γ) in the pre-fracture DIC images (Figure 7.18(d-e)). These are likely weak areas in the interlaminar consolidation of the laminates, initiating shear cracking which promotes accelerated failure of the specimens. In contrast, the HP specimens did not show any pronounced local peaks in the strain fields of the pre-fracture DIC data (Figure 7.18(f)).

The quarter-inch reference specimens showed very similar results as the half-inch reference specimens (Figure 7.19). The consolidation difficulties of the RT specimens, however, resulted in more severe premature delamination and lower overall compressive strength results. Delamination and subsequent buckling of the sublaminates again was the prevalent failure mode of both, RT and HP specimens and the bending strain exceeded the 10 % limit of the test standard (Figure 7.19(b-c)). Whereas in the half-inch samples the strain fields had to be used to detect damage initiation, this can already be seen in the form of clear longitudinal cracks in the pre-fracture image data of the quarter-inch samples (Figure 7.19(d)). The DIC measurements of the HP quarter-inch specimens were slightly disturbed by adhesive contamination of the speckle pattern from the strain gauge application, but did not show any local strain maxima, as observed in the RT specimens (Figure 7.19(e)).

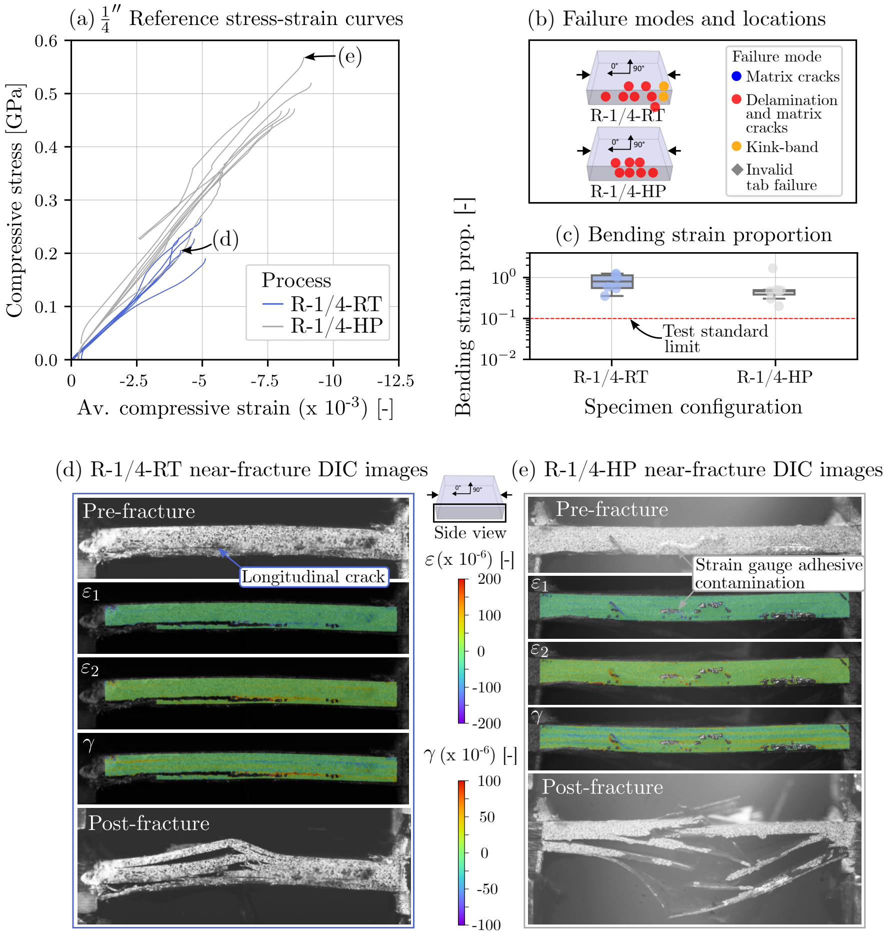

Figure 7.19: Reference quarter-inch specimen compressive test results

The stress-strain curves and failure modes of the RT gap defect specimens are presented in Figure 7.20. The conspicuous curve of the G-1/2-w specimen group is probably due to a detachment of the strain gauge or slight buckling of the upper layer to which the strain gauge was attached (Figure 7.20(a)). Lower ultimate strength values were again achieved for the quarter-inch specimens. While through-thickness matrix shear cracking was the prevalent failure mode of the half-inch gap defect specimens, more severe delamination was observed in all quarter-inch gap defect specimens. All specimens again exceeded the test standard bending strain limit (Figure 7.20(b-c)). A combination of through-thickness shear cracking and local kink band failure was observed in the example G-1/2-w specimen DIC analysis in Figure 7.20(d). For this specimen, no shear crack initiation can be recognized in the pre-fracture strain plots.

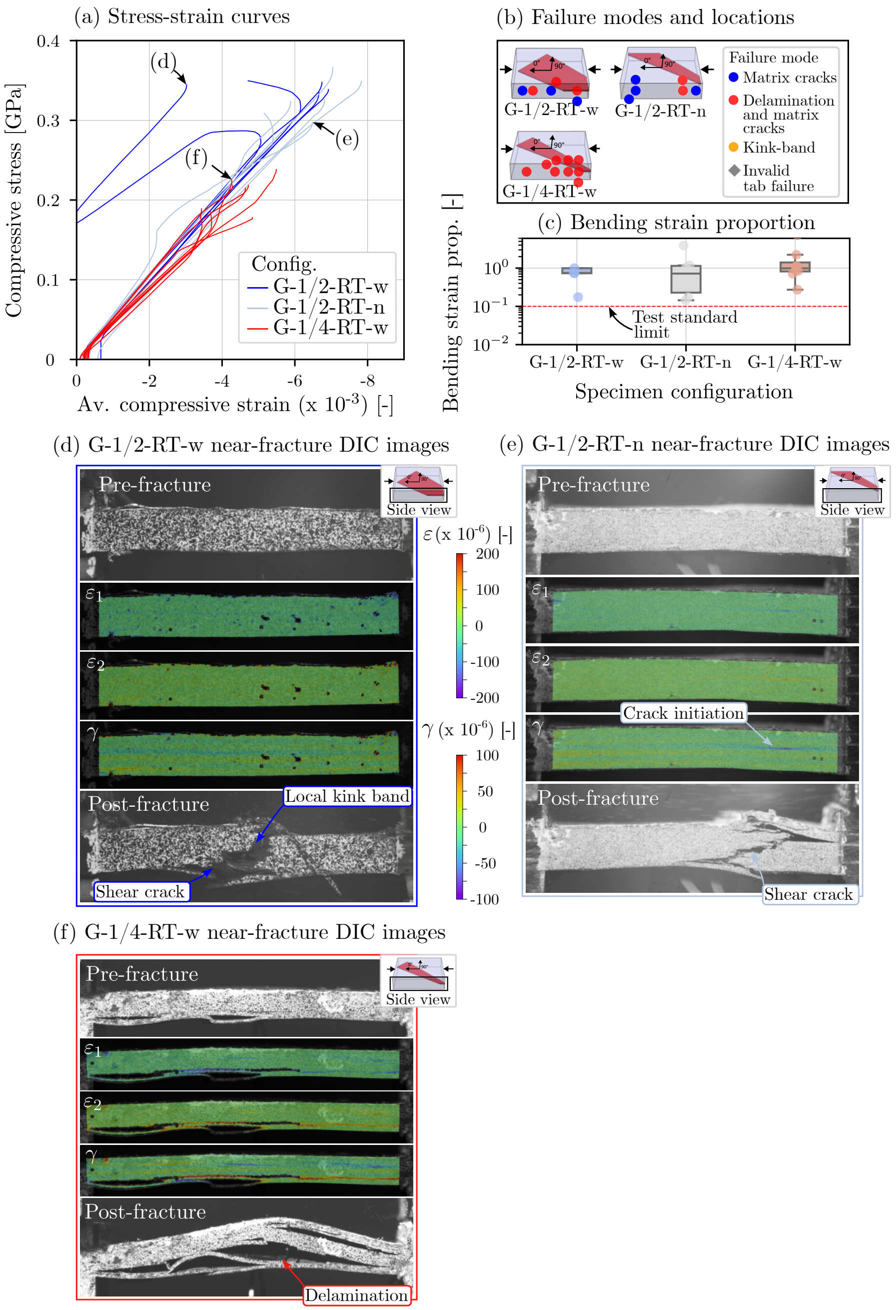

Figure 7.20: Room temperature gap specimen compressive test results

(a) Gap/overlap stress-strain curves

(b) Failure modes and locations

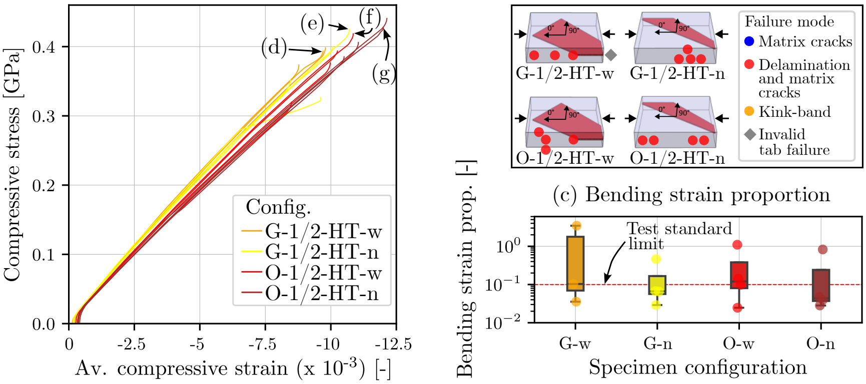

(c) Bending strain proportion

(d) G-1/2-HT-w near-fracture DIC images

(e) G-1/2-HT-n near-fracture DIC images

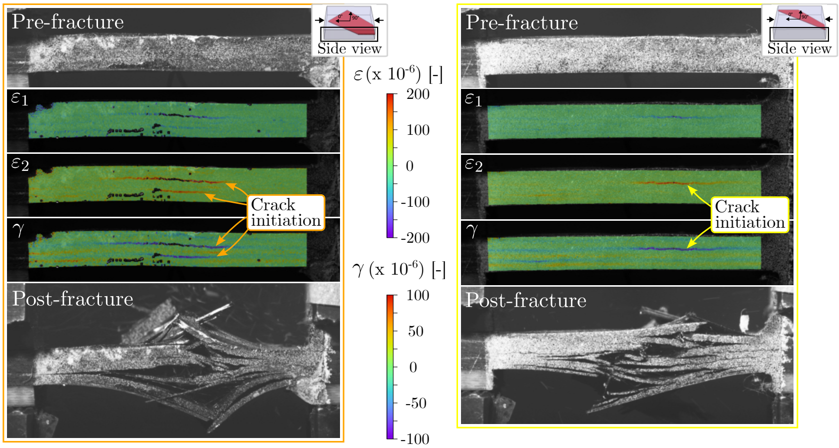

(f) O-1/2-HT-w near-fracture DIC images

(g) O-1/2-HT-n near-fracture DIC images

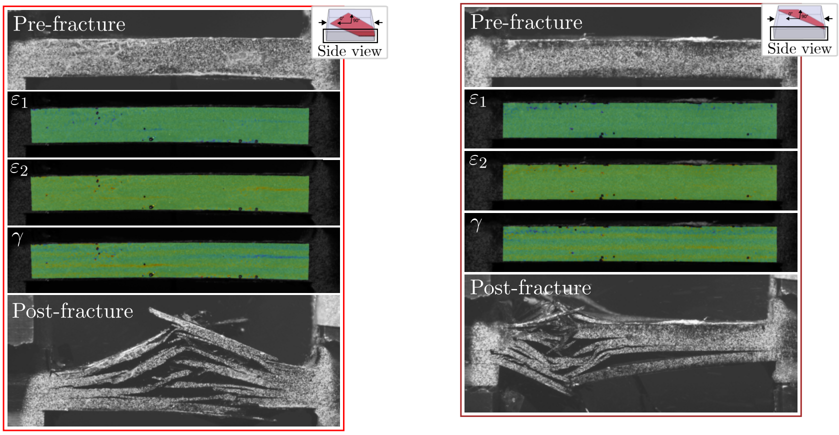

Figure 7.21: Heated tooling gap and overlap specimen compressive test results

In contrast, the G-1/2-n example specimen in Figure 7.20(e) shows local shear strain peak at the location of the subsequent through-thickness shear crack failure of the specimen. In this case, the strain peak is in the area of the gap defects in ply 9 of the laminate and could be related to the defect. However, a local connection could not be identified for all samples. The quarter-inch specimens all showed significant delamination and buckling of detached layers resulting in premature failure of the specimens (Figure 7.20(f)). The influence of the gap defects is probably masked by the generally poor consolidation.

The HT process configuration was used to compare the influence of gap and overlap defects on the mechanical properties. The compressive stress-strain curves and failure modes of this comparison are presented in Figure 7.21. Delamination was detected consistently as the failure mode for all HT gap and overlap defect specimens (Figure 7.21(b)). While the failure modes were similar, the pre-fracture strain field analysis showed significantly more pronounced local shear and principal strain peaks in the gap specimens (Figure 7.21(d-e)), compared to the more uniform strain distributions of the overlap specimens (Figure 7.21(f-g)). In some specimens, such as the ones presented in Figure 7.21(d) and (e), a local connection with the gap defects in ply 9 can again be determined. However, this could not be reliably proven for all specimens. No significant difference between the narrow and wide defect portions was identified.

Finally, the HP stress-strain curves and failure modes are presented in Figure 7.22. The two stress-strain curves, which exceed the other curves by around 100 MPa, both originated from the additional pressed 300 mm x 300 mm laminate 7, which supports the thesis of the more uniform consolidation of this panel (Figure 7.22(a)). Like the reference samples, all hot-pressed samples with gap defects also failed in the delamination failure mode (Figure 7.22(b)). Most specimens showed uniform principal and shear strain fields, as in the example plots in Figure 7.22(d) and (f). Areas of slightly increased local shear strain are observed in some specimens (Figure 7.22(e)) but are overall significantly less pronounced than in the in-situ consolidated specimens.

The comparison of quasi-isotropic, 39 ° and 51 ° reference specimens yielded statistically significant differences only in HP 39 ° and 51 ° results. This difference could be either due to hot pressing creating better consolidation and thus making ply stacking sequence more relevant than in in-situ specimens or due to varying hot-press consolidation quality throughout the laminate. For both laminates, HP quarter-inch and half-inch, however, higher strength was observed for 39 ° specimens than for 51 ° specimens. To ensure consistency with the tensile test analysis, the 39 ° reference samples were also used to analyze the compressive results.

(a) Gap stress-strain curves

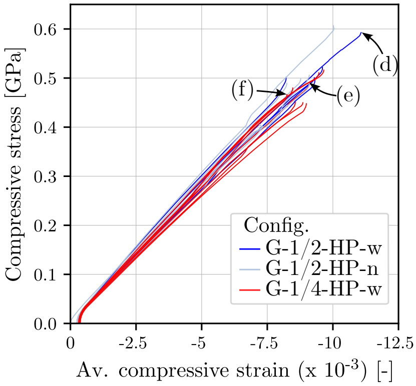

(b) Failure modes and locations

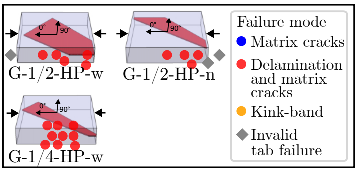

(c) Bending strain proportion

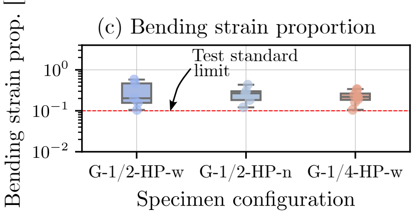

(d) G-1/2-HP-w near-fracture DIC images

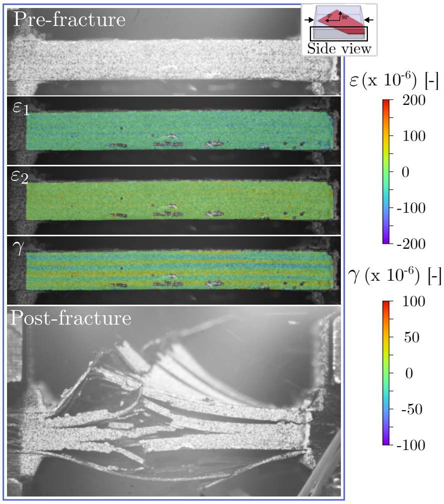

(e) G-1/2-HP-n near-fracture DIC images

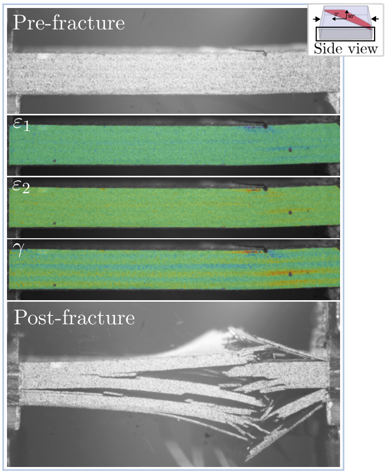

(f) G-1/4-HP-w near-fracture DIC images

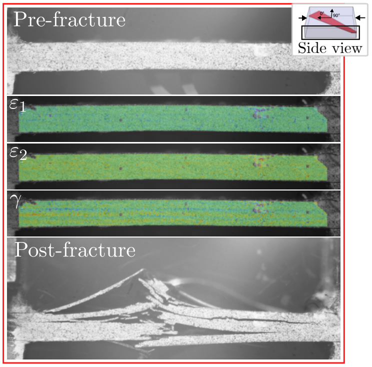

Figure 7.22: Hot pressed gap and overlap specimen compressive test results

The compressive strength and modulus results are presented in Figure 7.23. Initially, the reference RT, HT and HP results were compared with each other in order to quantify the influence of the different manufacturing processes. The defect specimens were then compared with the respective reference specimens within one of the three manufacturing processes. Normality and comparability of variances were validated for all compared parameter sets using the Shapiro-Wilk test and Levene's Variance test, respectively.

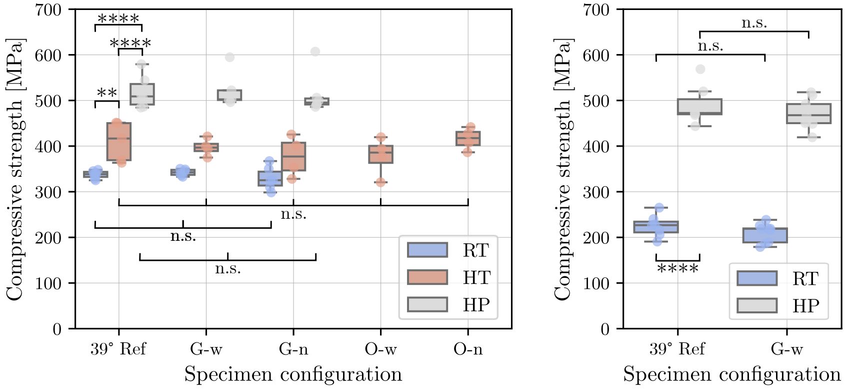

(a) $\frac{1}{2}''$ Compressive strength results

(b) $\frac{1}{4}''$ Compressive strength results

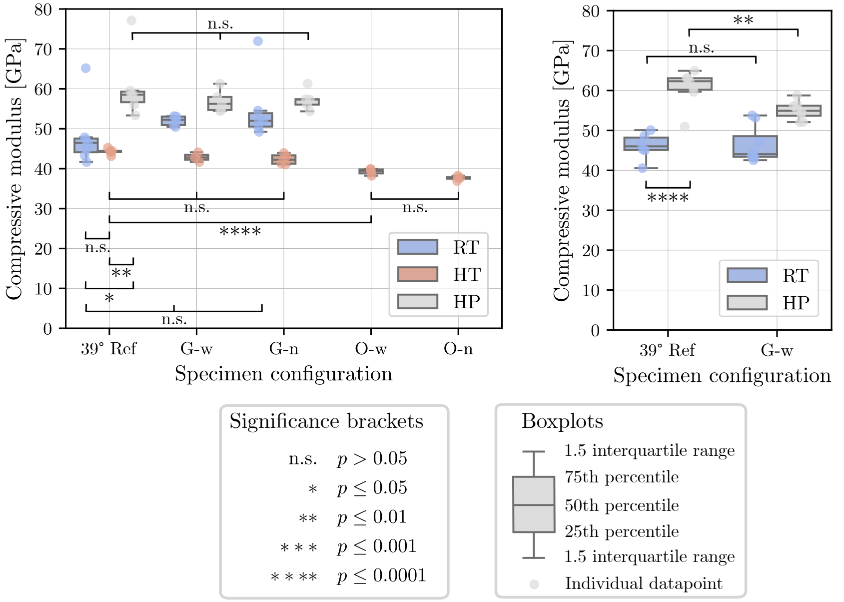

(c) $\frac{1}{2}''$ Compressive modulus results

(d) $\frac{1}{4}''$ Compressive modulus results

Figure 7.23: Compressive strength and modulus results of reference, gap and overlap defect specimens

The results of the statistical analysis following independent t-test or one way ANOVA and Tukey's range test for two or three and more parameter groups, respectively, are indicated in the respective figures using significance brackets.

Consistent with recent publications [106, 160], compressive properties were more sensitive to manufacturing conditions (RT, HT, HP) than tensile properties. In the group of the half-inch specimens, a significant difference of -18.1 % and -33.5 % compressive strength was found between the HT and RT samples and the HP reference, respectively (Figure 7.23(a)). An even larger 52 % compressive strength knockdown was observed in the quarter-inch RT specimens compared to the HP reference (Figure 7.23(b)). This can again be explained by the poorer in-situ consolidation outcome of the quarter-inch laminate, which has an even greater effect on the compressive properties and therefore exerts a stronger influence on strength results.

In comparison, the influence of the defects could be categorized as comparatively low. No statistically significant compressive strength difference could be determined for any of the tested configurations.

The compressive modulus results showed no statistically significant difference between the half-inch RT and HT and the quarter-inch RT reference specimens. A 24.3 % and 26.3 % knockdown can be observed between the HP reference specimen and the in-situ consolidated configurations for half-inch and quarter-inch modulus results, respectively. For the half-inch specimen group, no statistically significant effect of the gap defects could be found. The HT overlap specimen group showed a slight reduction in the compressive modulus of up to 15.8 % in relation to the reference samples. No statistically significant difference, however, was observed between the narrow and wide overlap defect specimens. The only other statistically significant impact of defects was observed in the quarter-inch HP gap defect specimens, which showed a 11.9 % decrease over the reference HP quarter-inch specimens. Overall, no clear influence of the defects on the compressive properties of the tested laminates can be recognized within the scope of the available test data.

An overview of the influences of all defect configurations on the respective tensile and compressive properties is presented in Table 7.2. For most configurations no statistically significant influence of the defects could be identified. Smaller effects, however, could have potentially remained undetected in the statistical evaluation due to partially large variances or low sample number. Configurations that achieved consistently low variance, yielded the most significant results, as observed for example in the HT tensile specimen group.

Table 7.2: Overview of the influence of defects on mechanical properties: statistically significant changes in the median values compared to the reference median of the respective sample configuration rounded to integer percentages

Configuration	Tensile strength	Tensile modulus	Comp. strength	Comp. modulus
G-1/2-RT-w	-	-	-	-
G-1/2-RT-n	-	-	-	-
G-1/4-RT-w	-	-8 %	-	-
G-1/2-HT-w	-9 %	-5 %	-	-
G-1/2-HT-n	-9 %	-8 %	-	-
O-1/2-HT-w	-	-5 %	-	-11 %*
O-1/2-HT-n	-	-5 %	-	-15 %*
G-1/2-HP-w	-	-	-	-
G-1/2-HP-n	-	-	-	-
G-1/4-HP-w	-13 %	-9 %	-	-12 %*

- no statistically significant effect

* non-standard test result: greater than 10 % bending strain

7.3 Conclusion

This present work shows that the transient track start and end sections, which are introduced into the center of the laminate by gap or overlap defects, lead to considerable process temperature fluctuations and geometrical tolerances in the defect sections of the resulting laminate. For in-situ consolidated laminates, the microanalysis additionally showed small triangular pores at the contour of the gap defect edges. In comparison, overlaps resulted in less severe porous areas, which were located outside the defect contour. Defect edges covered with a subsequent ply in the same orientation as the edge resulted in significantly lower or no detectable porosity.

Despite these aggravations of the laminate composition, tensile and compressive test results showed only very small, if any statistically significant impact of the defects on the investigated mechanical properties. Overlap specimens showed slight tensile strength advantages over gap defect specimens, however they achieved a slightly lower compressive modulus. The matrix dominated failure modes of the compressive tests showed a large impact of the manufacturing configuration with hot pressed specimens yielding the highest strength and modulus results, respectively. Heated tooling specimens achieved overall higher compressive strength but lower modulus results than the unheated tooling baseline specimens.

In comparison, the influence of the defects on the compressive properties was negligible. The realistically staggered defect design presented a subcritical disruption of the laminate composition and significant strength reductions likely require superimposed defect patterns. A detailed failure mode analysis showed co-location of gap defects and crack initiation positions in some of the in-situ consolidated compressive specimens, which, however, did not result in lower ultimate strength of those specimens. As consistently shown through all analysis results, the quarter-inch laminates exhibited excessive porosity and suboptimal consolidation, which resulted from a deviating process window. To this end, no definitive conclusion could be drawn as to whether narrower tape and the resulting smaller defects yielded better mechanical properties than larger half-inch defects. In an initial analysis no deviating consolidation pressure and process temperatures could be found. Further work should therefore carry out a comprehensive parameter study for the quarter-inch material to determine the optimum process window and in-situ AFP parameters for the material.

This work provides initial proof that geometry-related defects could be permitted in in-situ AFP laminates without having to accept significant reductions in the mechanical properties. Future work will elaborate on the results of this work, investigating larger specimens with more complex defect patterns.

Chapter 8

Conclusion and Implications

The aim of this work was to analyze the impact of geometry-induced defects of complex part geometries on in-situ AFP-manufactured laminates and to develop layup strategies that take these effects into account. This represents an important step in evaluating the suitability of the in-situ AFP process for complex structures and possible applications.

8.1 Summary of Results

Through a systematic derivation of geometry-induced defects, a triangular correlation between angle deviation, steering and coverage defects (gaps and overlaps) was demonstrated for all three investigated complex geometries: constant curvature Variable Stiffness Panel, spherical hydrogen tank and double-curved fuselage section. Theoretically optimized layup strategies with through-thickness defect staggering were developed and resulting coverage defect geometries and path curvatures were determined for the following investigations of these defects.

For constant geodesic curvature (steering) a novel concept of critical arc length was developed and validated expanding the design space of usable steering radii by introducing radius-dependent arc length limits. The interlaminar mechanical properties and critical process parameters were confirmed for subcritical arc lengths. An empirical model was developed to predict the steering-induced geometry changes of the consolidated tape. From the model, optimized layup paths were derived to minimize resulting gap defects between narrowing steered tows. While the results are very specific to the combination of end-effector, material and specific process parameters, the mechanisms can be derived in general and the methodology presented can be applied to the respective machine-material configuration.

The detailed analysis of realistic triangular gap and overlap defects showed porosity in the defect area for subsequent plies with different orientation than the ply containing the defect. Overall the realistically staggered defects, however, resulted in a subcritical disruption of the laminate composition and the resulting coupon-level mechanical properties showed little if any statistically significant impact of defects. Suboptimal consolidation results in the quarter-inch laminates did not allow a final conclusion to be drawn on the comparison of tape widths in the context of coverage defects.

8.2 Discussion

The combination of obtained results provides coherent implications for an optimized layup strategy. In the triangular optimization problem between angle deviation, in-plane curvature and coverage defects, an acceptable initial strategy would be to start with the boundary condition of the maximum allowable angular deviation of, for example, $\pm 3^\circ$ and to determine the tape width (quarter or half-inch) based on the resulting geodesic curvatures. The empirical steering model methodology developed in this work for the respective combination of machine, material and process parameters can be used for this purpose. Steering defects can be avoided by using uncritical steering radii or arc lengths below the critical arc length for the respective steering radius. The critical arc length criterion significantly expands the design space to steering radii which were previously considered too small for AFP manufacturing. Herein lies another advantage of thermoplastic AFP with in-situ consolidation, as the complete consolidation prevents delayed occurrence of out-of-plane wrinkles and larger in-plane curvatures can be achieved overall. Steering-induced narrowing needs to be considered so as to not contribute to the in-situ AFP process signature by introducing additional widespread longitudinal gap defects throughout the laminate. This can be achieved by steering-optimized layup trajectories, as presented in this work. The resulting triangular coverage defects should then be distributed using through-thickness staggering in order to avoid co-location of defects. Distributed through-thickness staggered coverage defects were shown to likely be uncritical and can be strategically implemented into the complex laminates to keep the angle deviation and geodesic path curvature within subcritical range. The presented work thus outlines an extended design space for layup strategies of complex part geometries, thereby exploiting the full potential of in-situ AFP for complex geometries.

The application of the in-situ AFP process for the production of large thermoplastic composite structures and the utilization of the theoretical manufacturing time advantages by eliminating autoclave post-consolidation to achieve high-rate CFRP production, however, also depends on a number of other factors which are beyond the scope of this work: Cost-competitive commercial-grade thermoplastic prepreg tape needs to achieve sufficient quality and specific characteristics such as a resin-rich, even tape surface, which are vital for reaching high-quality in-situ consolidated laminates. In-line quality control plays another key role in the future success of the technology. In-situ AFP provides the unique opportunity to measure all relevant process parameters in the exact moment of consolidation throughout the entire manufactured part. Currently ongoing research work implementing camera-based or laser scanning systems along with concomitant software could in the future replace the time-consuming, sometimes manual inspection of each layer. Monitoring process temperatures, consolidation pressure distribution and in-coming, as well as deposited tape dimensions and composition could provide comprehensive data sets, which could be used for quality inspection of the final part. Further development of optimized heat sources and end effectors for multi-tape layup with in-situ consolidation, using for example modular or variable spot size lasers can thereupon complement in-situ AFP to become a mature manufacturing technology and suitable alternative to established thermoset AFP and autoclave consolidation.

However, the major leverage effect of thermoplastic composite production only arises when additive manufacturing processes are combined with thermoplastic joining and automated assembly processes. Joining processes such as resistance welding or ultrasonic welding need to be further developed and, in particular, the interfaces to laminate production need to be taken into account so that in-situ AFP-manufactured components can be reliably joined. In this way, a new type of dust-free, additive structural component production can ultimately be achieved, enabling the economies of scale required for the high-rate production of next-generation large passenger aircraft.

8.3 Limitations and outlook

The experimental results in this work were limited to single tow layup, constant geodesic curvature and coupon-level mechanical tests. Future work will extend the empirical model to S-curves to provide fully-optimized layup paths for in-situ AFP VSP design. Another useful follow-up development would be the extension of the model to non-constant curvature applications such as linear curvature variation VSP design or free-form double-curved geometries. In a follow-up PhD project, advanced meshing techniques based on the results of this work are currently developed to simulate in-situ AFP-manufactured Variable Stiffness Panels with realistic process signature. This will be validated by sub-component level tests, investigating the effects of complex geometry-induced defect patterns on larger structures. Advanced in-line measurement of consolidated tape width via laser line scanning is investigated in another follow-up research project in order to replace time-consuming optical 3D scans with continuous in-line measurements, which can be used to provide a large database for future steering models. Finally, further work is required to optimize the transient track start and end sections via improved process control and examine tape straightening effects, which will further increase the technological maturity of the in-situ AFP process.

8.4 Conclusion

This work represents an important contribution to the research field of in-situ AFP and thermoplastic aerospace structures in general. Initial proof was provided that high quality complex in-situ AFP-manufactured structures could be achieved. A comprehensive analysis of the correlation of complex geometries and resulting defects was presented for relevant applications. A novel empirical methodology was introduced, expanding the design space of usable path curvatures and deriving optimized coverage for steered plies. A detailed analysis of the impact of realistic triangular gap and overlap defects on the in-situ AFP laminate micro structure and mechanical properties was given. The work presented provides a very good basis for further detailed investigations on the subject of in-situ AFP for complex structures, some of which have already been started.

Appendix

A1 Literature

Table 8.1: Literature overview of achieved relative Short Beam Strength of in-situ AFP compared to press- and autoclave-consolidated reference samples

Reference	Material	Test standard	Stacking sequence	AFP process				Reference process		Relative strength [%]
				Heat source	v_{layup} [mm/s]	T_tool [°C]	Strength [MPa]	Process	Strength	
Mantell et al. 1992 [25]	AS4/PEEK (APC-2)	ASTM D2344 - flat	$[0]_{16}$	Nitrogen HGT	3.6	93	32.6	HP	72.4	45
Mazumdar and Hoa 1995 [44]	AS4/PEEK (APC-2)	SBS - ring	$[0]_{10}$	CO_2 L	13	-	39.6	-	-	
Agarwal et al. 1995 [40]	AS4/PEEK (APC-2)	ASTM D2344 - ring	$[0]_{25}$	CO_2 L (lens)	15	-	50	-	-	-
Roselli and Santare 1997 [41]	IM7/PEEK (APC-2)	ASTM D2344 - ring	$[0]_{40}$	CO_2 L	20	-	46	-	-	-
Pistor et al. 1999 [70]	CF/PEKK (55 % FVF)	ASTM D2344 - ring	UD	L (scanning mirror)	15	-	29	-	-	-
Hulcher et al. 2002 [84]	IM7/PEEK (APC-2)	SBS	UD	Infrared	30.5	-	54	-	-	-
Tierney and Gillespie 2006 [82]	AS4/PEEK (APC-2)	ASTM D2344 - flat	UD	Double nitrogen HGT	30	-	57 ±10	A-RC	92±2	62
Khan and Schledjewski 2010 [39]	CF/PEEK (Suprem)	DIN EN 2563 - flat	$[0]_{15}$	Oxygen-hydrogen HF	50	280	85.5	A-RC	94	91
Gruber et al. 2012 [35]	AS4/PEEK (APC-2)	SBS	$[0]_{20}$	Double nitrogen HGT	30.5	-	80.2	A-RC	105.5	76
Gruber et al. 2012 [35]	Experimental grade AS4/PEEK (APC-2)	SBS	$[0]_{20}$	Double nitrogen HGT	30.5	-	89.9	A-RC	105.5	85
Gruber et al. 2012 [35]	Pre-autoclaved AS4/PEEK (APC-2)	SBS	$[0]_{20}$	Double nitrogen HGT	30.5	-	111	A-RC	105.5	105
Qureshi et al. 2014 [29]	AS4/PEEK (Tencate TC1200 59 % FVF)	ASTM D2344 - ring	$[0]_{40}$	Nitrogen HGT	57	-	50.6 ± 1.4	A-RC	92.7 ±3.2	55
Qureshi et al. 2014 [29]	AS4/PEEK (Tencate TC1200 59 % FVF)	ASTM D2344 - ring	$[0]_{40}$	Nitrogen HGT	95	-	46.6 ± 1.9	A-RC	92.7 ±3.2	50
Qureshi et al. 2014 [29]	AS4/PEEK (Tencate TC1200 59 % FVF)	ASTM D2344 - ring	$[0]_{40}$	Diode L (line)	127	-	78.9 ± 2.4	A-RC	92.7 ±3.2	85
Comer et al. 2015 [51]	IM7/PEEK (Suprem 60 % FVF)	EN 2563 - flat	$[0]_{16}$	Diode L (rect.)	133	150	78	A	112	70
Stokes-Griffin and Compston 2015 [36]	AS4/PEEK (Suprem 60 % FVF)	ASTM D2344 - flat	$[0]_{20}$	Diode L (rect.)	100	-	98 ± 0.8	A-RC	94.8 [39]	103
Stokes-Griffin and Compston 2015 [36]	AS4/PEEK (Suprem 60 % FVF)	ASTM D2344 - flat	$[0]_{20}$	Diode L (rect.)	400	-	93.5 ± 1.7	A-RC	94.8 [39]	99
Wanigasekara et al. 2020 [154]	AS4/PEEK (APC-2)	ASTM D2344 - flat	$[0]_{21}$	Nitrogen HGT	76	-	51.7 ± 1.1	-	-	-
Saenz-Castillo et al. 2020 [116]	AS4/PEEK (APC-2)	EN 2563	$[0]_{16}$	Diode L (rect.)	33.3	200	71 ± 2	HP	109 ± 8	65
Hoang et al. 2020 [155]	AS4D/PEKK (Tencate TC1320)	ASTM D2344 - flat	$[45/0/45/0/90/45/45/90]_S$	Diode L (rect.)	40	-	19.9 ±2	HP-R	92.2 ±8	22
Samak et al. 2020 [158]	AS4/PEEK (Suprem 60 % FVF)	ASTM D2344	[0/±45]n	Diode L (rect.)	116.7	-	48.2 ±3.8	-	-	-
Chanteli et al. 2020 [62]	IMS65/PEEK (Teijin)	ASTM D2344	$[0]_{16}$	Diode L (rect.)	50	-	42.0 ± 1	A-RC	104.9 ± 5	40
Chanteli et al. 2020 [62]	IMS65/PEEK (Teijin)	ASTM D2344	$[-45/0/45/90]_{2S}$	Diode L (rect.)	50	-	20.3 ± 1	A-RC	41.1 ± 6	50
Chen et al. 2021 [156]	CF/PPS (TU100)	ASTM D2344	$[0]_{16}$	Diode L (rect.)	183.3	60	49.2	A-RC	66	75
Miao et al. 2021 [45]	AS4/PEEK	ISO 14130:1997	$[0]_{14}$	YAG L (circ.)	13.3	-	50.0 ±0.18	-	-	–
Oromiehie et al. 2021 [157]	AS4/PEEK (APC-2)	ASTM D2344	$[0]_{21}$	Nitrogen HGT	76	-	62 ±1	-	-	-
Seneviratne et al. 2021 [159]	T700GC/LM-PAEK (Toray TC1225)	ASTM D2344	$[45/0/-45/90]_{3S}$	Diode L (rect.)	130	170	41.5±1	HP	76.5	54
Heathman et al. 2023 [65]	CF/LM-PAEK (Suprem 55 % FVF)	ASTM D2344	$[0]_{32}$	Diode L (rect.)	50	100	62.7 ±1.2	HP-RC	75.7 ±2.2	83
Heathman et al. 2023 [65]	CF/LM-PAEK (Suprem 55 % FVF)	ASTM D2344	$[0]_{32}$	Diode L (rect.)	100	100	61.1 ±1	HP-RC	75.7 ±2.2	81
Heathman et al. 2023 [65]	CF/LM-PAEK (Suprem 55 % FVF)	ASTM D2344	$[0]_{32}$	Diode L (rect.)	150	100	55 ±1	HP-RC	75.7 ±2.2	73
Kirchhoff et al 2023 [149]	CF/LM-PAEK (Suprem 55 % FVF)	ASTM D2344	$[0]_{46}$	Diode L (rect.)	100	150	57.7 ±0.8	HP-RC	96.5	60
Kirchhoff et al 2023 [149]	CF/LM-PAEK (Suprem 55 % FVF)	ASTM D2344	$[0]_{46}$	Diode L (rect.)	200	150	41.5 ±0.8	HP-RC	96.5	43
Yap et al. 2023 [150]	CF/LM-PAEK (Toray)	ASTM D2344	$[0]_{48}$	Diode L (rect.)	100	100	48.5 ± 1.2	-	-	-
Perez-Martin et al. 2023 [68]	AS7/PEKK	ASTM D2344	$[0]_{10}$	Diode L (rect.)	66.7	-	29.3 ±1.7	HP	100.1 ±3.1	29
Schiel et al. 2023 [160]	T700/LM-PAEK (Toray TC1225 60 % FVF)	EN 2563 - flat	$[0]_{12}$	Diode L (rect.)	125	200	57.1 ± 2	HP-RC	87.7±1	65
Schiel et al. 2023 [160]	T700/LM-PAEK (Toray TC1225 60 % FVF)	EN 2563 - flat	$[0]_{12}$	Diode L (rect.)	125	20	46 ± 1.5	HP-RC	87.7±1	53
Pourahmadi et al 2024 [161]	AS4/PEEK (APC-2)	ASTM D2344	$[0]_{17}$	Nitrogen HGT	50.8	-	54.5 ±1.1	A-RC	86.2 ± 1.1	63
Chadwick et al. 2025 [313]	CF/PPS (Suprem 55 % FVF)	EN 2563 - flat	$[0]_{11}$	Diode L (rect.)	125	250	77.2 ± 1.2	HP-RC	95.6 ±1.4	81

HGT - Hot gas torch
HF - Hot flame
L - Laser
IR - Infrared
A - Autoclave
HP - Hot press
RC - Re-consolidated

Table 8.2: Literature overview of achieved laminate porosity of in-situ AFP samples

Reference	Material	Test method	Stacking sequence	AFP process			
				Heat source	v_{layup} [mm/s]	T_{tool} [°C]	Porosity [%]
Agarwal et al. 1995 [40]	AS4/PEEK (APC-2)	Photomicrograph	$[0]_{25}$	CO_2 laser with lens	15	-	1.4 ±0.4
Roselli et al. 1997 [42]	IM7/PEEK (APC-2)	Photomicrograph	$[0]_{40}$	CO_2 laser	20	-	2.6
Pistor et al. 1999 [70]	CF/PEKK (55 % FVF)	Density analysis	UD	Laser with scanning mirror	15	-	5
Hulcher et al. 2002 [84]	IM7/PEEK (APC-2)	Acid digestion	UD	Infrared	30.5	-	5.6
Hulcher et al. 2002 [84]	IM7/PEEK (APC-2)	Acid digestion	$[45/\text{-}45/0/90]_S$	Infrared	30.5	-	8.3
Tierney et al. 2003 [119]	AS4/PEEK (APC-2)	Photomicrograph	UD	Double nitrogen hot gas torch	40	-	1.5 ±0.5
Khan and Schledjewski 2010 [38]	AS4/PEEK	Photomicrograph	$[0]_{15}$	Oxygen-hydrogen hot flame	83.3	280	1.5 ± 1
Comer et al. 2015 [51]	IM7/PEEK (Suprem 60 % FVF)	Photomicrograph	$[0]_{16}$	Diode laser (rectangular)	133	150	2.8
Shadmehri et al. 2018 [28]	AS4/PEEK (APC-2)	Photomicrograph	$[0]_{24}$	Nitrogen hot gas torch	50.8	-	0.4 ± 0.2
Shadmehri et al. 2018 [28]	AS4/PEEK (APC-2)	Photomicrograph	$[0]_{24}$	Nitrogen hot gas torch (double repass)	50.8	-	0.2 ± 0.1
Saenz-Castillo et al. 2019 [53]	AS4/PEEK (APC-2)	Acid digestion	$[45/\text{-}45]_{4S}$	Diode laser (scanner system)	16.7	200	1.6
Saenz-Castillo et al. 2020 [116]	AS4/PEEK (APC-2)	Acid digestion	$[0]_{16}$	Diode laser (rectangular)	33.3	200	3 ±0.2
Hoang et al. 2020 [155]	AS4D/PEKK (Tencate TC1320)	Acid digestion	$[45/0/45/0/90/45/45/90]_S$	Diode laser (rectangular)	40	-	5.8±0.3
Samak et al. 2020 [158]	AS4/PEEK (Suprem 60 % FVF)	Photomicrograph	[0/±45]n	Diode laser (rectangular)	116.7	-	1.6
Chanteli et al. 2020 [62]	IMS65/PEEK (Teijin)	Matrix burn off	$[0]_{16}$	Diode laser (rectangular)	50	-	4.2
Chen et al. 2021 [156]	CF/PPS (TU100)	Photomicrograph	$[0]_{16}$	Diode laser (rectangular)	183.3	60	2.3
Miao et al. 2021 [45]	AS4/PEEK	Photomicrograph	$[0]_{14}$	YAG laser (23 mm circular spot)	13.3	-	0.02
Seneviratne et al. 2021 [159]	T700GC/LM-PAEK (Toray TC1225)	Acid digestion	$[45/0/\text{-}45/90]_{3S}$	Diode Laser (rectangular)	130	170	4.8
Zhao et al. 2021 [64]	CF/PPS (TU100)	Photomicrograph	UD	Diode laser (rectangular)	100	120	2.5
Song et al. 2022 [122]	CF/PPS	Photomicrograph	$[0]_6$	Diode laser (rectangular)	183.3	-	2
Heathman et al. 2023 [65]	CF/LM-PAEK (Suprem 55 % FVF)	Photomicrograph	$[0]_{32}$	Diode laser (rectangular)	50	100	0.2
Heathman et al. 2023 [65]	CF/LM-PAEK (Suprem 55 % FVF)	Photomicrograph	$[0]_{32}$	Diode laser (rectangular)	100	100	0.4
Heathman et al. 2023 [65]	CF/LM-PAEK (Suprem 55 % FVF)	Photomicrograph	$[0]_{32}$	Diode laser (rectangular)	150	100	2.2 ±0.4
Perez-Martin et al. 2023 [68]	AS7/PEKK	Photomicrograph	$[0]_{10}$	Diode laser (rectangular)	66.7	-	3.7±0.5
Martin et al. [166]	T700/LM-PAEK (Toray 60 % FVF)	Acid digestion	$[0/90]_{4S}$	Diode laser (rectangular)	16.7	180	1.2
Pourahmadi et al. 2024 [161]	AS4/PEEK (APC-2)	Photomicrograph	$[0]_{17}$	Nitrogen hot gas torch	50.8	-	1.6
Raps et al. 2024 [106]	AS7/LM-PAEK (Suprem 55 % FVF)	Micro-computed tomography	$[0/45/90/\text{-}45]_{2S}$	Diode laser (rectangular)	125	200	0.9 ± 0.3
Chadwick et al. 2025 [313]	CF/PPS	Micro-computed tomography	$[0]_{11}$	Diode laser (rectangular)	125	250	1.11
Chadwick et al. 2025 [313]	CF/PPS	Micro-computed tomography	$[0/45/90/\text{-}45]_{3S}$	Diode laser (rectangular)	125	250	1.1

Table 8.3: Literature overview of achieved relative tensile results of autoclave-consolidated thermoset samples with rectangular defects compared to defect-free reference

Reference	**Stacking Sequence**	**Defect Design**	**AFP Process**	**Proportional Results**	
				Strength [%]	**Modulus [%]**
Guin et al. 2018 [228]	$[+45/\text{-}45/90/0]_{2S}$	1.27 mm gaps in all 90°	AFP + autoclave	101	100.5
Guin et al. 2018 [228]	$[+45/\text{-}45/90/0]_{2S}$	1.27 mm gaps in all plies	AFP + autoclave	65	100.8
Woigk et al. 2018 [244]	$[+ - 45\ /90\ /\ 45\ /0\ ]_{3S}$	2mm aligned Gaps	Hand layup + autoclave	98.7	109.9
Woigk et al. 2018 [244]	$[+ - 45\ /90\ /\ 45\ /0\ ]_{3S}$	2mm aligned Overlaps	Hand layup + autoclave	103	108.5
Woigk et al. 2018 [244]	$[+ - 45\ /90\ /\ 45\ /0\ ]_{3S}$	2mm Staggered Gaps	Hand layup + autoclave	99.8	104.4
Woigk et al. 2018 [244]	$[+ - 45\ /90\ /\ 45\ /0\ ]_{3S}$	2mm aligned Gaps and Overlaps	Hand layup + autoclave	92.6	103.6
Croft et al. 2011 [225]	$[0]_8$	2 aligned gaps in 0° plies (one tow wide)	AFP + autoclave	97.9	
Croft et al. 2011 [225]	$[0]_8$	2 aligned overlap in 0° plies (one tow wide)	AFP + autoclave	101	
Croft et al. 2011 [225]	$[0]_8$	2 aligned combined half-gap-overlap in 0° plies (one tow wide)	AFP + autoclave	96.6	
Nguyen et al. 2019 [230]	$[\ 45/0/\ 45/90]_{2S}$	0.794 mm 90° gaps aligned	AFP + autoclave	90.6	99.3
Nguyen et al. 2019 [230]	$[\ 45/0/\ 45/90]_{2S}$	1.588 mm 90° gaps aligned	AFP + autoclave	89.2	96.5
Nguyen et al. 2019 [230]	$[\ 45/0/\ 45/90]_{2S}$	3.175 mm 90° gaps aligned	Hand layup + autoclave	86.8	102.4
Nguyen et al. 2019 [230]	$[\ 45/0/\ 45/90]_{2S}$	6.35 mm 90° gaps aligned	Hand layup + autoclave	90.3	96.5
Nguyen et al. 2019 [230]	$[\ 45/0/\ 45/90]_{2S}$	12.7 mm 90° gaps aligned	Hand layup + autoclave	73.9	101.4
Nguyen et al. 2019 [230]	$[\ 45/0/\ 45/90]_{2S}$	0.794 mm 0° and 90° gaps aligned	AFP + autoclave	90.3	104.5
Nguyen et al. 2019 [230]	$[\ 45/0/\ 45/90]_{2S}$	1.588 mm 0° and 90° gaps aligned	AFP + autoclave	94.4	94.1
Nguyen et al. 2019 [230]	$[\ 45/0/\ 45/90]_{2S}$	3.175 mm 0° and 90° gaps aligned	Hand layup + autoclave	78.8	91.3
Nguyen et al. 2019 [230]	$[\ 45/0/\ 45/90]_{2S}$	6.35 mm 0° and 90° gaps aligned	Hand layup + autoclave	66.3	79.9
Nguyen et al. 2019 [230]	$[\ 45/0/\ 45/90]_{2S}$	12.7 mm 0° and 90° gaps aligned	Hand layup + autoclave	46.5	61.4
Nguyen et al. 2019 [230]	$[\ 45/0/\ 45/90]_{2S}$	0.794 mm 90° gaps staggered	AFP + autoclave	95.5	102.8
Nguyen et al. 2019 [230]	$[\ 45/0/\ 45/90]_{2S}$	1.588 mm 90° gaps staggered	AFP + autoclave	95.5	96.2
Nguyen et al. 2019 [230]	$[\ 45/0/\ 45/90]_{2S}$	3.175 mm 90° gaps staggered	Hand layup + autoclave	91.3	95.5
Nguyen et al. 2019 [230]	$[\ 45/0/\ 45/90]_{2S}$	6.35 mm 90° gaps staggered	Hand layup + autoclave	78.1	89.9
Nguyen et al. 2019 [230]	$[\ 45/0/\ 45/90]_{2S}$	12.7 mm 90° gaps staggered	Hand layup + autoclave	80.5	81.2
Nguyen et al. 2019 [230]	$[\ 45/0/\ 45/90]_{2S}$	0.794 mm 0° and 90° gaps staggered	AFP + autoclave	97.6	100.3
Nguyen et al. 2019 [230]	$[\ 45/0/\ 45/90]_{2S}$	1.588 mm 0° and 90° gaps staggered	AFP + autoclave	95.8	99.3
Nguyen et al. 2019 [230]	$[\ 45/0/\ 45/90]_{2S}$	3.175 mm 0° and 90° gaps staggered	Hand layup + autoclave	91.7	97.6
Nguyen et al. 2019 [230]	$[\ 45/0/\ 45/90]_{2S}$	6.35 mm 0° and 90° gaps staggered	Hand layup + autoclave	78.5	93.1
Nguyen et al. 2019 [230]	$[\ 45/0/\ 45/90]_{2S}$	12.7 mm 0° and 90° gaps staggered	Hand layup + autoclave	79.9	81.2
Nguyen et al. 2019 [230]	$[\ 45/0/\ 45/90]_{2S}$	0.794 mm 90° overlaps aligned	AFP + autoclave	98.3	97.9
Nguyen et al. 2019 [230]	$[\ 45/0/\ 45/90]_{2S}$	1.588 mm 90° overlaps aligned	AFP + autoclave	83.7	91.3
Nguyen et al. 2019 [230]	$[\ 45/0/\ 45/90]_{2S}$	3.175 mm 90° overlaps aligned	Hand layup + autoclave	95.5	97.6
Nguyen et al. 2019 [230]	$[\ 45/0/\ 45/90]_{2S}$	6.35 mm 90° overlaps aligned	Hand layup + autoclave	77.8	98.6
Nguyen et al. 2019 [230]	$[\ 45/0/\ 45/90]_{2S}$	12.7 mm 90° overlaps aligned	Hand layup + autoclave	92	102.8
Nguyen et al. 2019 [230]	$[\ 45/0/\ 45/90]_{2S}$	0.794 mm 0° and 90° overlaps aligned	AFP + autoclave	107.6	103.5
Nguyen et al. 2019 [230]	$[\ 45/0/\ 45/90]_{2S}$	1.588 mm 0° and 90° overlaps aligned	AFP + autoclave	101	100.7
Nguyen et al. 2019 [230]	$[\ 45/0/\ 45/90]_{2S}$	3.175 mm 0° and 90° overlaps aligned	Hand layup + autoclave	100.3	106.9
Nguyen et al. 2019 [230]	$[\ 45/0/\ 45/90]_{2S}$	6.35 mm 0° and 90° overlaps aligned	Hand layup + autoclave	92.7	108

Table 8.4: Literature overview of achieved relative tensile results of autoclave-consolidated thermoset samples with rectangular defects compared to defect-free reference

Reference	Stacking Sequence	Defect Design	AFP Process	Proportional Results	
				Strength [%]	Modulus [%]
Nguyen et al. 2019 [230]	$[\ 45/0/\ 45/90]_{2S}$	12.7 mm 0° and 90° overlaps aligned	Hand layup + autoclave	112.9	121.2
Nguyen et al. 2019 [230]	$[\ 45/0/\ 45/90]_{2S}$	0.794 mm 90° overlaps staggered	AFP + autoclave	106.6	95.1
Nguyen et al. 2019 [230]	$[\ 45/0/\ 45/90]_{2S}$	1.588 mm 90° overlaps staggered	AFP + autoclave	102.4	109.4
Nguyen et al. 2019 [230]	$[\ 45/0/\ 45/90]_{2S}$	6.35 mm 90° overlaps staggered	Hand layup + autoclave	111.5	109
Nguyen et al. 2019 [230]	$[\ 45/0/\ 45/90]_{2S}$	12.7 mm 90° overlaps staggered	Hand layup + autoclave	123.6	109
Nguyen et al. 2019 [230]	$[\ 45/0/\ 45/90]_{2S}$	0.794 mm 0° and 90° overlaps staggered	AFP + autoclave	106.9	98.6
Nguyen et al. 2019 [230]	$[\ 45/0/\ 45/90]_{2S}$	1.588 mm 0° and 90° overlaps staggered	AFP + autoclave	99	96.9
Nguyen et al. 2019 [230]	$[\ 45/0/\ 45/90]_{2S}$	6.35 mm 0° and 90° overlaps staggered	Hand layup + autoclave	109	106.3
Nguyen et al. 2019 [230]	$[\ 45/0/\ 45/90]_{2S}$	12.7 mm 0° and 90° overlaps staggered	Hand layup + autoclave	119.5	122.2
Nartey et al. 2020 [233]	$[45/90/\text{-}45/0]_{3S}$	4 mm gap and 4mm overlap in 2 90° plies	Hand layup + autoclave	91.5	
Nartey et al. 2020 [233]	$[45/90/\text{-}45/0]_{3S}$	4 mm gap and 4mm overlap in 6 90° plies	Hand layup + autoclave	84	
Nartey et al. 2020 [233]	$[45/90/\text{-}45/0]_{3S}$	6 mm gap and 6mm overlap in 4 90° plies	Hand layup + autoclave	87.2	
Nartey et al. 2020 [233]	$[45/90/\text{-}45/0]_{3S}$	6 mm gap and 6mm overlap in 6 90° plies	Hand layup + autoclave	78.8	
Suemasu et al. 2021 [245]	$[45/0/\text{-}45/90]_{2S}$	Gaps 3.175 mm staggered	AFP + autoclave	81.9	99.6
Suemasu et al. 2021 [245]	$[45/0/\text{-}45/90]_{2S}$	Overlaps 3.175 mm staggered	AFP + autoclave	81.7	99.8
Del Rossi et al. 2021 [227]	$[45_f/(\text{-}\ 45/0/45\ /90)_2]_S$ with fabric layers	4 staggered 1.27 mm half gap overlaps in 0°	AFP + autoclave	97	
Del Rossi et al. 2021 [227]	$[45_f/(\text{-}\ 45/0/45\ /90)_2]_S$ with fabric layers	7 staggerd 1.27 mm half gap overlaps in 0°	AFP + autoclave	100.6	
Del Rossi et al. 2021 [227]	$[45_f/(\text{-}\ 45/0/45\ /90)_2]_S$ with fabric layers	10 staggered 1.27 mm half gap overlaps in 0°	AFP + autoclave	102.2	
Del Rossi et al. 2021 [227]	$[45_f/(\text{-}\ 45/0/45\ /90)_2]_S$ with fabric layers	4 staggered 1.27 mm half gap overlaps in 45°	AFP + autoclave	97.4	
Del Rossi et al. 2021 [227]	$[45_f/(\text{-}\ 45/0/45\ /90)_2]_S$ with fabric layers	7 staggered 1.27 mm half gap overlaps in 45°	AFP + autoclave	96.8	
Del Rossi et al. 2021 [227]	$[45_f/(\text{-}\ 45/0/45\ /90)_2]_S$ with fabric layers	10 staggered 1.27 mm half gap overlaps in 45°	AFP + autoclave	89.3	
Del Rossi et al. 2021 [227]	$[45_f/(\text{-}\ 45/0/45\ /90)_2]_S$ with fabric layers	4 staggered 1.27 mm half gap overlaps in 90°	AFP + autoclave	98.9	
Del Rossi et al. 2021 [227]	$[45_f/(\text{-}\ 45/0/45\ /90)_2]_S$ with fabric layers	7 staggered 1.27 mm half gap overlaps in 90°	AFP + autoclave	95.9	
Del Rossi et al. 2021 [227]	$[45_f/(\text{-}\ 45/0/45\ /90)_2]_S$ with fabric layers	4 aligned 1.27 mm half gap overlaps in 0°, 45° and 90°	AFP + autoclave	91.1	
Del Rossi et al. 2021 [227]	$[45_f/(\text{-}\ 45/0/45\ /90)_2]_S$ with fabric layers	4 staggered 2.54 mm half gap overlaps in 0°	AFP + autoclave	101.9	
Del Rossi et al. 2021 [227]	$[45_f/(\text{-}\ 45/0/45\ /90)_2]_S$ with fabric layers	7 staggered 2.54 mm half gap overlaps in 0°	AFP + autoclave	100	
Del Rossi et al. 2021 [227]	$[45_f/(\text{-}\ 45/0/45\ /90)_2]_S$ with fabric layers	4 staggered 2.54 mm half gap overlaps in 45°	AFP + autoclave	94.2	
Del Rossi et al. 2021 [227]	$[45_f/(\text{-}\ 45/0/45\ /90)_2]_S$ with fabric layers	7 staggered 2.54 mm half gap overlaps in 45°	AFP + autoclave	96.4	
Boeckl et al. 2023 [248]	$[+45_2/\text{-}45_2/0_2/90_2]_S$	2 aligned 3.175 mm gap in 90°	AFP + autoclave	101.9	
Boeckl et al. 2023 [248]	$[+45_2/\text{-}45_2/0_2/90_2]_S$	4 aligned 3.175 mm gap in 90°	AFP + autoclave	79.6	
Boeckl et al. 2023 [248]	$[+45_2/\text{-}45_2/0_2/90_2]_S$	2 aligned 3.175 mm overlap in 90°	AFP + autoclave	100.1	
Boeckl et al. 2023 [248]	$[+45_2/\text{-}45_2/0_2/90_2]_S$	4 aligned 3.175 mm overlap in 4 90°	AFP + autoclave	88.2	

Table 8.5: Literature overview of achieved relative compressive results of autoclave-consolidated thermoset samples with rectangular defects compared to defect-free reference

Reference	Stacking Sequence	Defect Design	AFP Process	Proportional Results	
				Strength [%]	**Modulus [%]**
Guin et al. 2018 [228]	$[+45/-45/90/0]_{2S}$	1.27 mm gaps in all 90°	AFP + autoclave	97.2	97.2
Guin et al. 2018 [228]	$[+45/-45/90/0]_{2S}$	1.27 mm gaps in all plies	AFP + autoclave	73	81
Woigk et al. 2018 [244]	$[+ - 45\ /90\ /\ 45\ /0\ ]_{3S}$	2mm aligned Gaps	Hand layup + autoclave	107.6	97.4
Woigk et al. 2018 [244]	$[+ - 45\ /90\ /\ 45\ /0\ ]_{3S}$	2mm aligned Overlaps	Hand layup + autoclave	109.5	99.3
Woigk et al. 2018 [244]	$[+ - 45\ /90\ /\ 45\ /0\ ]_{3S}$	2mm Staggered Gaps	Hand layup + autoclave	101.3	100
Woigk et al. 2018 [244]	$[+ - 45\ /90\ /\ 45\ /0\ ]_{3S}$	2mm aligned Gaps and Overlaps	Hand layup + autoclave	85.3	93.9
Suemasu et al. 2021 [245]	$[45/0/-45/90]_{2S}$	Gaps 3.175 mm staggered	AFP + autoclave	92.4	99.8
Suemasu et al. 2021 [245]	$[45/0/-45/90]_{2S}$	Overlaps 3.175 mm staggered	AFP + autoclave	95.1	100
Croft et al. 2011 [225]	$[0]_{16}$	2 aligned gap in 0° plies (one tow wide)	AFP + autoclave	99.2	
Croft et al. 2011 [225]	$[0]_{16}$	2 aligned overlap in 0° plies (one tow wide)	AFP + autoclave	107.2	
Croft et al. 2011 [225]	$[0]_{16}$	2 aligned half-gap-overlap in 0° plies (one tow wide)	AFP + autoclave	100	
Nguyen et al. 2019 [230]	$[45/0/45/90]_{2S}$	0.794 mm 90° gaps aligned	AFP + autoclave	84.7	97.2
Nguyen et al. 2019 [230]	$[45/0/45/90]_{2S}$	1.588 mm 90° gaps aligned	AFP + autoclave	93.4	98.3
Nguyen et al. 2019 [230]	$[45/0/45/90]_{2S}$	3.175 mm 90° gaps aligned	Hand layup + autoclave	82.3	90.6
Nguyen et al. 2019 [230]	$[45/0/45/90]_{2S}$	6.35 mm 90° gaps aligned	Hand layup + autoclave	69.8	75.3
Nguyen et al. 2019 [230]	$[45/0/45/90]_{2S}$	0.794 mm 0° and 90° gaps aligned	AFP + autoclave	81.2	87.8
Nguyen et al. 2019 [230]	$[45/0/45/90]_{2S}$	1.588 mm 0° and 90° gaps aligned	AFP + autoclave	81.6	88.2
Nguyen et al. 2019 [230]	$[45/0/45/90]_{2S}$	3.175 mm 0° and 90° gaps aligned	Hand layup + autoclave	72.9	70.8
Nguyen et al. 2019 [230]	$[45/0/45/90]_{2S}$	6.35 mm 0° and 90° gaps aligned	Hand layup + autoclave	44.1	45.1
Nguyen et al. 2019 [230]	$[45/0/45/90]_{2S}$	0.794 mm 90° gaps staggered	AFP + autoclave	92	92.4
Nguyen et al. 2019 [230]	$[45/0/45/90]_{2S}$	1.588 mm 90° gaps staggered	AFP + autoclave	83	87.8
Nguyen et al. 2019 [230]	$[45/0/45/90]_{2S}$	3.175 mm 90° gaps staggered	Hand layup + autoclave	71.5	71.9
Nguyen et al. 2019 [230]	$[45/0/45/90]_{2S}$	0.794 mm 0° and 90° gaps staggered	AFP + autoclave	88.9	92
Nguyen et al. 2019 [230]	$[45/0/45/90]_{2S}$	1.588 mm 0° and 90° gaps staggered	AFP + autoclave	97.2	92.7
Nguyen et al. 2019 [230]	$[45/0/45/90]_{2S}$	3.175 mm 0° and 90° gaps staggered	Hand layup + autoclave	62.1	78.1
Nguyen et al. 2019 [230]	$[45/0/45/90]_{2S}$	6.35 mm 0° and 90° gaps staggered	Hand layup + autoclave	67	76
Nguyen et al. 2019 [230]	$[45/0/45/90]_{2S}$	0.794 mm 90° overlaps aligned	AFP + autoclave	99	95.8
Nguyen et al. 2019 [230]	$[45/0/45/90]_{2S}$	1.588 mm 90° overlaps aligned	AFP + autoclave	85.4	89.9
Nguyen et al. 2019 [230]	$[45/0/45/90]_{2S}$	3.175 mm 90° overlaps aligned	Hand layup + autoclave	81.9	85.8
Nguyen et al. 2019 [230]	$[45/0/45/90]_{2S}$	6.35 mm 90° overlaps aligned	Hand layup + autoclave	86.8	91.3
Nguyen et al. 2019 [230]	$[45/0/45/90]_{2S}$	0.794 mm 0° and 90° overlaps aligned	AFP + autoclave	94.8	115.3
Nguyen et al. 2019 [230]	$[45/0/45/90]_{2S}$	1.588 mm 0° and 90° overlaps aligned	AFP + autoclave	110.4	100.7
Nguyen et al. 2019 [230]	$[45/0/45/90]_{2S}$	3.175 mm 0° and 90° overlaps aligned	Hand layup + autoclave	93.1	96.9
Nguyen et al. 2019 [230]	$[45/0/45/90]_{2S}$	6.35 mm 0° and 90° overlaps aligned	Hand layup + autoclave	106.9	113.9
Nguyen et al. 2019 [230]	$[45/0/45/90]_{2S}$	0.794 mm 90° overlaps staggered	AFP + autoclave	91.3	87.5
Nguyen et al. 2019 [230]	$[45/0/45/90]_{2S}$	1.588 mm 90° overlaps staggered	AFP + autoclave	101.4	95.5
Nguyen et al. 2019 [230]	$[45/0/45/90]_{2S}$	6.35 mm 90° overlaps staggered	Hand layup + autoclave	94.4	95.8
Nguyen et al. 2019 [230]	$[45/0/45/90]_{2S}$	0.794 mm 0° and 90° overlaps staggered	AFP + autoclave	104.2	99.7
Nguyen et al. 2019 [230]	$[45/0/45/90]_{2S}$	1.588 mm 0° and 90° overlaps staggered	AFP + autoclave	100	93.7
Nguyen et al. 2019 [230]	$[45/0/45/90]_{2S}$	6.35 mm 0° and 90° overlaps staggered	Hand layup + autoclave	97.6	113.9

Table 8.6: Literature overview of achieved relative compressive results of autoclave-consolidated thermoset samples with rectangular defects compared to defect-free reference

Reference	Stacking Sequence	Defect Design	AFP Process	Proportional Results	
				Strength [%]	Modulus [%]
Nartey et al. 2020 [233]	$[45/90/\text{-}45/0]_{3S}$	4 mm gap and 4mm overlap in 4 90° plies	Hand layup + autoclave	79.7	
Nartey et al. 2020 [233]	$[45/90/\text{-}45/0]_{3S}$	4 mm gap and 4mm overlap in 6 90° plies	Hand layup + autoclave	63.2	
Nartey et al. 2020 [233]	$[45/90/\text{-}45/0]_{3S}$	6 mm gap and 6mm overlap in 4 90° plies	Hand layup + autoclave	83.6	
Nartey et al. 2020 [233]	$[45/90/\text{-}45/0]_{3S}$	6 mm gap and 6mm overlap in 6 90° plies	Hand layup + autoclave	64.5	
Del Rossi et al. 2021 [227]	$[45_f/(\text{-}\ 45/0/45\ /90)_2]_S$ with fabric layers	4 staggered 1.27 mm half gap overlaps in 45°	AFP + autoclave	80.1	
Del Rossi et al. 2021 [227]	$[45_f/(\text{-}\ 45/0/45\ /90)_2]_S$ with fabric layers	7 staggered 1.27 mm half gap overlaps in 45°	AFP + autoclave	78	
Del Rossi et al. 2021 [227]	$[45_f/(\text{-}\ 45/0/45\ /90)_2]_S$ with fabric layers	10 staggered 1.27 mm half gap overlaps in 45°	AFP + autoclave	74	
Del Rossi et al. 2021 [227]	$[45_f/(\text{-}\ 45/0/45\ /90)_2]_S$ with fabric layers	4 staggered 1.27 mm half gap overlaps in 90°	AFP + autoclave	81	
Del Rossi et al. 2021 [227]	$[45_f/(\text{-}\ 45/0/45\ /90)_2]_S$ with fabric layers	7 staggered 1.27 mm half gap overlaps in 90°	AFP + autoclave	84.2	
Del Rossi et al. 2021 [227]	$[45_f/(\text{-}\ 45/0/45\ /90)_2]_S$ with fabric layers	4 aligned 1.27 mm half gap overlaps in 0°, 45° and 90°	AFP + autoclave	73.1	
Del Rossi et al. 2021 [227]	$[45_f/(\text{-}\ 45/0/45\ /90)_2]_S$ with fabric layers	4 staggered 2.54 mm half gap overlaps in 45°	AFP + autoclave	86	
Del Rossi et al. 2021 [227]	$[45_f/(\text{-}\ 45/0/45\ /90)_2]_S$ with fabric layers	7 staggered 2.54 mm half gap overlaps in 45°	AFP + autoclave	81	
Sawicki et al. 1998 [243]	$[45/\text{-}45_2/45/(0_2/90/0_2/\pm45)_2/0_2/90/0_2/\text{-}45/45_2/45]$	0.76 mm combined Gap / Overlap in each 90° ply	Hand layup	91.4	
Sawicki et al. 1998 [243]	$[45/\text{-}45_2/45/(0_2/90/0_2/\pm45)_2/0_2/90/0_2/\text{-}45/45_2/45]$	2.54 mm combined Gap / Overlap in each 90° ply	Hand layup	87.1-92.5	

A2 Constant curvature Variable Stiffness Panel Algorithm

This appendix chapter is a detailed explanation of the analytical calculations of the constant curvature Variable Stiffness Panel algorithm published in [296]. The algorithm was also implemented in Python as a Juyter notebook using the math package for the analytical equations and NumPy, Matplotlib and seaborn for visualization. Each course of the constant curvature Variable Stiffness Panel comprises n parallel tows. The reference curve defined in equation 5.1 determines the centerline of the center course which leads through the coordinate origin. Subsequent course reference curves are shifted along the y-axis by the shifting distance D_0. For a 100 % coverage ratio, D_0 can be calculated as the course width in y-direction at $x = 0$ [192]:

$$D_0 = 2\left(-\sqrt{\left(\rho - \frac{w_c}{2}\right)^2 - (\rho \cdot cos(T_0))^2} + \rho \cdot sin(T_0)\right) \tag{8.1}$$

where w_c is the course width. For a 0 % coverage ratio, the shifting distance $D_{0,gaps}$ can be calculated as the course width plus one additional tow of the subsequent course in y-direction at $x = 0$:

$$D_{0,gaps} = D_0 - \sqrt{\left(\rho - \frac{w_c - w_t}{2}\right)^2 - (\rho \cdot cos(T_0))^2} + \rho \cdot sin(T_0) \tag{8.2}$$

The centerlines of subsequent courses can then be calculated using the initial reference curve (Equation 5.1) and the respective shifting distance. For 100 % coverage ratio:

$$y(x,j) = \begin{cases} \sqrt{\rho^2 - (x - \rho \cdot cos(T_0))^2} - \rho \cdot sin(T_0) + j \cdot D_0 & \text{if } x < 0 \\ -\sqrt{\rho^2 - (x + \rho \cdot cos(T_0))^2} + \rho \cdot sin(T_0) + j \cdot D_0 & \text{if } x \geq 0 \end{cases} \tag{8.3}$$

and for 0 % overage ratio:

$$y(x,j) = \begin{cases} \sqrt{\rho^2 - (x - \rho \cdot cos(T_0))^2} - \rho \cdot sin(T_0) + j \cdot D_{0,gaps} & \text{if } x < 0 \\ -\sqrt{\rho^2 - (x + \rho \cdot cos(T_0))^2} + \rho \cdot sin(T_0) + j \cdot D_{0,gaps} & \text{if } x \geq 0 \end{cases} \tag{8.4}$$

where j is an integer variable that is iterated over the number of courses.

In order to avoid overlaps of subsequently added courses, tows need to be cut at the upper or lower boundary of the course. The layup strategy which is presented by Fayazbakhsh [192] uses one sided tow cuts at the upper course boundary. In order to determine the tow cut positions, the intersections between the lower boundary of the subsequent course and the tows of the center course have to be determined. Due to the parallel layup of the tows in a course, the inflection point of the tows shifts in comparison to the reference curve. For the case differentiation of the parallel shifted curve functions, the x-coordinate of the inflection point thus has to be be determined. For the lower boundary of all courses, the x-coordinate of the inflection point can be calculated as:

$$B_0 = \frac{1}{2} \cdot w_c \cdot cos(T_0) \tag{8.5}$$

It is the same for all coverage ratios. The lower boundary curves of the courses can then be calculated for 100 % coverage ratio as:

$$y_{bottom,overlaps}(x,j) = \begin{cases} \sqrt{(\rho - \frac{w_c}{2})^2 - (x - \rho \cdot cos(T_0))^2} - \rho \cdot sin(T_0) + j \cdot D_0 & \text{if } x \leq B_0 \\ -\sqrt{(\rho + \frac{w_c}{2})^2 - (x + \rho \cdot cos(T_0))^2} + \rho \cdot sin(T_0) + j \cdot D_0 & \text{if } x > B_0 \end{cases} \tag{8.6}$$

For the lower boundary curves of 0 % coverage ratio layup, the shifting distance $D_{0,gaps}$ is used:

$$y_{bottom,gaps}(x,j) = \begin{cases} \sqrt{(\rho - \frac{w_c}{2})^2 - (x - \rho \cdot cos(T_0))^2} - \rho \cdot sin(T_0) + j \cdot D_{0,gaps} & \text{if } x \leq B_0 \\ -\sqrt{(\rho + \frac{w_c}{2})^2 - (x + \rho \cdot cos(T_0))^2} + \rho \cdot sin(T_0) + j \cdot D_{0,gaps} & \text{if } x > B_0 \end{cases} \tag{8.7}$$

For the tow cuts of 100 % coverage ratio layup, the intersection between the lower course boundary curve of the course above the main course and the lower boundaries of the individual tows of the main course need to be calculated. The x-coordinate of the inflection point of the individual tows can be calculated as:

$$B(i) = w_c \cdot (\frac{1}{2} - \frac{i}{n}) \cdot w_c \cdot cos(T_0) \tag{8.8}$$

where i is an integer variable that is iterated over the number of tows and n is the total number of parallel tows of each course. The lower boundaries of the individual tows are defined as:

$$y_{tows,bottom}(x,i) = \begin{cases} \sqrt{(\rho - \frac{w_c}{2} + i \cdot w_t)^2 - (x - \rho \cdot cos(T_0))^2} - \rho \cdot sin(T_0) + j \cdot D_{0,gaps} \\ \text{if } x \leq B(i) \\ -\sqrt{(\rho + \frac{w_c}{2} - i \cdot w_t)^2 - (x + \rho \cdot cos(T_0))^2} + \rho \cdot sin(T_0) + j \cdot D_{0,gaps} \\ \text{if } x > B(i) \end{cases} \tag{8.9}$$

Equating the functions of the lower tow boundaries of the main course and the lower course boundary curve of the course above the main course results in the intersection points which define the tow cut locations.

$$x_{intersect,overlaps}(i) = \begin{cases} (D_0 \cdot \rho \cdot cos(T_0) - \frac{1}{4} \cdot (-(-2D_0 + i \cdot w_t + w_t) \cdot (2D_0 + i \cdot w_t + w_t) \cdot \\ (-2D_0 - w_c + i \cdot w_t + 2\rho + w_t) \cdot (2D_0 - w_c + i \cdot w_t + 2\rho + w_t))^{\frac{1}{2}} / D_0 \\ \text{if } B(i) \leq 0 \\ (-D_0 \cdot \rho \cdot cos(T_0) + \frac{1}{4} \cdot ((-2D_0 + i \cdot w_t + w_t) \cdot (2D_0 + i \cdot w_t + w_t) \cdot \\ (2D_0 - w_c + i \cdot w_t - 2\rho + w_t) \cdot (2D_0 + w_c - i \cdot w_t + 2\rho - w_t))^{\frac{1}{2}}) / D_0) \\ \text{if } B(i) > 0 \end{cases} \tag{8.10}$$

Similarly, for the tow cuts of 0 % coverage ratio layup, equating the lower course boundary curve of the course above the main course and the upper boundaries of the individual tows of the main course yields the intersection points which define the tow cut locations.

$$x_{intersect,gaps}(i) = \begin{cases} \rho \cdot (D_0^2 + 2D_0 \cdot D_{0,gaps} + D_{0,gaps}^2) \cdot cos(T_0) - \frac{1}{2} \cdot (-(D_0 + D_{0,gaps} - i \cdot w_t - w_t) \cdot \\ (D_0 + D_{0,gaps} + i \cdot w_t + w_t) \cdot (D_0 + D_{0,gaps} - w_c + i \cdot w_t + 2\rho + w_t) \cdot \\ (D_0 + D_{0,gaps} + w_c - i \cdot w_t - 2\rho - w_t))^{\frac{1}{2}} \cdot \\ (D_0 + D_{0,gaps}))/(D_0^2 + 2D_0 \cdot D_{0,gaps} + D_{0,gaps}^2 \\ \text{if } B(i) \leq 0 \\ (-\rho \cdot (D_0^2 + 2D_0 \cdot D_{0,gaps} + D_{0,gaps}^2) \cdot cos(T_0) + \frac{1}{2} \cdot (-(D_0 + D_{0,gaps} - i \cdot w_t - w_t) \cdot \\ (D_0 + D_{0,gaps} + i \cdot w_t + w_t) \cdot (D_0 + D_{0,gaps} - w_c + i \cdot w_t - 2\rho + w_t) \cdot \\ (D_0 + D_{0,gaps} + w_c - i \cdot w_t + 2\rho - w_t))^{\frac{1}{2}} \cdot \\ (D_0 + D_{0,gaps}))/(D_0^2 + 2D_0 \cdot D_{0,gaps} + D_{0,gaps}^2 \\ \text{if } B(i) > 0 \end{cases} \tag{8.11}$$

Inserting the $x_{intersect,overlaps}(i)$ and $x_{intersect,gaps}(i)$ into the lower course boundary curve for the respective coverage ratio yields the corresponding y-coordinates. Figure 8.1 shows the intersection points and resulting tow cuts for 100 % coverage ratio (Figure 8.1(b)) and 0 % coverage ratio (Figure 8.1(c)).

The novel approach presented in this work, cutting tows only on the inside radius of the steered course, requires adjustments to the layup strategy introduced above. For the reference curve, which is the subject of this explanation, the tow cuts for $x \leq 0$ are performed at the lower boundary of the course and for $x > 0$ at the upper boundary of the course. While for $x > 0$ thus the lower course boundary curve of the course above the main course is used for tow cut definition as in the one-sided tow cut strategy, for $x \leq 0$, the upper course boundary curve of the course below the main course is used to determine the intersection points.

Similar to the bottom boundary curves, the upper course boundary curves for 100 % coverage ratio can be calculated following:

$$y_{upper,overlaps}(x,j) = \begin{cases} \sqrt{(\rho + \frac{w_c}{2})^2 - (x - \rho \cdot cos(T_0))^2} - \rho \cdot sin(T_0) + j \cdot D_0 & \text{if } x \leq -B_0 \\ -\sqrt{(\rho - \frac{w_c}{2})^2 - (x + \rho \cdot cos(T_0))^2} + \rho \cdot sin(T_0) + j \cdot D_0 & \text{if } x > -B_0 \end{cases} \tag{8.12}$$

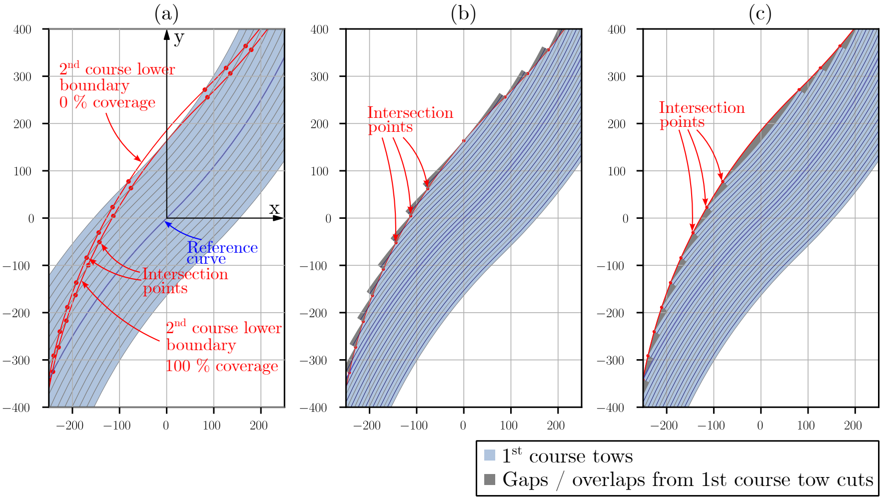

Figure 8.1: Constant curvature Variable Stiffness Panel design with one-sided tow cuts: (a) definition of intersection points, (b) 100 % coverage ratio tow cuts, (c) 0 % coverage ratio tow cuts

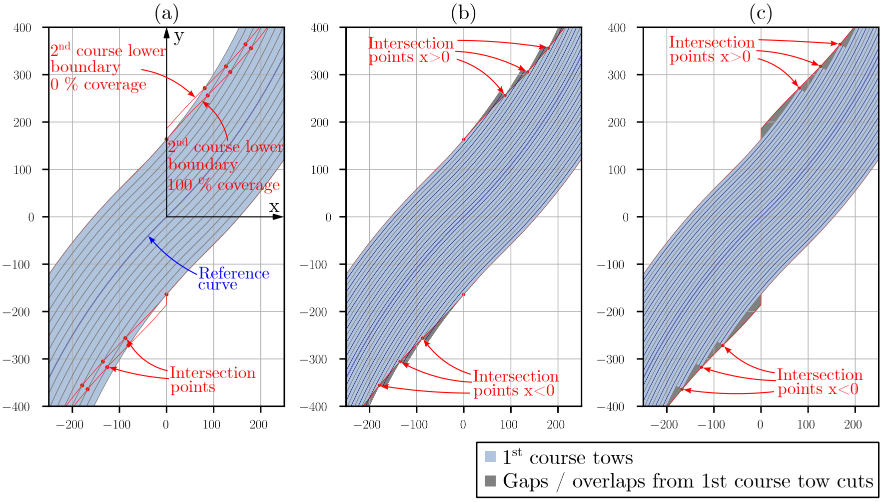

Figure 8.2: Constant curvature Variable Stiffness Panel design with tow cuts at the inner radius: (a) definition of intersection points, (b) 100 % coverage ratio tow cuts, (c) 0 % coverage ratio tow cuts

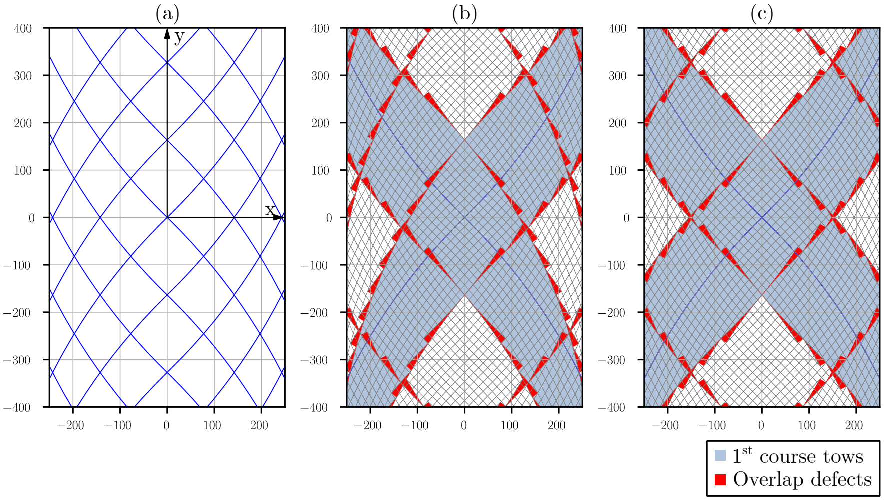

Figure 8.3: Mirrored constant curvature Variable Stiffness plies: (a) Mirrored reference curves, (b) One-sided tow cuts and 100 % coverage ratio, (c) tow cuts at the inner radius and 100 % coverage ratio tow cuts

The upper course boundary curves for 0 % coverage ratio can be calculated following:

$$y_{upper,gaps}(x,j) = \begin{cases} \sqrt{(\rho+\frac{w_c}{2})^2-(x-\rho\cdot cos(T_0))^2}-\rho\cdot sin(T_0)+j\cdot D_{0,gaps} & \text{if } x \leq -B_0 \\ -\sqrt{(\rho-\frac{w_c}{2})^2-(x+\rho\cdot cos(T_0))^2}+\rho\cdot sin(T_0)+j\cdot D_{0,gaps} & \text{if } x > -B_0 \end{cases} \tag{8.13}$$

For $x \leq 0$, intersection points for tow cut positions are determined by equating $y_{upper,overlaps}(x,j)$ and $y_{upper,gaps}(x,j)$ with $y_{tows,bottom}(x,i)$ and $y_{tows_{upper}}(x,i)$ for 0 % and 100 % coverage ratio, respectively. For $x > 0$, intersection points for tow cut positions are determined by equating $y_{bottom,overlaps}(x,j)$ and $y_{bottom,gaps}(x,j)$ with $y_{tows,bottom}(x,i)$ and $y_{tows_{upper}}(x,i)$ for 0 % and 100 % coverage ratio, respectively. The resulting boundary curves and intersection points are presented in figure 8.2(a). The respective tow cuts and defects are shown in figure 8.2(b) and (c), for 0 % and 100 % coverage ratio, respectively.

In order to enable a symmetric Variable Stiffness Panel design, mirrored plies have to be created. For the presented reference curve and path propagation strategy, the paths are mirrored on the y-axis. The definition of reference and boundary curves is given in the python script. Figure 8.3(a) shows shifted reference curves for the mirrored ply orientation and Figure 8.3(a) and (b) show resulting defect patterns for 100 % coverage ratio and one-sided tow cuts and tow cuts at the inner radius, respectively. Due to the symmetry condition, all resulting defects are equivalent for both orientations. It is therefore sufficient to determine the defect geometries for one direction only. The three primary defect types, steering radius and

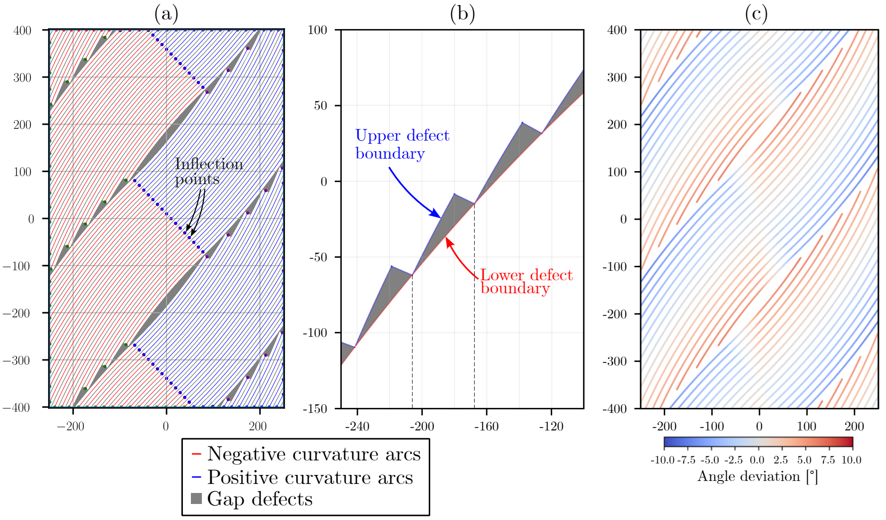

Figure 8.4: Variable Stiffness defect analysis: (a) Steering arc length analysis, (b) Defect area analysis, (c) Angle deviation analysis

arc length, gap or overlap defect dimensions and angle deviation are determined analytically. From the tow-cut positions, inflection points, ply boundaries and steering radii of individual tows, the arc lengths are calculated. Arc lengths calculation is visualized for 0 % coverage ratio and tow cuts at the inner radius in Figure 8.4(a). The curvature direction changes at the inflection point of each individual tow. Gap or overlap defect areas are determined by integrating the upper and lower defects boundary over the length in x-direction of each individual defect and calculating the difference of the two integrals. The length of each individual defect is calculated using the euclidean distance along the major cathetus of the triangluar defect. The width of each defect corresponds to the tape width (Figure 8.4(b).

The reference value of the angle at each x-position is defined by the reference curve $y(x)$. For each tow, the local angle deviation θ_{dev} at each x-position can be calculated as the difference between the derivatives of the respective tow center curve and the reference curve:

$$\theta_{dev}(x,i) = \arctan\left(\frac{dy_{tows}(x,i)}{dx}\right) - \arctan\left(\frac{dy(x)}{dx}\right) \tag{8.14}$$

For the current example with 100 % coverage ratio and tow cuts at the inner radius, the angular deviation is shown in figure 8.4(c). The python algorithm is divided into three Jupyter Notebooks. The first Jupyter Notebook VSP-one-sided.ipynb is a detailed description of the one-sided tow cut strategy for both 0 % and 100 % coverage ratio. The second Jupyter Notebook VSP-inner-radius.ipynb describes the novel strategy with tow cuts at the inner radius for both 0 % and 100 % coverage ratio. The design and analysis algorithms of the different VSP strategies were also extracted into callable functions. The Jupyter Notebook

Table 8.7: Complex fuselage section layup strategy: start point coordinates for fixed angle reference curves, maximum and minimum number of parallel tows

Ply	x [mm]	y [mm]	z [mm]	Max. n [-]	Min. n [-]
1st ±45 °	4300	0	631	160	16
2nd ±45 °	4300	2.48	631	144	16
3rd ±45 °	4300	4.95	631	128	16
4th ±45 °	4300	7.42	631	112	16
1st 0 °	4300	-7	631	64	16
2nd 0 °	4300	-3.5	631	56	16
3rd 0 °	4300	0	631	48	16
4th 0 °	4300	3.5	631	40	16
1st 90 °	2500	0	498	576	-
2nd 90 °	2503.5	0	498	576	-
3rd 90 °	2507	0	498	576	-
4th 90 °	2510.5	0	498	576	-

VSP-parameter-study.ipynb uses these functions to compare the defects for varying input parameters.

A3 Results of complex fuselage geometry analysis

This Appendix chapter presents the developed layup strategy and concomitant angle deviation and steering defects for the complex fuselage geometry. The quasi-isotropic laminate with the ply stacking sequence $[45°/0°/\text{-}45°/90°]_{2S}$ contains four plies of each orientation. In order to avoid through-thickness superimposition of tow boundaries a staggering distance of the consolidated tow width, divided by the number of plies of the same orientation was used (3.5 mm). Table 8.7 presents the resulting start point of each ply. For reasons of symmetry, the 45 ° and -45 ° ply have the same start points. The superimposition of coverage (gap and overlap) defects was avoided by a second staggering value. The number of parallel tows of the first parallel set was iteratively decreased for each subsequent ply of the same orientation by the smallest number of parallel tows in the ply, divided by the total number of sets of the ply. Table 8.8 presents the maximum angle deviation and minimum steering radius of the first ply of each orientation. The maximum values however occurred in very small edge areas, whereas the bulk of the plies showed much less sever angle deviation and geodesic path curvature. Figures 8.5-8.7 present the sets of parallel tows, angle deviation and steering analysis plots for the first ply of each of the main ply orientations.

(a) 1st 45° ply parallel layup sections

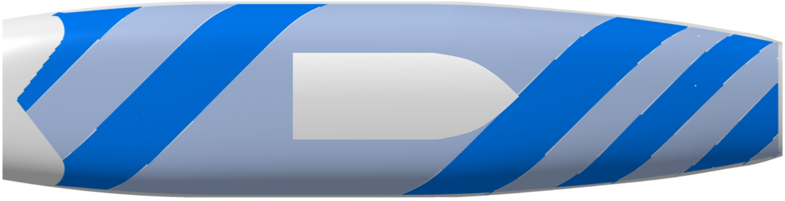

(b) Angle deviation of 1st 45° ply

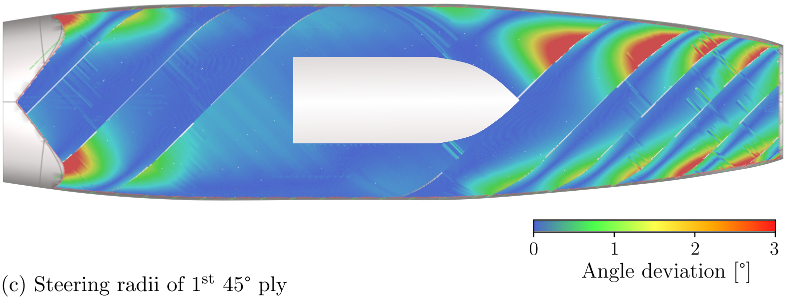

(c) Steering radii of 1st 45° ply

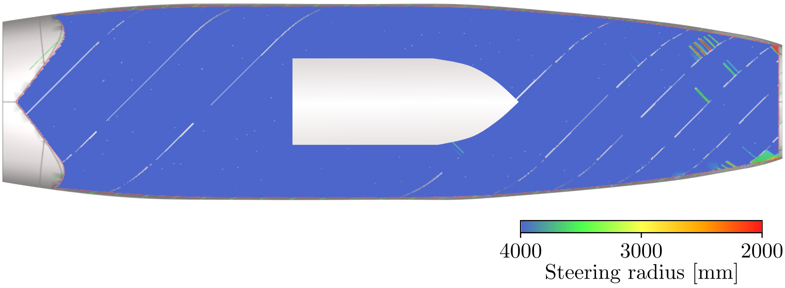

Figure 8.5: Complex fuselage geometry layup analysis results of 1st 45 ° ply

(a) 1st 0° ply parallel layup sections

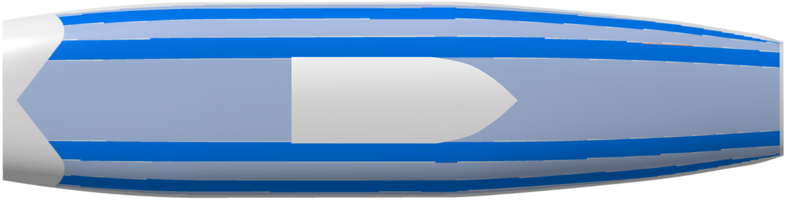

(b) Angle deviation of 1st 0° ply

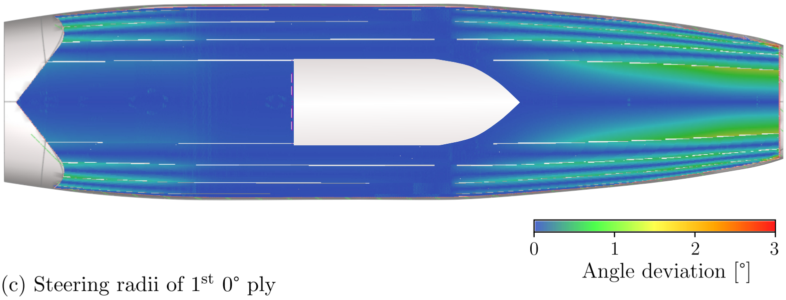

(c) Steering radii of 1st 0° ply

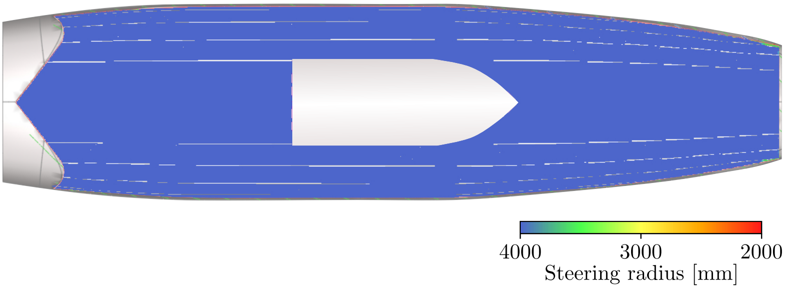

Figure 8.6: Complex fuselage geometry layup analysis results of 1st 0 ° ply

(a) 1^{st} 90° ply parallel layup sections

(b) Angle deviation of 1^{st} 90° ply

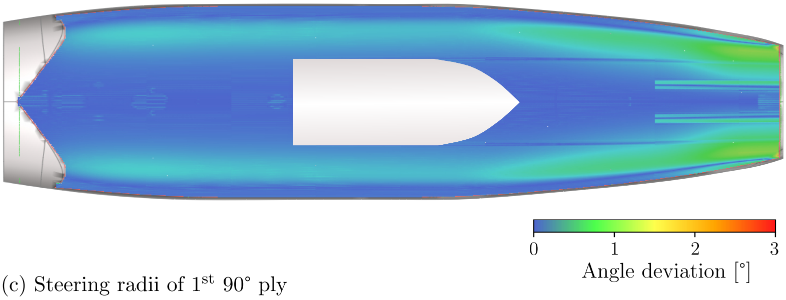

(c) Steering radii of 1^{st} 90° ply

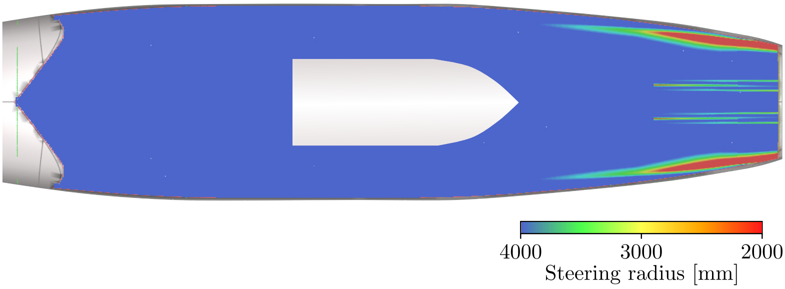

Figure 8.7: Complex fuselage geometry layup analysis results of 1^{st} 90 ° ply

Table 8.8: Angle deviation and steering results of complex fuselage geometry

Ply	Max. angle deviation [°]	Min. steering radius [mm]
1st ±45 °	4.8	1002
1st 0 °	3.7	2556
1st 90 °	2.4	538

A4 Bivariate spline coefficients

This section supplements information on the bivariate spline fits in Chapter 6 as presented in [306]. Half-inch outside edge bivariate spline coefficients:

Knot vector T_x = $[2.78951e^{-14}, 2.78951e^{-14}, 2.78951e^{-14}, 2.78951e^{-14},$ 0.249939, 0.249939, 0.249939, 0.249939]

Knot vector T_y =[1000, 1000, 1000, 1000, 1500, 1500, 1500, 1500]

2D B-spline coefficients: [6.45582, 6.54539, 6.54539, 6.669, 6.98806, 6.45912, 6.45912, 6.29628, 6.71699, 6.51175, 6.51175, 6.4396, 6.58677, 6.45109, 6.45109, 6.02875]

Half-inch inside edge bivariate spline coefficients:

Knot vector T_x = $[-1.70108e^{-12}, -1.70108e^{-12}, -1.70108e^{-12}, -1.70108e^{-12},$ 0.318275, 0.318275, 0.318275, 0.318275]

Knot vector T_y =[1000, 1000, 1000, 1000, 1500, 1500, 1500, 1500]

2D B-spline coefficients: [-7.59577, -7.3603, -7.3603, -7.31099, -9.24179, -9.63879, -9.63879, -9.56711, -5.28991, -5.88401, -5.88401, -6.20487, -7.67588, -7.25631, -7.25631, -7.49023]

Quarter-inch outside edge bivariate spline coefficients:

Knot vector T_x = $[1.10612e^{-12}, 1.10612e^{-12}, 1.10612e^{-12}, 1.10612e^{-12},$ 0.249939, 0.249939, 0.249939, 0.249939]

Knot vector T_y =[1000, 1000, 1000, 1000, 2000, 2000, 2000, 2000]

2D B-spline coefficients: [3.0756, 3.51888, 3.18803, 3.67935, 3.85118, 4.33503, 4.61062, 4.19819, 3.18508, 3.78765, 3.11964, 3.77772, 3.97662, 3.74949, 4.4902, 3.59517]

Quarter-inch inside edge bivariate spline coefficients:

Knot vector T_x = [0.000628381, 0.000628381, 0.000628381, 0.000628381, 0.25418, 0.25418, 0.25418, 0.25418]

Knot vector T_y =[1000, 1000, 1000, 1000, 2000, 2000, 2000, 2000]

2D B-spline coefficients: [-4.89414, -5.39781, -4.22882, -4.80241, -4.86876, -5.02925, -4.66134, -4.91733, -4.85568, -3.07546, -4.93219, -3.71276, -3.76164, -4.07977, -3.54249, -4.36585]

Bibliography

[1] "Boeing 787 from the Ground Up," `https://www.boeing.com/commercial/aeromagazine/articles/qtr_4_06/article_04_2.html`, 2023, Accessed: 2023-10-03.

[2] "A350 Less Weight. Less Fuel. More Sustainable." `https://aircraft.airbus.com/en/aircraft/a350-clean-sheet-clean-start/a350-less-weight-less-fuel-more-sustainable`, 2023, Accessed: 2023-10-03.

[3] Hepher, T., "Airbus eyes slower, more feasible recovery after supply snags," `https://www.reuters.com/business/aerospace-defense/airbus-targets-720-deliveries-2023-2023-02-16/`, 2023, Accessed: 2023-10-08.

[4] Young, R., "Hi-Rate Composite Aircraft Manufacturing (HiCAM) Project," `https://www.toraytac.com/media/f41b20a2-eda7-412c-9699-64af602c4621/Mki5yA/TAC/Documents/Programs/HiCAMOverviewMar_2022_Short.pdf`, 2023, Accessed: 2023-10-08.

[5] "Clean Sky 2 Joint Undertaking DEVELOPMENT PLAN," `https://www.clean-aviation.eu/sites/default/files/2022-03/CS2DP-October-2021.pdf`, 2021, Accessed: 2021-10-28.

[6] Gipson, L., "Hi-Rate Composite Aircraft Manufacturing Project," `https://www.nasa.gov/directorates/armd/aavp/hicam/`, 2023, Accessed: 2023-10-08.

[7] Grimsley, B. W., Cano, R. J., Hudson, T. B., Palmieri, F. L., Wohl, C. J., Ledesma, R. I., Sreekantamurthy, T., Stelter, C. J., Assadi, M. D., Jordan, R. F., Rower, J. H., Edahl, R. A., Shiflett, J. C., Connell, J. W., , and Jensen, B. J., "In-Situ Consolidation Automated Fiber Placement of Thermoplastic Composites for High-Rate Aircraft Manufacturing," *SAMPE Conferene and Exhibition*, 2022.

[8] Krueger, R. and Bergan, A., "Advances in Thermoplastic Composites Over Three Decades–A Literature Review," Tech. rep., NASA Langley Research Center, 2024.

[9] Larsen, L., Endrass, M., Jarka, S., Bauer, S., and Janek, M., “Exploring ultrasonic and resistance welding for thermoplastic composite structures: Process development and application potential,” *Composites Part B: Engineering*, Vol. 289, 2025, pp. 111927.

[10] Lukaszewicz, D. H. J. A., Ward, C., and Potter, K. D., “The engineering aspects of automated prepreg layup: History, present and future,” *Composites Part B: Engineering*, Vol. 43, No. 3, 4 2012, pp. 997–1009.

[11] Yassin, K. and Hojjati, M., “Processing of thermoplastic matrix composites through automated fiber placement and tape laying methods A review,” *Journal of Thermoplastic Composite Materials*, Vol. 31, No. 12, 2018, pp. 1676–1725.

[12] Martin, I., Saenz del Castillo, D., Fernandez, A., and Güemes, A., “Advanced Thermoplastic Composite Manufacturing by In-Situ Consolidation: A Review,” *Journal of Composites Science*, Vol. 4, No. 4, 2020.

[13] Brasington, A., Sacco, C., Halbritter, J., Wehbe, R., and Harik, R., “Automated fiber placement: A review of history, current technologies, and future paths forward,” *Composites Part C: Open Access*, Vol. 6, 2021, pp. 100182.

[14] Boon, Y. D., Joshi, S. C., and Bhudolia, S. K., “Review: Filament Winding and Automated Fiber Placement with In Situ Consolidation for Fiber Reinforced Thermoplastic Polymer Composites,” *Polymers*, Vol. 13, No. 12, 2021.

[15] Hardesty, E., Goldsworthy, W., and Karlson, H., “Geodesic path length compensator for composite-tape placement head,” U.S. Patent No. US3810805A, 1972.

[16] Evans, D. O., *Fiber Placement*, Springer US, pp. 476–487.

[17] Anderson, R. L. and Grant, C. G., “Advanced fiber placement of composite fuselage structures,” *NASA. Langley Research Center, First NASA Advanced Composites Technology Conference, Part 2*, 1991.

[18] Good, D. E. and Mazza, L. T., “Advanced composite airframe program: Today’s technology,” *NASA, Washington, NASA (Army Rotorcraft Technology. Volume 2: Materials and Structures, Propulsion and Drive Systems, Flight Dynamics and Control, and Acoustics*, 1988.

[19] Good, D. and Kay, B. F., “New Technology on ACAP,” *AIAA/ASME/ASCE/AHS Structures, Structural Dynamics and Materials Conference*, 1983.

[20] Grant, C. G. and Benson, V. M., “Automated fiber placement: Evolution and current demonstrations,” *NASA. Langley Research Center, Third NASA Advanced Composites Technology Conference, Volume 1, Part 2*, 1993.

[21] Evans, D. O., Vaniglia, M. M., and Hopkins, P. C., "Fiber placement process study," *Tomorrow's Materials: Today.*, Vol. 34, 1989, pp. 1822–1833.

[22] Bullock, F., Kowalski, S., and Young, R., "Automated prepreg tow placement for composite structures." *ADVANCED MATERIALS: THE CHALLENGE FOR THE NEXT DECADE.*, Vol. 1, 1990, pp. 734–745.

[23] Vickers, J. H. and Pelham, L. I., "Automated fiber placement composite manufacturing: The mission at MSFC's Productivity Enhancement Complex," *NASA, Washington, Technology 2002: The Third National Technology Transfer Conference and Exposition, Volume 2*, 1993.

[24] Beyeler, E., Phillips, W., and Güçeri, S. I., "Experimental Investigation of Laser-Assisted Thermoplastic Tape Consolidation," Vol. 1, No. 1, 1988, pp. 107–121.

[25] Mantell, S. C., Wang, Q., and Springer, G. S., "Processing Thermoplastic Composites in a Press and by Tape Laying—Experimental Results," *Journal of Composite Materials*, Vol. 26, No. 16, 1992, pp. 2378–2401.

[26] Mazumdar, S. K. and Hoa, S. V., "Determination of Manufacturing Conditions for Hot-Gas-Aided Thermoplastic Tape Winding," *Journal of Thermoplastic Composite Materials*, Vol. 9, No. 1, 1996, pp. 35–53.

[27] Cano, R. J., Belvin, H. L., Hulcher, A. B., and Grenoble, R. W., "Studies on automated manufacturing of high performance composites," *American Helicopter Society Hampton Roads Chapter, Structure Specialists' Meeting*, 2001.

[28] Shadmehri, F., Hoa, S. V., Fortin-Simpson, J., and Ghayoor, H., "Effect of in situ treatment on the quality of flat thermoplastic composite plates made by automated fiber placement (AFP)," *Advanced Manufacturing: Polymer & Composites Science*, Vol. 4, No. 2, 2018, pp. 41–47.

[29] Qureshi, Z., Swait, T., Scaife, R., and El-Dessouky, H. M., "In situ consolidation of thermoplastic prepreg tape using automated tape placement technology: Potential and possibilities," *Composites Part B: Engineering*, Vol. 66, 2014, pp. 255–267.

[30] Lamontia, M. A., Gruber, M. B., Waibel, B. J., Cope, R. D., and Hulcher, A. B., "Conformable compaction system used in automated fiber placement of large composite aerospace structures," *23rd SAMPE EUROPE Conference, Paris*, 2002, pp. 9–11.

[31] Lamontia, M. A., Funck, S. B., Gruber, M. B., Cope, R. D., Waibel, B. J., and Gopez, N. M., "Manufacturing flat and cylindrical laminates and built up structure using

automated thermoplastic tape laying, fiber placement, and filament winding," *SAMPE JOURNAL*, Vol. 39, No. 2, 3 2003, pp. 30–38.

[32] Lamontia, M. A. and Gruber, M. B., "Limitations on mechanical properties in thermoplastic laminates fabricated by two processes: automated thermoplastic tape placement and filament winding," *26th SAMPE Europe conference, Paris*, 2005.

[33] Lamontia, M. A., Gruber, M. B., Tierney, J. J., Gillespie Jr, J. W., Jensen, B. J., and Cano, R. J., "Modeling the accudyne thermoplastic in situ ATP process," *30th International SAMPE Europe Conference, Paris*, 2009.

[34] Lamontia, M. A., Gruber, M. B., Tierney, J. J., Gillespie Jr, J. W., Jensen, B. J., and Cano, R. J., "In situ thermoplastic ATP needs flat tapes and tows with few voids," *30th international SAMPE Europe conference, Paris*, 2009.

[35] Gruber, M. B., Lockwood, I. Z., Dolan, T. L., Funck, S. B., Tierney, J. J., Simacek, P., Gillespie Jr, J. W., Advani, S. G., Jensen, B. J., Cano, R. J., et al., "Thermoplastic in situ placement requires better impregnated tapes and tows," *Proceedings of the 2012 SAMPE conference and exhibition, Baltimore, MD*, 2012.

[36] Stokes-Griffin, C. M. and Compston, P., "The effect of processing temperature and placement rate on the short beam strength of carbon fibre–PEEK manufactured using a laser tape placement process," *Composites Part A: Applied Science and Manufacturing*, Vol. 78, 2015, pp. 274–283.

[37] "Trelleborg Group Website," `https://www.trelleborg.com/en/seals/products-and-solutions/advanced-composites/composite-structures/processes`, 2023, Accessed: 2023-11-19.

[38] Khan, M. A., Mitschang, P., and Schledjewski, R., "Tracing the Void Content Development and Identification of its Effecting Parameters during in Situ Consolidation of Thermoplastic Tape Material," *Polymers and Polymer Composites*, Vol. 18, No. 1, 2010, pp. 1–15.

[39] Khan, M. A., Mitschang, P., and Schledjewski, R., "Identification of some optimal parameters to achieve higher laminate quality through tape placement process," *Advances in Polymer Technology*, Vol. 29, No. 2, 2010, pp. 98–111.

[40] Agarwal, V., Mccullough, R. L., and Schultz, J. M., "The Thermoplastic Laser-Assisted Consolidation Process-Mechanical and Microstructure Characterization," *Journal of Thermoplastic Composite Materials*, Vol. 9, No. 4, 1996, pp. 365–380.

[41] Rosselli, F. and Santare, M. H., "Comparison of the short beam shear (SBS) and interlaminar shear device (ISD) tests," *Composites Part A: Applied Science and Manufacturing*, Vol. 28, No. 6, 1997, pp. 587–594.

[42] Rosselli, F., Santare, M. H., and Güçeri, S. I., "Effects of processing on laser assisted thermoplastic tape consolidation," *Composites Part A: Applied Science and Manufacturing*, Vol. 28, No. 12, 1997, pp. 1023–1033.

[43] Pistor, C. M. and Güçeri, S. I., "Crystallinity of On-Line Consolidated Thermoplastic Composites," *Journal of Composite Materials*, Vol. 33, No. 4, 1999, pp. 306–324.

[44] Mazumdar, S. K. and Hoa, S. V., "Application of Taguchi method for process enhancement of on-line consolidation technique," *Composites*, Vol. 26, No. 9, 1995, pp. 669–673.

[45] Miao, Q., Dai, Z., Ma, G., Niu, F., and Wu, D., "Effect of consolidation force on interlaminar shear strength of CF/PEEK laminates manufactured by laser-assisted forming," *Composite Structures*, Vol. 266, 2021, pp. 113779.

[46] Schledjewski, R. and Miaris, A., "Thermoplastic tape placement by means of diode laser heating," *International SAMPE symposium and exhibition (proceedings) (Vol. 54)*, 2009.

[47] Grouve, W. J. B., Warnet, L. L., Rietman, B., Visser, H. A., and Akkerman, R., "Optimization of the tape placement process parameters for carbon–PPS composites," *Composites Part A: Applied Science and Manufacturing*, Vol. 50, 2013, pp. 44–53.

[48] Henne, F., Ehard, S., Kollmannsberger, A., Hoeck, B., Sause, M., and Drechsler, K., "Thermoplastic in situ fiber placement for future solid rocket motor casings manufacturing," *Proceedings of the 9th SAMPE Europe Technical Conference & Table Top Exhibition*, 2014.

[49] Comer, A., Hammond, P., Ray, D., Lyons, J., Obande, W., Jones, D., O'Higgins, R., and McCarthy, M., "Wedge peel interlaminar toughness of carbon-fibre/PEEK thermoplastic laminates manufactured by laser-assisted automated-tape-placement (LATP)," *Proceedings of the 9th SAMPE Europe Technical Conference & Table Top Exhibition*, Vol. 14, 2014, pp. 10–11.

[50] Stokes-Griffin, C. M. and Compston, P., "Laser-Assisted Tape Placement of Thermoplastic Composites: The Effect of Process Parameters on Bond Strength," *Sustainable Automotive Technologies 2013*, edited by J. Wellnitz, A. Subic, and R. Trufin, Springer International Publishing, 2014, pp. 133–141.

[51] Comer, A. J., Ray, D., Obande, W. O., Jones, D., Lyons, J., Rosca, I., O'Higgins, R. M., and McCarthy, M. A., "Mechanical characterisation of carbon fibre-PEEK manufactured

by laser-assisted automated-tape-placement and autoclave," *Composites Part A: Applied Science and Manufacturing*, Vol. 69, 2 2015, pp. 10–20.

[52] Ray, D., Comer, A. J., Lyons, J., Obande, W., Jones, D., Higgins, R. M. O., and McCarthy, M. A., "Fracture toughness of carbon fiber/polyether ether ketone composites manufactured by autoclave and laser-assisted automated tape placement," *Journal of Applied Polymer Science*, Vol. 132, No. 11, 3 2015.

[53] Saenz-Castillo, D., Martín, M. I., Calvo, S., Rodriguez-Lence, F., and Güemes, A., "Effect of processing parameters and void content on mechanical properties and NDI of thermoplastic composites," *Composites Part A: Applied Science and Manufacturing*, Vol. 121, 2019, pp. 308 – 320.

[54] Zinnecker, V., Backmann, V., Stokes-Griffin, C., Drechsler, K., and Compston, P., "Laser-assisted thermoplastic tape placement: Effects of consolidation roller diameter on wedge peel strength of CF/PA 6," *SAMPE Europe Conference 2020*, 2020.

[55] Schiel, I., Raps, L., Chadwick, A. R., Schmidt, I., Simone, M., and Nowotny, S., "An investigation of in-situ AFP process parameters using CF/LM-PAEK," *Advanced Manufacturing: Polymer & Composites Science*, Vol. 6, No. 4, 2020, pp. 191–197.

[56] Raps, L., Chadwick, A. R., Schiel, I., and Schmidt, I., "CF/LM-PAEK: Characterisation and sensitivity to critical process parameters for automated fibre placement," *Composite Structures*, Vol. 284, 2022, pp. 115087.

[57] Raps, L., Chadwick, A. R., Schiel, I., and Nowotny, S., "High speed processing of low-melt polyaryletherketone prepreg using in-situ consolidation Automated Fiber Placement," *Proceedings of SAMPE North America Conference*, 2023.

[58] Kotzur, K., Chadwick, A. R., and Löbbecke, M., "Moderation of thermoplastic composite crystallinity and mechanical properties through in-situ manufacturing and post-manufacturing tempering: Part 2 – Morphological characterisation," *Composites Part A: Applied Science and Manufacturing*, Vol. 163, 2022, pp. 107225.

[59] Chadwick, A. R., Kotzur, K., and Nowotny, S., "Moderation of thermoplastic composite crystallinity and mechanical properties through in-situ manufacturing and post-manufacturing tempering: Part 1 - Mechanical characterisation," *Composites Part A: Applied Science and Manufacturing*, 2021, pp. 106286.

[60] Khudiakova, A., Brunner, A. J., Wolfahrt, M., and Pinter, G., "Quantification Approaches for Fatigue Crack Resistance of Thermoplastic Tape Layered Composites with Multiple Delaminations," *Materials*, Vol. 14, No. 6, 2021.

[61] Khudiakova, A., Brunner, A. J., Wolfahrt, M., Wettemann, T., Godec, D., and Pinter, G., "On the investigation of quasi-static crack resistance of thermoplastic tape layered composites with multiple delaminations: Approaches for quantification," *Composites Part A: Applied Science and Manufacturing*, Vol. 149, 2021, pp. 106484.

[62] Chanteli, A., Bandaru, A. K., Peeters, D., O'Higgins, R. M., and Weaver, P. M., "Influence of repass treatment on carbon fibre-reinforced PEEK composites manufactured using laser-assisted automatic tape placement," *Composite Structures*, Vol. 248, 2020, pp. 112539.

[63] Zhao, D., Liu, W., Yue, G., Song, Q., Chen, J., and Pan, L., "Determination of thermal degradation for high-performance thermoplastic composites manufactured by laser-assisted automated fibre placement," *High Performance Polymers*, Vol. 0, No. 0, 2021, pp. 09540083211044677.

[64] Zhao, D., Chen, J., Zhang, H., Liu, W., Yue, G., and Pan, L., "Effects of processing parameters on the performance of carbon fiber reinforced polyphenylene sulfide laminates manufactured by laser-assisted automated fiber placement," *Journal of Composite Materials*, Vol. 56, No. 3, 2022, pp. 427–439.

[65] Heathman, N., Koirala, P., Yap, T., Emami, A., and Tehrani, M., "In situ consolidation of carbon fiber PAEK via laser-assisted automated fiber placement," *Composites Part B: Engineering*, Vol. 249, 2023, pp. 110405.

[66] Heathman, N. T., Kirchhoff, J. G., Yap, T., and Tehrani, M., "Understanding Interlaminar Bonding and Fracture Toughness in in-situ consolidated Automated Fiber Placement of Carbon Fiber LMPAEK Composites," *SAMPE 2023 Conference and Exhibition*, Soc. for the Advancement of Material and Process Engineering, 2023.

[67] E. Rodríguez-Senín, N. González-Castro, B. S. and Coto, I., "A STUDY ON CONSOLIDATION OF THERMOPLASTIC COMPOSITES WITH IN-SITU AUTOMATED FIBER PLACEMENT PROCESS," *23rd International Conference on Composite Materials (ICCM23)*, 2023.

[68] Pérez-Martín, H., Buchalik-Bopp, S., Guettler, B. E., Mackenzie, P., Baidak, A., Ó Brádaigh, C. M., and Ray, D., "Effect of crystallinity and morphology on the mechanical properties of CF/PEKK composites manufactured under compression moulding and automated tape placement," *Materials Today Communications*, Vol. 36, 2023, pp. 106442.

[69] Stokes-Griffin, C., *A combined optical-thermal model for laser-assisted fibre placement of thermoplastic composite materials*, Ph.D. thesis.

[70] Pistor, C. M., Yardimci, M. A., and Güçeri, S. I., "On-line consolidation of thermoplastic composites using laser scanning," *Composites Part A: Applied Science and Manufacturing*, Vol. 30, No. 10, 1999, pp. 1149–1157.

[71] Kollmannsberger, A., *Heating characteristics of fixed focus laser assisted Thermoplastic-Automated Fiber Placement of 2D and 3D parts*, Ph.D. thesis, Technische Universität München, 2019.

[72] Wang, F., Zhong, L., Tang, X., Xu, C., and Wan, C., "A homogeneous focusing system for diode lasers and its applications in metal surface modification," *Optics & Laser Technology*, Vol. 102, 2018, pp. 197–206.

[73] Köhler, B., Noeske, A., Kindervater, T., Wessollek, A., Brand, T., and Biesenbach, J., "11-kW direct diode laser system with homogenized 55× 20 mm2 Top-Hat intensity distribution," *High-Power Diode Laser Technology and Applications V*, Vol. 6456, SPIE, 2007, pp. 214–225.

[74] Laskin, A., Kaiser, P., Laskin, V., and Ostrun, A., "Laser beam shaping for biomedical microscopy techniques," *Biophotonics: Photonic Solutions for Better Health Care V*, edited by J. Popp, V. V. Tuchin, D. L. Matthews, and F. S. Pavone, Vol. 9887, International Society for Optics and Photonics, SPIE, 2016, p. 98872E.

[75] Song, Y., Chen, Y., Xin, J., and Sun, T., "Two-dimensional beam shaping and homogenization of high power laser diode stack with rectangular waveguide," *Frontiers of Optoelectronics*, Vol. 12, 2019, pp. 311–316.

[76] Kölzer, P., *Temperaturerfassungssystem und Prozessregelung des laserunterstützten Wickelns und Tapelegens von endlos faserverstärkten thermoplastischen Verbundkunststoffen*, Ph.D. thesis, 2008.

[77] Assadi, M. D., "High Speed AFP Processing of Thermoplastics," *SAMPE Journal*, Vol. 57, No. 5, 2021.

[78] Weiler, T., Emonts, M., Wollenburg, L., and Janssen, H., "Transient thermal analysis of laser-assisted thermoplastic tape placement at high process speeds by use of analytical solutions," *Journal of Thermoplastic Composite Materials*, Vol. 31, No. 3, 2018, pp. 311–338.

[79] Weiler, T., Emonts, M., and Janssen, H., "On the use of flexible intensity distributions for thermoplastic tape placement by means of vertical-cavity surface-emitting laser (vcsel)," *3rd International Conference on Thermoplastic Composites, At Bremen*, 2016.

[80] Brecher, C., Emonts, M., Striet, P., Voell, A., Stollenwerk, J., and Janssen, H., "Adaptive tape placement process control at geometrically changing substrates," *Procedia CIRP*, Vol. 85, 2019, pp. 207–211, 2nd CIRP Conference on Composite Material Parts Manufacturing, 10-11 October 2019, Advanced Manufacturing Research Centre, UK.

[81] Zenker, Thomas und Schwab, M., "Analysis of Fiber Steering Effects in Thermoplastic Automated Fiber Placement," *ECCM18 - 18th European Conference on Composite Materials*, 2018.

[82] Tierney, J. and J. W. Gillespie, J., "Modeling of In Situ Strength Development for the Thermoplastic Composite Tow Placement Process," *Journal of Composite Materials*, Vol. 40, No. 16, 2006, pp. 1487–1506.

[83] Yousefpour, A. and Nejhad, M. N. G., "Experimental and Computational Study of APC-2/AS4 Thermoplastic Composite C-Rings," *Journal of Thermoplastic Composite Materials*, Vol. 14, No. 2, 2001, pp. 129–145.

[84] Hulcher, A., McGowan, D., Grimsley, B., Belvin, H., and Johnson, N., "Processing and testing of thermoplastic composite cylindrical shells fabricated by automated fiber placement," *47th International SAMPE Symposium and Exhibition*, 2002, pp. 1812–1826.

[85] Sun, W.-C., Mantell, S. C., and Stelson, K. A., "Demonstration of Bond Quality Improvement for Closed Loop Control of Thermoplastic Tape-Laying," *Journal of Composite Materials*, Vol. 35, No. 1, 2001, pp. 57–76.

[86] Deden et al., "Optimizing in-situ Consolidation of Xenon Flashlamp based Automated Fiber Placement," *Aerospace Europe Conference*, 2020.

[87] Fricke, D., Doll, G., Nowotny, S., and Poursartip, A., "Manufacturing simulation of the in-situ tape laying process for thermoplastic carbon fiber reinforced tapes," *SAMPE 2018 Technical Conference and Exhibition*, 5 2018.

[88] Fricke, D., "Fertigungssimulation des Tapelegeprozesses mit in-situ Konsolidierung von faserverstärkten thermoplastischen Tapes," *Deutscher Luft- und Raumfahrtkongress 2019*, 9 2019.

[89] Fricke, D. and Fischer, F., "Process Simulation of the In-Situ Automated Fiber Placement Process for Thermoplastic Composites," *SAMPE Europe Conference 2020*, September 2020.

[90] Fricke, D., "Numeric optimization of in-situ consolidated panels with different tape sequence strategies," *SAMPE Europe*, September 2021.

[91] Fricke, D., Raps, L., and Schiel, I., "Prediction of warping in thermoplastic AFP-manufactured laminates through simulation and experimentation," *Advanced Manufacturing: Polymer & Composites Science*, Vol. 8, No. 1, 2022, pp. 1–10.

[92] Lichtinger, R., Hörmann, P., Stelzl, D., and Hinterhölzl, R., "The effects of heat input on adjacent paths during Automated Fibre Placement," *Composites Part A: Applied Science and Manufacturing*, Vol. 68, 2015, pp. 387–397.

[93] Kollmannsberger, A., Lichtinger, R., Hohenester, F., Ebel, C., and Drechsler, K., "Numerical analysis of the temperature profile during the laser-assisted automated fiber placement of CFRP tapes with thermoplastic matrix," *Journal of Thermoplastic Composite Materials*, Vol. 31, No. 12, 12 2018, pp. 1563–1586.

[94] Grouve, W., *Weld strength of laser-assisted tape-placed thermoplastic composites*, Ph.D. thesis, 2012.

[95] Stokes-Griffin, C. M. and Compston, P., "A combined optical-thermal model for near-infrared laser heating of thermoplastic composites in an automated tape placement process," *Composites Part A: Applied Science and Manufacturing*, Vol. 75, 2015, pp. 104–115.

[96] Hosseini, S. A., Baran, I., van Drongelen, M., and Akkerman, R., "On the temperature evolution during continuous laser-assisted tape winding of multiple C/PEEK layers: The effect of roller deformation," *International Journal of Material Forming*, 2020, pp. 1–19.

[97] Oromiehie, E., Prusty, B. G., Compston, P., and Rajan, G., "In situ process monitoring for automated fibre placement using fibre Bragg grating sensors," *Structural Health Monitoring*, Vol. 15, No. 6, 2016, pp. 706–714.

[98] Saenz Del Castillo, D., Martin, I., Rodriguez-Lence, F., and GUEMES, A., "On-line monitoring of a laser-assisted fiber placement process with CFR thermoplastic matrix by using fiber Bragg gratings," *8th European workshop on structural health monitoring (EWSHM 2016)*, 2016.

[99] Grove, S. M., "Thermal modelling of tape laying with continuous carbon fibre-reinforced thermoplastic," *Composites*, Vol. 19, No. 5, 1988, pp. 367–375.

[100] Weiler, T., *Thermal skin effect in laser-assisted tape placement of thermoplastic composites; 1. Auflage*, Dissertation, RWTH Aachen University, Aachen, 2019, Veröffentlicht auf dem Publikationsserver der RWTH Aachen University; Dissertation, RWTH Aachen University, 2019.

[101] Reichardt, J., Baran, I., and Akkerman, R., “New analytical and numerical optical model for the laser assisted tape winding process,” *Composites Part A: Applied Science and Manufacturing*, Vol. 107, 2018, pp. 647–656.

[102] Di Francesco, M., Veldenz, L., Dell’Anno, G., and Potter, K., “Heater power control for multi-material, variable speed Automated Fibre Placement,” *Composites Part A: Applied Science and Manufacturing*, Vol. 101, 2017, pp. 408–421.

[103] Suemasu, H., Yuichiro, A. O. K. I., HOSHI, H., TATEISHI, Y., SUGIMOTO, S., and NAKAMURA, T., “Thermal Analysis for In-Situ Consolidation in the AFP Process,” *Composites Part A: Applied Science and Manufacturing*, 2023, pp. 107577.

[104] Stokes-Griffin, C. M. and Compston, P., “Investigation of sub-melt temperature bonding of carbon-fibre/PEEK in an automated laser tape placement process,” *Composites Part A: Applied Science and Manufacturing*, Vol. 84, 2016, pp. 17–25.

[105] Schaefer, Y., “Entwicklung einer Methodik zur Quantifizierung von Porositaet und Faserondulationen in thermoplastischem Faserverbund (Bachelorarbeit),” Tech. rep., Universität Stuttgart, 2023.

[106] Raps, L., Chadwick, A. R., Mössinger, I., Vinot, M., Behling, T., and Schaefer, Y., “Characteristics of in-situ automated fiber placement carbon-fiber-reinforced low-melt polyaryl ether ketone laminates part 2: Effect of prepreg composition,” *Journal of Composite Materials*, Vol. 58, No. 13, 2024, pp. 1523–1535.

[107] Mantell, S. C. and Springer, G. S., “Manufacturing Process Models for Thermoplastic Composites,” *Journal of Composite Materials*, Vol. 26, No. 16, 1992, pp. 2348–2377.

[108] Yang, F. and Pitchumani, R., “A fractal Cantor set based description of interlaminar contact evolution during thermoplastic composites processing,” *Journal of Materials Science*, Vol. 36, No. 19, 2001, pp. 4661 – 4671.

[109] Yang, F. and Pitchumani, R., “Fractal Description of Interlaminar Contact Development during Thermoplastic Composites Processing,” *Journal of Reinforced Plastics and Composites*, Vol. 20, No. 7, 2001, pp. 536–546.

[110] Khodaei, A. and Shadmehri, F., “Intimate contact development for automated fiber placement of thermoplastic composites,” *Composites Part C: Open Access*, Vol. 8, 2022, pp. 100290.

[111] Celik, O. and Teuwen, J. J. E., “Effects of Process Parameters on Intimate Contact Development in Laser Assisted Fiber Placement,” *Proceedings of the 4th Automated Composites Manufacturing (ACM4)*, 2019, pp. 25–26.

[112] Çelik, O., Peeters, D., Dransfeld, C., and Teuwen, J., "Intimate contact development during laser assisted fiber placement: Microstructure and effect of process parameters," *Composites Part A: Applied Science and Manufacturing*, Vol. 134, 2020, pp. 105888.

[113] Hoa, S. V., Hoang, M. D., and Simpson, J., "Manufacturing procedure to make flat thermoplastic composite laminates by automated fibre placement and their mechanical properties," *Journal of Thermoplastic Composite Materials*, Vol. 30, No. 12, 9 2016, pp. 1693–1712.

[114] Yang, F. and Pitchumani, R., "Healing of thermoplastic polymers at an interface under nonisothermal conditions," *Macromolecules*, Vol. 35, No. 8, 2002, pp. 3213–3224.

[115] Yang, F. and Pitchumani, R., "Nonisothermal Healing and Interlaminar Bond Strength Evolution During Thermoplastic Matrix Composites Processing," *Polymer Composites*, Vol. 24, No. 2, 2003, pp. 263 – 278, Cited by: 57.

[116] Saenz-Castillo, D., Martín, M. I., García-Martínez, V., Ramesh, A., Battley, M., and Güemes, A., "A comparison of mechanical properties and X-ray tomography analysis of different out-of-autoclave manufactured thermoplastic composites," *Journal of Reinforced Plastics and Composites*, Vol. 39, No. 19-20, 2020, pp. 703–720.

[117] Çelik, O., Choudhary, A., Peeters, D., Teuwen, J., and Dransfeld, C., "Deconsolidation of thermoplastic prepreg tapes during rapid laser heating," *Composites Part A: Applied Science and Manufacturing*, Vol. 149, 2021, pp. 106575.

[118] Ranganathan, S., Advani, S. G., and Lamontia, M. A., "A Non-Isothermal Process Model for Consolidation and Void Reduction during In-Situ Tow Placement of Thermoplastic Composites," *Journal of Composite Materials*, Vol. 29, No. 8, 1995, pp. 1040–1062.

[119] Tierney, J. and John W. Gillespie, J., "Modeling of Heat Transfer and Void Dynamics for the Thermoplastic Composite Tow-Placement Process," *Journal of Composite Materials*, Vol. 37, No. 19, 2003, pp. 1745–1768.

[120] Pitchumani, R., Ranganathan, S., Don, R. C., Gillespie, J. W., and Lamontia, M. A., "Analysis of transport phenomena governing interfacial bonding and void dynamics during thermoplastic tow-placement," *International Journal of Heat and Mass Transfer*, Vol. 39, No. 9, 1996, pp. 1883–1897.

[121] Pitchumani, R., J. W. Gillespie, J., and Lamontia, M. A., "Design and Optimization of a Thermoplastic Tow-Placement Process with In-Situ Consolidation," *Journal of Composite Materials*, Vol. 31, No. 3, 1997, pp. 244–275.

[122] Song, Q., Liu, W., Chen, J., Zhao, D., Yi, C., Liu, R., Geng, Y., Yang, Y., Zheng, Y., and Yuan, Y., "Research on Void Dynamics during In Situ Consolidation of CF/High-Performance Thermoplastic Composite," *Polymers*, Vol. 14, No. 7, 2022.

[123] Zhang, D., Heider, D., and John W Gillespie, J., "Determination of void statistics and statistical representative volume elements in carbon fiber-reinforced thermoplastic prepregs," *Journal of Thermoplastic Composite Materials*, Vol. 30, No. 8, 2017, pp. 1103–1119.

[124] E. Tobin, R. M. O. and Weaver, P. M., "The Influence of Processing Parameters on Tape Deconsolidation in Thermoplastic Composites," *23rd International Conference on Composite Materials (ICCM23)*, 2023.

[125] Vohlídal, J., "Polymer degradation: a short review," *Chemistry Teacher International*, Vol. 3, No. 2, 2021, pp. 213–220.

[126] Cogswell, F. N., *Thermoplastic aromatic polymer composites: a study of the structure, processing and properties of carbon fibre reinforced polyetheretherketone and related materials*, Elsevier, 2013.

[127] Day, M., Cooney, J. D., and Wiles, D. M., "The thermal stability of poly (aryl-ether–ether-ketone) as assessed by thermogravimetry," *Journal of applied polymer science*, Vol. 38, No. 2, 1989, pp. 323–337.

[128] Fink, B. K., Gillespie, J. W., and Ersoy, N. B., *Thermal degradation effects on consolidation and bonding in the thermoplastic fiber-placement process*, Army Research Laboratory, 2000.

[129] Gaitanelis, D., Chanteli, A., Worrall, C., Weaver, P. M., and Kazilas, M., "A multi-technique and multi-scale analysis of the thermal degradation of PEEK in laser heating," *Polymer Degradation and Stability*, Vol. 211, 2023, pp. 110282.

[130] Veazey, D., Hsu, T., and Gomez, E. D., "Next generation high-performance carbon fiber thermoplastic composites based on polyaryletherketones," *Journal of Applied Polymer Science*, Vol. 134, No. 6, 2017.

[131] Tregub, A., Harel, H., Marom, G., and Migliaresi, C., "The influence of thermal history on the mechanical properties of poly(ether ether ketone) matrix composite materials," *Composites Science and Technology*, Vol. 48, No. 1, 1993, pp. 185–190, Special Issue Microphenomena in Advanced Composites.

[132] Quan, H., Li, Z.-M., Yang, M.-B., and Huang, R., "On transcrystallinity in semi-crystalline polymer composites," *Composites Science and Technology*, Vol. 65, No. 7, 2005, pp. 999–1021.

[133] Gao, S.-L. and Kim, J.-K., "Cooling rate influences in carbon fibre/PEEK composites. Part 1. Crystallinity and interface adhesion," *Composites Part A: Applied Science and Manufacturing*, Vol. 31, No. 6, 2000, pp. 517–530.

[134] Gao, S.-L. and Kim, J.-K., "Cooling rate influences in carbon fibre/PEEK composites. Part II: interlaminar fracture toughness," *Composites Part A: Applied Science and Manufacturing*, Vol. 32, No. 6, 2001, pp. 763–774.

[135] Gao, S.-L. and Kim, J.-K., "Correlation among crystalline morphology of PEEK, interface bond strength, and in-plane mechanical properties of carbon/PEEK composites," *Journal of Applied Polymer Science*, Vol. 84, No. 6, 2002, pp. 1155–1167.

[136] Tierney, J. J. and Gillespie Jr., J. W., "Crystallization kinetics behavior of PEEK based composites exposed to high heating and cooling rates," *Composites Part A: Applied Science and Manufacturing*, Vol. 35, No. 5, 2004, pp. 547–558.

[137] Guan, X. and Pitchumani, R., "Modeling of spherulitic crystallization in thermoplastic tow-placement process: spherulitic microstructure evolution," *Composites Science and Technology*, Vol. 64, No. 9, 2004, pp. 1363–1374.

[138] Gordnian, K., *Crystallization and thermo-viscoelastic modelling of polymer composites*, Ph.D. thesis.

[139] Teltschik, J., Fricke, D., and Horn, M., "Efficient Determination of Material Parameters for Robust Process Simulation of Semi-Crystalline Thermoplastic Composites," *ITHEC 2020 – International Conference and Exhibition on Thermoplastic Composites*, Oktober 2020.

[140] Parlevliet, P. P., Bersee, H. E. N., and Beukers, A., "Residual stresses in thermoplastic composites—A study of the literature—Part I: Formation of residual stresses," *Composites Part A: Applied Science and Manufacturing*, Vol. 37, No. 11, 2006, pp. 1847–1857.

[141] Parlevliet, P. P., Bersee, H. E. N., and Beukers, A., "Residual stresses in thermoplastic composites – a study of the literature. Part III: Effects of thermal residual stresses," *Composites Part A: Applied Science and Manufacturing*, Vol. 38, No. 6, 2997, pp. 1581–1596.

[142] Chapman, T. J., J.W. Gillespie, J. R., Pipes, R. B., Manson, J.-A. E., and Seferis, J. C., "Prediction of Process-Induced Residual Stresses in Thermoplastic Composites," *Journal of Composite Materials*, Vol. 24, No. 6, 1990, pp. 616–643.

[143] Parlevliet, P. P., Bersee, H. E. N., and Beukers, A., "Residual stresses in thermoplastic composites—A study of the literature—Part II: Experimental techniques," *Composites Part A: Applied Science and Manufacturing*, Vol. 38, No. 3, 2007, pp. 651–665.

[144] Lu, H., Schlottermuller, M., Himmel, N., and Schledjewski, R., "Effects of Tape Tension on Residual Stress in Thermoplastic Composite Filament Winding," *Journal of Thermoplastic Composite Materials*, Vol. 18, No. 6, 2005, pp. 469–487.

[145] Siddharth Pantoji, C. K. and Peeters, D., "Measuring Sources of Manufacturing Process Variations in Automated Fiber Placement Composites," *23rd International Conference on Composite Materials (ICCM23)*, 2023.

[146] Wang, E. L. and Gutowski, T. G., "Laps and gaps in thermoplastic composites processing," *Composites Manufacturing*, Vol. 2, No. 2, 1991, pp. 69 – 78.

[147] Mayer, M., Schuster, A., Brandt, L., Deden, D., and Fischer, F., "Integral quality assurance method for a CFRP aircraft fuselage skin: Gap and overlap measurement for thermoplastic AFP," *International Conference on Flexible Automation and Intelligent Manufacturing*, Springer, 2023, pp. 525–534.

[148] Yadav, N. and Schledjewski, R., "Parametric Effect on inline Width Control For Thermoplastic automated Tape Layup," *23rd International Conference on Composite Materials (ICCM23)*, 2023.

[149] Kirchhoff, J., Tehrani, M., Heathman, N., Yap, T., and Koirala, P., "In-Situ Consolidated Automated Fiber Placement Carbon Fiber PAEK Composites," *23rd International Conference on Composite Materials (ICCM23)*, 2023.

[150] Yap, T., Tamijani, A. Y., and Tehrani, M., "Aerospace Quality In-situ Consolidated Thermoplastic Composite Structures via Automated Fiber Placement: Effects of Staggering on Part Performance," *AIAA SCITECH 2023 Forum*, 2023.

[151] Stokes-Griffin, C., Kollmannsberger, A., Compston, P., and Drechsler, K., "The effect of processing temperature on wedge peel strength of CF/PA6 laminates manufactured in a laser tape placement process," *Composites Part A: Applied Science and Manufacturing*, Vol. 121, 2019, pp. 84–91.

[152] Comer, A. J., Katnam, K. B., Stanley, W. F., and Young, T. M., "Characterising the behaviour of composite single lap bonded joints using digital image correlation," *International Journal of Adhesion and Adhesives*, Vol. 40, 1 2013, pp. 215–223.

[153] Zinnecker, V., Stokes-Griffin, C. M., Khudiakova, A., Wolfahrt, M., and Compston, P., "A comparative study for shear testing of thermoplastic-based composites and metal-composite hybrids," *Composites Part A: Applied Science and Manufacturing*, Vol. 137, 2020, pp. 105953.

[154] Wanigasekara, C., Oromiehie, E., Swain, A., Prusty, B. G., and Nguang, S. K., "Machine Learning Based Predictive Model for AFP-Based Unidirectional Composite Laminates," *IEEE Transactions on Industrial Informatics*, Vol. 16, No. 4, 4 2020, pp. 2315–2324.

[155] Hoang, V.-T., Kwon, B.-S., Sung, J.-W., Choe, H.-S., Oh, S.-W., Lee, S.-M., Kweon, J.-H., and Nam, Y.-W., "Postprocessing method-induced mechanical properties of carbon fiber-reinforced thermoplastic composites," *Journal of Thermoplastic Composite Materials*, Vol. 36, No. 1, 2020, pp. 432–447.

[156] Chen, J., Fu, K., and Li, Y., "Understanding processing parameter effects for carbon fibre reinforced thermoplastic composites manufactured by laser-assisted automated fibre placement (AFP)," *Composites Part A: Applied Science and Manufacturing*, Vol. 140, 2021, pp. 106160.

[157] Oromiehie, E., Gain, A. K., and Prusty, B. G., "Processing parameter optimisation for automated fibre placement (AFP) manufactured thermoplastic composites," *Composite Structures*, Vol. 272, 2021, pp. 114223.

[158] Samoil Samak, M., Risteska, S., and Dukovski, V., "Some Experimental Investigation of Products from Thermoplastic Composite Materials Manufactured with Robot and LAFP," *International Journal of Engineering Research & Technology (IJERT)*, 2020.

[159] Seneviratne, W., Tomblin, J., and Schmitz, I., "Process Optimization for In-Situ Consolidation of Thermoplastic Structures with Fiber Steering Using Various Heating Methods and Tooling Concepts," *SAMPE neXus 2021*, The Society for the Advancement of Material and Process Engineering (SAMPE), 2021.

[160] Mössinger, I., Raps, L., Fricke, D., Freund, J., Löbbecke, M., and Chadwick, A. R., "Characteristics of in-situ automated fiber placement carbon-fiber-reinforced low-melt polyaryl ether ketone laminates part 1: Manufacturing influences," *Journal of Composite Materials*, Vol. 58, No. 15, 2024, pp. 1769–1787.

[161] Pourahmadi, E., Shadmehri, F., and Ganesan, R., "Interlaminar shear strength of Carbon/PEEK thermoplastic composite laminate: Effects of in-situ consolidation by automated fiber placement and autoclave re-consolidation," *Composites Part B: Engineering*, Vol. 269, 2024, pp. 111104.

[162] ASTM International, Subcommittee: D30.04, "ASTM D2344/D2344M-22 Standard Test Method for Short-Beam Strength of Polymer Matrix Composite Materials and Their Laminates," `https://www.astm.org/d2344_d2344m-22.html`, 2022.

[163] Wichita State University, "TC1225 Specification," `https://www.wichita.edu/industry_and_defense/NIAR/Research/torray-tc1225.php`, 2020.

[164] Zhou, G., Nash, P., Whitaker, J., and Jones, N., "Double beam shear (DBS) as a new test method for determining interlaminar shear properties of composite laminates," *ECCM16 - 16th European Conference on Composite Materials*, 4 2014.

[165] International Organization for Standardization, Technical Committee: ISO/TC 61/SC 13, "ISO 19927 Determination of interlaminar strength and modulus by double beam shear test," `https://www.astm.org/d2344_d2344m-22.html`, 2018.

[166] Martín, I., Fernández, K., Cuenca, J., Sánchez, C., Anaya, S., and Élices, R., "Design and manufacture of a reinforced fuselage structure through automatic laying-up and in-situ consolidation with co-consolidation of skin and stringers using thermoplastic composite materials," *Heliyon*, Vol. 9, No. 1, 2023, pp. e12728.

[167] Lamontia, M., Cope, R., Gruber, M. B., and B.J.Waibel, "Stringer-, honeycomb core-, and tigr-stiffened skins, and ring-stiffened cylinders fabricated from automated thermoplastic fiber placement and filament winding," Tech. rep., Accudyne Systems, Inc., 2002.

[168] Chadwick, A. and Willmeroth, M., "Use of in-process monitoring and ultrasound to detect defects in thermoplastic AFP-produced parts," *22nd Internationa Conference on Composite Materials (ICCM22)*, 8 2019.

[169] Oromiehie, E., Garbe, U., and Prusty, B. G., "Porosity analysis of carbon fibre-reinforced polymer laminates manufactured using automated fibre placement," *Journal of Composite Materials*, Vol. 54, No. 9, 2020, pp. 1217–1231.

[170] Harik, R., Saidy, C., Williams, S. J., Gurdal, Z., and Grimsley, B., "Automated fiber placement defect identity cards: cause, anticipation, existence, significance, and progression," *SAMPE 2018*, 2018.

[171] Heinecke, F. and Willberg, C., "Manufacturing-Induced Imperfections in Composite Parts Manufactured via Automated Fiber Placement," *Journal of Composites Science*, Vol. 3, No. 2, 2019.

[172] Brasington, A., Halbritter, J., Wehbe, R., and Harik, R., "Bayesian optimization for process planning selections in automated fiber placement," *Journal of Composite Materials*, Vol. 56, No. 28, 2022, pp. 4275–4296.

[173] Rousseau, G., Wehbe, R., Halbritter, J., and Harik, R., "Automated Fiber Placement Path Planning: A state-of-the-art review," *Computer-Aided Design and Applications*, Vol. 16, No. 2, 2019, pp. 172–203.

[174] Shirinzadeh, B., Cassidy, G., Oetomo, D., Alici, G., and Ang Jr, M. H., "Trajectory generation for open-contoured structures in robotic fibre placement," *Robotics and Computer-Integrated Manufacturing*, Vol. 23, No. 4, 2007, pp. 380–394.

[175] Patrikalakis, N. M., "Surface-to-surface intersections," *IEEE Computer Graphics and Applications*, Vol. 13, No. 1, 1993, pp. 89–95.

[176] Krishnan, S. and Manocha, D., "An Efficient Surface Intersection Algorithm Based on Lower-Dimensional Formulation," *ACM Transactions on Graphics*, Vol. 16, No. 1, 1997, pp. 74 – 106, Cited by: 107; All Open Access, Bronze Open Access.

[177] Brandis, H., *Konzeption eines integrierten Tape-Legesystems für die Applikation nichtabwickelbarer Luftfahrzeugstrukturen aus faserverstärktem Kunststoff*, Ph.D. thesis.

[178] Wunsch, M., *Herstellung von faserverstärkten Strukturen mittels modifizierter Bandlegetechnik*, Ph.D. thesis, 2001.

[179] Scholliers, J. and Van Brussel, H., "Computer-integrated filament winding: computer-integrated design, robotic filament winding and robotic quality control," *Composites Manufacturing*, Vol. 5, No. 1, 1994, pp. 15–23.

[180] Eslami, M. and Mohtashami, V., "Geodesic Path Computation on Connected Trimmed Surfaces," *IEEE Transactions on Antennas and Propagation*, Vol. 70, No. 11, 2022, pp. 10885–10893.

[181] Gurdal, Z. and Olmedo, R., "In-plane response of laminates with spatially varying fiber orientations - Variable stiffness concept," *AIAA JOURNAL*, Vol. 31, No. 4, 1993, pp. 751–758.

[182] Tatting, B., Gürdal, T., and Jegley, D., "Design and Manufacture of Elastically TailoredTow Placed Plates," Tech. rep., ADOPTECH, Inc., Blacksburg, Virginia.

[183] Gurdal, Z., Tatting, B., and Wu, K., "Tow-placement technology and fabrication issues for laminated composite structures," *46th AIAA/ASME/ASCE/AHS/ASC structures, structural dynamics and materials conference*, 2005.

[184] Lopes, C. S., Camanho, P. P., Guerdal, Z., and Tatting, B. F., "Progressive failure analysis of tow-placed, variable-stiffness composite panels," *International Journal of Solids and Structures*, Vol. 44, No. 25-26, 12 2007, pp. 8493–8516.

[185] Lopes, C. S., Remmers, J. J., and Gürdal, Z., "Influence of Porosity on the Interlaminar Shear Strength of Fibre-Metal Laminates," Vol. 383, 2008, pp. 35–52.

[186] Blom, A., Stickler, P., and Gurdal, Z., "Design and Manufacture of a Variable-Stiffness Cylindrical Shell," *Proceedings of the SAMPE Europe 30th International Conference*, 1 2009.

[187] Blom, A. W., Tatting, B. F., Hol, J. M. A. M., and Gürdal, Z., "Fiber path definitions for elastically tailored conical shells," *Composites Part B: Engineering*, Vol. 40, No. 1, 1 2009, pp. 77–84.

[188] Blom, A. W., Lopes, C. S., Kromwijk, P. J., Gurdal, Z., and Camanho, P. P., "A Theoretical Model to Study the Influence of Tow-drop Areas on the Stiffness and Strength of Variable-stiffness Laminates," *Journal of Composite Materials*, Vol. 43, No. 5, 3 2009, pp. 403–425, 22nd Annual Technical Conference of the American-Society-for-Composites, Seattle, WA, SEP 17-19, 2007.

[189] Blom, A. W., Abdalla, M. M., and Gurdal, Z., "Optimization of course locations in fiber-placed panels for general fiber angle distributions," *Composites Science and Technology*, Vol. 70, No. 4, 4 2010, pp. 564–570.

[190] Blom, A. W., Stickler, P. B., and Gürdal, Z., "Optimization of a composite cylinder under bending by tailoring stiffness properties in circumferential direction," *Composites Part B: Engineering*, Vol. 41, No. 2, 2010, pp. 157–165.

[191] Nik, M. A., Fayazbakhsh, K., Pasini, D., and Lessard, L., "Optimization of variable stiffness composites with embedded defects induced by Automated Fiber Placement," *Composite Structures*, Vol. 107, 1 2014, pp. 160–166.

[192] Fayazbakhsh, K., *The impact of gaps and overlaps on variable stiffness composites manufactured by Automated Fiber Placement*, Ph.D. thesis, 2014.

[193] Gürdal, Z., Tatting, B. F., and Wu, C. K., "Variable stiffness composite panels: Effects of stiffness variation on the in-plane and buckling response," *Composites Part A: Applied Science and Manufacturing*, Vol. 39, No. 5, 2008, pp. 911–922.

[194] Lopes, C. S., Gürdal, Z., and Camanho, P. P., "Tailoring for strength of composite steered-fibre panels with cutouts," *Composites Part A: Applied Science and Manufacturing*, Vol. 41, No. 12, 12 2010, pp. 1760–1767.

[195] Kim, B. C., Hazra, K., Weaver, P., and Potter, K., "Limitations of fibre placement techniques for variable angle tow composites and their process-induced defects," *Proceedings of the 18th International Conference on Composite Materials (ICMM18), Jeju, Korea*, 2010, pp. 21–26.

[196] Tam, A. S. and Gutowski, T. G., "The kinematics for forming ideal aligned fibre composites into complex shapes," *Composites Manufacturing*, Vol. 1, No. 4, 1990, pp. 219–228.

[197] Land, I. B., *Design and manufacture of advanced composite aircraft structures using automated tow placement*, Ph.D. thesis.

[198] Wang, H., Chen, J., Fan, Z., Xiao, J., and Wang, X., "Experimental Investigation on the Influence of Fiber Path Curvature on the Mechanical Properties of Composites," *Materials*, Vol. 14, No. 10, 2021, pp. 2602.

[199] Oya, N. and Johnson, D. J., "Longitudinal compressive behaviour and microstructure of PAN-based carbon fibres," *Carbon*, Vol. 39, No. 5, 2001, pp. 635–645.

[200] Zenker, T., *Einfluss prozessspezifischer Designparameter des Thermoplastischen Automated Fiber Placements auf die Bauteilqualität in Abhängigkeit der Prozesskette*, Ph.D. thesis, Technische Universität München, 2022.

[201] Belhaj, M. and Hojjati, M., "Wrinkle formation during steering in automated fiber placement: Modeling and experimental verification," *Journal of Reinforced Plastics and Composites*, Vol. 37, No. 6, 2018, pp. 396–409.

[202] Pan, H., Yang, D., Qu, W., Li, J., and Ke, Y., "Process-dependent wrinkle formation for steered tow during automated fiber placement: Modeling and experimental verification," *Thin-Walled Structures*, Vol. 180, 2022, pp. 109928.

[203] Smith, R. P., Qureshi, Z., Scaife, R. J., and El-Dessouky, H. M., "Limitations of processing carbon fibre reinforced plastic/polymer material using automated fibre placement technology," *Journal of Reinforced Plastics and Composites*, Vol. 35, No. 21, 2016, pp. 1527–1542.

[204] Akbarzadeh, A. H., Nik, M. A., and Pasini, D., "The role of shear deformation in laminated plates with curvilinear fiber paths and embedded defects," *Composite Structures*, Vol. 118, 12 2014, pp. 217–227.

[205] Blom, A. W., *Structural performance of fiber-placed, variable-stiffness composite conical and cylindrical shells*, Ph.D. thesis, 2010.

[206] Peeters, D. M. J., Lozano, G. G., and Abdalla, M. M., "Effect of steering limit constraints on the performance of variable stiffness laminates," *Computers and Structures*, Vol. 196, 2 2017, pp. 94–111.

[207] Bakhshi, N. and Hojjati, M., "An experimental and simulative study on the defects appeared during tow steering in automated fiber placement," *Composites Part A: Applied Science and Manufacturing*, Vol. 113, 2018, pp. 122–131.

[208] Hörmann, P. M., *Thermoset automated fibre placement – on steering effects and their prediction*, Ph.D. thesis, Technische Universität München, 2015.

[209] Matveev, M. Y., Schubel, P. J., Long, A. C., and Jones, I. A., "Understanding the buckling behaviour of steered tows in Automated Dry Fibre Placement (ADFP)," *Composites Part A: Applied Science and Manufacturing*, Vol. 90, 2016, pp. 451–456.

[210] Rajan, S., Sutton, M. A., Wehbe, R., Tatting, B., Gürdal, Z., Kidane, A., and Harik, R., "Experimental investigation of prepreg slit tape wrinkling during automated fiber placement process using StereoDIC," *Composites Part B: Engineering*, Vol. 160, 2019, pp. 546–557.

[211] Zhao, C., Xiao, J., Huang, W., Huang, X., and Gu, S., "Layup quality evaluation of fiber trajectory based on prepreg tow deformability for automated fiber placement," *Journal of Reinforced Plastics and Composites*, Vol. 35, No. 21, 2016, pp. 1576–1585.

[212] Wehbe, R., Sacco, C., Baz Radwan, A., Albazzan, M., and Harik, R., "Influence of process parameters in AFP fiber steering on cylinders: Constant curvature paths," *Composites Part C: Open Access*, Vol. 2, 2020, pp. 100036.

[213] Beakou, A., Cano, M., Le Cam, J.-B., and Verney, V., "Modelling slit tape buckling during automated prepreg manufacturing: A local approach," *Composite Structures*, Vol. 93, No. 10, 2011, pp. 2628–2635.

[214] Wehbe, R., Tatting, B., Rajan, S., Harik, R., Sutton, M., and Gurdal, Z., "Geometrical modeling of tow wrinkles in automated fiber placement," *Composite Structures*, Vol. 246, 8 2020.

[215] Wu, K., Tatting, B., Smith, B., Stevens, R., Occhipinti, G., Swift, J., Achary, D., and Thornburgh, R., "Design and Manufacturing of Tow-Steered Composite Shells Using Fiber Placement," *50th AIAA/ASME/ASCE/AHS/ASC Structures, Structural Dynamics, and Materials Conference*, 2012.

[216] Kim, B. C., Potter, K., and Weaver, P. M., "Continuous tow shearing for manufacturing variable angle tow composites," *Composites Part A: Applied Science and Manufacturing*, Vol. 43, No. 8, 2012, pp. 1347–1356.

[217] Kim, B. C., Weaver, P. M., and Potter, K., "Manufacturing characteristics of the continuous tow shearing method for manufacturing of variable angle tow composites," *Compoistes Part A: Applied Science and Manufacturing*, Vol. 61, 2014, pp. 141–151.

[218] Zenker, T. and Gnaedinger, M., "Consolidation Behavior of Fiber Steered Thermoplastic Automated Fiber Placement Preforms," *5th International Conference & Exhibition onThermoplastic Composites*, 11 2020.

[219] Clancy, G., Peeters, D., Oliveri, V., Jones, D., O'Higgins, R. M., and Weaver, P. M., "A study of the influence of processing parameters on steering of carbon Fibre/PEEK tapes using laser-assisted tape placement," *Composites Part B: Engineering*, Vol. 163, 4 2019, pp. 243–251.

[220] Rajasekaran, A. and Shadmehri, F., "Steering of carbon fiber/PEEK tapes using Hot Gas Torch-assisted automated fiber placement," *Journal of Thermoplastic Composite Materials*, Vol. 0, No. 0, 2022, pp. 08927057211067962.

[221] Oromiehie, E., Prusty, B. G., Compston, P., and Rajan, G., "Automated fibre placement based composite structures: Review on the defects, impacts and inspections techniques," *Composite Structures*, Vol. 224, 9 2019, pp. 110987.

[222] Yadav, N. and Schledjewski, R., "Review of in-process defect monitoring for automated tape laying," *Composites Part A: Applied Science and Manufacturing*, Vol. 173, 2023, pp. 107654.

[223] Jegley, D. C., Tatting, B. F., and Guerdal, Z., "Automated Finite Element Analysis of Elastically-Tailored Plates," Tech. rep., NASA Langley Research Center, 2003.

[224] Mishra, V., Peeters, D. M. J., and Abdalla, M. M., "Stiffness and buckling analysis of variable stiffness laminates including the effect of automated fibre placement defects," *Composite Structures*, Vol. 226, 10 2019.

[225] Croft, K., Lessard, L., Pasini, D., Hojjati, M., Chen, J., and Yousefpour, A., "Experimental study of the effect of automated fiber placement induced defects on performance of composite laminates," *Composites Part A: Applied Science and Manufacturing*, Vol. 42, No. 5, 5 2011, pp. 484–491.

[226] Falcó, O., Mayugo, J. A., Lopes, C. S., Gascons, N., Turon, A., and Costa, J., "Variable-stiffness composite panels: As-manufactured modeling and its influence on the failure behavior," *Composites Part B: Engineering*, Vol. 56, 2014, pp. 660–669.

[227] Del Rossi, D., Cadran, V., Thakur, P., Palardy-Sim, M., Lapalme, M., and Lessard, L., "Experimental investigation of the effect of half gap/half overlap defects on the strength of composite structures fabricated using automated fibre placement (AFP)," *Composites Part A: Applied Science and Manufacturing*, Vol. 150, 2021, pp. 106610.

[228] Guin, W. E., Jackson, J. R., and Bosley, C. M., "Effects of tow-to-tow gaps in composite laminates fabricated via automated fiber placement," *Composites Part A: Applied Science and Manufacturing*, Vol. 115, DEC 2018, pp. 66–75.

[229] Nguyen, M. H., Vijayachandran, A. A., Davidson, P., Call, D., Lee, D., and Waas, A. M., "Effect of Automated Fiber Placement (AFP) Manufacturing Signature on Mechanical Performance," *AIAA Scitech 2019 Forum*, 2019.

[230] Nguyen, M. H., Vijayachandran, A. A., Davidson, P., Call, D., Lee, D., and Waas, A. M., "Effect of automated fiber placement (AFP) manufacturing signature on mechanical performance of composite structures," *Composite Structures*, Vol. 228, 2019, pp. 111335.

[231] Jamora, V. C., Rauch, V., Kravchenko, S. G., and Kravchenko, O. G., "Effect of Resin Bleed Out on Compaction Behavior of the Fiber Tow Gap Region during Automated Fiber Placement Manufacturing," *Polymers*, Vol. 16, No. 1, 2023.

[232] Marouene, A., Legay, P., and Boukhili, R., "Experimental and numerical investigation on the open-hole compressive strength of AFP composites containing gaps and overlaps," *Journal of Composite Materials*, Vol. 51, No. 26, 11 2017, pp. 3631–3646.

[233] Nartey, M., Zhang, T., Gong, B., Wang, J., Peng, S., Wang, H., and Peng, H.-X., "Understanding the impact of fibre wrinkle architectures on composite laminates through tailored gaps and overlaps," *Composites Part B: Engineering*, Vol. 196, 9 2020, pp. 108097.

[234] Tang, Y., Wang, W., Wang, H., Li, J., and Ke, Y., "Influences of wrinkles induced by tows' offset in automated fiber placement on the bending properties of composites," *Composite Structures*, Vol. 297, 2022, pp. 115964.

[235] Lan, M., Cartie, D., Davies, P., and Baley, C., "Microstructure and tensile properties of carbon-epoxy laminates produced by automated fibre placement: Influence of a caul plate on the effects of gap and overlap embedded defects," *Composites Part A: Applied Science and Manufacturing*, Vol. 78, 11 2015, pp. 124–134.

[236] Lan, M., Cartie, D., Davies, P., and Baley, C., "Influence of embedded gap and overlap fiber placement defects on the microstructure and shear and compression properties of carbon-epoxy laminates," *Composites Part A: Applied Science and Manufacturing*, Vol. 82, 3 2016, pp. 198–207.

[237] Li, X., Hallett, S. R., and Wisnom, M. R., "Modelling the effect of gaps and overlaps in automated fibre placement (AFP)-manufactured laminates," *Science and Engineering of Composite Materials*, Vol. 22, No. 2, SI, 3 2015, pp. 115–129.

[238] Anay, R., Miller, D., Tessema, A., Wehbe, R., Ziehl, P., Tatting, B., Gurdal, Z., Harik, R., and Kidane, A., "An experimental investigation concerning the effect of AFP defects on progressive damage in CFRP coupons," *Composite Structures*, Vol. 279, 2022, pp. 114725.

[239] Falcó, O., Lopes, C. S., Naya, F., Sket, F., Maimí, P., and Mayugo, J. A., "Modelling and simulation of tow-drop effects arising from the manufacturing of steered-fibre composites," *Composites Part A: Applied Science and Manufacturing*, Vol. 93, 2017, pp. 59–71.

[240] Falco, O., Mayugo, J. A., Lopes, C. S., Gascons, N., and Costa, J., "Variable-stiffness composite panels: Defect tolerance under in-plane tensile loading," *Composites Part A: Applied Science and Manufacturing*, Vol. 63, AUG 2014, pp. 21–31.

[241] Falcó, O., Lopes, C. S., Mayugo, J. A., Gascons, N., and Renart, J., "Effect of tow-drop gaps on the damage resistance and tolerance of Variable-Stiffness Panels," *Composite Structures*, Vol. 116, 2014, pp. 94–103.

[242] Zhang, Z., Chen, C., Zhang, S., Guo, C., Ni, M., Liu, X., Yang, K., Chen, Q., and Wang, H., "Effect of AFP induced triangular gaps on manufacturing quality and stress distribution of composite panels," *Composites Science and Technology*, Vol. 243, 2023, pp. 110222.

[243] Sawicki, A. and Minguett, P., "The effect of intraply overlaps and gaps upon the compression strength of composite laminates," *39th AIAA/ASME/ASCE/AHS/ASC Structures, Structural Dynamics, and Materials Conference and Exhibit*, 1998, p. 1786.

[244] Woigk, W., Hallett, S. R., Jones, I, M., Kuhtz, M., Hornig, A., and Gude, M., "Experimental investigation of the effect of defects in Automated Fibre Placement produced composite laminates," *Composite Structures*, Vol. 201, 10 2018, pp. 1004–1017.

[245] Suemasu, H., Aoki, Y., Sugimoto, S., and Nakamura, T., "Effect of gap on strengths of automated fiber placement manufactured laminates," *Composite Structures*, Vol. 263, 2021, pp. 113677.

[246] Zhou, W., Cheng, Q., Xu, Q., Zhu, W., and Ke, Y., "Deformation and fracture mechanisms of automated fiber placement pre-preg laminates under out-of-plane tensile loading," *Composite Structures*, Vol. 255, 2021, pp. 112948.

[247] Ju, X., Xiao, J., Wang, D., Zhao, C., Gao, T., and Wang, X., "Effect of gaps/overlaps induced waviness on the mechanical properties of automated fiber placement (AFP)-manufactured composite laminate," *Materials Research Express*, Vol. 9, No. 4, 2022, pp. 045305.

[248] Böckl, B., Wedel, A., Misik, A., and Drechsler, K., "Effects of defects in automated fiber placement laminates and its correlation to automated optical inspection results," *Journal of Reinforced Plastics and Composites*, Vol. 42, No. 1-2, 2023, pp. 3–16.

[249] Nguyen, M. H., Davidson, P., and Waas, A. M., "Experimental and numerical study on the tensile failure behavior of toughened-interlayer composite laminates with automated fiber placement (AFP) induced gap and overlap defects," *International Journal of Material Forming*, 2020, pp. 1–15.

[250] Ghayour, M., Ganesan, R., and Hojjati, M., "Flexural response of composite beams made by Automated Fiber Placement process: Effect of fiber tow gaps," *Composites Part B: Engineering*, Vol. 201, 2020, pp. 108368.

[251] Qian, S., Liu, X., Ye, Y., Xu, Q., Zhang, T., and Li, X., "Effect of gap and overlap fiber placement defects on the delamination behavior of L-shaped composite laminates," *Composite Structures*, Vol. 268, 2021, pp. 113963.

[252] Cartié, D., Lan, M., Davies, P., and Baley, C., "Influence of Embedded Gap and Overlap Fiber Placement Defects on Interlaminar Properties of High Performance Composites," *Materials*, Vol. 14, No. 18, 2021.

[253] Marrouze, J. P., Housner, J., and Abdi, F., "Effect of manufacturing defects and their uncertainties on strength and stability of stiffened panels," *ICCM19, Montreal Canada*, 2013.

[254] Zhang, X. Z., Bai, R. X., Lei, Z. K., Zhu, Y. G., Geng, C. H., Feng, Y., Zhong, Z., and Wu, W., "Study on tensile properties of composite laminates with gap defects," *2nd International Workshop on Materials Science and Mechanical Engineering*, edited by Fan, HJ, Vol. 504, 2019.

[255] Ghayour, M., Hojjati, M., and Ganesan, R., "Induced defect layer method to characterize the effect of fiber tow gaps for the laminates manufactured by automated fiber placement technique," *Journal of Composite Materials*, 2021, pp. 00219983211031649.

[256] Falcó Salcines, O. et al., *Analysis of process-induced defects on steered-fiber panels for aeronautical applications*, Ph.D. thesis, 2014.

[257] Nimbal, S. S., Banker, M. M., Roopa, A., Varughese, B., and Sundaram, R., "Effect of Gap Induced Waviness on Compressive Strength of Laminated Composites," *Materials Today: Proceedings*, Vol. 4, No. 8, 2017, pp. 8355–8369, International Conference on Advancements in Aeromechanical Materials for Manufacturing (ICAAMM), MLR Inst Technol, Hyderabad, INDIA, 2016.

[258] Swingle, N., Brasington, A., Halbritter, J., and Harik, R., "Automated Fiber Placement Laminate Level Optimization for Mitigation of Through Thickness Defect Stacking," *Sampe Journal*, Vol. 59, No. 6, 2023, pp. 32–47.

[259] Zenker, T., Bruckner, F., and Drechsler, K., "Effects of defects on laminate quality and mechanical performance in thermoplastic Automated Fiber Placement-based process chains," *Advanced Manufacturing: Polymer & Composites Science*, Vol. 5, No. 4, 2019, pp. 184–205.

[260] Rakhshbahar, M. and Sinapius, M., "A novel approach: combination of automated fiber placement (AFP) and additive layer manufacturing (ALM)," *Journal of Composites Science*, Vol. 2, No. 3, 2018, pp. 42.

[261] Clancy, G. J., O'Higgins, R., and Weaver, P. M., "Spreading of Carbon Fiber/Thermoplastic Pre-preg Tapes," *AIAA Scitech 2020 Forum*, 2020, p. 0481.

[262] Clancy, G., Peeters, D., O'Higgins, R. M., and Weaver, P. M., "In-line variable spreading of carbon fibre/thermoplastic pre-preg tapes for application in automatic tape placement," *Materials & Design*, Vol. 194, 2020, pp. 108967.

[263] Peeters, D., Deane, M., O'Higgins, R., and Weaver, P. M., "Morphology of ply drops in thermoplastic composite materials manufactured using laser-assisted tape placement," *Composite Structures*, Vol. 251, 11 2020.

[264] Ribeiro, P., Akhavan, H., Teter, A., and Warmiński, J., "A review on the mechanical behaviour of curvilinear fibre composite laminated panels," *Journal of Composite Materials*, Vol. 48, No. 22, 2014, pp. 2761–2777.

[265] Alhajahmad, A., Abdalla, M. M., and Gürdal, Z., "Optimal Design of Tow-Placed Fuselage Panels for Maximum Strength with Buckling Considerations," *Journal of Aircraft*, Vol. 47, No. 3, 5 2010, pp. 775–782.

[266] Huang, G., Wang, H., and Li, G., "An efficient reanalysis assisted optimization for variable-stiffness composite design by using path functions," *Composite Structures*, Vol. 153, 10 2016, pp. 409–420.

[267] Xia, Q. and Shi, T., "Optimization of composite structures with continuous spatial variation of fiber angle through Shepard interpolation," *Composite Structures*, Vol. 182, 12 2017, pp. 273–282.

[268] Hong, Z., Peeters, D., and Turteltaub, S., "An enhanced curvature-constrained design method for manufacturable variable stiffness composite laminates," *Computers & Structures*, Vol. 238, 10 2020.

[269] Mori, Y., Matsuzaki, R., and Kumekawa, N., "Variable thickness design for composite materials using curvilinear fiber paths," *Composite Structures*, Vol. 263, 2021, pp. 113723.

[270] Ghiasi, H., Fayazbakhsh, K., Pasini, D., and Lessard, L., "Optimum stacking sequence design of composite materials Part II: Variable stiffness design," *Composite Structures*, Vol. 93, No. 1, 2010, pp. 1–13.

[271] Lozano, G. G., Tiwari, A., and Turner, C., "A design algorithm to model fibre paths for manufacturing of structurally optimised composite laminates," *Composite Structures*, Vol. 204, 11 2018, pp. 882–895.

[272] Zheng, Z., Bai, R. X., Lei, Z. K., Zhu, Y. G., and Zhang, X. Z., "Failure analysis of variable-stiffness laminate considering manufacturing defects," *2nd international Workshop on Materials Science and Mechanical Engineering (IWMSME2018)*, edited by Fan, HJ, Vol. 504, IOP PUBLISHING LTD, 2018.

[273] Vijayachandran, A. A. and Waas, A. M., "Minimizing stress concentrations using steered fiberpaths and incorporating realistic manufacturing signatures," *International Journal of Non-Linear Mechanics*, Vol. 146, 2022, pp. 104160.

[274] Fayazbakhsh, K., Nik, M. A., Pasini, D., and Lessard, L., "Defect layer method to capture effect of gaps and overlaps in variable stiffness laminates made by Automated Fiber Placement," *Composite Structures*, Vol. 97, 2013, pp. 245 – 251.

[275] Marouene, A., Boukhili, R., Chen, J., and Yousefpour, A., "Effects of gaps and overlaps on the buckling behavior of an optimally designed variable-stiffness composite laminates - A numerical and experimental study," *Composite Structures*, Vol. 140, 4 2016, pp. 556–566.

[276] Marouene, A., Boukhili, R., Chen, J., and Yousefpour, A., "Buckling behavior of variable-stiffness composite laminates manufactured by the tow-drop method," *Composite Structures*, Vol. 139, 2016, pp. 243–253.

[277] Khani, A., Abdalla, M. M., Gurdal, Z., Sinke, J., Buitenhuis, A., and Van Tooren, M. J. L., “Design, manufacturing and testing of a fibre steered panel with a large cut-out,” *Composite Structures*, Vol. 180, 11 2017, pp. 821–830.

[278] Zhu, Y., Liu, J., Liu, D., Xu, H., Yan, C., Huang, B., and Hui, D., “Fiber path optimization based on a family of curves in composite laminate with a center hole,” *Composites Part B: Engineering*, Vol. 111, 2 2017, pp. 91–102.

[279] Peeters, D. M. J., Irisarri, F.-X., Groenendijk, C., and Ruzek, R., “Optimal design, manufacturing and testing of non-conventional laminates,” *Composite Structures*, Vol. 210, 2 2019, pp. 29–40.

[280] Blom, A., Stickler, P., Rassaian, M., and Gürdal, Z., “Bending Test of a Variable-Stiffness Fiber Reinforced Composite Cylinder,” *51st AIAA/ASME/ASCE/AHS/ASC Structures, Structural Dynamics, and Materials Conference*, 2010.

[281] Oliveri, V., Zucco, G., Peeters, D., Clancy, G., Telford, R., Rouhi, M., McHale, C., O’Higgins, R. M., Young, T. M., and Weaver, P. M., “Design, Manufacture and Test of an In-Situ Consolidated Thermoplastic Variable-Stiffness Wingbox,” *AIAA Journal*, Vol. 57, No. 4, 4 2019, pp. 1671–1683.

[282] Peeters, D., Clancy, G. J., Oliveri, V., O’Higgins, R., Jones, D., and Weaver, P. M., “Thermoplastic composite stiffener design with manufacturing considerations,” *2018 AIAA/ASCE/AHS/ASC Structures, Structural Dynamics, and Materials Conference*, 2018.

[283] Deden, D., Brandt, L., Mayer, M., Henning, D., Hellbach, O., and Fischer, F., “Full-Scale Application of in-situ Automated Fiber Placement for the Production of a Fuselage Skin Segment,” *SAMPE Europe 23 Conference*, Oktober 2023.

[284] Fischer, F., “Building the MFFD upper shell - Production technologies for the world’s largest thermoplastic composite structure,” *AIAA SciTech Forum*, Januar 2022.

[285] Fischer, F., Endraß, M., Deden, D., Brandt, L., Engelschall, M., Mayer, M., Vistein, M., Schönheits, M., Gänswürger, P., Görick, D., Schuster, A., Jarka, S., Bauer, S., Hellbach, O., Schmorell, D., Larsen, L.-C., Frommel, C., Huber, A., and Joos, M., “Production of the Thermoplastic Composite Upper Shell for the MFFD,” *Deutscher Luft- und Raumfahrtkongress (DLRK 2023)*, September 2023.

[286] Fischer, F., Endraß, M., Deden, D., Brandt, L., Engelschall, M., Gänswürger, P., Mayer, M., Vistein, M., Schönheits, M., Schuster, A., Jarka, S., Bauer, S., Hellbach, O., Larsen, L.-C., Kupke, M., and Ferstl, S., “How to Produce a Thermoplastic Fuselage,”

6th International Conference & Exhibition on Thermoplastic Composites (ITHEC 2022), Vol. 6, Oktober 2022.

[287] "The JEC Composites Innovation Awards: 2023 Official finalists line up," `https://www.jeccomposites.com/press/the-jec-composites-innovation-awards-2023-official-finalists-line-up/`, Accessed: 2023-02-07.

[288] Zuazo, M., "Manufacture process of structuralupper skin panel highly integrated incarbon fibre reinforced thermoplasticmaterial," *Proceedings of the 20th International Conference on Composite Materials*, 2023.

[289] German Aerospace Center (DLR), "MFFD – using thermoplastics to replace aluminium in aircraft construction," `https://www.dlr.de/en/latest/news/2023/03/mffd-thermoplastics-instead-of-aluminium-in-aircraft-construction`, 2023.

[290] Raps, L., Photograph of CETIM Krueger wing flap at JEC World 2025, 2025.

[291] Bayer, N., *Multi-Level Analysis for DataDriven Defect Detection in Thermoplastic AFP Manufacturing Processes for Composite Structures*, Master's thesis, 2024.

[292] ASTM International, Subcommittee: E07.06, "ASTM E1001-21 Standard Practice for Detection and Evaluation of Discontinuities by the Immersed Pulse-Echo Ultrasonic Method Using Longitudinal Waves," `https://www.astm.org/e1001-21.html`, 2021.

[293] Airbus S.A.S Engineering Directorate, "AITM1-0007 AITM Airbus Test Method Fibre Reinforced Plastics Determination of Plain, Open Hole and Filled Hole Tensile Strength," 2016.

[294] Airbus S.A.S Engineering Directorate, "AITM1-0008 AITM Airbus Test Method Fibre Reinforced PlasticsDetermination of Plain, Open Hole and Filled Hole Compression Strength," 2015.

[295] ASTM International, Subcommittee: D30.04, "ASTM D7264 Standard Test Method for Flexural Properties of Polymer Matrix Composite Materials," `https://www.astm.org/d7264_d7264m-21.html`, 2007.

[296] Raps, L., Chadwick, A. R., and Voggenreiter, H. F., "Layup Strategies for in-situ Automated Fiber Placementof Complex Geometries," *7th International Symposium on Automated Composite Manufacturing, Delft, the Netherlands*, 2026.

[297] German Aerospace Center (DLR), "CFK-Booster für Ariane 6 erfolgreich getestet," `https://www.dlr.de/de/aktuelles/nachrichten/2017/20170721_`

`cfk-booster-fuer-ariane-6-erfolgreich-getestet_23395`, 2017, Accessed: 2024-07-09.

[298] Sharma, P., Sharma, S., Bera, T., Semwal, K., Badhe, R. M., Sharma, A., Kapur, G. S., Ramakumar, S. S. V., and Neogi, S., "Effects of dome shape on burst and weight performance of a type-3 composite pressure vessel for storage of compressed hydrogen," *Composite Structures*, Vol. 293, 2022, pp. 115732.

[299] Vasiliev, V. V., *Composite pressure vessels: Design, analysis, and manufacturing*, Bull Ridge Corporation, 2009.

[300] McCarville, D. A., Guzman, J. C., Dillon, A. K., Jackson, J. R., and Birkland, J. O., "3.5 Design, Manufacture and Test of Cryotank Components," *Comprehensive Composite Materials II*, edited by P. W. Beaumont and C. H. Zweben, Elsevier, pp. 153–179.

[301] Blacker, C. and Tsyganenko, P., "Logarithmic spirals on surfaces of constant Gaussian curvature," *Involve, a Journal of Mathematics*, Vol. 17, No. 4, 2024, pp. 689–708.

[302] Fricke, D., Tröger, S., Schneider, M., and Kerker, K., "Entwicklung eines induktionsbeheizten Werkzeugs für out-of-autoclave-Fertigungsprozesse für Faserverbundbauteile," *Deutscher Luft- und Raumfahrtkongress (DLRK 2023)*, September 2023.

[303] Airbus Engineering Directorate, "AIPS03-02-019 Manufacture of Monolithic Parts with Thermoset Prepreg Materials," 2016.

[304] Raps, L., Chadwick, A., Fricke, D., and Schaefer, Y., "Steering Limitations for in-situ Autoated Fibre Placement Manufactured Structures," *International Conference on Composite Materials (ICCM) 23*, 2023.

[305] Raps, L., Chadwick, A. R., and Voggenreiter, H. F., "Steering for in-situ AFP-manufactured structures: Part 1 - Critical arc length," *Composite Structures*, Vol. 381, 2026, pp. 120023.

[306] Raps, L., Chadwick, A. R., Schäfer, Y., and Voggenreiter, H. F., "Steering for in-situ AFP-manufactured structures: Part 2 - Optimized layup strategy," *Composite Structures*, Vol. 381, 2026, pp. 120024.

[307] Raps, L., Atzler, F., Chadwick, A. R., and Voggenreiter, H., "In-situ automated fiber placement gap defects filled by fused granular fabrication," *Manufacturing Letters*, Vol. 40, 2024, pp. 125–128.

[308] Raps, L., Chadwick, A. R., and Voggenreiter, H. F., "Effect of geometry-induced triangular gap and overlap defects on in-situ AFP-manufactured structures," *Composite Structures*, Vol. 373, 2025, pp. 119556.

[309] KUKA Roboter GmbH, "KR QUANTEC ultra Mit F- und C-Varianten Betriebsanleitung," 2013.

[310] KUKA Deutschland GmbH, "KUKA Positionierer DKP-400 Betriebsanleitung," 2019.

[311] Zhou, W., "Theory and Experiment of Industrial Robot Accuracy Compensation Method Based on Spatial Interpolation," *Journal of Mechanical Engineering*, Vol. 49, 2013, pp. 42.

[312] ASTM International, Subcommittee: D30.04, "ASTM D6641/D6641M-16e2 Standard Test Method for Compressive Properties of Polymer Matrix Composite Materials Using a Combined Loading Compression (CLC) Test Fixture," `https://www.astm.org/d6641_d6641m-16e02.html`, 2023.

[313] Chadwick, A. R., Doll, G., Christ, U., Maier, S., and Lansky, S., "Performance of In-situ Automated Fibre Placement Parts," *Composites Part A: Applied Science and Manufacturing*, Vol. 192, 2025, pp. 108725.